Simulation of 3-D Crack Growth in Welded Structures based on Residual Stresses Obtained from Detailed Welding Process Models

Simulation of 3-D Crack Growth in Welded Structures based on Residual Stresses Obtained from Detailed Welding Process Models

by

Haomin Fu

A Dissertation

Presented to the Graduate and Research Committee

of Lehigh University

in Candidacy for the Degree of

Doctor of Philosophy

in

Mechanical Engineering

Lehigh University

May 2025

Approved and recommended for acceptance as a dissertation in partial fulfillment of the requirements for the degree of Doctor of Philosophy

Haomin Fu

Simulation of 3-D Crack Growth in Welded Structures based on Residual Stresses Obtained from Detailed Welding Process Models

April 23, 2025

Defense Date

Dr. Herman F. Nied

Dissertation Director

April 23, 2025

Approved Date

Committee Members:

Dr. Herman F. Nied

Dr. Hannah Dailey

Dr. Edmund Webb III

Dr. Richard Sause

Dr. Sena Kizildemir

ACKNOWLEDGEMENTS

The successful completion of this dissertation would not have been possible without the support and assistance of many professors, colleagues, classmates, and my family. I would like to express my heartfelt gratitude to all those who have helped and supported me throughout this journey.

First and foremost, I would like to extend my sincere thanks to my advisor, Professor Herman Nied, for his invaluable guidance throughout every stage of this research. From topic selection and research direction to data analysis and academic writing, Professor Nied devoted great effort and provided patient, detailed explanations to my questions. His rigorous academic attitude and rich research experience have been profoundly influential and have laid a solid foundation for my future academic pursuits.

I am also deeply grateful to the professors, colleagues, and fellow students in my department for their generous support in both professional and technical aspects. I would like to thank Professor Carlos Romero at the Energy Research Center for providing project and funding support during my research. I am especially thankful to my friends and colleagues Dr. Julio Bravo, Yi Ding, Zeyuan Tian, and Jincheng Liu and all my fellow colleagues in ERC for their continuous encouragement and support in both my academic and personal life. Your presence and motivation helped me persevere through this journey.

I would also like to express my sincere appreciation to Dr. Adrian Loghin at Simmetrix, Inc., for his assistance and support in learning and utilizing SimModeler, and to Mr. Ramon Juan Silva at ESI, Inc., for his technical support with SYSWELD.

During the writing of this dissertation, my parents and friends provided unwavering encouragement and support. Their care in daily life, emotional comfort, and continual motivation helped me overcome difficulties and maintain a positive mindset during challenging times.

Finally, I would like to express my deepest gratitude to everyone who has supported me in my academic and personal life. I am fully aware that this dissertation may contain shortcomings, and I sincerely welcome any comments and suggestions from experts and faculty.

TABLE OF CONTENTS

LIST OF FIGURES

LIST OF TABLES

Abstract

Residual stresses are one of the major contributors to structural failure. For instance, the residual stresses induced by straightening processes in railway tracks can lead to vertical cracks that compromise structural integrity. Welding, as a widely used manufacturing technique, introduces significant residual stresses, which are particularly problematic in large structures where post-weld heat treatment is not feasible. Among the adverse effects of welding residual stress, its impact on fatigue crack growth is a critical concern, as it can increase the stress intensity factor (SIF) at the crack tip, thereby reducing fatigue life, and alter crack propagation trajectories, making them difficult to predict. Extensive research has been conducted on finite element (FE) simulations of welding processes and fracture mechanics; however, studies that integrate detailed welding process models with fatigue crack growth models remain scarce. Most existing works focus only on computing SIFs under residual stress conditions without incorporating comprehensive fatigue crack propagation simulations. To address this gap, this study employs a finite element method to integrate detailed welding models with fatigue fracture mechanics models for fatigue crack growth simulations in residual stress environments. The welding finite element simulations include hot cracking tests and multiple welding techniques, while the fatigue crack growth simulations are conducted using the Paris law, the maximum stress criterion, and the Walker equation. The results encompass residual stress distributions for different welding techniques, quantification of welding hot cracking tests, automated optimization and computation using APDL scripting, as well as SIF calculations and crack trajectory predictions under residual stress conditions. This research integrates detailed welding residual stress fields with the Walker equation in fracture mechanics to improve the

accuracy of crack growth simulations, providing a more reliable method for fatigue life assessment in welded structures.

Keywords: Fatigue Crack Growth, Welded Structures, Residual Stress, Finite Element Simulation, Walker Equation

1. Introduction

1.1. General Background

Welding is widely utilized in various industries due to its efficiency and versatility. However, one of its major drawbacks is the introduction of residual stresses, which can significantly affect the structural integrity and service life of welded components. These stresses primarily arise due to nonuniform thermal expansion and contraction during welding, leading to stress accumulation. In large-scale welded structures where post-weld heat treatment (PWHT) is not feasible, residual stress becomes even more problematic, contributing to distortion, premature cracking, and unpredictable fracture behavior.

Moreover, in addition to considering the influence of welding residual stress on fatigue crack propagation, it is also necessary to account for the initial cracks caused by hot cracking that may form during the welding process. During welding, if the tensile strain experienced by the molten metal region during solidification exceeds a critical threshold, hot cracks will develop. Hot cracking weldability tests are commonly used to examine and quantify the conditions under which hot cracks form. However, these tests only consider the effects of mechanical external loads and fail to account for the thermal stresses induced by the welding heat source and the shrinkage of the metal during solidification.

This study aims to integrate welding simulation with three-dimensional crack simulation using the finite element method to fill the gap in accurately predicting crack initiation and propagation in the presence of welding residual stresses. The research includes finite element-based three-dimensional crack propagation simulations, an investigation of the influence of the shear center on crack growth, hot cracking weldability test model based on the three-dimensional finite element method, simulations of various

welding processes, and crack propagation simulations under welding residual stress conditions.

1.2. Fatigue Crack Simulation Tool

An important concept in structural mechanics, is that the fundamental state of stress at a point should be characterized in terms of the principal stresses, since these three quantities are invariant with respect to the coordinate system. Thus, all stress-based failure criteria in continuum mechanics are most effectively expressed in terms of the principal stresses. For example, when a solid circular cylinder is subjected to pure torsion, the shear stresses on the cylinder's outermost radial surface, can alternatively be expressed in terms of the principal stresses. In pure torsion, the maximum and minimum principal stresses are given by the tensile (maximum) and compressive (minimum) principal stress components oriented at ±45° with respect to the cylinder's axis. A very effective demonstration of how the principal stresses control brittle fracture behavior can be performed by twisting a brittle solid cylinder, e.g., a piece of chalk, until it fractures. The resulting fracture will consistently result in a spiral crack that initiates at a 45° angle with respect to the cylinder's axis. Such fracture behavior is shown in Figure 1, for a typical spiral fracture in a solid PMMA rod subjected to pure torsion.

The simple explanation for this behavior is that brittle fracture will progress in a direction that favors crack growth perpendicular to the maximum principal stress in tension. Since most brittle solids have numerous, randomly oriented, surface defects: A small crack oriented perpendicular to the maximum principal stress will be subjected to the most severe tensile loading and will be the flaw most likely to propagate in a critical manner.

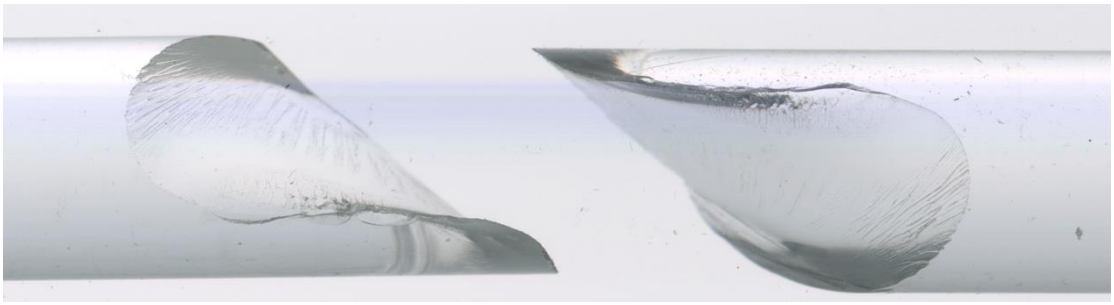

Figure 1. Spiral fracture in a Polymethyl methacrylate (PMMA) solid cylindrical rod subjected to pure torsion.

Even in cases where initial surface cracks are not aligned normal to the maximum principal stress, the state of stress at the crack tip characterized by the mixed-mode stress intensity factors will cause an advancing crack to quickly turn so that it is reoriented perpendicular to the maximum (tensile) principal stress, i.e., 45° with respect to the axis of twist. This description of torsional fracture, based solely on the principal surface stresses, represents an overly simplified 2-D viewpoint, since it does not consider the full 3-D nature of the propagating crack. A 3-D surface crack will propagate locally at different angles with respect to the crack front, in both the radial and axial directions, resulting in a characteristic spiral-shaped torsional fracture whose shape is dictated by both the loading and the evolving crack geometry. Spiral fractures in cylinders represent an important example of crack propagation that can only be completely assessed using computational techniques that incrementally advance the crack front, resulting in crack surfaces that continuously evolve in a general 3-D manner.

Crack initiation and propagation is of considerable concern in rotating machinery, where fracture of a shaft can result in catastrophic failure [1]. In torque transmitting metal shafts, shaft fracture is usually attributed to subcritical fatigue crack growth that occurs over many alternating load cycles [2]. The three most important loading conditions that contribute to crack growth in cylindrical shafts are: 1) axial tension, 2) bending, and 3)

torsion. For shafts subjected to alternating axial and bending loads, surface cracks tend to grow in a plane perpendicular to the shaft axis and can be adequately characterized by a planar semi-circular, or semi-elliptic, crack front [3]-[7]. The methodology for predicting planar crack growth only requires determination of the mode I, i.e., K_I, stress intensity factor along the crack front in order to predict of the shape and depth of the evolving crack. Predictions for fatigue crack growth for very small cracks subjected to torsional fatigue can also be obtained based solely on mode I stress intensity factors, since near the surface of the cylinder, the crack will grow perpendicular to the maximum principal stress oriented at 45° with respect to the cylinder axis. However, it is observed that under torsional fatigue conditions and maximum load fracture, cracks do not remain planar, but grow in a helical, or spiral shape as shown in Figure 1. Thus, as noted in [4]-[5], noticeable discrepancies arise in torsion between overly simplified computational predictions and experimental crack growth measurements, and these discrepancies are most likely attributed to missing mode II and mode III contributions in the planar crack growth model. However, inclusion of K_{II} and K_{III} stress intensity factors in a 3-D crack growth model will result in nonplanar crack growth, which in turn greatly increases the complexity of determining the stress intensity factors as the crack grows.

Spiral, or helical cracks, are of considerable interest in the fracture of brittle materials that exhibit minimal fatigue crack growth prior to catastrophic fracture. In fact, it has been shown that due to its high geometric constraint, spiral notch torsion tests [8]-[9] can be used to determine valid fracture toughness, K_{IC}, values using smaller test specimens to satisfy the necessary plane strain conditions. An important example of brittle spiral fractures is the fracture of the human femoral bone subjected to a single torsional overload

[10]-[13]. Though there exists a large body of medical and bioengineering literature associated with the classification and treatment of torsional fractures in human femurs, there doesn't appear to be a complete analysis of how spiral crack progresses during the torsional fracture process based on nonuniform femur bone geometry. The femur, the largest and heaviest bone in the human body, appears to exhibit identical helical cracking characteristics observed in the fracture of a hollow circular cylinder subjected to torsion [11]-[13].

Accurate predictions for the direction of a propagating 3-D crack, subjected to general loading conditions, requires the calculation of the mixed-mode stress intensity factors K_I, K_{II}, and K_{III} at all points along an arbitrarily shaped (nonplanar) 3-D crack front. Using the local values of the stress intensity factors, predictions can then be made for an incremental advance of the crack front to determine the evolving shape of the advancing crack. Powerful computational techniques are available for the accurate calculation of stress intensity factors for 3-D cracks with more-or-less arbitrary shape [14]. These computational techniques include boundary element methods [15], virtual crack extension [16], and modified finite element methods [14], [18]-[24]. Two approaches dominate the applicable finite element techniques for calculating stress intensity factors in 3-D. One approach involves the direct calculation of the stress intensity factors by including the stress intensity factors as additional degrees of freedom in the element stiffness matrix [21]-[23]. This "enriched" crack tip element approach embeds the well-known analytic asymptotic displacement and stress fields for a crack in an elastic material into the element stiffness formulation. One benefit of this approach is that there is generally no need for special crack tip mesh refinement using the finite element model. The second, but closely

related alternative finite element approach, is to include the well-known $1/\sqrt{r}$ stress singularity in a crack tip "wedge" element (collapsed hexahedron) and suitably reposition the location of the crack tip element's mid-side nodes, e.g., the "1/4-point element" for elements with a single mid-side node. This type of crack tip element requires a highly refined "tunnel" mesh around the crack front to properly capture the asymptotic displacements and stresses in the circumferential direction with respect to the plane of the crack. Using this method, the stress intensity factors are not included as additional unknowns in the finite element solution procedure, but are determined from the crack front nodal displacements during postprocessing. Both approaches work equally well, though creation of the "tunnel" mesh does rely on a specialized meshing algorithm for properly constructing the modified crack tip elements and the creation of a refined mesh around the crack front [24]. Finite element stress intensity factor solutions for various 3-D surface crack orientations, in solid and hollow cylinders, subjected to tension and torsional loading are given in [25]-[29]. In addition, a number of investigators have also effectively used the Boundary Element Method (BEM) to evaluate 3-D cracks in solid cylindrical bars subjected to tension/torsion loading [30]-[32].

Fatigue crack growth of surface cracks, in both solid and hollow cylinders, subjected to combined loading with a significant torsional component, has been examined experimentally [33]-[35] and computationally [36]-[37]. The computational simulations of nonplanar fatigue crack growth for a 3-D surface crack in a solid cylinder are in excellent agreement with the experimental measurements. However, the available studies of torsional fatigue crack growth in solid and hollow cylinders have been limited to nonplanar crack propagation for relatively small cracks and do not extend the crack growth to large-

scale cracking that could be characterized by a fully formed helical crack. This is quite understandable, since the complexity of the evolving nonplanar 3-D crack requires continuous updating of the cracked geometry as the crack incrementally grows both in radial depth and spirals around the cylinder's axis. In this study, 3-D crack growth simulations were performed for both solid and hollow cylinders to demonstrate how the final fractured spiral geometry is obtained, while also quantifying the stress intensity factors as a function of position along the evolving crack front. The simulations in this study are shown to be in excellent agreement with torsion fracture experiments performed on both solid and hollow cylinders.

1.3. Crack Issue with Shear Center of Structures

When simulating the surface crack of a cantilever beam, we observed that the application of loads at different positions directly influences K_{II}, This phenomenon is evidently due to the fact that the applied load is not aligned with the shear center of the beam's cross-section, thereby inducing rotation in the beam.

The main purpose of this study is to describe a simple procedure for the determination of the axis of twist for elastic bars subjected to torsion. A secondary objective is to review the relationship between the axis of twist and the shear center for cantilever beams subjected to transverse loading. The methodology for the determination of the axis of twist relies on displacements obtained from the elastic solution of the relevant torsion problem. In most cases, the desired displacements can be readily obtained directly from analytical solutions, or a displacement file generated by a finite element program.

The theory associated with the elastic torsional behavior of noncircular bars is a fundamental topic in the classical theory of elasticity [38]-[39]. Using Saint-Venant's semi-

inverse method, exact torsion solutions can be obtained for bars with noncircular cross-sections where it is assumed that: 1) the bar's projected cross-sectional shape does not vary along its length, 2) the twist per unit length (rate of twist), θ, remains constant, 3) the strains and displacements are small, and 4) the out-of-plane warping displacement can be expressed solely as a function of x and y, i.e., $w = w(x, y)$. In Saint-Venant's theory it is assumed that the applied torque T rotates each cross-section and causes a uniform twist per unit length θ, resulting in a total angle of twist for any value of z given by (Figure 2.).

$$\alpha = \theta \cdot z \tag{1}$$

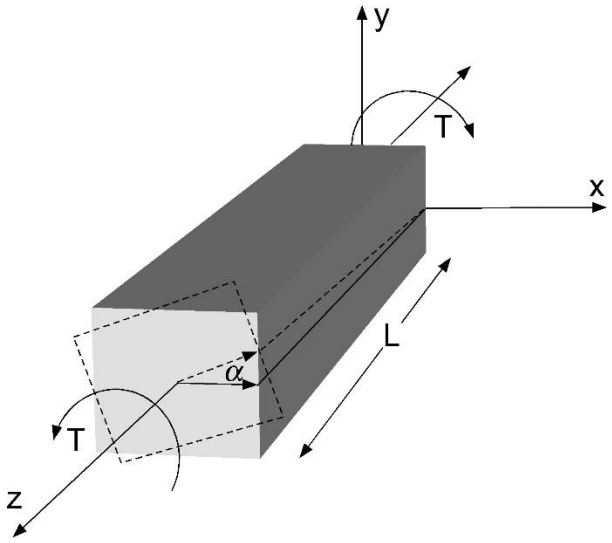

Figure 2. Noncircular bar subjected to applied torque T.

For small angles of twist, the displacements in the x and y directions are given respectively by,

$$u = -\alpha y = -\theta z y \tag{2}$$

$$v = \alpha x = \theta z x \tag{3}$$

The out-of-plane displacement in the z-direction is unknown and is designated as $w = w(x, y)$. In Saint-Venant's torsion theory, the out-of-plane displacement is usually expressed in terms of the rate of twist θ and a warping function φ, defined as

$$w(x,y) = \theta\varphi(x,y) \tag{4}$$

The relationship between the rate of twist θ and torque T can be expressed symbolically in the familiar form used for a rod with a circular cross-section, i.e.,

$$\theta = \frac{T}{\mu J_e} \tag{5}$$

where, μ is the elastic shear modulus and J_e represents an "equivalent" to the polar moment of inertia given by,

$$J_e = \iint_A \left(x^2 + y^2 + x\frac{\partial\varphi}{\partial y} - y\frac{\partial\varphi}{\partial x}\right) dx\, dy \tag{6}$$

It should be noted that the rate of twist and the torsional stresses do not depend on any prior knowledge of the location of the "center of twist", i.e., the warping function and shear stresses do not depend on the location of the coordinate system. This may seem somewhat surprising; however, the displacement components u and v are linear functions of x and y, and each cross section rotates as a rigid body about the z axis, without deforming within the x-y plane. In addition to a rotation, points in the cross section will also have an arbitrary rigid-body translation, but this does not affect the strains and stresses, since these quantities are expressed in terms of derivatives of the displacements.

Solutions obtained using Saint-Venant's semi-inverse approach satisfy the equations of elasticity, i.e., equilibrium and strain compatibility, as well as the traction free boundary conditions on the bar's lateral surfaces. The stresses on the end faces of the bar, normal to the z-axis, also satisfy the equilibrium conditions, i.e., there are no net resultant forces in the x and y directions. The moments generated by the solution's shear stresses on the end faces, when integrated over the surface area, are equal to the applied torque T (Figure 2). It is important to note that the torsion solutions obtained using Saint-Venant's semi-inverse

method do not result in zero displacements at the "fixed" end of the bar, where the angle of rotation is zero. In the classical elastic torsion theory, the warpage displacements in the z-direction given by (4) persist along the entire length of the bar. As shown in [38], the fixing of a plane in the cross-section prevents local warpage in the axial direction, and thus results in a very different stress state in the neighborhood of the fixed surface. Such fixed boundary constraints not only alter the shear stress components σ_{xz} and σ_{yz}, but also introduce an axial stress σ_x and a shear stress component σ_{xy} that do not arise in Saint-Venant's torsion solution. The resulting stresses near the fixed end of the bar decay rapidly in the axial direction and also depend on the bar's elastic properties E and v.

The center of twist is the one point in the plane of the cross-section that does not experience any rotation and about which all other material points in the cross-section rotate. For a bar with a nonuniform cross section that varies as a function of z, one can visualize a locus of points that represent centers of twist that also vary as a function z. If a torsional moment is applied as shown in Figure 2, all points in the cross section will rotate about the center of twist and not experience any additional transverse displacements in the x-y plane, i.e., no bending will occur.

For a bar with a symmetric cross section the center of twist will coincide with the centroid of the cross section. As shown in [40], for nonsymmetrical cross sections, the center of twist can be calculated using Saint-Venant's warping function $\varphi(x, y)$ (4). For example, from [40]-[41]the center of twist (x_T, y_T) is given by

$$x_T = -\frac{1}{I_{xx}} \iint_A y\varphi(x, y)\, dx\, dy \tag{7}$$

$$y_T = -\frac{1}{I_{yy}} \iint_A x\varphi(x, y)\, dx\, dy \tag{8}$$

where A is the cross-sectional area and I_{xx} and I_{yy} are the 2nd area moments given by

$$I_{xx} = \iint_A y^2 \, dx \, dy \tag{9}$$

$$I_{yy} = \iint_A x^2 \, dx \, dy \tag{10}$$

The center of twist provided by (7)-(8) assumes the classical Saint-Venant displacement boundary conditions on the cross section at z = 0, i.e., u = v = 0. However, it also admits an out-of-plane warpage $w(x, y)$ on this plane in order to satisfy Saint-Venant's torsion conditions and the necessary traction free boundary conditions. Though the average out-of-plane displacement on the cross-section is zero [40], i.e.,

$$\iint_A w(x, y) \, dx \, dy = 0 \tag{11}$$

rigid clamping at z = 0 is only approximated. Because of Saint-Venant's principle that the details concerning how the end loading is distributed on the surface has a diminishingly small effect on the stresses away from the boundary, eqn. (7)-(8) is adequate for the determination of the center of twist for most engineering applications. But as noted in [40]-[41], the location of the center of twist is independent of Poisson's ratio v. This is a consequence of the quasi-rigid boundary condition assumed in Saint-Venant's formulation for the determination of the warping function $\varphi(x, y)$ and is not true for a more rigidly constrained boundary condition at z = 0.

1.4. Crack Simulation in Welding Residual Stresses Condition and Hot Cracking

The primary cause of residual stresses in welding is the non-uniform heating distribution. During the welding process, the heat source is applied to the weld specimen, creating a temperature gradient. The highest temperature is concentrated at the center of the heat-

affected zone, gradually decreasing outward. As the temperature drops significantly beyond the heated region, thermal expansion occurs in the heated zone, while the surrounding colder region constrains this expansion, leading to the development of residual stresses. If these residual stresses are not properly controlled during welding, distortion may occur, negatively affecting the structural integrity of the welded component.

Steel structures subjected to cyclic loading are often susceptible to fatigue crack formation in the weld region, and the presence of weld residual stresses can significantly accelerate crack growth and make its behavior more difficult to predict. [42] This complexity stems from the fact that the residual stress distribution is influenced by a number of factors, including weld heat input, welding speed, boundary conditions and material properties. As a result, the residual stress field in a cooled structure is often very heterogeneous and the spatial distribution is complex. For example, in regions dominated by tensile residual stresses, the presence of cracks can lead to the growth of fatigue cracks even in the case of externally loaded compression cycles. [43] In addition, in the transition region where the residual stresses change from tensile to compressive, there may be a significant change in the stress ratio at the crack tip. This variation may result in the location of the maximum stress intensity factor being different from the location of the fastest growing crack, thus complicating the prediction of crack extension paths. Therefore, in structures containing weld residual stresses, it is inaccurate to assess fatigue crack life and growth direction based solely on external loading conditions. A comprehensive understanding of the interaction between the residual stress field and applied loads is required to accurately predict crack behavior.

Many researchers have simulated fatigue fracture behavior in the presence of welding residual stresses. [44]-[46] However, many of these studies have simplified the welding process, such as idealizing the welding heat source, which limits the accuracy of the resulting residual stress field. For example, R. Gadallah et al. [47]-[48] performed detailed welding simulations and then calculated the stress intensity factor (SIF) for through-thickness cracks and surface cracks in a multi-pass welding model, taking into account the effect of superimposed residual stresses. However, their study did not include the prediction of fatigue crack growth. In another study, D. Malschaert et al. [43] performed a comprehensive welding simulation of a T-joint structure and subsequently predicted fatigue crack extension for surface cracks in the welded structure. However, the crack growth simulations were limited to a two-dimensional plane and did not consider the three-dimensional extension behavior of the cracks. These limitations highlight the need for further research that combines realistic simulations of the welding process with fully three-dimensional fatigue crack growth analysis in a residual stress environment.

In addition to the residual stresses that welding imposes on a structure, hot cracking may form during the welding process. During weld metal solidification, most alloys undergo a temperature range where ductility is significantly reduced. [49] Hot cracking typically occurs within this low-ductility temperature range when externally applied or thermally induced strains exceed a critical threshold. Numerous testing methods have been developed to assess hot cracking susceptibility, which can be broadly categorized into two types: self-restraint tests and externally loaded tests. [50]

One widely used self-restraint test for evaluating solidification cracking susceptibility is the Houldcroft test, also known as the fishbone test. This test involves a specimen with

multiple slots of varying depths. The welding direction is indicated by an arrow in the diagram. The slot depth increases linearly along the welding path, with deeper slots providing greater compliance and reducing the thermal stresses acting on the corresponding weld area. Hot cracking typically initiates at the start of the weld and propagates along the welding direction. Crack susceptibility in the Houldcroft test is quantified by the ratio of crack length to total welding length.

The Varestraint test is a widely used quantitative method for comparing the hot cracking susceptibility of different materials. This test is performed by depositing a weld bead on a cantilevered specimen positioned over an underlying curved block. The welding arc initiates at the free end of the specimen and progresses until reaching the tangential contact point between the specimen and the block. During the test, an external strain is applied to force the specimen to conform to the curvature of the block. The high external strain induces hot cracking within the weld zone. The magnitude of the applied external strain can be calculated based on the radius of the block and the thickness of the specimen. Consequently, the Varestraint test provides a direct correlation between the applied strain and crack length (or total crack length), enabling a quantitative assessment of a material's susceptibility to hot cracking.

To further investigate the relationship between applied strain and crack propagation, an alternative version of the test, known as the trans-Varestraint test, has been developed. In this modified test, the applied strain is oriented perpendicular to the welding direction. Under this loading configuration, all weld beads experience the same magnitude of applied strain, and hot cracking propagates along the welding direction, making the measurement of crack length more straightforward.

While weldability tests effectively visualize the susceptibility of different material combinations to cracking, they do not establish a direct quantitative relationship between strains and hot cracking. To address this limitation, researchers have developed the Brittleness Temperature Range (BTR) method based on the trans-Varestraint test. The Brittle Temperature Range (BTR) method defines the critical strain values for a given material at different temperatures during solidification. The upper and lower limits of the method correspond to the liquidus and solidus temperatures of the material, respectively. As the temperature in the liquid metal region drops to the melting point and solidification begins, the strain-temperature variation at that location is tracked (typically starting at zero strain because the material is initially in the liquid state). By comparing the actual strain at each temperature step with the critical strain value defined by the BTR curve, the susceptibility to hot cracking can be assessed. If the strain measured at a given temperature exceeds the corresponding critical strain, it indicates that hot cracking has occurred at that location. [49]

However, Trans Varestraint test primarily considers tensile strains due to externally applied mechanical loads and ignores other important sources of strain, such as thermal strains from welding heat sources and tensile strains due to volume contraction during solid-liquid phase transformation of metals. [50] As a result, BTR curves derived from mechanical loading alone tend to underestimate the actual critical strain values, leading to conservative predictions of hot crack susceptibility. In order to more accurately assess the true hot cracking behavior, the combined effects of mechanical strain, thermal strain, and solidification-induced shrinkage must be considered in the BTR assessment.

The aim of this study is to combine detailed welding simulations with 3D crack modeling through finite element analysis in order to predict fatigue fracture in a 3D crack model subjected to a welding residual stress environment. In addition, finite element simulations of hot cracking susceptibility tests were performed to obtain accurate BTR curves, which were then used to predict the possibility of hot crack formation during the welding process.

2. Methodology

2.1. Finite Element Method in Fracture Mechanics

2.1.1. Cracked Cylinder Models

In an effort to model continuous spiral fracture behavior in solid and hollow cylinders, full 3-D finite element simulations were performed using circular cylinders with identical diameters, lengths, and initial surface crack geometries, as shown in Figure 3 and Figure 4. In these figures, (D_s, D_h) represent the diameters and (L_s, L_h) lengths of the uncracked solid and hollow cylinders, respectively. An initial surface crack was oriented at an angle $\theta = 45°$ to the cylinder's axis. This initial orientation of the crack plane subjected the surface crack to the maximum principal stress in torsion; resulting in essentially pure mode I crack growth at the onset of the simulation. Cross-sections A-A and B-B in Figure 3 and Figure 4 represent elliptical cutting planes in the solid and hollow cylinders on the same plane that contains the semicircular surface crack. The semicircular surface crack has an initial crack length (depth) given by C_d and a crack mouth surface dimension D_c (see Figure 3 and Figure 4). Note that the surface crack is not fully semicircular, since it's geometry is defined by the intersection of a small semicircle with the larger ellipse of the 45° cut cylinder plane (Figure 3(b)).

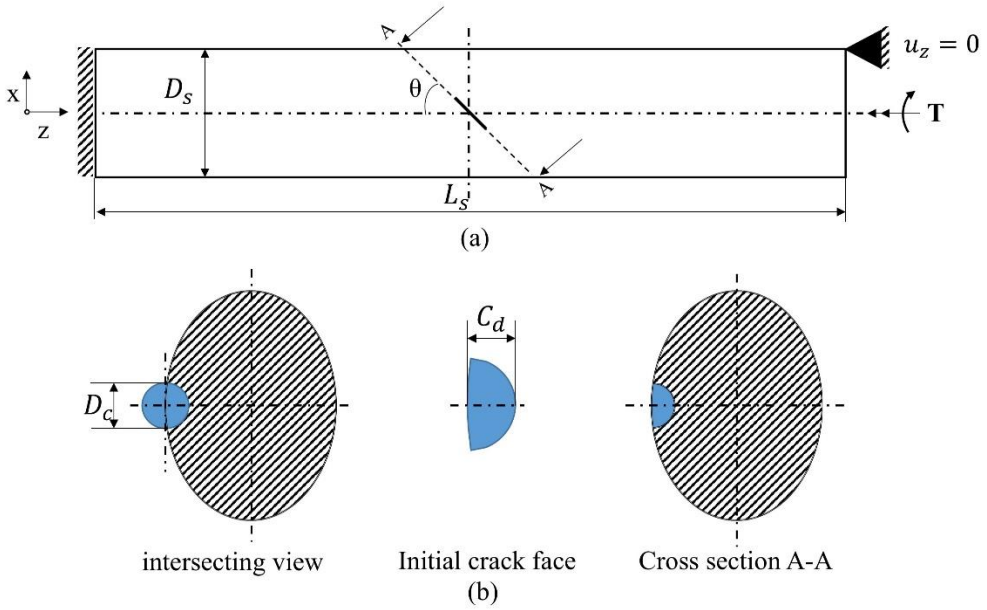

Figure 3. a) Solid cylinder under pure torsion with b) inclined semi-circular crack.

Boundary conditions imposed on both cylinder models are also depicted in Figure 3 and Figure 4. One end of the cylinder is fixed in terms of displacements and rotations, i.e., ($u_x = u_y = u_z = 0$) and ($\theta_x = \theta_y = \theta_z = 0$). At the opposite end of the cylinder, where the torque T is applied, the cylinder displacement is constrained in the z direction and rotation is only permitted about the z-axis, i.e., ($u_z = 0$), ($\theta_x = \theta_y = 0$). The direction of the external torque T is matched to the crack angle so that the crack is perpendicular to the direction of the maximum principal stress on the surface of the cylinder.

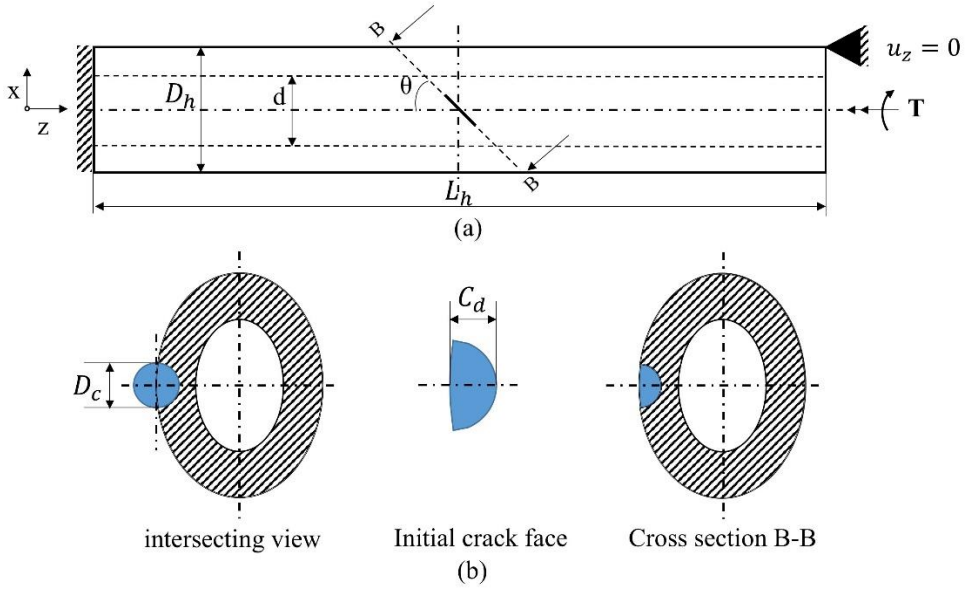

Figure 4. a) Hollow cylinder under pure torsion with b) inclined semi-circular crack.

2.1.2. Crack Growth Simulation Procedure

Simulation of 3-D crack growth requires accurate calculation of the stress intensity factors K_I, K_{II}, and K_{III}, at a large number of points along the crack front. Once the stress intensity factors have been determined, the crack front can be incrementally advanced in a direction based on a suitable mixed-mode crack growth criterion. If a finite element procedure is used to determine the stress intensity factors, a new cracked geometry mesh must be generated, and the stress intensity factors recomputed as the crack front advances. Thus, finite element-based crack growth simulations rely heavily on efficient adaptive remeshing. The methodology for simulation of 3-D crack growth used in this study follows the general finite element approach described in [51]-[52] for incremental crack advance, with the main difference in the current study being the use of commercially available finite element software ANSYS [53] for calculation of the stress intensity factors and SimModeler [54] for the adaptive meshing. The use of SimModeler for creation of the "tunnel" crack front mesh utilized by ANSYS, provides an efficient

remeshing algorithm that simultaneously automates the incremental crack advancement and meshing needed for the repetitive calculations in the continuously changing crack geometry.

2.1.3. Crack Growth Direction and Incremental Crack Advancement

In this study, the incremental simulation of directional crack growth is based on the maximum circumferential stress criteria [55], where the crack front is advanced in a direction perpendicular to the maximum local circumferential stress at the crack tip. This maximum circumferential stress can be determined from the asymptotic crack tip stresses and is expressed in terms of the mixed-mode stress intensity factors K_I and K_{II} at any position along the crack front. Assuming that the critical principal stress for crack advance under mixed-mode conditions is identical to the critical stress necessary for crack growth under mode-I conditions, the angle for crack advance $_p$ can be determined from [55],

$$K_I \sin\theta_P + K_{II}(3\cos\theta_P - 1) = 0 \tag{12}$$

Solving for $_p$,

$$\left(\tan\frac{\theta_P}{2}\right)_{1,2} = \frac{1}{4}\frac{K_I}{K_{II}} \mp \frac{1}{4}\sqrt{\left(\frac{K_I}{K_{II}}\right)^2 + 8} \tag{13}$$

In (13), for$K_{II} > 0$, the negative sign is taken on the square root term and when $K_{II} < 0$ the sign is positive. With the angle of local crack growth $_p$ established, the local increment of crack advance, a, for subcritical crack growth, can be determined using an

empirical crack growth rate law based on the amplitude of the alternating stress intensity factor, e.g., the Paris-Erdogan law [56] given by

$$\frac{da}{dN} = C\left(\Delta K_{eq}\right)^{\alpha} \tag{14}$$

where a is the crack length, N the number of cycles, C and experimentally determined constants, and

$$\Delta K_{eq} = K_{eq}^{Max} - K_{eq}^{Min} \tag{15}$$

In (14)-(15), K_{eq} represents an "equivalent" alternating stress intensity factor amplitude under mix-mode loading conditions, obtained by equating the mixed-mode strain energy release rate to the strain energy release rate for crack advance under pure mode I conditions. In terms of the computed stress intensity factors K_I, K_{II}, K_{III},

$$K_{eq} = \sqrt{\left(K_I cos^3\frac{\theta_P}{2} - 3K_{II}cos^2\frac{\theta_P}{2}sin\frac{\theta_P}{2}\right)^2 + \frac{1}{1-V}K_{III}^2} \tag{16}$$

where E is Young's modulus, ν is Poisson ratio, and μ is the shear modulus. Local crack advancement at any arbitrary point on the crack front is specified by

$$\Delta a = \Delta a_{max}\left(\frac{K_{eq}}{K_{eq}^{Max}}\right)^{\alpha} \tag{17}$$

where $a_{\max}$ is a user specified increment tolerance for crack advance in the direction of $_p$ at the point on the crack front where $K_{eq} = K_{eq}^{Max}$. From (14), the number of cycles N needed for the propagating crack front by an increment a, is finally given by

$$\Delta N = \Delta a \cdot \left[C\left(\Delta K_{eq}\right)^{\alpha}\right]^{-1} \tag{18}$$

The incremental crack front advancement specified by (17) requires a continuous advancement of the nodes that define the crack front, which in turn requires continuous

remeshing along the crack front. In this study, this was smoothly handled by the use of the SimModeler software [54]. The number of cycles, N, needed for the crack to grow to a certain distance and depth, was not of primary interest in this study, i.e., the subcritical fatigue crack growth model simply provided a convenient method for generating the spiral shaped crack geometry observed in solid and hollow cylinders subjected to torsional loading.

2.1.4. Calculation of Stress intensity Factors (K_I, K_{II}, K_{III})

Calculation of stress intensity factors in ANSYS [53] is a relatively automated post-processing procedure that uses a displacement correlation technique based on the nodal displacements close to the crack tip. In conjunction with the well-known analytic asymptotic displacements at the crack tip, the stress intensity factors can be accurately calculated using a sufficiently refined crack tip "tunnel" mesh with crack tip elements that contain the correct singular asymptotic stress behavior. For elements based on quadratic displacement shape functions, this is accomplished by using collapsed hexahedron or tetrahedron elements with the mid-side nodes moved to the quarter-point nearest to the node located on the crack front. Numerous publications, e.g., [14]-[24], provide details. For this technique to properly capture the angular dependence of the displacements and stresses around the crack tip, the crack tip mesh must employ multiple circular rings of elements around the crack tip elements to transition from the refined crack tip mesh to the nearby "regular" elements. This is best accomplished by using automated meshing software that creates a refined tunnel mesh defined for an arbitrary crack front arc. Two typical finite element meshes used for the solid cylinder and the

hollow cylinder, $r_1/r = 0.5$, with a small semi-elliptic surface crack, are shown in Figure 5. This figure also shows the sequence of progressive mesh refinement around the crack tip, i.e., the necessary "tunnel" mesh. The tunnel mesh refinement depicted on the cylinder surface is extended into the cylinder depth along the entire crack front. In this study, SimModeler [54] was used to efficiently perform this meshing task, which also automates the process for computing $_p$ and K_{eq} at the crack tip nodes, (13) and (16), based on the values of K_I, K_{II}, and K_{III}, returned by ANSYS.

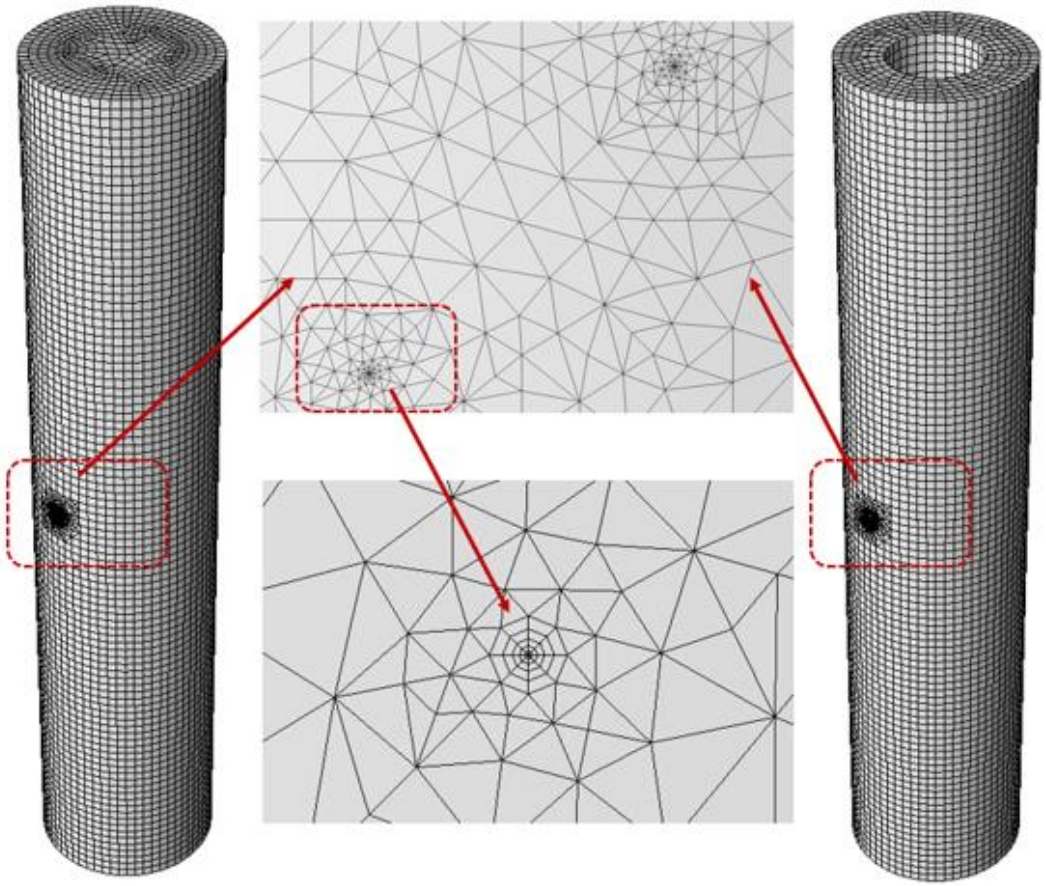

Figure 5. Finite element meshes for solid and hollow cylinders containing small semi-elliptic surface cracks oriented at 45° on cylinder surface. Inset shows local surface mesh refinement at crack tips.

2.2. A Direct Method for Determination of Shear Center

Although eqns. (7)-(10) provide a useful method for determining the centers of twist, it is still necessary to determine the warping function (x, y) and integrate over the cross-sectional area A of the beam. A more practical approach for finding the center of twist in any cross section can be based directly on a point's coordinates before deformation and displacements in the plane. Let the coordinates of a point in the cross-section be specified with respect to an $\bar{x}$, $\bar{y}$ coordinate system with an origin located at $x = x_0$, $y = y_0$. In general, $x = x_0$ and $y = y_0$ will not be the center of twist. A point initially located at position $(\bar{x}_1, \bar{y}_1)$, moves to a position $(\bar{x}_2, \bar{y}_2)$ after the cross section is subjected to a rigid body rotation through an angle measured with respect to a translated x, y axes with its origin at the center of twist. Knowing the displacements u and v, the new position of the point after rotation is given by

$$\bar{x}_2 = u + \bar{x}_1 \tag{19}$$

$$\bar{y}_2 = v + \bar{y}_1 \tag{20}$$

In the x, y coordinate system whose origin is located at the center of twist, the radius r measured from the center of twist to the coordinates $(\bar{x}_1, \bar{y}_1)$ before, and $(\bar{x}_2, \bar{y}_2)$ after deformation, must be the same. Thus,

$$r^2 = x_1^2 + y_1^2 = (x_0 + \bar{x}_1)^2 + (y_0 + \bar{y}_1)^2 \tag{21}$$

$$r^2 = x_2^2 + y_2^2 = (x_0 + \bar{x}_2)^2 + (y_0 + \bar{y}_2)^2 = \left((x_0 + \bar{x}_1) + u\right)^2 + \left((y_0 + \bar{y}_1) + v\right)^2 \tag{22}$$

Setting (21) and (22) equal to one another, the condition for locating the unknown position (x_0, y_0) is given by

$$(x_0 + \bar{x}_1)^2 + (y_0 + \bar{y}_1)^2 - \left((x_0 + \bar{x}_1) + u\right)^2 - \left((y_0 + \bar{y}_1) + v\right)^2 = 0 \tag{23}$$

The expression in (23) is a function $f\left(x_0, y_0, \bar{x}_1, \bar{y}_1, u, v\right) = 0$, where there are only two unknowns, x_0 and y_0. In theory, it should be possible to solve this nonlinear equation exactly by selecting two different points in the cross section, paired with two sets of known u, v displacements. However, in a finite element calculation where many displacements can be accurately determined in a given plane, a more effective approach is to determine the values of x_0 and y_0 that minimizes the square of the error for a large number of displacements. Assuming that there are n sample points, the error function to be minimized is obtained from (23)

$$E = \sum_{i=1}^{n} \delta_i^2 = \sum_{i=1}^{n} (2u_i x_0 + 2u_i \bar{x}_{1i} + u_i^2 + 2v_i y_0 + 2v_i \bar{y}_{1i} + v_i^2)^2 \qquad (24)$$

Minimizing the error function in (24), with respect to x_0 and y_0, simply involves setting the partial derivatives $\frac{E}{x_0}$, $\frac{E}{y_0}$ equal to zero. This results in two "normal" equations for the unknowns x_0 and y_0,

$$(2u_i^2)x_0 + (2v_i u_i)y_0 + (2u_i^2 \bar{x}_{1i} + u_i^3 + 2v_i u_i \bar{y}_{1i} + v_i^2 u_i) = 0 \qquad (25)$$

$$(2v_i^2)y_0 + (2v_i u_i)x_0 + (2v_i^2 \bar{y}_{1i} + v_i^3 + 2v_i u_i \bar{x}_{1i} + u_i^2 v_i) = 0 \qquad (26)$$

The solution to these two linear equations (25)-(26) for x_0 and y_0 is given by,

$$x_0 = \frac{c \cdot e - b \cdot f}{a \cdot e - b \cdot d} \qquad (27)$$

$$y_0 = \frac{a \cdot f - c \cdot d}{a \cdot e - b \cdot d} \qquad (28)$$

where,

$$a = \sum_{i=1}^{n} 2u_i^2 \, , b = \sum_{i=1}^{n} 2v_i u_i \, , c = -\sum_{i=1}^{n} (2u_i^2 \bar{x}_{1i} + u_i^3 + 2v_i u_i \bar{y}_{1i} + v_i^2 u_i) \qquad (29)$$

$$d = \sum_{i=1}^{n} 2v_i u_i \, , e = \sum_{i=1}^{n} 2v_i^2 \, , c = -\sum_{i=1}^{n} (2v_i^2 \bar{y}_{1i} + v_i^3 + 2v_i u_i \bar{x}_{1i} + u_i^2 v_i) \qquad (30)$$

The location of the center of twist with respect to the arbitrary $\bar{x}$, $\bar{y}$ coordinate system is given by

$$x_T = -x_0, \qquad y_T = -y_0 \qquad (31)$$

Using the above least squares minimization procedure, the location of the center of twist can be determined from n displacement pairs calculated at n $\left(\bar{x}_1, \bar{y}_1\right)$ coordinate positions.

The center of twist, designated as $\left(x_T, y_T\right)$ is the one point in the cross section which does not experience any rotation and about which all points in the cross section rotate. An axis of twist, for a bar with varying cross sections, can be developed from a sequence of cross-sections along the bar's axis. The shear center, or flexural center, designated as $\left(x_F, y_F\right)$, can be defined as the point, or axis, in a cantilever beam's cross-section where the application of a transverse load will only result in transverse displacements and no twisting. Using energy methods and the Maxwell-Betti reciprocal theorem [57], it can be shown that the location of the center of twist coincides with the location of the beam's shear center if the same support boundary conditions exist in both problems. Knowledge of the location of the center of twist is of great practical importance, since it can provide a straightforward technique for determining the shear center. The literature describing the relationship between the center of twist and the shear center is somewhat confusing. This is primarily because the early publications on this topic [38]-[41] and [57]-[58] did not have access to accurate solutions to both the torsion and cantilever beam problem with

identical support boundary conditions. For example, solutions for the location of the shear center obtained for a cantilever beam using Saint-Venant's semi-inverse method are shown to depend on Poisson's ratio [38]-[39], [41], [60]-[61], and yet the center of twist, eqn.(7)-(8), does not depend on Poisson's ratio [40]. The "discrepancy" is that the support boundary conditions for these two problems are not identical, i.e., for the cantilever beam the displacements on the $z = 0$ plane are not identical to the displacements on this same plane as obtained from Saint-Venant's semi-inverse solution for torsion. In fact, neither solution strictly enforces a true fixed displacement constraint for all points on the $z = 0$ plane. The torsion problem permits out-of-plane warpage on the $z = 0$ plane with no displacements in the x and y direction, while the cantilever beam problem permits in-plane x and y displacements, characteristic of anticlastic curvature, in addition to displacements in the z direction. Analytical solutions for torsion and bending problems with identical support boundary conditions are generally not available and must be evaluated numerically. The finite element method permits accurate numerical solutions for both torsion and cantilever beam problems with identical fixed boundary conditions and thus the equivalency of the shear center and the center of twist can be demonstrated numerically.

2.3. Finite Element Method Employed in Hot Cracking and Welding Simulation

Weldability tests are commonly employed to assess the susceptibility of metals to hot cracking during welding. These tests can be categorized into two major types: self-restraint tests and externally applied restraint tests. In self-restraint tests, the geometry of the test specimen provides varying degrees of constraint during welding, requiring only the welding process to be performed on the specimen. In contrast, externally applied restraint

tests introduce additional tensile strain during welding to induce hot cracking. Compared to self-restraint tests, externally applied restraint tests allow for better quantification of a material's susceptibility to hot cracking by adjusting the level of applied tensile strain.

However, both self-restraint and externally applied restraint tests neglect the influence of thermal stresses introduced by the welding heat source in the molten zone, as well as the rapid volumetric changes associated with phase transformation during metal solidification. To address these limitations, this study employs three-dimensional finite element simulations to reproduce hot cracking susceptibility tests while incorporating the effects of thermal stress and metal solidification under the existing constraint conditions. Specifically, an elasto-plastic thermo-mechanical coupling analysis using the finite element method is conducted to simulate the weldability tests of austenitic stainless steel 316, material properties shown in Figure 6-Figure 10, including the Trans Varestraint Test and the Houldcroft Test.

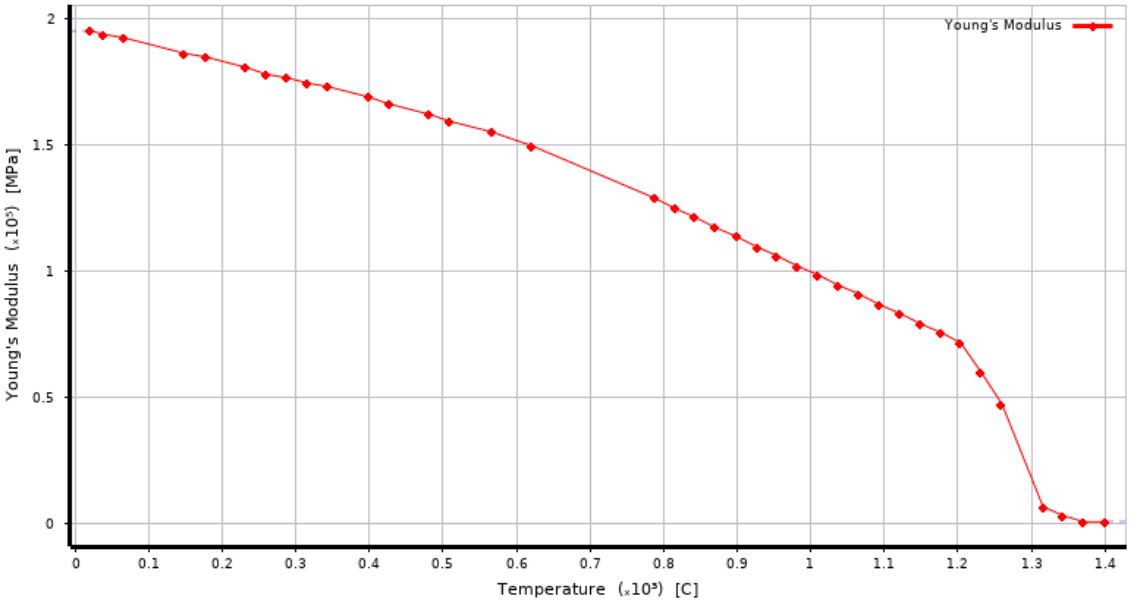

Figure 6. Young's Modulus of SS316

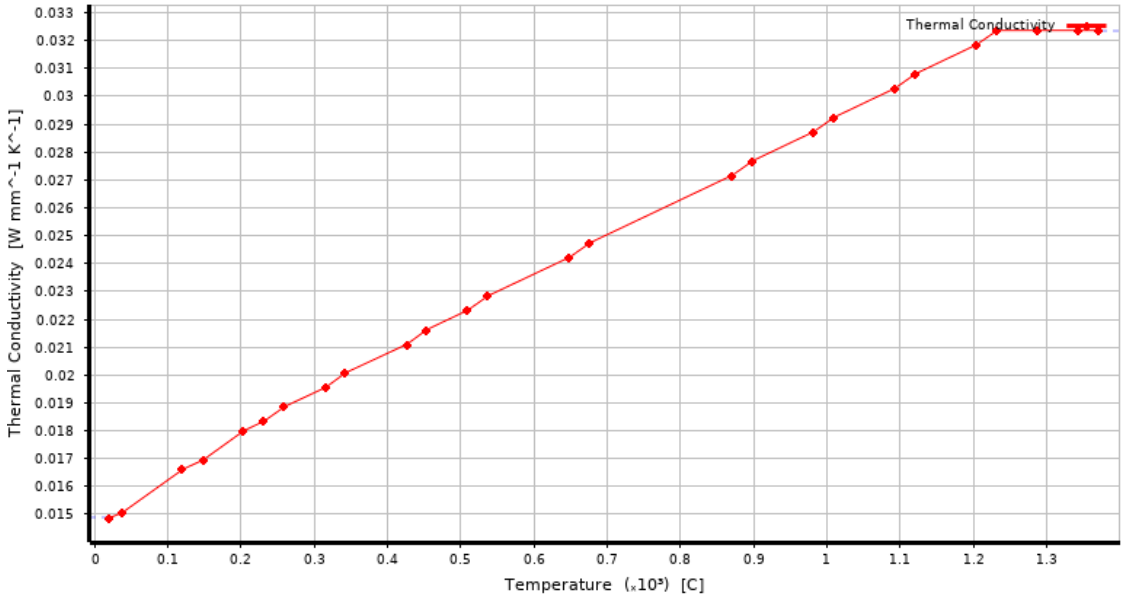

Figure 7. Isotropic Thermal Conductivity

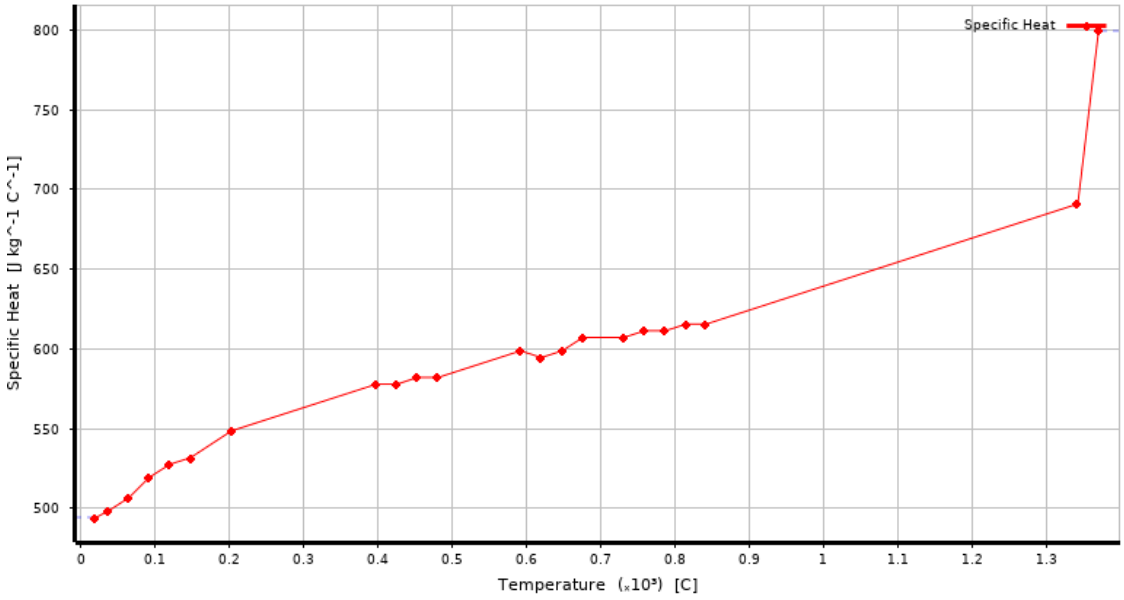

Figure 8. Specific Heat

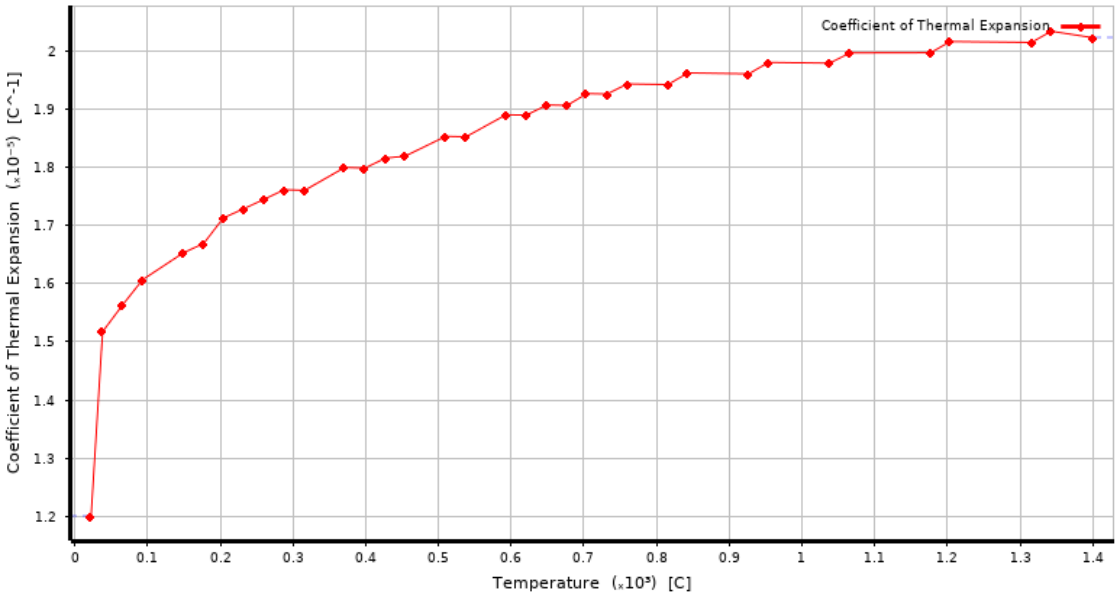

Figure 9. Coefficient of Thermal Expansion

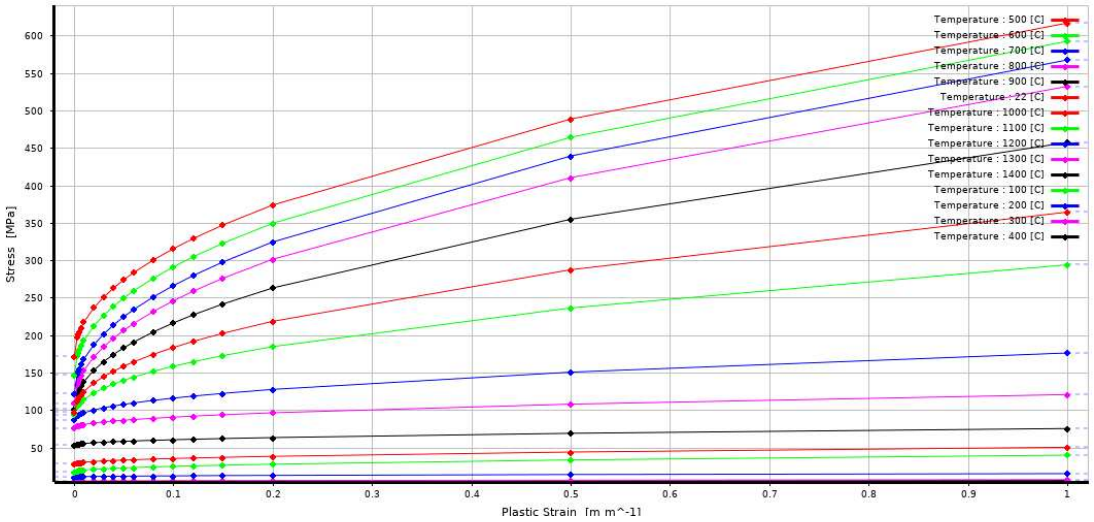

Figure 10. Multilinear Isotropic Hardening

By reproducing weldability tests in a three-dimensional finite element model, the curves used to quantify hot cracking susceptibility, Brittleness Temperature Range (BTR), can be updated based on finite element simulation results and subsequently employed to assess the occurrence of hot cracking.

Accurate three-dimensional welding simulations are also incorporated in this study. These simulations enable precise determination of the strain-temperature evolution in the

welded region. By integrating the updated BTR, the likelihood of hot cracking formation can be predicted. Furthermore, welding simulations provide the residual stress distribution of the structure after cooling, which can be utilized in crack propagation simulations under welding residual stress conditions.

2.3.1. Finite Element Method in Weldability Test

This study primarily focuses on the Trans Varestraint Test and the Houldcroft Test, where the Trans Varestraint Test represents an externally applied restraint test, while the Houldcroft Test is classified as a self-restraint test. By developing finite element models for both hot cracking susceptibility tests, a more precise determination of the critical values for hot crack initiation can be achieved.

Trans Varestraint Test

The Trans Varestraint Test is a weldability test in which a force is applied at the edge of a specimen during autogenous welding, perpendicular to the specimen surface, causing the specimen to bend. This bending induces tensile strain in the weld region. A curved bending block is positioned beneath the specimen to determine the magnitude of the tensile strain experienced in the welded area. When the external load is applied at the specimen edge, the specimen undergoes rapid deformation and conforms to the shape of the bending block. By adjusting the radius of curvature of the bending block, the tensile strain applied to the weld zone can be precisely controlled.

The primary distinction between the Trans Varestraint Test and the Varestraint Test lies in the alignment of the applied tensile strain with the welding direction. In the Trans-Varestraint Test, the welding direction is perpendicular to the applied tensile strain, ensuring that the weld seam experiences a uniform tensile strain across the specimen. This

configuration allows for the quantification of the critical conditions for hot cracking while ensuring that temperature remains the only variable. Additionally, since hot cracks form along a single direction within the weld seam, they are easier to measure.

In contrast, the Varestraint Test applies tensile strain parallel to the welding direction. This results in simultaneous variations in both temperature and externally applied strain during testing, leading to irregular and non-uniform crack formation. Consequently, measuring and quantifying hot cracking susceptibility become more challenging in the Varestraint Test.

Therefore, the Trans Varestraint Test is commonly used to quantify the critical conditions for hot cracking, specifically defining the Brittleness Temperature Range (BTR). The figure illustrates the schematic representation of the Trans Varestraint Test, where the specimen dimensions are L = 350 mm, W = 150 mm, t = 9 mm and R is the radius of the bending block.

In the schematic, as shown in Figure 11, points A, B, and C represent the welding stop point, the point where the external load is applied, and the welding start point, respectively. Tungsten Inert Gas (TIG) welding is employed in this study as the welding method. The welding process initiates at point C, and as the heat source progresses toward point B, an external load is applied at the edge of the specimen. However, the heat source is not interrupted and continues moving forward until it reaches point A.

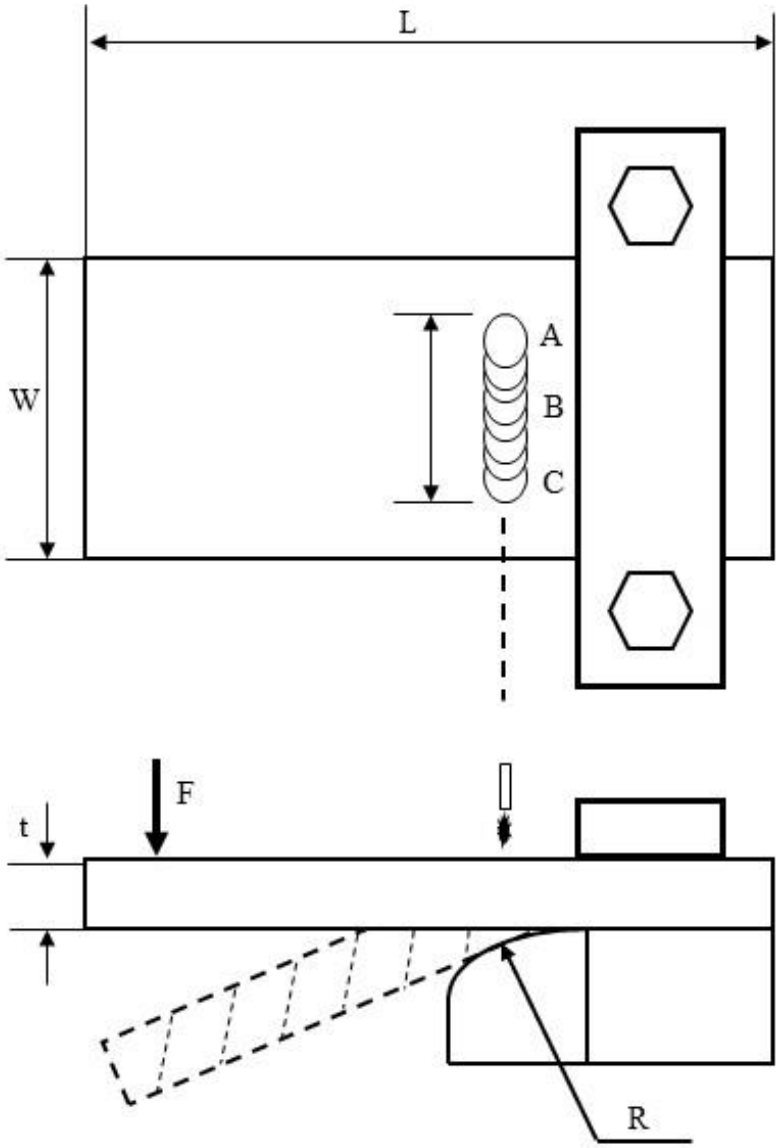

Figure 11. Schematic of Trans Varestraint Test

The Figure 12 illustrates the Trans Varestraint Test model in ANSYS. As shown, a rigid surface is placed beneath the welding specimen, serving as the bending block. By adjusting the radius of the rigid surface, the applied tensile strain in the specimen can be controlled.

A force perpendicular to the specimen surface is applied at one end of the sample, which is activated when the welding heat source passes through point B. Meanwhile, a fixed constraint is imposed at the opposite end of the specimen to restrict its movement. This

setup effectively replicates the experimental conditions required to study hot cracking susceptibility in the Trans Varestraint Test.

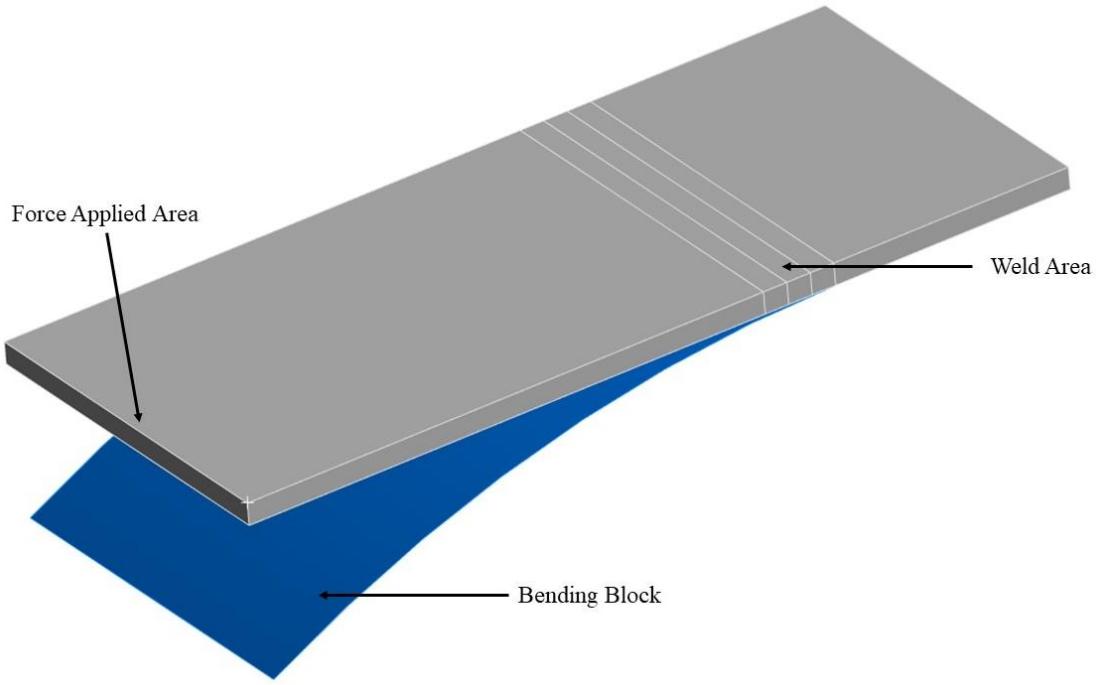

(a)

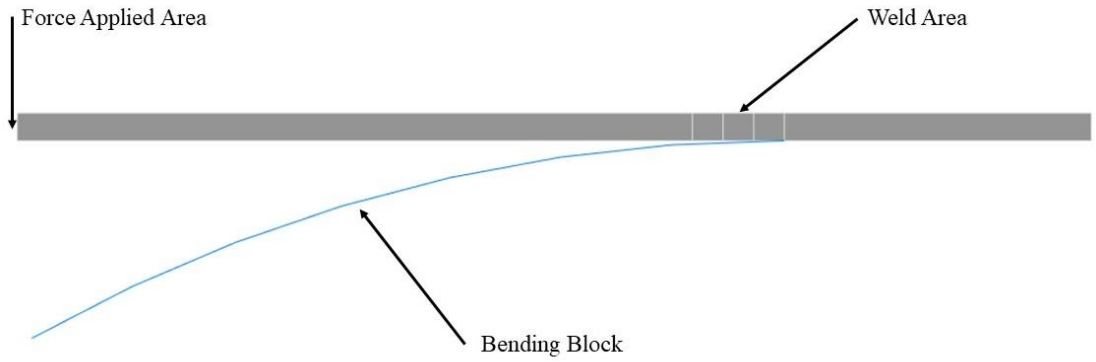

(b)

Figure 12. Model of Trans Varestraint Test: (a) ISO view; (b) Side view.

The Figure 13 illustrates the three-dimensional finite element mesh for the Trans Varestraint Test model. To accurately capture and compute the variations in tensile strain

within the welded region, a refined mesh is applied specifically to the welding area. This mesh refinement enhances the accuracy of strain distribution calculations, ensuring a more precise representation of the welding-induced thermal and mechanical effects in the finite element simulation.

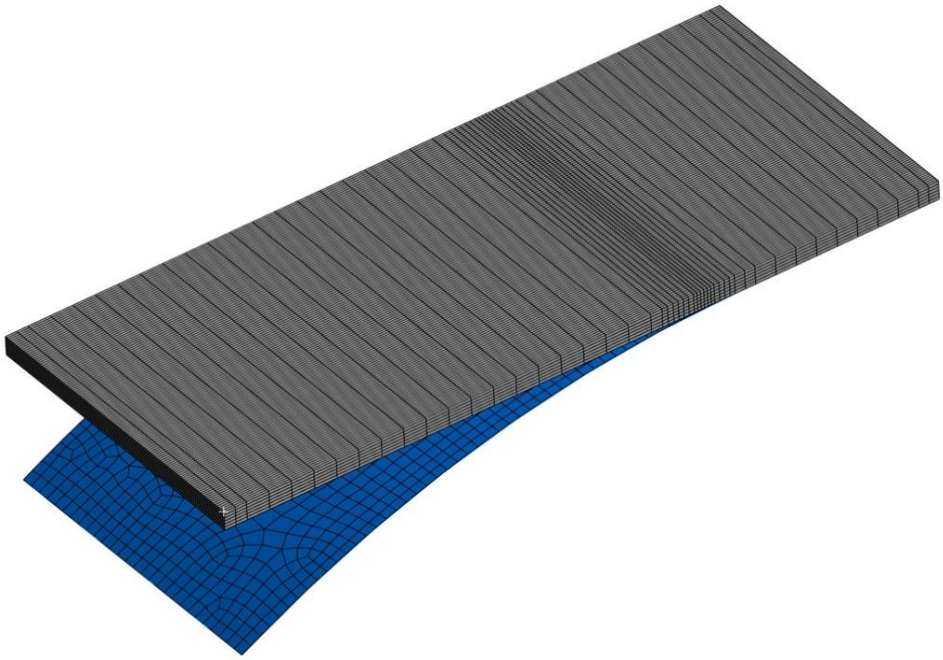

Figure 13. Mesh of Trans Varestraint Test Model

Additionally, to accurately reproduce the heat source characteristics of TIG welding and account for the volume and strain changes induced by the phase transformation during metal melting and solidification, an APDL command stream was developed. This command stream incorporates a moving double ellipsoid heat source model and utilizes the element birth and death technique to simulate the welding process in the Trans Varestraint Test. The complete APDL command stream is provided in the appendix.

In the equations, a, b and c represent the dimensions of the heat source in the x, y and z directions, respectively. x_0 and y_0 denote the initial position of the heat source; t represents

time, while v is the welding speed; U and I correspond to the voltage and current, respectively; η represents the welding efficiency.

$$q_f(x,y,z,t) = \frac{6\sqrt{3}fQ}{abc\pi\sqrt{\pi}} exp\left(\frac{-3(x-x_0)^2}{a^2}\right) exp\left(\frac{-3(y-y_0)^2}{b^2}\right) exp\left(\frac{-3\left(z-v(t+t_0)\right)^2}{c^2}\right) \quad (32)$$

$$Q = \eta UI \quad (33)$$

HouldCroft Test

Unlike the Trans Varestraint Test, the Houldcroft Test is classified as a self-restraint test. As shown in the schematic diagram, the specimen contains multiple slots of varying depths, which provide different levels of rigidity across the specimen. Due to this characteristic, the Houldcroft Test is also referred to as the fishbone test, as shown in Figure 14.

Although this test is more convenient to perform since it does not require the application of additional tensile strain, it does not allow for accurate measurement of strain variations within the welded region. As a result, it is not suitable for quantifying the critical conditions for hot cracking susceptibility. This study includes the Houldcroft Test for two key reasons: 1. Simplified testing procedure, making it easy to implement; 2. Evaluation of the effect of welding speed on hot cracking, by correlating the results with the Brittleness Temperature Range (BTR) obtained from the Trans Varestraint Test.

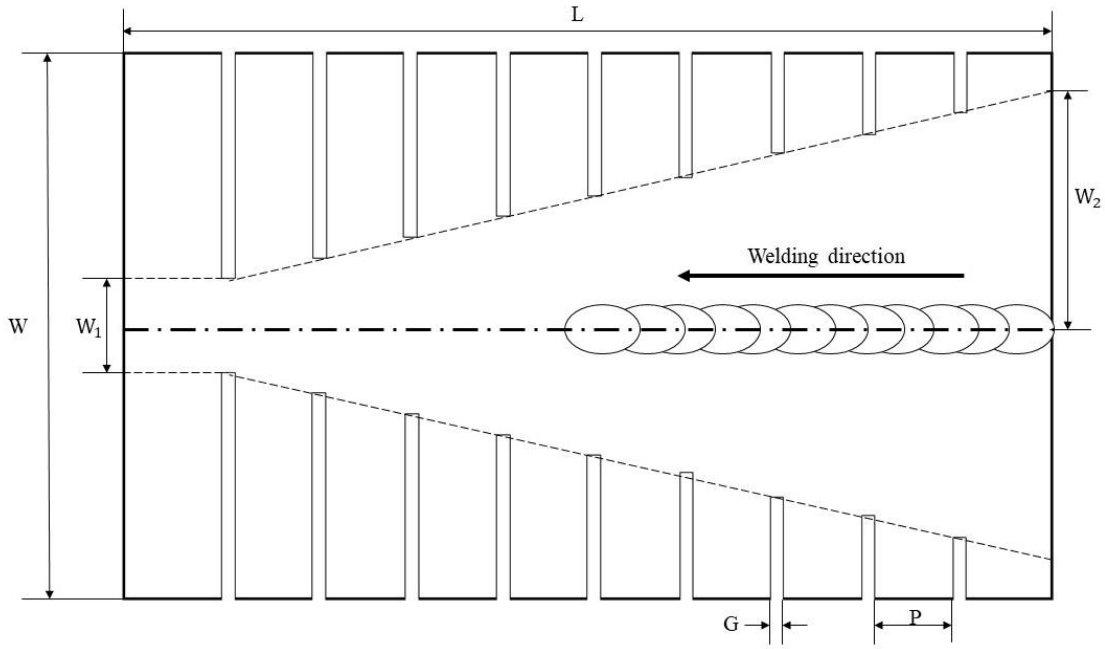

Figure 14. Schematic of Houldcroft Test

Table 1. Parameter of Houldcroft Test

Parameter	W	W_1	W_2	L	G	P
Value(mm)	44.6	7.72	38.78	76	1	6.5

The finite element model for the Houldcroft Test was developed in SYSWELD. The Figure 15 illustrates the mesh discretization of the test specimen, where the welding region is refined with a denser mesh to ensure accurate computation of strain variations during the welding process. The specimen has a thickness of t=3 mm.

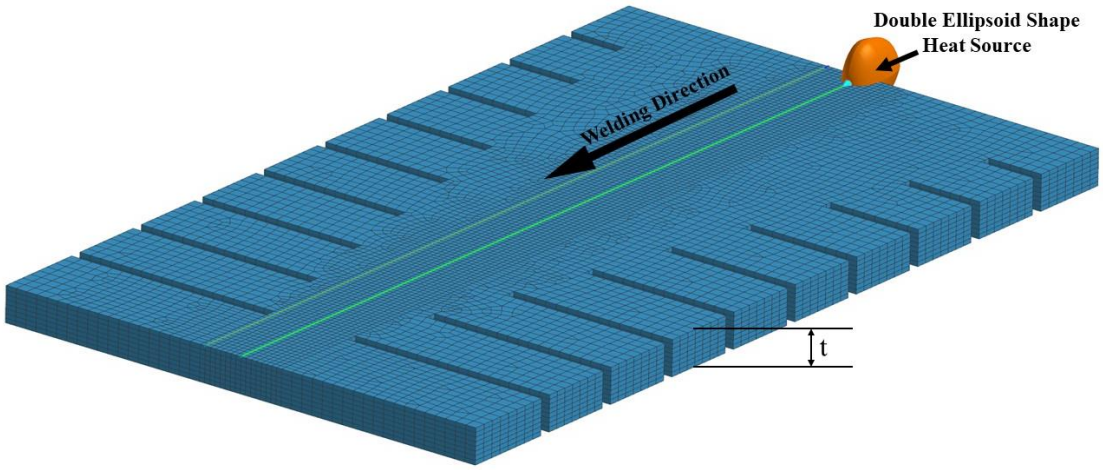

Figure 15. Houldcroft Test in SYSWELD

2.3.2. Finite Element Method in Welding Process

This study aims to investigate the propagation of three-dimensional cracks in a welding residual stress environment. To obtain the residual stress distribution, finite element simulations were conducted for two common welding configurations: T-joint welding and multi-pass welding. Both welding models, T-joint welding and multi-pass welding, were developed and simulated in SYSWELD to obtain the residual stresses distribution.

T-joint Welding

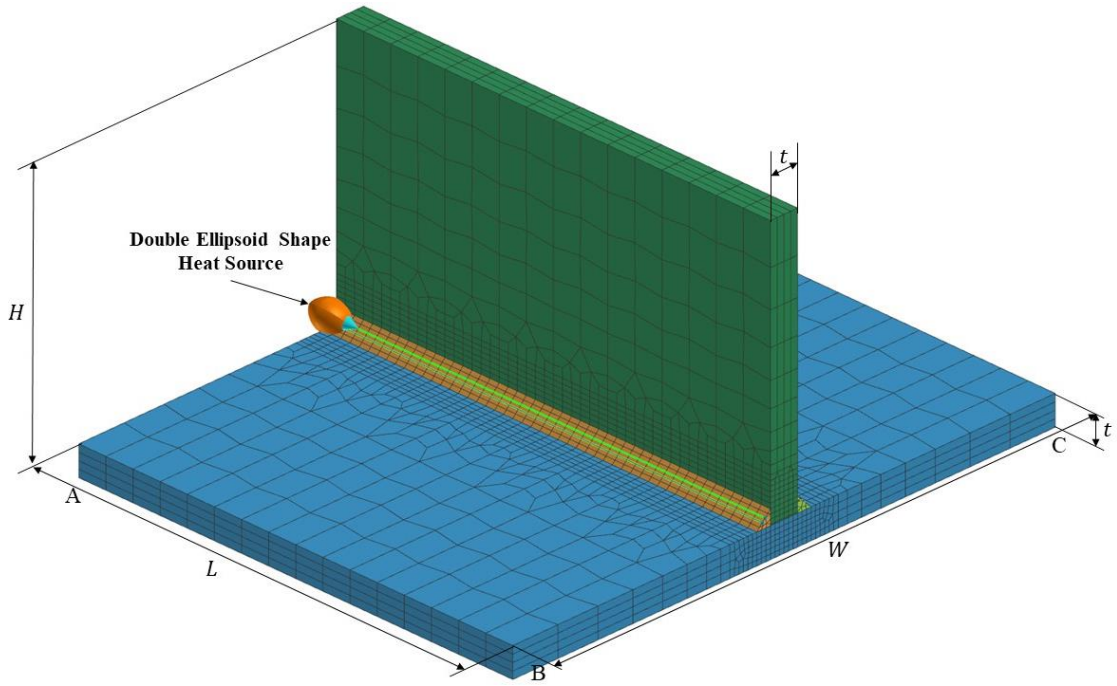

Figure 16. FE Model with Dimensions and Boundary Conditions of T-Joint Welding

Table 2 Parameter of T-joint welding model

Parameter	H	L	W	t
Value (mm)	60	96	120	6

Multi-pass welding

Similar to the aforementioned models, the finite element model for multi-pass welding serves as the first step in the four-step numerical calculation process. This model is used to obtain the temperature evolution of weld bead nodes over time and the welding residual stress distribution in the structure after cooling. The simulation employs transient thermal analysis to compute the temperature field and a transient nonlinear mechanical model to determine the stress-strain field. As previously mentioned, austenitic stainless steel 316 is used as the material for this model.

As illustrated in the Figure 17-Figure 18, the multi-pass welding model consists of six weld layers, with slight variations in heat input due to differences in the size and shape of the weld bead interfaces. To ensure high accuracy, a refined mesh is applied in the welded region. The boundary conditions for the multi-pass welding model are indicated in the figure at points A, B, and C: Point A (u=v=w=0); Point B (u=v=0); Point C (v=0). These boundary conditions are designed to replicate the unconstrained conditions used during the welding process.

The dimensional parameters of the model and the heat input parameters are provided in the corresponding tables. These tables outline the geometric specifications of the multi-pass welding model and the thermal input conditions used in the simulation, ensuring accurate replication of the welding process.

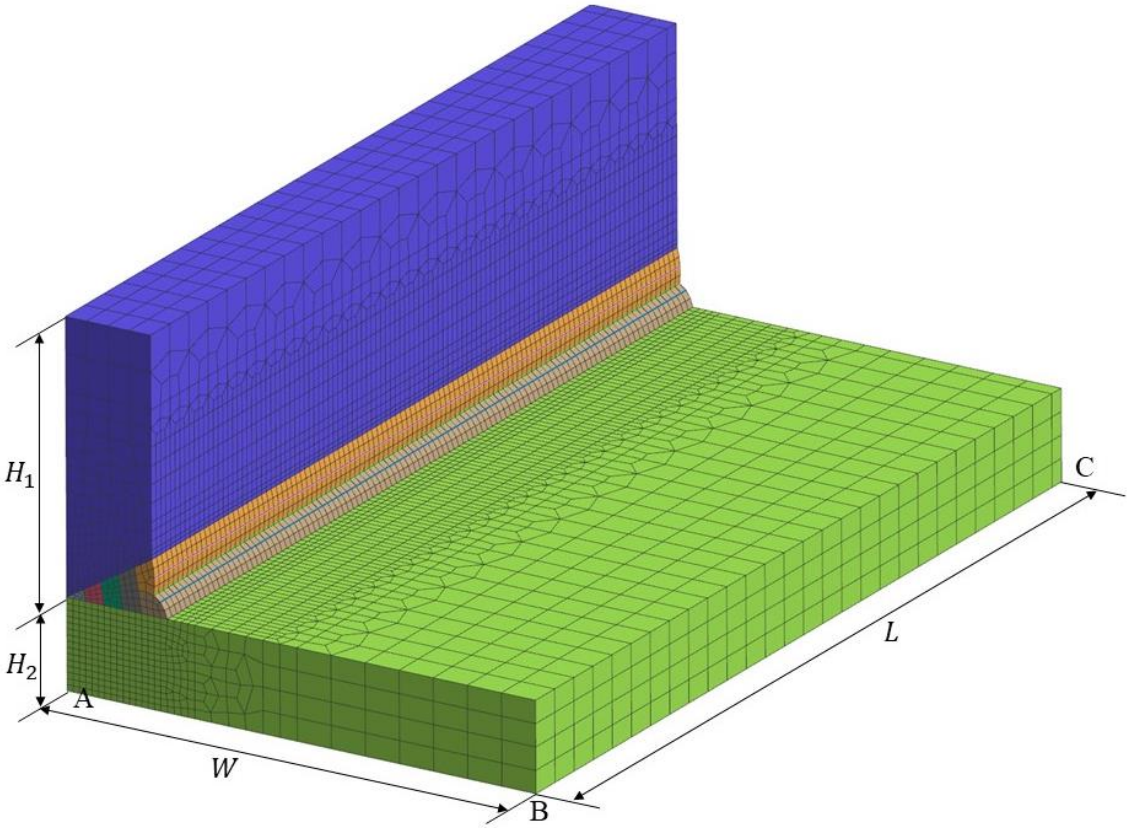

Figure 17. FE Model with Dimensions and Boundary Conditions of Multi-pass Welding

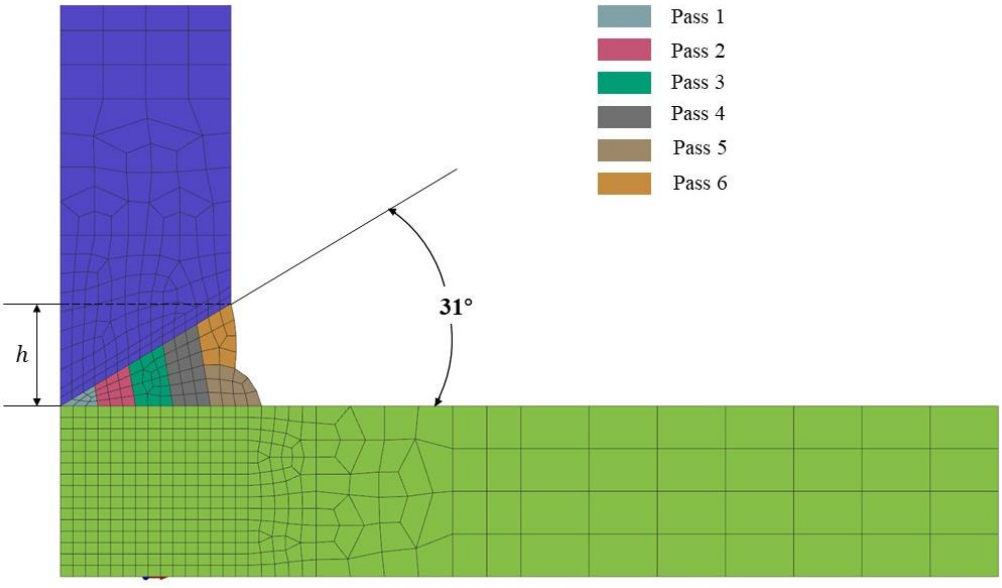

Figure 18. Angle and size of weld beads

2.4. Fatigue Crack Growth (FCG) Simulation under Welding Residual Stresses Conditions

The fatigue crack growth process is usually divided into three stages: initiation stage, short crack growth stage and long crack growth stage. [43] In this study, special attention is paid to the simulation and analysis of long crack extension under the influence of welding residual stresses. In the case of long cracks, the crack size is significantly larger than the microstructural characteristics of the material and the plastic zone at the crack tip. Therefore, the application of Linear Elastic Fracture Mechanics (LEFM) is appropriate and sufficient to achieve the objectives of this study. Welding residual stresses obtained using the methodology described in Section 2.3 were applied to the fatigue crack growth model, illustrated in Section 2.1, through a mapping method, embedded code in Ansys [53], as initial loads. The application of these mapped residual stresses in FCG model is shown in Figure 19.

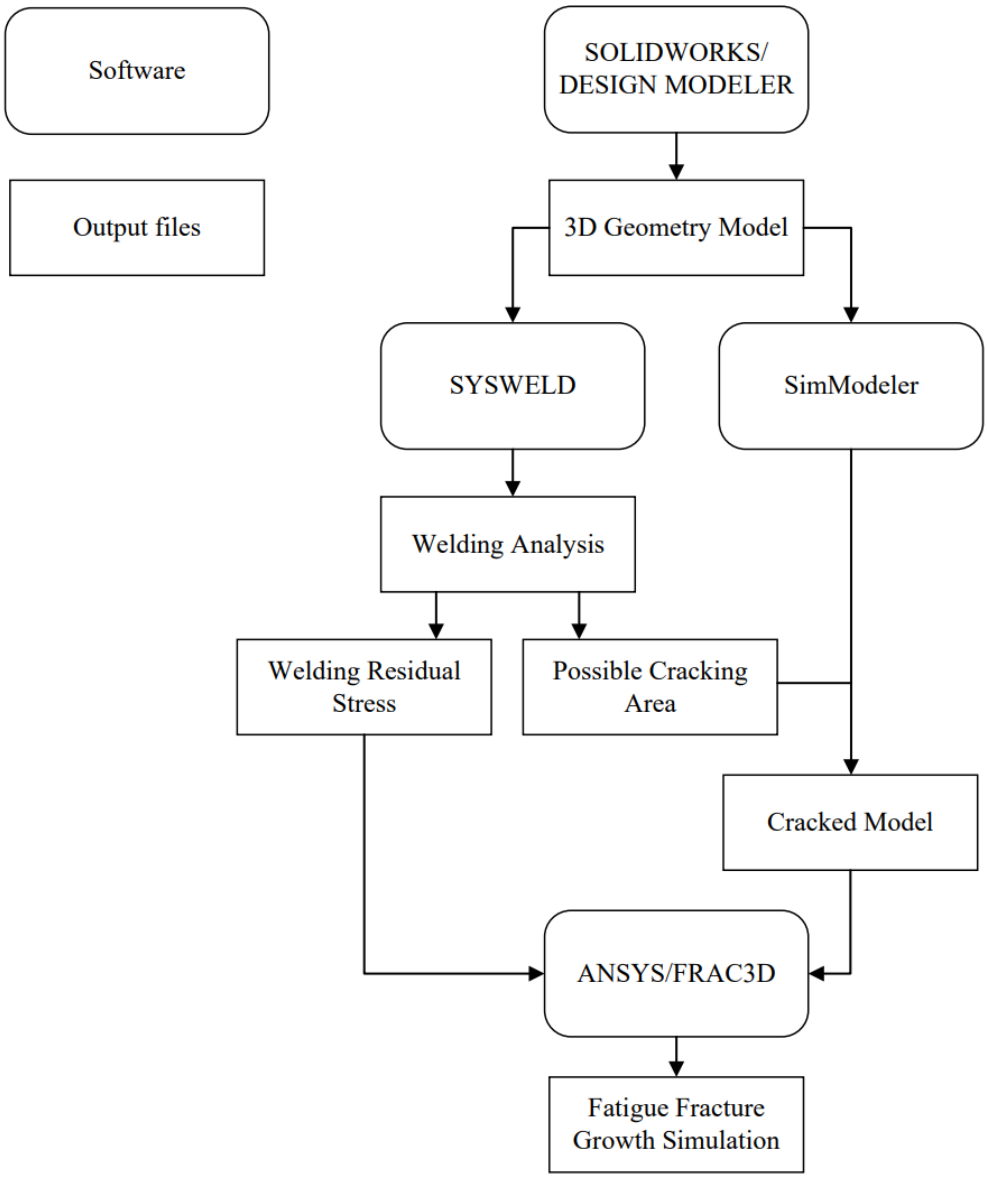

Figure 19. Flow chart of FCG simulation in welded structures

Figure 20 illustrates the boundary conditions applied to a FCG model that includes welding residual stresses. To ensure that the residual stresses are accurately mapped onto a model with a completely different mesh, the new model (FCG model) must use the same boundary conditions as the original welding simulation. This consistency ensures the validity of the mapped residual stress field. In addition, a tensile stress of 50 MPa was applied to both side surfaces of the model to represent the cyclic external loading used in

the FCG simulation. The boundary conditions are used in both T-joint welding model and Multi-pass model.

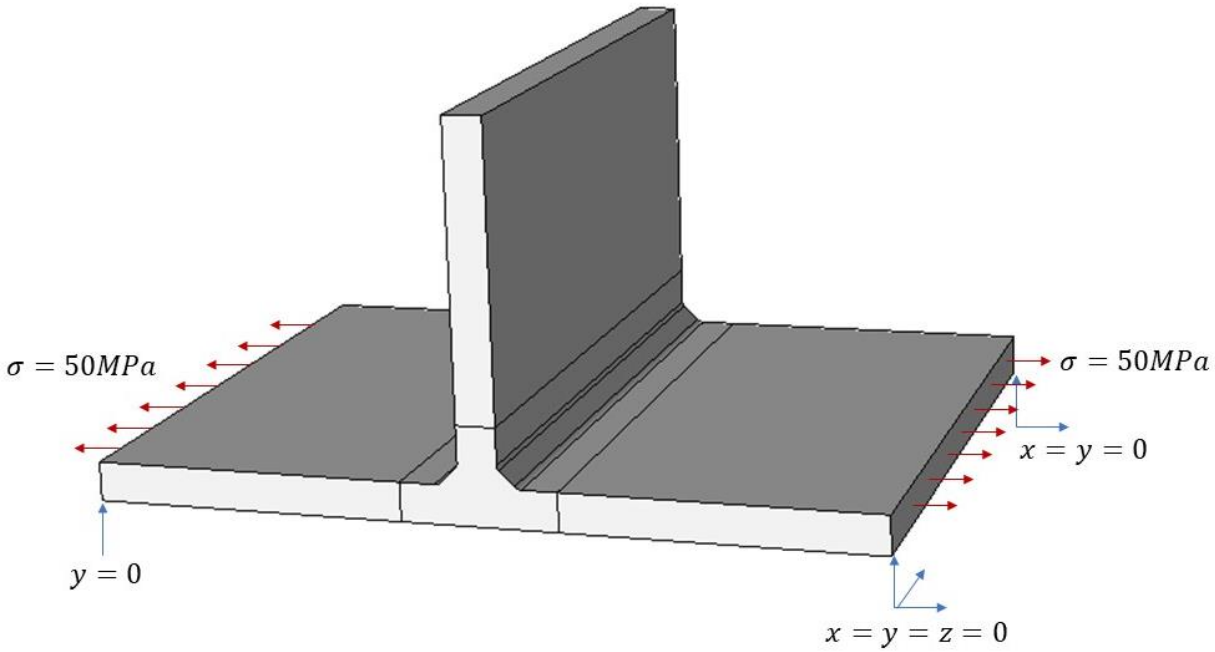

Figure 20. Boundary conditions of cracked welded model

The crack location is determined based on the region of maximum tensile residual stress, which is described in detail in Section 3.6. A semicircular surface crack with a radius of 2 mm was introduced on the model surface as the initial crack. In order to fully analyze the FCG behavior under the influence of welding residual stresses, the Walker equation [62] was used as the main fatigue crack growth criterion in this study, as shown in (33). In addition, the Paris law (14) and the maximum stress intensity factor criterion were used for comparative analysis to evaluate the effect of different fracture criteria on FCG prediction under residual stress conditions.

$$\frac{da}{dN} = C\left(\frac{\Delta K_{eq}}{(1-R)^{1-m}}\right)^{n} \tag{33}$$

Where,

$$R = \frac{K_{min}}{K_{max}} \tag{34}$$

$$K_{min} = K_{RS} - K_L, K_{max} = K_{RS} + K_L \tag{35}$$

Where K_{min} is minimum stress intensity factor; K_{RS} is stress intensity factor caused by residual stresses; K_L is stress intensity factor caused by cyclic external loads; stainless steel 316 constants were adopted from [63], i.e. $n = 3.159$, $m = 0.032922$ and $C = 1.67154 \cdot 10^{-13}$.

3. Results and Discussion

3.1. Crack Propagation Simulation Results

Starting with a small semi-circular surface crack oriented at 45° with respect to the cylinder axis, full 3-D simulations of crack growth behavior were performed using the methodology described in Section 2.1, for both solid and hollow cylinders. Referring to Figure 3, the ratio of the initial crack depth C_d, to the radius of the cylinder, $D_s/2$, was specified to be 0.05. In order to minimize end effects, a cylinder length-to-diameter ratio of $L_s/D_s = 5$, was used in the finite element models. Since the initial semi-circular crack is located in a plane perpendicular to the maximum principal stress, the mode-II and mode-III stress intensity factors are initially zero and K_I can be accurately determined as a function of along most of the crack front. The K_I stress intensity factors obtained for a small crack on the surface of a cylinder very closely match the K_I values available for a semicircular crack in a half-space. The curve fit solution for a semi-circular crack in a half-space, based on a variety of computational solutions, is given in [64]

$$K_I = \frac{2}{\pi}\sigma\sqrt{\pi a}\left(1.211 - 0.186\sqrt{\sin\theta}\right) \tag{36}$$

where a is the crack radius and is measured along the crack front from the free surface. Figure 21 shows a comparison of the nondimensional mode-I stress intensity factor for the semi-circular crack on the cylinder surface obtained using SimModeler and ANSYS in this study, with K_I values obtained from (36) and [32], which used the Boundary Element Method. As can be seen, all three are in very close agreement. In Figure 21, s^* is the nondimensional arc length along the crack front, i.e., $s^* = s/s_0$, where s is the distance

along the crack front measured from the free surface and s_0 is the crack front's total arc length. A nondimensional stress intensity factor K_I^* is given by

$$K_I^* = \frac{K_I}{K_0} \tag{37}$$

with,

$$K_0 = \sigma_0 \sqrt{\pi r} \tag{38}$$

In (38), $_0$ is the maximum principal stress on the cylinder surface, i.e., $_0 = Tr/J$, with $J = r^4/2$ for the solid cylinder, r the outer radius of the cylinder, $r = D_s/2$ (Figure 3), and T is the applied torque. Thus, for the cracked solid cylinder

$$K_0 = \frac{2}{\sqrt{\pi}} T r^{-\frac{5}{2}} \tag{39}$$

It should be noted that both (36) and the numerical solutions for the mode-I stress intensity factor shown in Figure 21 are not claimed to be accurate within $\pm 10°$ of the free surface, since the 3-D stress singularity at the crack tip changes at the point of intersection of the semi-circular crack front with the free surface, resulting in $K_I = 0$ on the free surface. As demonstrated in [23], finite element models with sufficient mesh refinement on the crack front near the free surface can capture this phenomenon, but once the crack begins to grow, the free surface intersection angle changes in such a way that the stress singularity quickly reverts back to the classical $1/\sqrt{r}$ asymptotic behavior. Thus, in this study, the details associated with this free-surface effect were ignored.

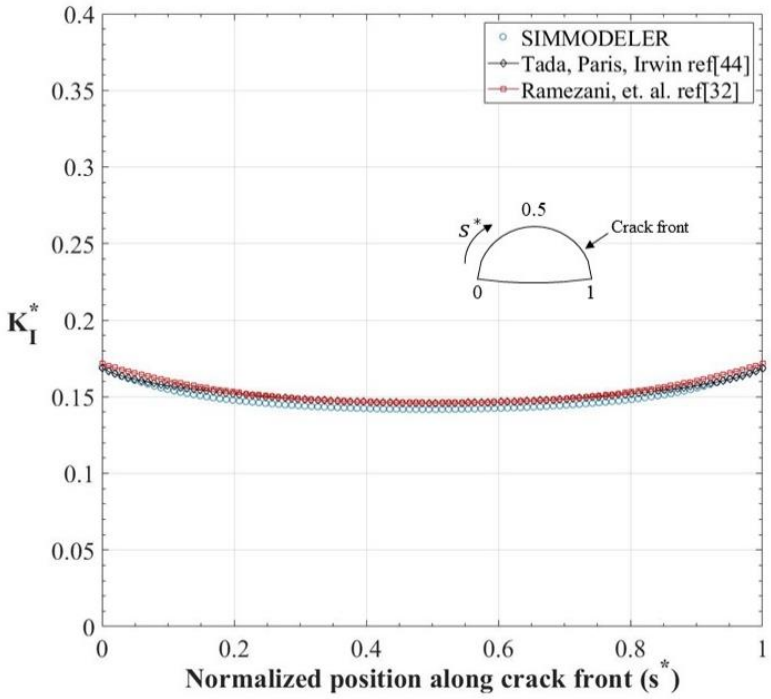

Figure 21. Comparison of normalized K_I^* for the initial semicircular surface crack with results from refs. [32, 62]

3.1.1. Crack Growth in Solid Cylinders

The progression of the spiral crack front that evolves from the semicircular surface crack is shown in Figure 22 and Figure 23. A typical computation for each crack configuration used approximately 238,000 elements and 356,000 nodes. In Figure 22 (a-c) the fine line contours depict the crack front at successive steps in the computation. In Figure 22 (a) and (c) arrows point to the initial crack location. Note that early in the simulation, the crack front contour lines are quite dense as the crack begins to grow from its initial surface flaw geometry. The crack increments controlled by a_{max} in (17) are maintained at small values early in the crack growth simulation in order to prevent any significant errors from propagating into later portions of the evolving crack geometry. As the evolving crack front spirals around the cylinder surface and traverses the cylinder diameter, the crack front was allowed to advance in larger incremental steps. Figure 22 (d) shows the final fracture

surface after the crack has almost completely traversed the diameter of the solid cylinder. The crack length a during propagation is represented by the crack length at its deepest point of penetration, i.e., where $s^* = 0.5$. This crack length can be normalized with respect to the outer radius r of the cylinder, e.g., a/r. Figure 23 shows the spiral crack growth from $a/r = 0.1$ to $a/r = 1.9$ as the crack front advances across the diameter of the cylinder.

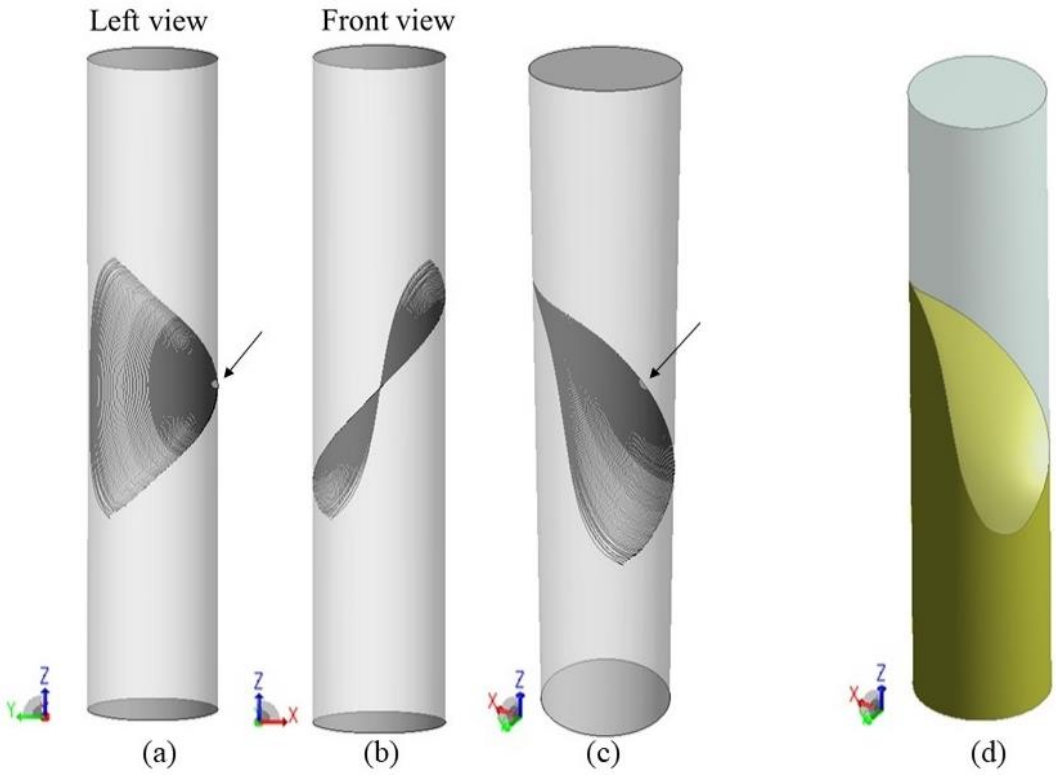

Figure 22. Different views showing the evolution of the spiral crack in the solid cylinder. Arrows point to initial surface crack location.

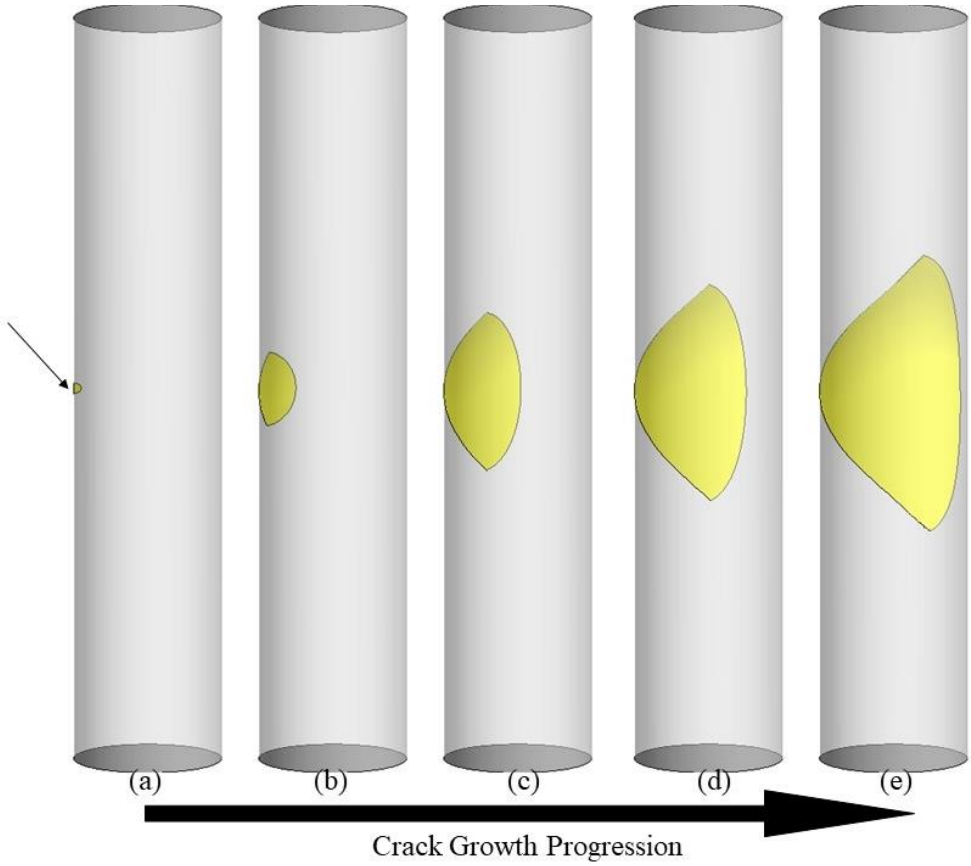

Figure 23. Crack progression in the solid cylinder (in (a) the small arrow points to location of initial surface crack).

Figure 24-Figure 26 show the variation in the mixed mode stress intensity factors, $K_I^*, K_{II}^*, K_{III}^*$, along the crack front as the crack grows. Since the magnitude of K_I is always much greater than K_{II} and K_{III}, crack growth in the solid cylinder under pure torsion conditions is K_I-dominated behavior. This mode I dominated behavior can also be seen in Figure 23, where the crack propagates at 45° to the cylinder axis on the outer surface of the cylinder, thus forming the spiral shape. At the midpoint of the crack front ($s^* = 0.5$) K_{II} remains zero and thus the direction of crack growth for this single point on the crack front does not change as the crack propagates. This is the only point on the crack front that propagates in a straight line across the diameter of the cylinder. As expected from the

imposed boundary conditions, the values of K_I^* (Figure 24) and K_{III}^* (Figure 26) are quite symmetric on the growing crack front and K_{II}^* (Figure 25) takes on an anti-symmetric character. Since K_{II} has only a minor effect on the propagation direction during most of the crack growth, it can be seen (Figure 23) that the crack front propagating within the cylinder body maintains a consistent shape during propagation. This suggests that a useful empirical expression can be obtained for K_I along the crack front for any depth of crack penetration.

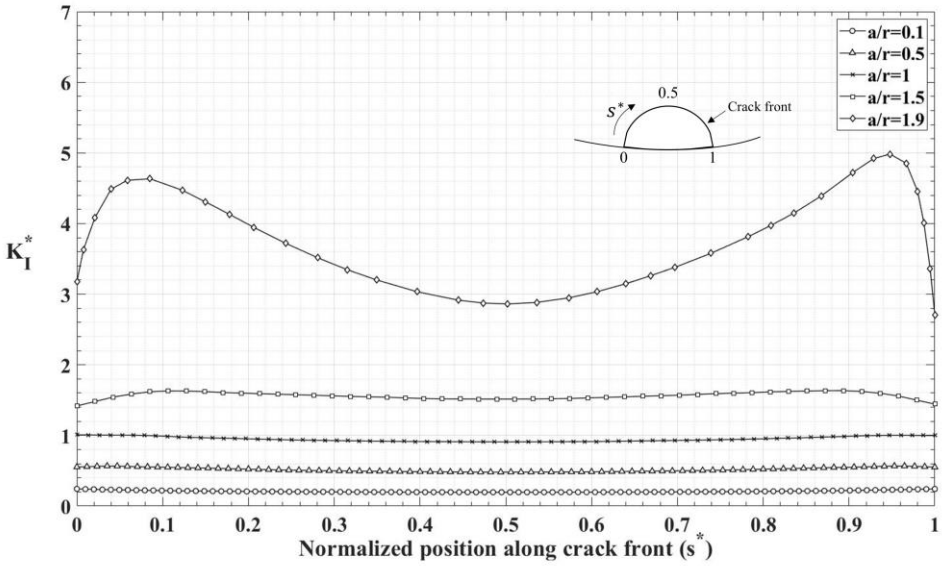

Figure 24. K_I^* on the crack front at different stages of crack growth in the solid cylinder.$K_I^* = K_I \,/\, K_0$

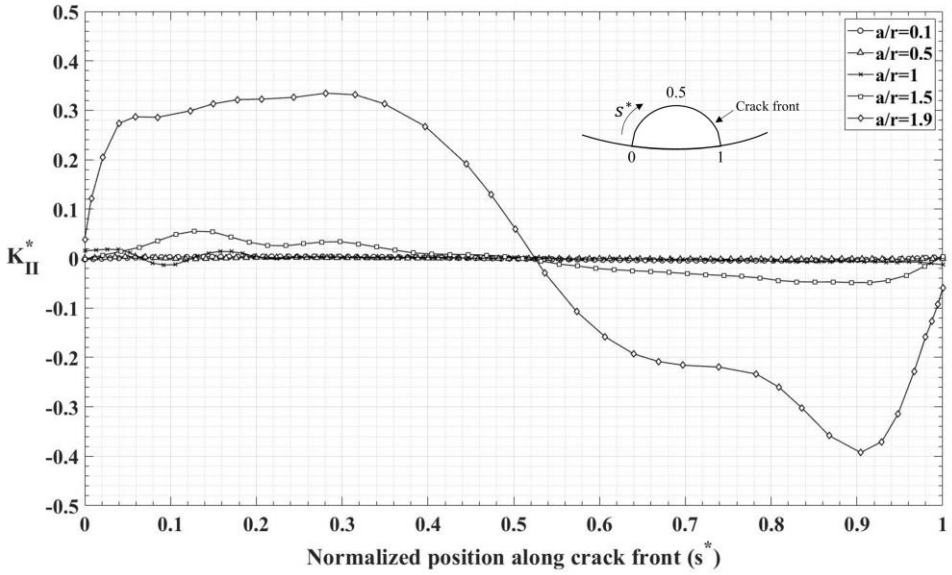

Figure 25. K_{II}^* on the crack front at different stages of crack growth in the solid cylinder.
$K_{II}^* = K_{II} \,/\, K_0$

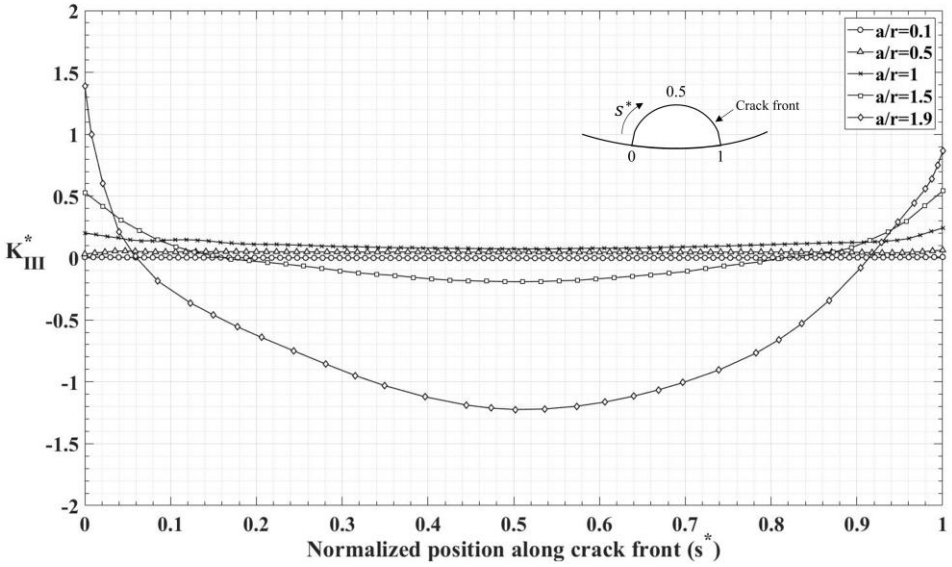

Figure 26. K_{III}^* on the crack front at different stages of crack growth in the solid cylinder.$K_{III}^* = K_{III} \,/\, K_0$

Figure. 27 contains a plot, in Cartesian coordinates, of the growing crack at specific points on the crack front, projected onto the cylinder's symmetry plane (the normal for this plane is aligned with the cylinder's axis). Because of the antisymmetric (spiral) shape of

the growing crack, only one half of the crack front is plotted on the projected circular cross-section in Figure. 27. The dashed lines in Figure. 27 represent the shape of the crack front projected onto this plane as the crack progresses through the solid cylinder. The advancing crack front continuously breaks through the outer surface of the solid cylinder at various values of x/r and y/r as shown by the dashed lines. The trajectories for seven nodes on the initial crack front (0°, 20°, 40°, 60°, 70°, 80° and 82°) are also plotted in Figure. 27 as solid lines orthogonal to the crack fronts and represent the individual trajectories for these points as the crack front advances. The symmetry point on the initial crack front, located at $s^* = 0.5$, is labeled as 0°. Since K_{II} always remains zero at this location, the crack front at this point advances in a straight line across the cylinder's diameter. Thus, at this one point the crack length a, which is also the deepest point of penetration along the crack front, is given by $a/r = x/r$. In contrast, all other points on the crack front have a more complex 3-D spatial trajectory. The plot in Figure. 27 can be used to determine the crack length, a/r, at the deepest point of crack penetration in the interior of the solid cylinder based on the observed locations of the crack front on the cylinder surface. If the polar angle between the two exposed crack fronts on the cylinder's surface is given by $2\ $, then $x/r = 1\ \cos\ $, $y/r = \sin\ $, and the value of a/r can be obtained directly from Figure. 27. For example, when the spiral crack fronts have propagated to points on the cylindrical surface where they are separated by an angle $2\ = 124°$, the planar coordinates in Figure. 27 are given by ($x/r = 0.53,\ y/r = 0.88$). The value of a/r can then be determined by following the crack front arc (dashed line) back to the 0° line. Thus, in this example, the interior central crack tip is located at $x/r = 1.0$.

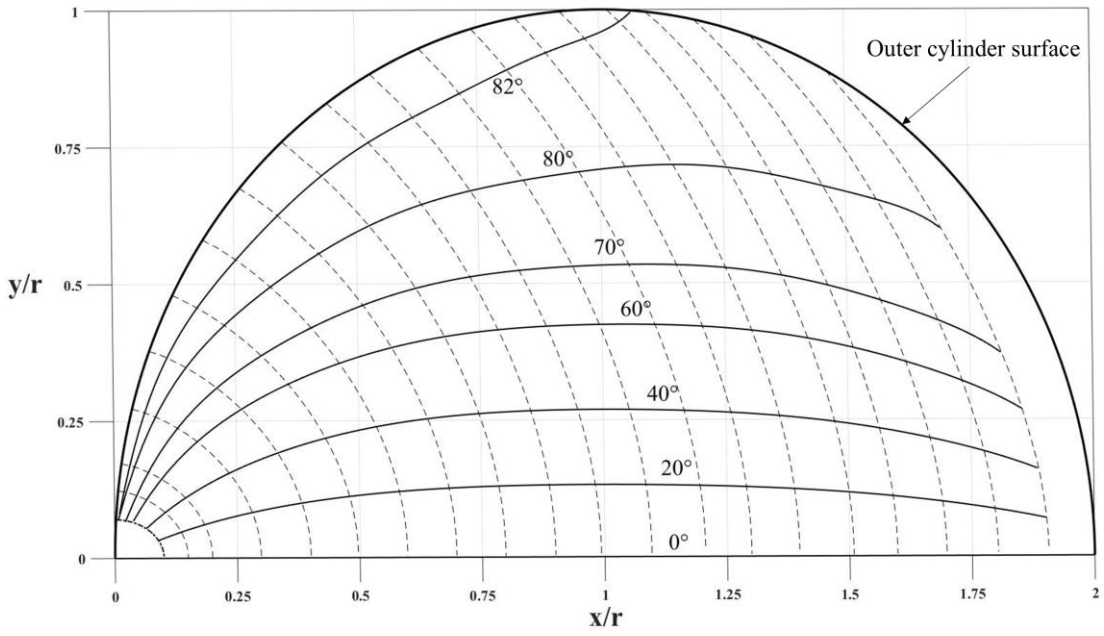

Figure. 27 Orthogonal crack trajectory diagram

Figure 28 contains plots of the normalized mode I stress intensity factor, K_I^*, for six of the orthogonal trajectories shown in Figure. 27, at 0°, 20°, 40°, 60°, 70° and 80°. These curves can be expressed empirically using a 5th order polynomial expression (40) and the coefficients given in Table 3.

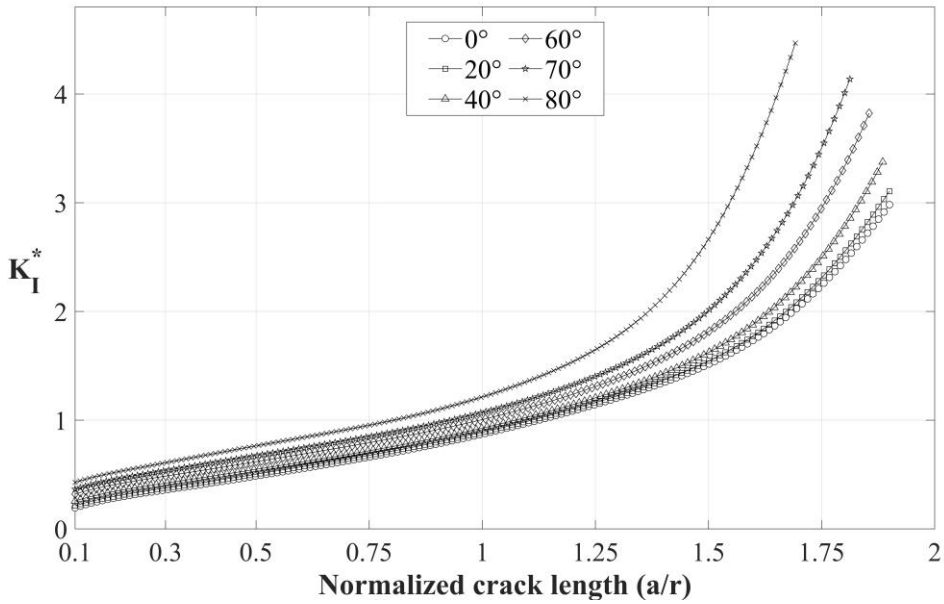

Figure 28. K_I^* at different positions on the crack front given as a function of a/r. $K_I^* = K_I \,/\, K_0$

$$K_I^* = C_0 + C_1\left(\frac{a}{r}\right) + C_2\left(\frac{a}{r}\right)^2 + C_3\left(\frac{a}{r}\right)^3 + C_4\left(\frac{a}{r}\right)^4 + C_5\left(\frac{a}{r}\right)^5 \qquad (40)$$

Table 3. Coefficients for K_I^* in (40) for the angles shown in Figure 28

	C_0	C_1	C_2	C_3	C_4	C_5
0°	0.0701	1.5389	-2.9146	4.1574	-2.6363	0.6604
20°	0.0808	1.5992	-3.1178	4.4585	-2.8458	0.7169
40°	0.0999	1.9174	-4.2693	6.1705	-3.9843	1.0001
60°	0.1526	2.0403	-4.7245	7.0077	-4.6840	1.2233
70°	0.1805	2.2622	-5.5069	8.3268	-5.7222	1.5398
80°	0.2275	2.4142	-5.9951	9.6070	-7.1646	2.1275

Equation (40) is particularly convenient for fatigue crack growth life estimates when the crack growth rate material constants C and , in the Paris-Erdogan eqn. (14), are known, e.g.,

$$N_f = \int_{a_i}^{a_{cr}} [C(\Delta K_I)^{\alpha}]^{-1} da \qquad (41)$$

In (41), the number of cycles for failure N_f are obtained by integration of (14), where a_i is the initial crack length, a_{cr} the critical crack length (determined from $K_I = K_{IC}$), and K_I is obtained from (40) using the 0° constants given in Table 3.

3.1.2. Crack Growth in Hollow Cylinders

Referring to Figure 3, the hollow cylinder geometry has an inner bore radius $r_1 = d/2$ and an outer radius $r = D_h/2$. The loading and remote boundary conditions for the hollow cylinders were identical to those used for the solid cylinder. In this study, cylinders with two different r_1/r ratios were examined in detail, $r_1/r = 0.5$ and $r_1/r = 0.25$. Calculation of stress intensity factors and crack growth for through-cracks in thin-walled tubes, i.e., $r_1/r > 0.9$, is greatly simplified by the assumption of plane stress conditions and a maximum principal stress that causes only pure mode I cracking behavior. However, crack growth behavior in thick-walled hollow cylinders is considerably more complex and distinctly different than the cracking behavior observed in solid cylinders. The general crack propagation process in hollow cylinders can be divided into four distinct stages: 1) a small surface crack on the outer radius r initially propagates in a manner similar to the crack growth behavior observed in solid cylinders, 2) the crack breaks through the inner r_1 wall surface, 3) resulting in two crack fronts that propagate in opposite spiral directions for approximately 170° around the cylinder, at which point, 4) both crack fronts appear to abruptly change direction and propagate vertically towards each other on a line parallel to the cylinder's axis. Figure 29 shows a typical fracture surface for a hollow cylinder, where crack growth starts from a small surface flaw on the left side of the picture. After the crack on the outer surface breaks through the cylinder's inner radius wall, the resulting two crack fronts propagate by spiraling in opposite directions. The sharp point at the crack front apex is formed when both of the spiraling crack fronts suddenly appear to "turn" ~140°, resulting in a vertical fracture that separates the hollow cylinder into two halves.

Figure 29. PMMA hollow cylinder fracture surface (pure torsion).$r_1/r = 0.5$

Figure 30-Figure 31 show the incremental crack growth results obtained from finite element simulations for $r_1/r = 0.5$, as the individual spiral crack fronts propagate approximately 170° around the cylinder. In the initial crack growth stage, the crack smoothly propagates through the cylinder wall from the semicircular surface starter crack (arrows in Figure 30(b), Figure 31(a)). Once the crack breaks through the hollow cylinder's inner wall at r_1 (Figure 31(b)) the crack separates into two crack fronts that grow in a spiral along the cylinder's axis (Figure 30(c), Figure 31(d)).

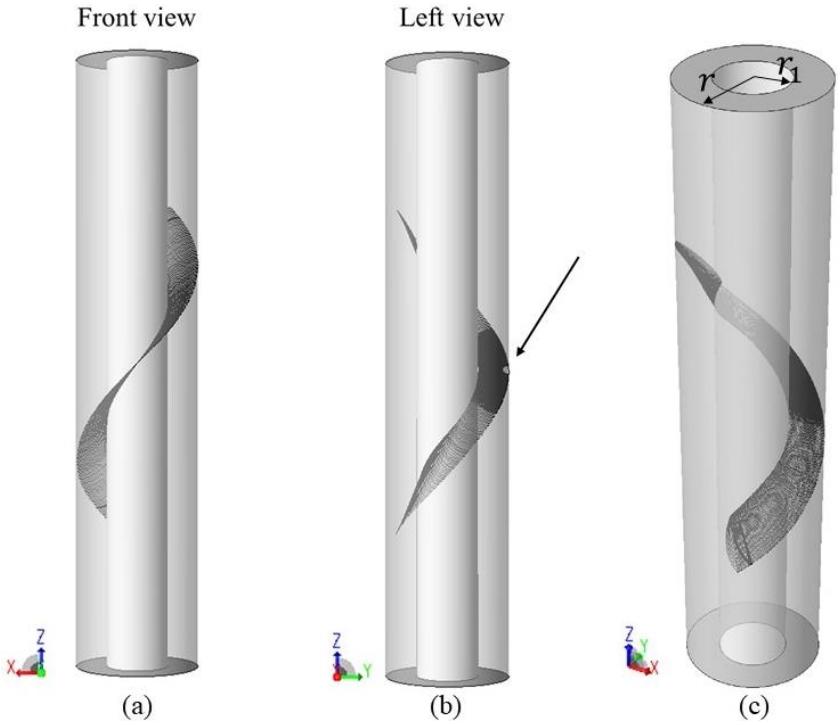

Figure 30. Different views showing the evolution of the spiral crack in a hollow cylinder with $r_1/r = 0.5$. Arrow points to the location of the initial surface crack.

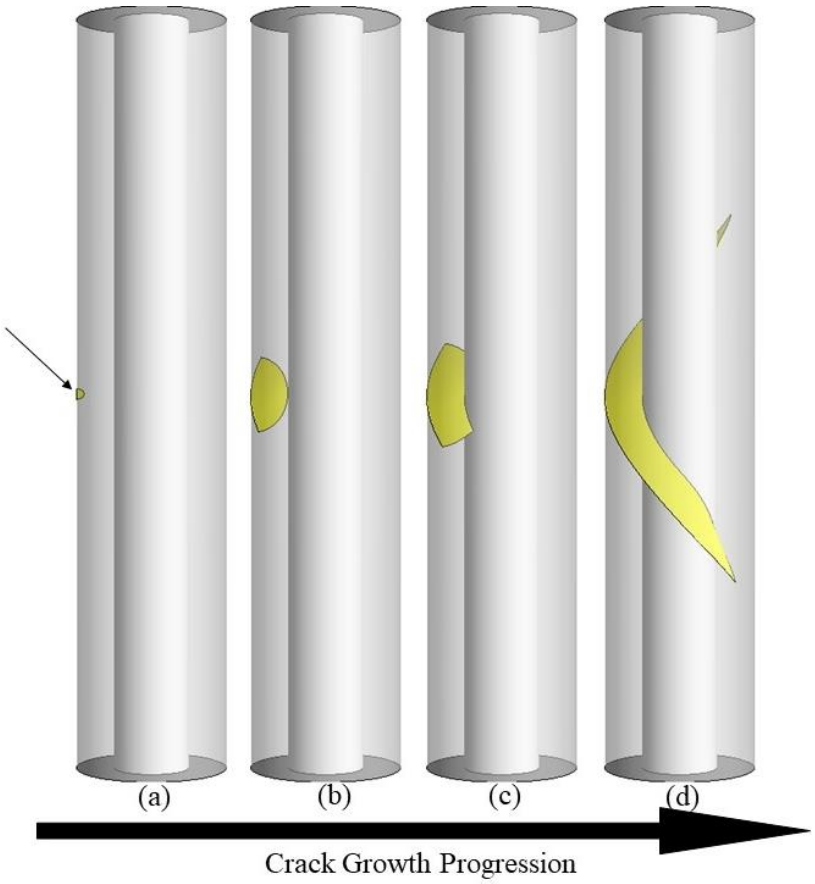

Figure 31. Crack progression in the hollow cylinder ($r_1/r = 0.5$). Small arrow points to location of the initial surface crack.

Figure 32 - Figure 34 contain plots of the nondimensional, mixed-mode, stress intensity factors, $K_I^*, K_{II}^*, K_{III}^*$, along the crack fronts at the four different stages in the crack progression depicted in Figure 31. The K^* nondimensional stress intensity factors shown in Figure 32-Figure 34 are defined in a manner similar to the solid cylinder case, i.e., (35)–(36), with the exception that $J = \left(r^4 \quad r_1^4\right)/2$ in the expression for $_0 = Tr/J$. Thus, for the plots in Figure 32-Figure 34, with $r_1/r = 0.5$,

$$K_0 = \frac{32}{15\sqrt{\pi}} T r^{-\frac{5}{2}} \tag{42}$$

After the surface crack has broken completely through the cylinder wall (labeled stage 2 in Figure 32-Figure 34), the crack front is constrained between the outer wall of the

cylinder r, $s^* = 0$, and the inner wall radius r_1, $s^* = 1$. The stress intensity factors for the narrow crack front growing in a spiral are labeled as stage 3 and 4 in Figure 32-Figure 34. As shown in Figure 32, as the crack spirals away from the crack initiation point, K_I^* near the outer wall surface becomes greater than K_I^* on the inner wall surface. Thus, the point located on the crack front on the outer radius r advances more rapidly than the point on the inner radius at r_1. It's also interesting to note that at stage 4, K_{II}^* in Figure 33, corresponding to the crack fronts in Figure 30(c) and Figure 31(d), shows a strong to + variation from the outer wall, $s^* = 0$, to the inner wall, $s^* = 1$, indicating a strong tendency for the crack front to become steeply inclined with respect to the plane of the growing crack front and the axis of the cylinder. This steep inclination in the crack front can be observed near the sharp point in Figure 29, where the elevation of the growing spiral crack front on the outer cylinder surface is greater than the elevation of the crack front on the inner wall. This "slant" in the plane of the crack front greatly increases the "sharpness" of the fracture point on the outer radius r as shown in Figure 29.

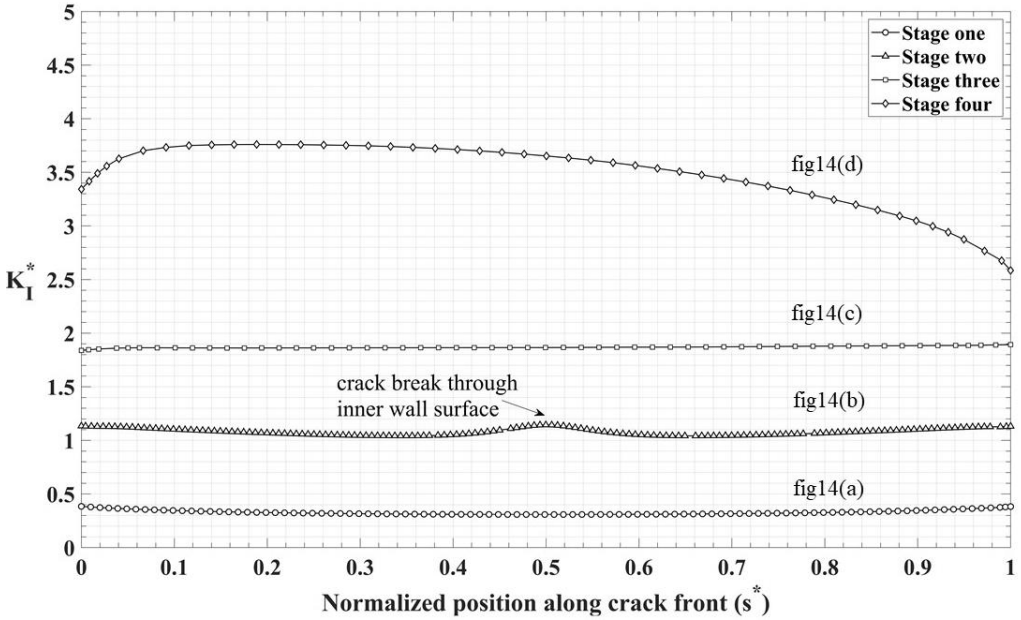

Figure 32. K_I^* on the crack front at different stages of crack growth in the hollow cylinder with $r_1/r = 0.5$. $K_I^* = K_I \,/\, K_0$

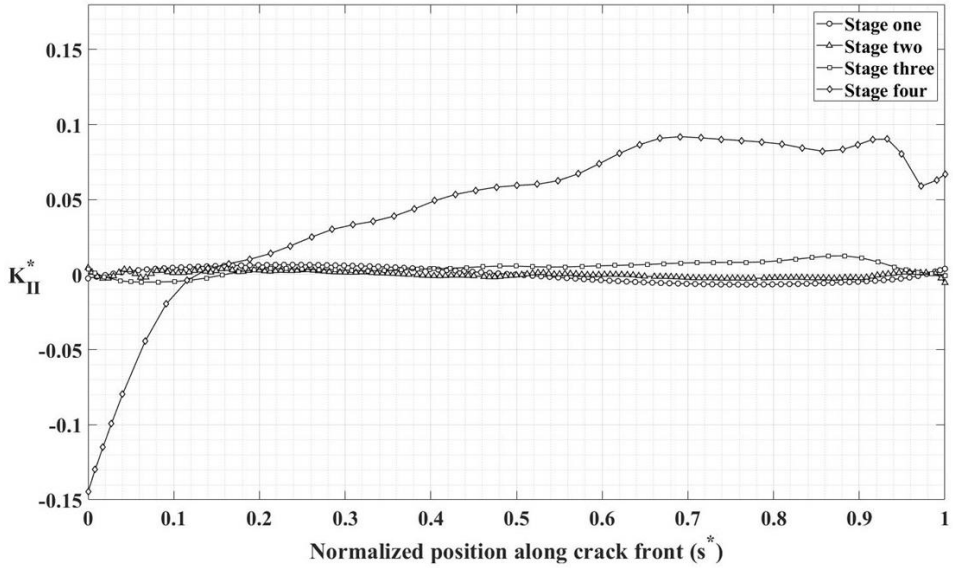

Figure 33. K_{II}^* on the crack front at different stages of crack growth in the hollow cylinder with $r_1/r = 0.5$. $K_{II}^* = K_{II} \,/\, K_0$

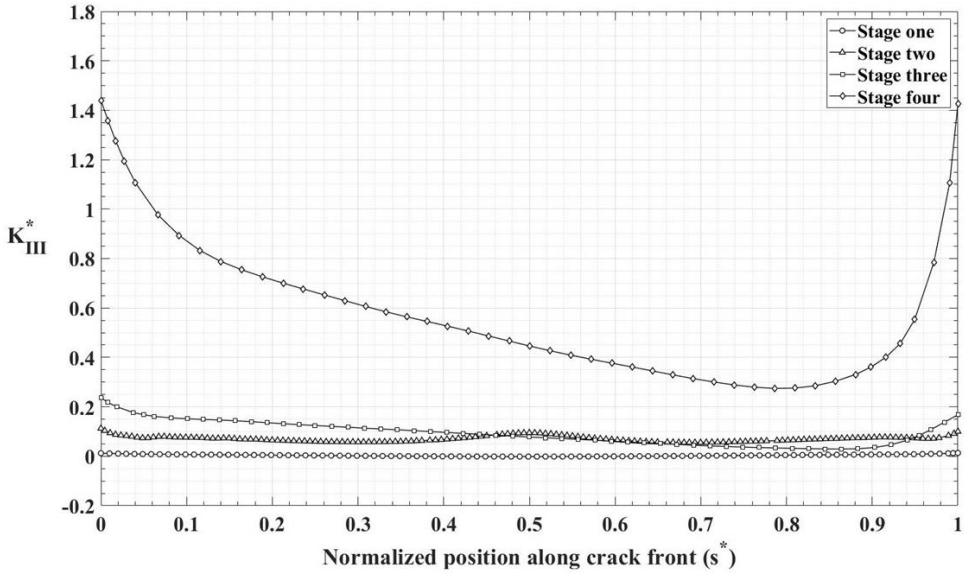

Figure 34. K^*_{III} on the crack front at different stages of crack growth in the hollow cylinder with $r_1/r = 0.5$. $K^*_{III} = K_{III} / K_0$

As was done for the solid cylinder case, an empirical curve fit can be performed to provide an accurate description of the stress intensity factors as a function of the crack length for the hollow cylinder. For the hollow cylinder, an empirical expression for K^*_{eq} (16), at the observable point on the crack front ($s^* = 0$) on the outer wall of the cylinder, can be given by

$$K^*_{eq} = C_0 + C_1\left(\frac{a}{r}\right) + C_2\left(\frac{a}{r}\right)^2 + C_3\left(\frac{a}{r}\right)^3 + C_4\left(\frac{a}{r}\right)^4 \tag{43}$$

In (43), the nondimensional crack length, a/r, is given by

$$\frac{a}{r} = \sqrt{1 + m^2}\theta \tag{44}$$

where a is the crack length described by a spiral on the cylinder's outer surface and

$$m = \frac{1}{r}\frac{dz}{d\theta} \tag{45}$$

In this case, ($r_1/r = 0.5$), m is constant and was determined from the crack growth simulations to be very close to $m = 1$, which was expected for crack growth on the

surface governed by the maximum principal stress oriented at 45° to the cylinder axis. Coefficients for (41) that provide an accurate fit for K_{eq}^{*} are given in Table 4, where the curve fit is broken into two separate angular ranges: 1) $0 \quad 0.255$, and 2) $0.255 \quad 0.8$. As can be seen in Figure 33-Figure 34, the mode II and mode III stress intensity factors provide only a slight contribution to K_{eq}^{*} up until the crack has grown to ~ 0.255 , thus $K_{eq}^{*} \simeq K_{I}^{*}$ for $0 \quad < 0.255$.

Table 4. Coefficients for K_{eq}^{*} in (43) for ($r_1/r = 0.5$)

	C_0	C_1	C_2	C_3	C_4
$0 \quad 0.255$	0.01449	5.56353	- 18.27520	31.65847	- 16.16537
$0.255 \quad 0.8$	- 1.13292	1.88860	1.13292		

Fatigue life due to subcritical crack growth for the $r_1/r = 0.5$ hollow cylinder can be obtained by direct integration in polar coordinates in a manner similar to the solid cylinder (41), i.e.,

$$N_f = \sqrt{2} r \int_{a_i}^{a_{cr}} \left[C \left(\Delta K_{eq} \right)^{\alpha} \right]^{-1} d\theta \tag{46}$$

where r is the outer radius of the hollow cylinder, K_{eq} is obtained from (43), C and are empirical constants, and describes the angular position of the spiral crack front in radians on the cylinder's outer radius.

Figure 35-Figure 36 show the finite element simulation results for crack growth in a hollow cylinder with $r_1/r = 0.25$. Crack evolution for this relatively thick-walled cylinder has characteristics of crack growth more closely resembling the cracking behavior observed in a solid cylinder, at least up until the final increments in the crack advance. To illustrate this, the incremental crack fronts obtained from the solid cylinder simulations are shown side-by-side in Figure 35(d) with the $r_1/r = 0.25$ hollow cylinder result (Figure 35(c)). In contrast to what was observed in the $r_1/r = 0.5$ case, the simulation results with the smaller hole, $r_1/r = 0.25$, give the appearance of an advancing crack front simply passing around an elliptical hole Figure 35(c)-Figure 36(d). After the crack has passed by the hole, the separated crack fronts rapidly grow towards each other from opposite vertical directions as depicted in Figure 35(a), Figure 35(c), and Figure 36(d), resulting in a small horizontal gap between the two crack fronts as shown in Fig. Figure 35(a).

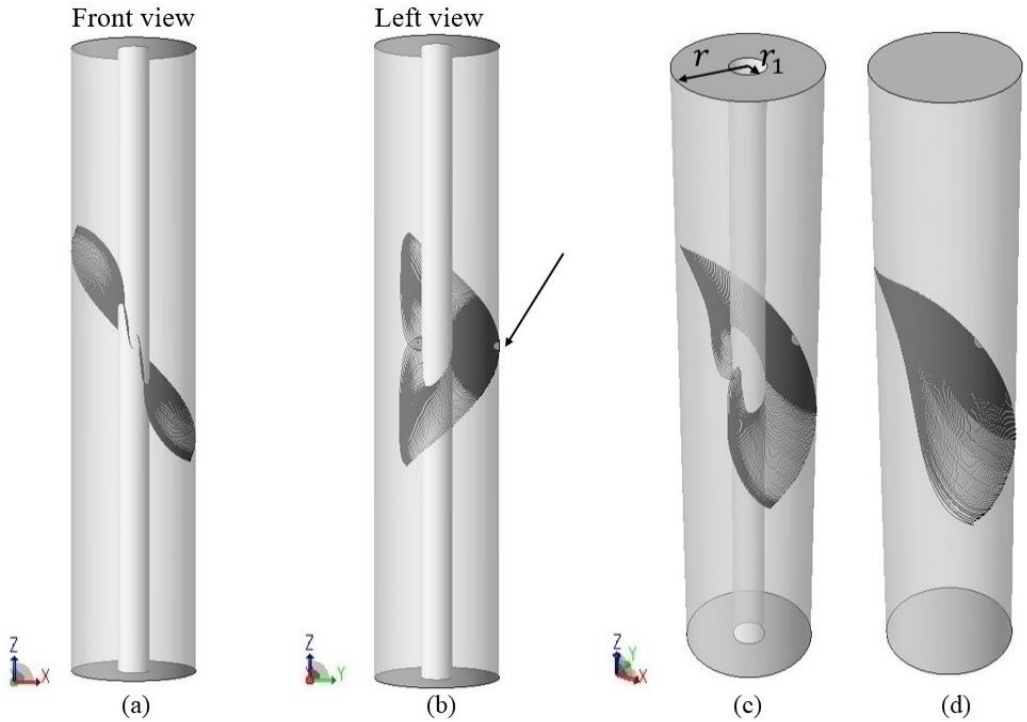

Figure 35. Different views (a)-(c) showing the evolution of the spiral crack in a hollow cylinder with $r_1/r = 0.25$. Arrow points to location of the initial surface crack. (d) Comparison with crack growth in a

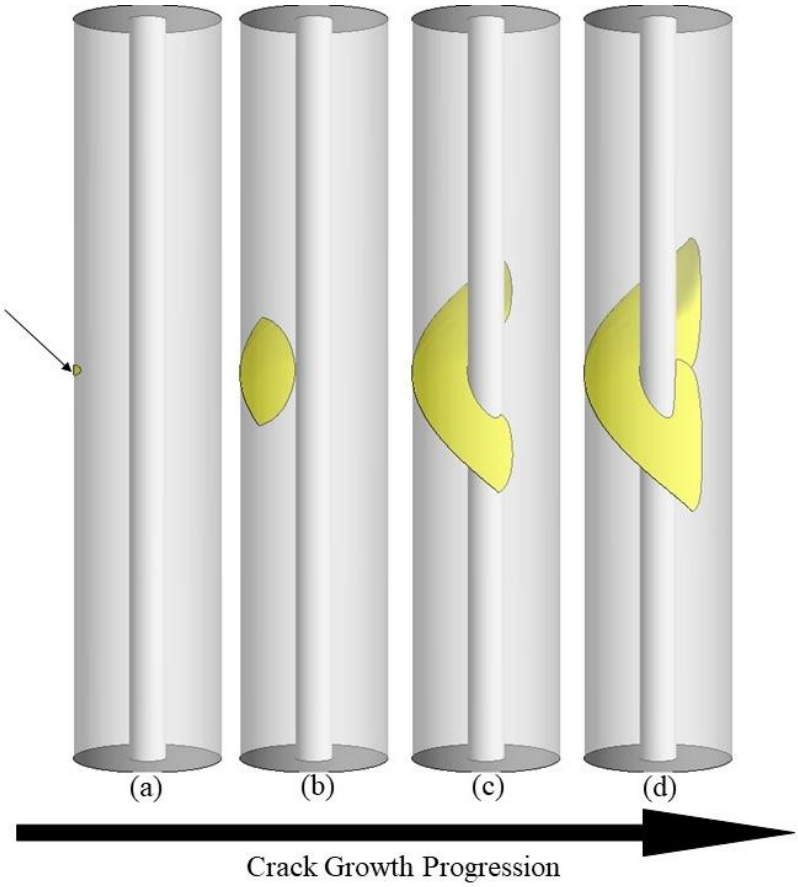

Figure 36. Crack progression in the hollow cylinder ($r_1/r = 0.25$). Small arrow points to location of the initial surface crack.

Figure 37 through Figure 39 provide the normalized stress intensity factors, $K_I^*, K_{II}^*, K_{III}^*$, for the four stages of the crack growth in the hollow cylinder depicted in Figure 37 with $r_1/r = 0.25$. The normalization constant, K_0, for $r_1/r = 0.25$, is given by

$$K_0 = \frac{512}{255\sqrt{\pi}} T r^{-\frac{5}{2}} \tag{47}$$

There are interesting differences in the mixed-mode stress intensity factors between $r_1/r = 0.25$ and $r_1/r = 0.5$, at similar stages of crack growth. At stage 3, K_I^* for $r_1/r = 0.25$ (Figure 37) on the inner wall ($s^* = 1$) drops below the K_I^* value computed when the crack front breaks through the inner wall in stage 2. This decrease in the mode I stress intensity factor is not observed in the thinner walled cylinder, $r_1/r = 0.5$ (Figure

32). Comparing Figure 38 and Figure 33, the difference in the computed K_{II}^{*} behavior between the two hollow cylinders is most pronounced at stage 4, after the crack fronts have spiraled ~340° around the cylinder. As noted previously, K_{II}^{*} for $r_1/r = 0.5$ (Figure 33) causes the advancing crack plane to slant downwards from the outer radius to the inner radius. However, because of the positive-negative-positive variation in K_{II}^{*} along the crack front for $r_1/r = 0.25$ (Figure 38), a more complicated curved crack surface occurs, as compared to the flat planar surface observed for the $r_1/r = 0.5$ case.

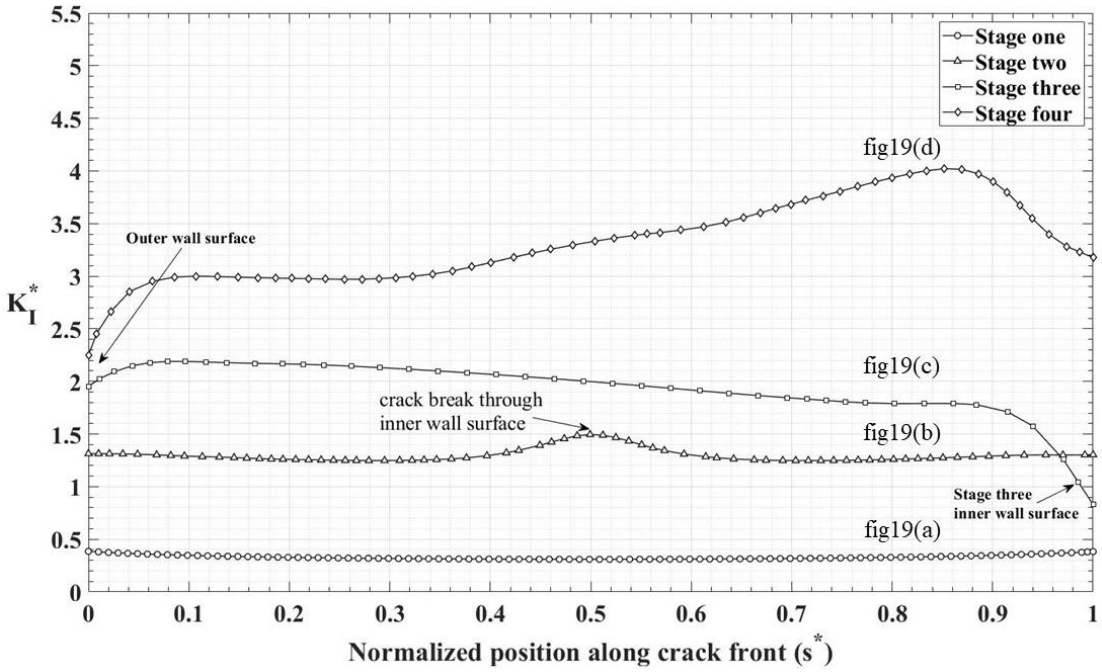

Figure 37. K_I^* on the crack front at different stages of crack growth in the hollow cylinder with $r_1/r = 0.25$. $K_I^* = K_I / K_0$

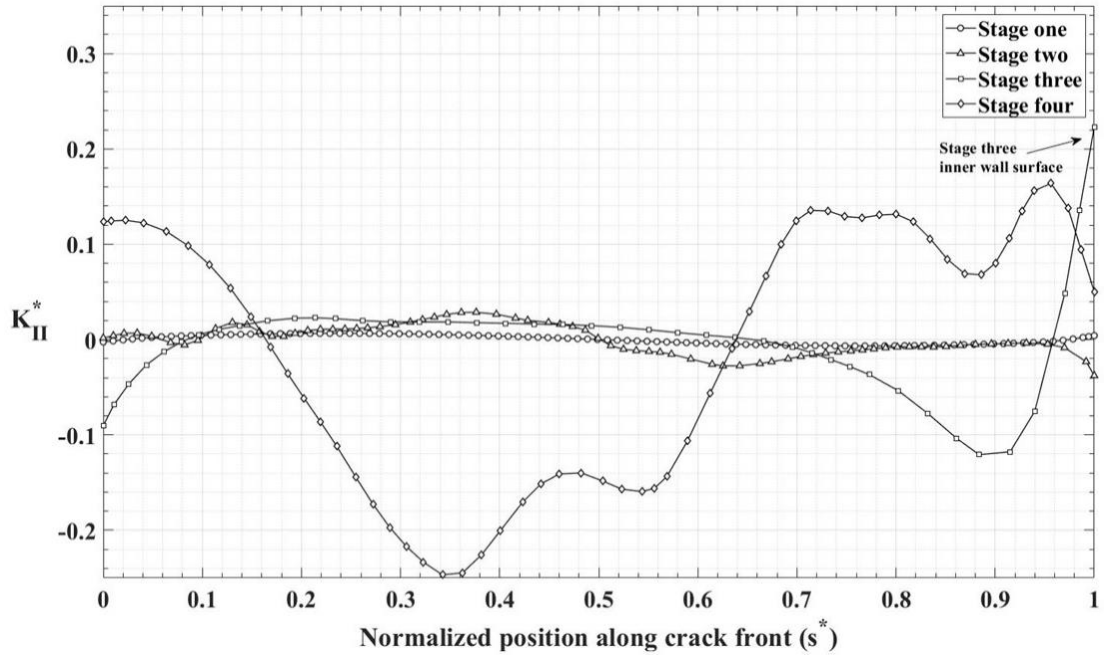

Figure 38. K_{II}^* on the crack front at different stages of crack growth in the hollow cylinder with $r_1/r = 0.25$. $K_{II}^* = K_{II} \,/\, K_0$

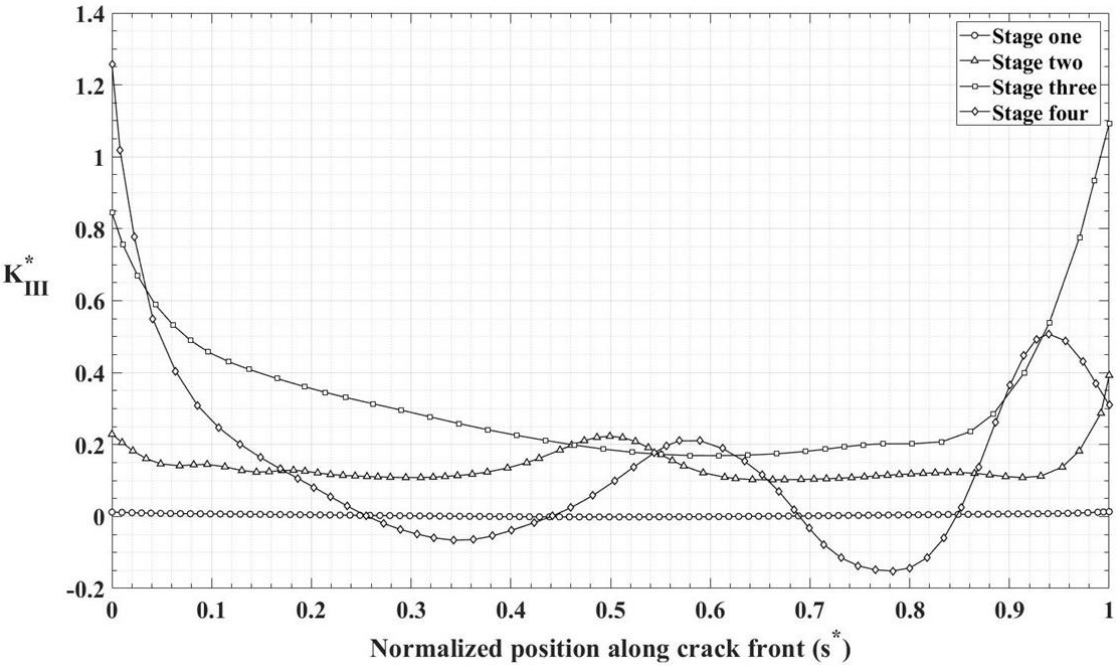

Figure 39. K_{III}^* on the crack front at different stages of crack growth in the hollow cylinder with $r_1/r = 0.25$. $K_{III}^* = K_{III} \,/\, K_0$

The finite element simulations for crack growth in hollow cylinders demonstrate that for hollow cylinders with small inner radii, there is a smooth transition from the type of

crack growth behavior observed in solid cylinders. The shape of these fracture surfaces take the smooth shapes depicted in Figure 35(c)-Figure 35(d). In comparison, the 3-D crack growth behavior for thinner-walled hollow cylinders can be best described by a narrow "ribbon" spiral as shown in Figure 30(c) and Figure 31(d).

Experimental observations of fracture in hollow cylinders demonstrate that it is very difficult, if not impossible, to generate a spiral fracture beyond 360°. As shown in Figure 30, after the spiral crack reaches ~340° around the cylinder circumference, vertical cracking occurs that joins the two opposite growing crack fronts, splitting the hollow cylinder vertically. What is the explanation for this? The computed mixed-mode stress intensity factors on the spiral crack fronts, Figure 32 – Figure 33, do not provide a sufficient change in the K_I / K_{II} ratio needed in (13) sufficient for such a radical change in the crack growth direction. What apparently occurs, after both ends of the spiral crack have propagated ~160°, is that new vertically oriented cracks branch off the existing spiral crack surfaces at a location slightly behind the existing spiral crack fronts. The reason for the formation of either one or two new cracks, and the driving force for the subsequent vertical crack growth, is a high circumferential tensile stress component that develops on the cylinder's inner wall surface. The high tensile stress on the inner radius is caused by a shift in the center of twist running down the axis of the cylinder as the spiral crack grows and the cracked portion of the cylinder opens up. The deformation that is responsible for this shift in the center of twist and the resulting circumferential stress on the cylinder's inner wall is shown in Figure 40. To fully visualize the circumferential tensile stress that develops, Figure 40(b) shows the circumferential stress on the "back" half of the cylinder, with the "front" half of the cylinder removed for clarity. This high

tensile stress is confined to a relatively narrow region between the two spiral crack fronts. On the opposite side of the cylinder wall, high compressive circumferential stresses develop as shown in Figure 40(c). The schematic diagram in Figure 41 helps to visualize the local bending moments in the hollow cylinder wall that cause circumferential tension on the inner radius r_1 and compression on the outer radius r, in the region between the two spiral crack fronts.

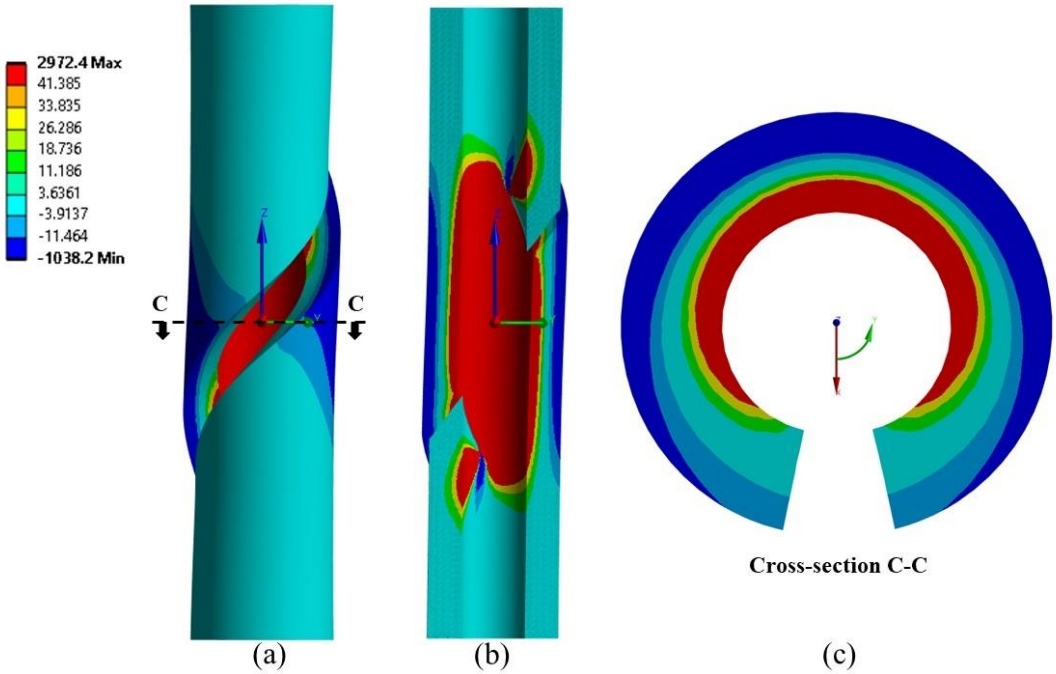

Figure 40. a) Local deformation from the spiral crack opening due to remote torsion, b) circumferential stress on vertical cross-section through the hollow cylinder, c) circumferential stress on plane C-C. $r_1/r = 0.5$

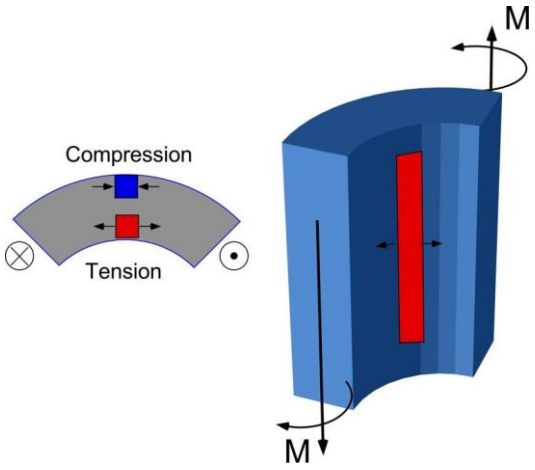

Figure 41. Schematic showing nature of local bending moments responsible for circumferential tension on the cylinder's inner wall and compression on the outer wall.

In an effort to simulate the observed final stage of crack growth behavior in hollow cylinders, small cracks were inserted on both of the existing spiral crack surfaces, slightly behind the main spiral crack fronts, on the inner cylinder wall. In the torsion experiments it was observed that it was possible for either one crack to form on each of the spiral crack surfaces, or a single crack might initiate on only one crack surface and propagate vertically to the other crack front. Figure 42 shows the crack growth simulation results (from four different angles). The two vertical cracks grow very quickly in the high tensile stress field depicted in Figure 40. In Figure 42, the vertical crack fronts have advanced 168 increments, propagating up to a point where only a very small uncracked ligament remains between the crack surfaces in the hollow cylinder. While the vertical cracks are propagating, there is only a small amount of further propagation of the essentially arrested spiral crack fronts. As shown in Figure 42(c), the two vertical cracks slightly bypass each other before a final merger that vertically splits the hollow cylinder. This behavior was also observed in the experimental testing. It is interesting to note the highly curved vertical crack fronts (Figure 42(b) and (d)), i.e., the vertical crack front on the inner wall surface grows faster than on the outer wall. This is due to the stress gradient,

through the cylinder wall thickness, from tension on the inner radius to compression on the outer radius, as shown in Figure 40.

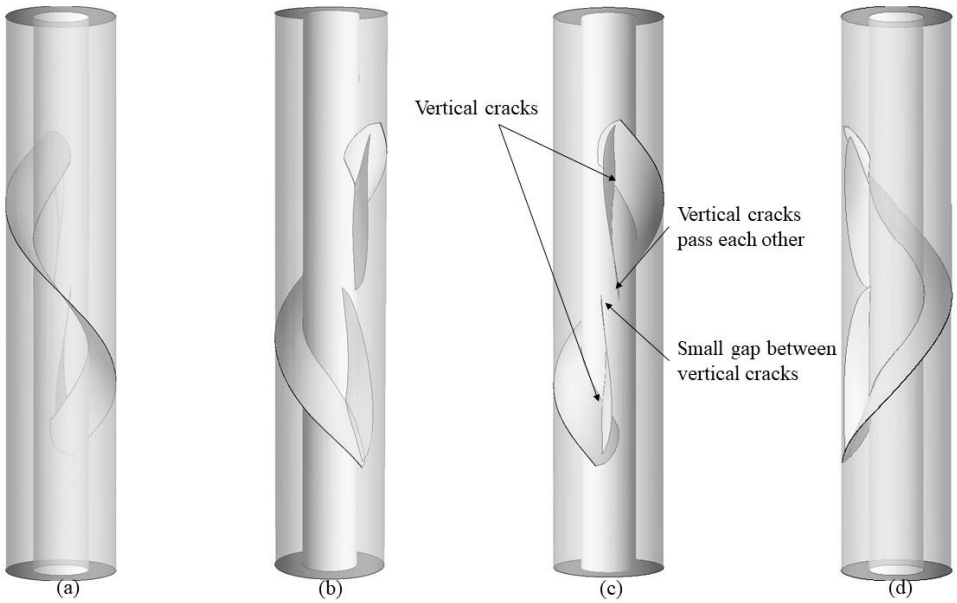

Figure 42. Simulation of vertical crack growth for two separate cracks branching from the spiral cracks.

3.1.3. Comparison of Test Results with Crack Growth Simulations

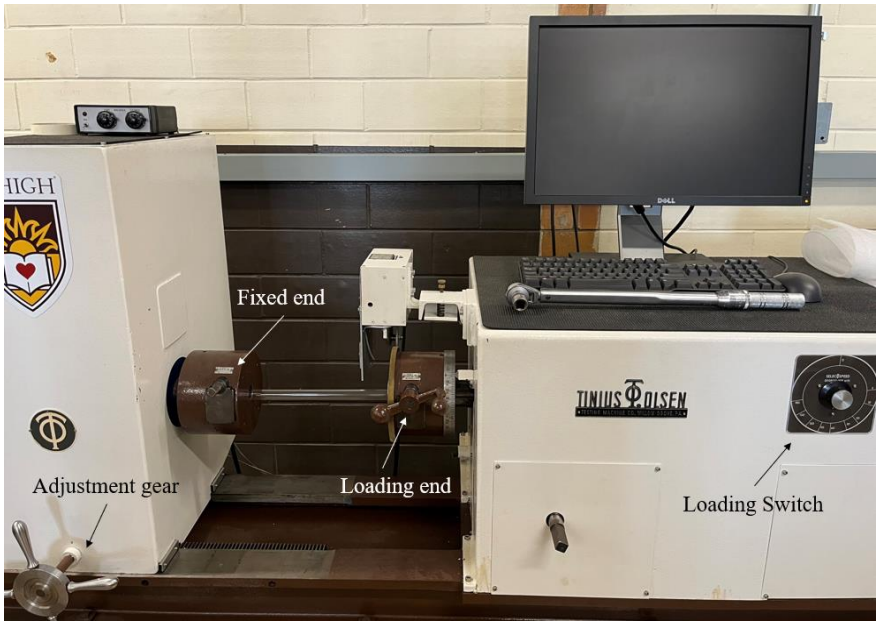

Figure 43. Torsion Experimental Setup

Fracture tests were conducted on solid and hollow (PMMA) acrylic cylinders subjected to torsion using the torsion-testing machine shown in Figure 43. In these tests, PMMA acrylic rods of length 30 mm, were clamped at both ends, and slowly twisted until sudden fracture occurred. The outer diameters of the cylinders were 12.7 mm (0.5 in) and the hollow cylinders had an inner bore diameter of 6.35 mm (0.25 in). A jeweler's saw was used to cut a very small straight surface notch oriented at 45° to the cylinder axis. The resulting spiral fractures were very reproducible, yielding the fracture surfaces shown in Figure 1 and Figure 29. The fracture surfaces contained clearly delineated "river patterns" pointing back to the initial surface crack, characteristic of cleavage fracture during rapid crack growth in brittle materials [65]. The main purpose of these torsion tests was to provide direct comparisons with the predicted fracture surfaces obtained from the computational simulations described in Section 3.1.

Experimental Results for Solid Cylinders

Figure 44 compares the experimental fracture surface from a solid acrylic cylinder with the fracture surface obtained from the numerical crack growth simulations. The simulation images are aligned with the photographs to show the close agreement between the experimental and predicted fractured surfaces. The arrows in Figure 44(d) indicate the direction of crack growth based on the "river patterns" visible on the fracture surface. These arrows also coincide with the predicted orthogonal crack front trajectories given in Figure. 27, terminating at the predicted intersection locations on the solid cylinder surface. It should be emphasized that the experiments use a small straight starter notch, while the crack growth simulations are based on a small semi-elliptical surface crack. But as observed, the shape of the initial surface flaw (as long it is small) has no significant

influence on the shape of the propagating crack once it has advanced a small distance away from the original surface crack.

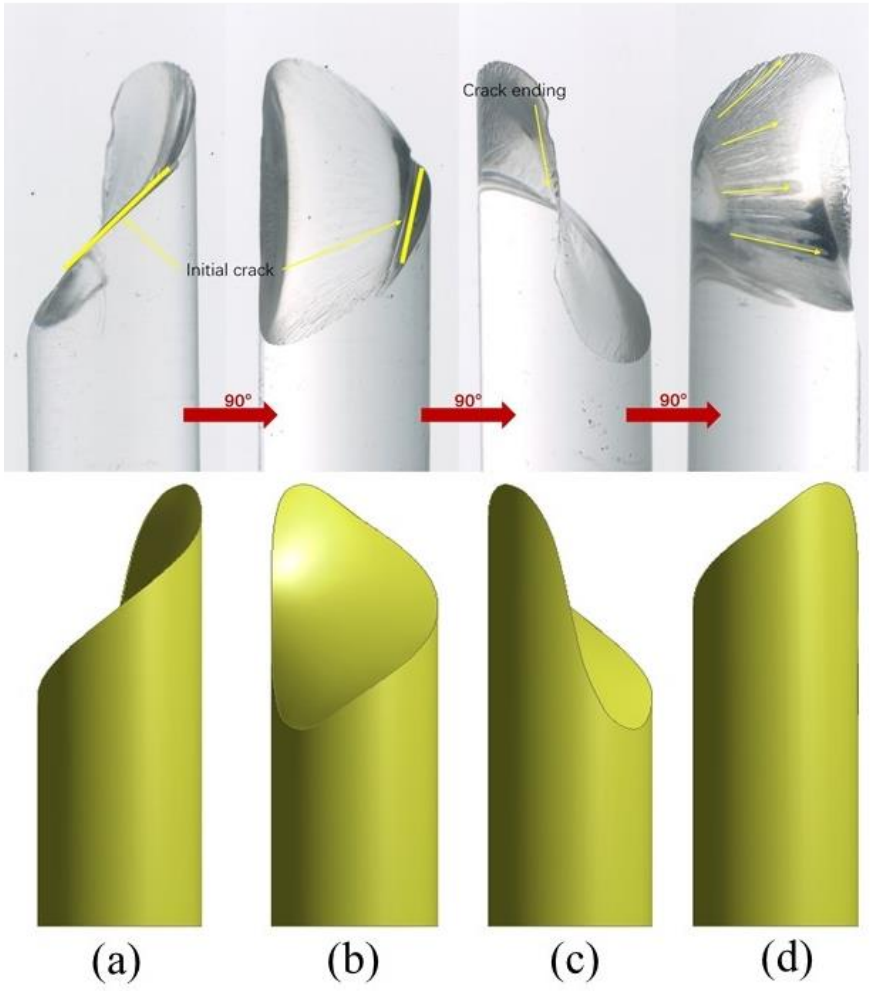

Figure 44. Fracture surface for solid cylinder subjected to pure torsion. Top – experimental results showing "river patterns." Bottom – fracture surfaces determined from numerical crack growth simulations.

Experimental Results for Hollow Cylinders

Torsion tests on PMMA acrylic cylinders with an inner and outer radii ratio of $r_1/r = 0.5$ were used to validate the growth of spiral fractures in hollow cylinders. Figure 45 compares a fractured hollow cylinder with the spiral fracture surfaces predicted from the numerical crack growth simulations. The arrows in Figure 45 show the location of the

initial crack in the central portion of the spiral fracture surface and the secondary vertical cracks that originate slightly behind the spiral crack front. The vertical cracks eventually meet at the locations shown in Figure 45. The geometric shapes of the spiral cracks obtained from the numerical simulations are in excellent agreement with the experimental tests. The inclusion of vertical cracking in the simulation results was because this behavior was observed in the experimental tests, i.e., initiation of vertical cracks on the spiral crack surfaces cannot be predicted based solely on a conventional mixed-mode crack growth methodology. As predicted by the simulations, a very large tensile stress arises on the inner wall of the hollow cylinder once the spiral crack has propagated circumferentially ~340°. Thus, any small defect on the spiral crack surface, in conjunction with the large circumferential tensile stress, will result in a new crack branching off vertically from the flank of the main spiral crack's surface.

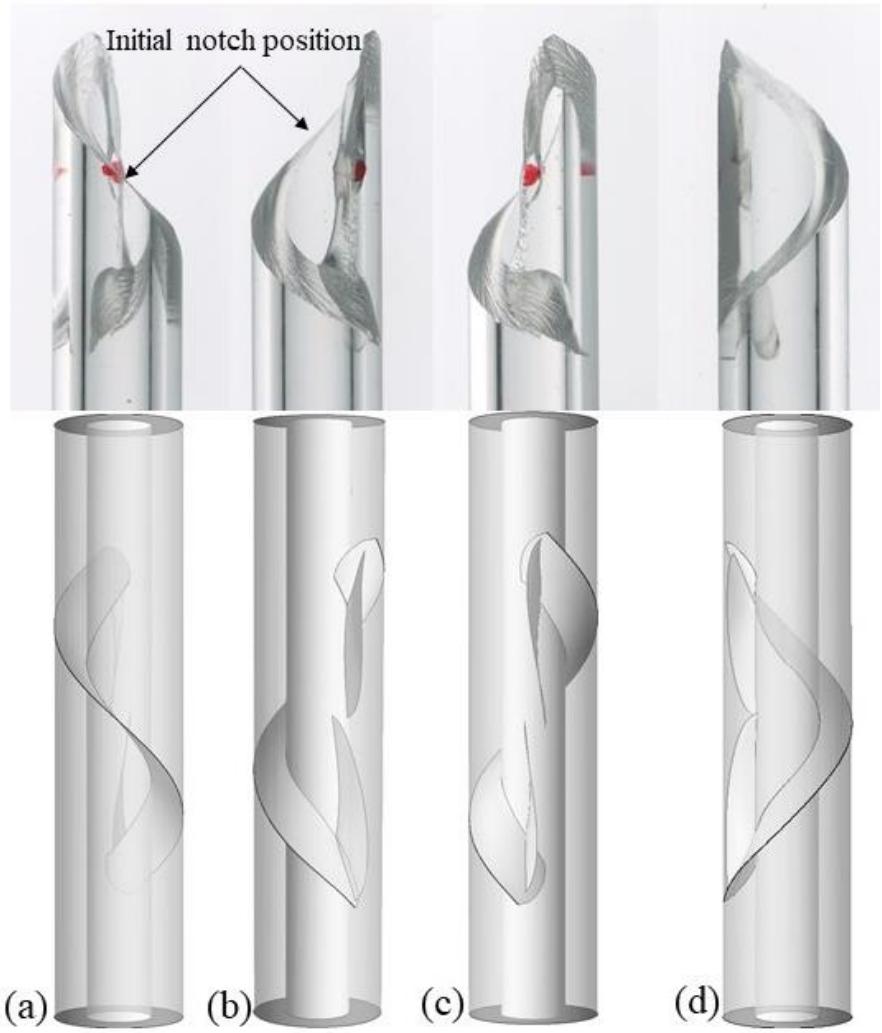

Figure 45. Comparison of experimental fracture surfaces for hollow cylinder ($r_1/r = 0.5$) subjected to pure torsion with crack growth simulations.

3.2. Shear Center Calculation Results

The finite element program Ansys [53] was used to generate the numerical results presented in this study. However, since the least squares calculation relies on displacements that can readily be obtained using any finite element program, the methodology is easily adapted to any other software. The finite element solution of the torsion problem requires application of distributed nodal forces on the exposed face of the beam structure at $z = L$ (Figure 2) equivalent to a specified torque. As long as the resultant forces in the x and y directions are zero, i.e.,

$$\int_A \sigma_{xz} dA = 0 \tag{48}$$

$$\int_A \sigma_{yz} dA = 0 \tag{49}$$

and the applied moment on the face is given by

$$M_T = \int_A \left(x\sigma_{zy} - y\sigma_{zx} \right) dA \tag{50}$$

the selection of a specific torque axis does not change the elastic torsion solution. A convenient method for application of a torque normal to a surface in Ansys, is to use a "virtual node" to remotely specify nodal forces that yield the desired torque. If a remote point is not specified, Ansys uses the surface's centroid for determining the equivalent nodal forces. Any suitable displacement boundary conditions can be specified on the $z = 0$ plane, but in most cases fixed boundary conditions will be of the greatest interest. Upon completion of the FEA elastic torsion calculation, interpolated coordinates and displacements are obtained on selected "cutting" planes along the model's z axis. For each plane these values are determined using the nodal coordinates and nodal displacements in conjunction with the element interpolation function. The appendix contains the APDL script file used to extract the nodal coordinates and displacements at specified planes along the axis of the 3D finite element model.

Semicircular Cross-Section

Figure 46 (a) depicts the finite element mesh for a straight extruded bar with a semicircular cross-section with a length to radius ratio, $L/r = 20$. In this model there are approximately 39,400 20-noded hexahedron elements and 174,244 nodes. Torsion and bending solutions for this problem are given in [38]-[39], [59], [61], [66]-[67]. In the finite

element model depicted in Figure 46, fixed displacement boundary conditions, $u = v = w = 0$, are specified on the $z = 0$ plane. $E = 200$ GPa, Poisson's ratio $= 0.3$, and thus the elastic shear modulus is given by $= 76.923$ GPa.

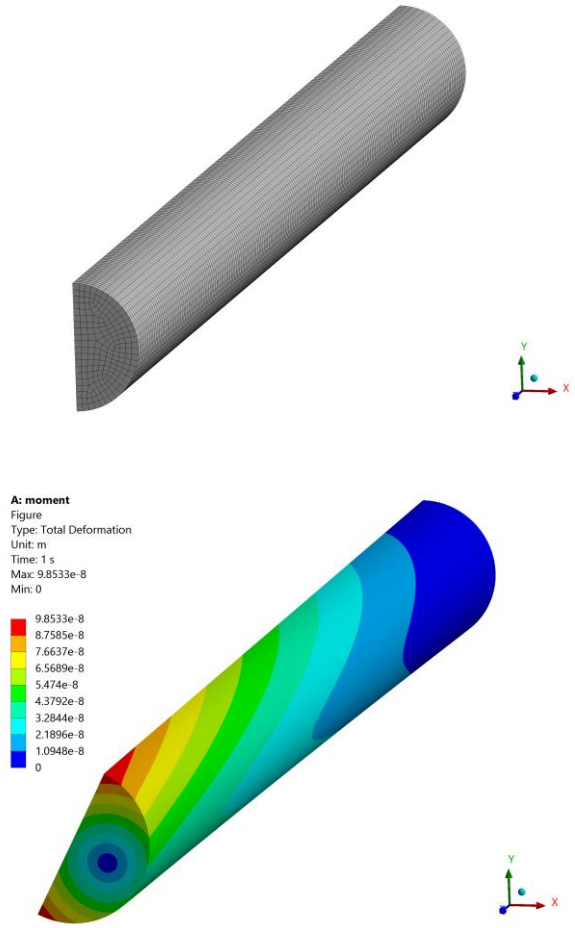

(a) (b)

Figure 46. a) Finite element mesh for a semicircular bar, L/r = 20. b) Deformation in semicircular bar subjected to applied torque.

Since the center of twist does not depend on the magnitude of the applied torque, contour plots of the resulting elastic displacements and stresses are only used for visualizing the overall deformation and spatial distribution of the stresses. The total deformation contour plot in Figure 46(b) shows lines of constant deformation, a scalar quantity, given in terms

of displacements as $= \sqrt{u^2 + v^2 + w^2}$. As shown in the figure, no displacements occur on the fixed boundary plane at $z = 0$ and the maximum displacements occur on the top and bottom of the semicircle's front face ($z = L$) where the torque is applied. The approximate location of the center of twist can also be seen in this figure, i.e., the small circle with zero deformation on the bar's front face. Figure 47 shows the stress distributions obtained from the torsion calculation. As expect, the shear stress component $_{xz}(x, y, L)$, Figure 47(a), is antisymmetric with respect to y and $_{yz}(x, y, L)$, Figure 47(b), is symmetric. Saint-Venant's semi-inverse solution of the torsion problem [38]-[39] assumes that $_{zz} = 0$ on all planes. However, since a fixed displacement boundary condition was used in this study (Figure 46(b)), a $_{zz}$ normal stress of considerable magnitude develops on the $z = 0$ plane as shown in Figure 47(c). The $_{zz}$ stresses are highest in magnitude (tension and compression) in a narrow zone parallel to the flat face of the semicircle at $z = 0$.

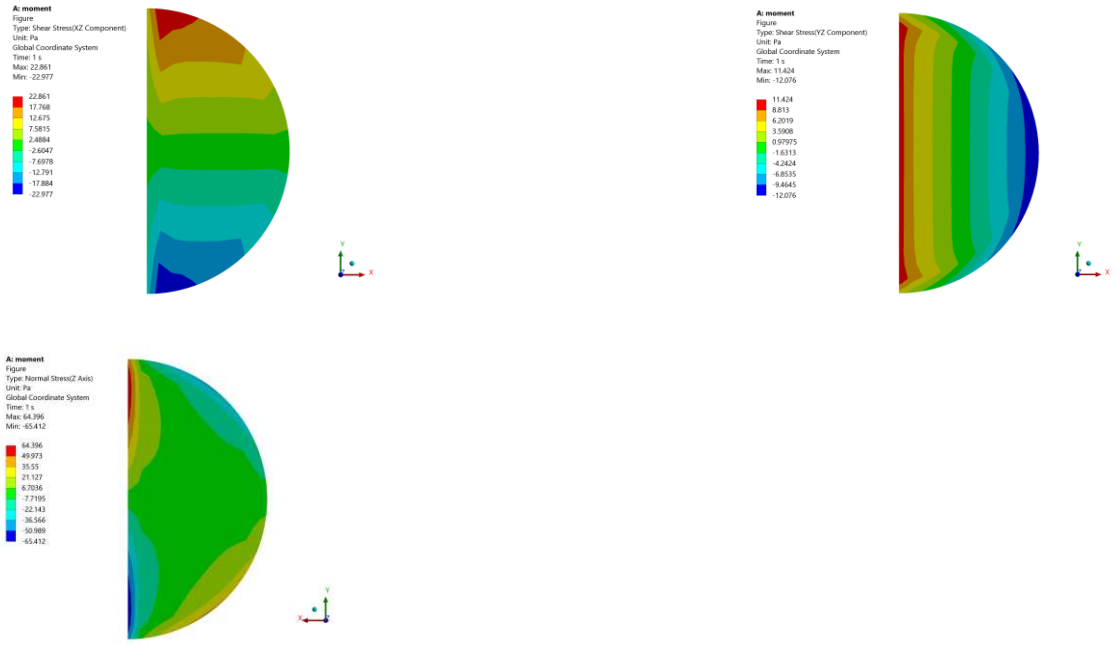

(a) (b) (c)

Figure 47. Contour plots of the stress components: a) $\sigma_{xz}(x, y, L)$, b) $\sigma_{yz}(x, y, L)$, c) $\sigma_{zz}(x, y, 0)$.

The displacements due to torsion obtained from the Ansys model can be extracted for an arbitrary number of cutting planes along the bar's z-axis (see code in Appendix). Once a cutting plane has been specified in Ansys, interpolated points that match the mesh configuration on the cutting plane are automatically generated. In this example, each cutting plane generates more than 3000 coordinate points with the respective displacements, which in turn can be used for the least squares calculation to determine the center of twist. The location of the center of twist (measured from the flat left side of the semicircle) was calculated to be ($x_T = 0.51015r$, $y_T = 0$). To verify convergence, calculations were performed with even more highly refined meshes, e.g., 153,000 elements, 645,000 nodes, resulting in virtually no detectable change in the result. As shown in the plot in Figure 48, the computed value for the center of twist remains essentially constant along the z-axis and only begins to deviate from $x_T = 0.51015r$ in the neighborhood of the $z = 0$ surface, i.e., when $z / L < 0.1$. In this region close to the fixed surface, the center of twist moves closer to the semicircular bar's flat vertical surface.

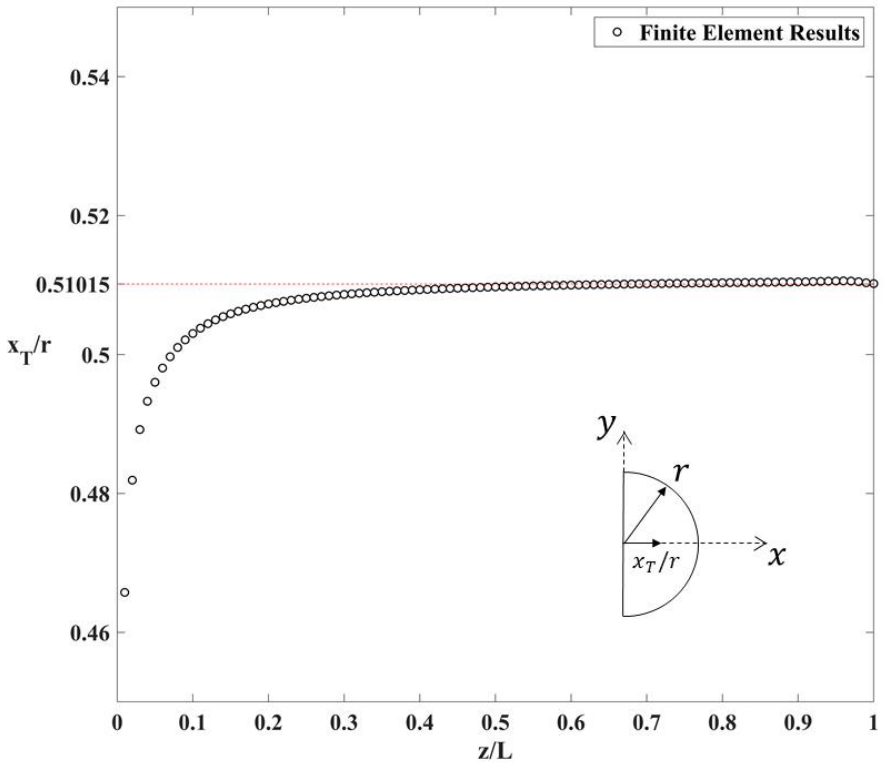

Figure 48. Plot showing the axis of twist for the semicircular bar as a function of z / L . $x_T = 0.51015r$.

For comparison, the value for the shear center for this problem using the less constrained "classical" Saint-Venant boundary conditions can be obtained from [38]-[39][1], and is given by

$$x_F = \frac{8r}{5\pi} + \frac{32\nu r(10-\pi^2)}{15(1+\nu)\pi^3} \tag{51}$$

i.e., $x_F = 0.5114r$ for $\nu = 0.3$. This is remarkably close to the computed value for the center of twist x_T obtained from the finite element calculation with fixed boundary conditions, especially when one takes into account the difference in the boundary

[1] There appears to be a typographical error for the shear center given on p. 239 in **Error! Reference source not found.**. The equation for the shear center should be divided by .

conditions and the fact that the solution (49) from [38]-[39] was derived by combining bending and torsion solutions obtained using two different support boundary conditions.

The location of the center of twist (and the shear center), depends (weakly) on the elastic material properties. For the semicircular bar depicted in Figure 46, changing Poisson's ratio causes a slight change in the location of the center of twist. For the same elastic modulus $E = 200$ GPa, varying Poisson's ratio from $= 0.01$ to $= 0.499$ changes the location of the center of twist from $x_T = 0.50827\,r$ to $x_T = 0.51088\,r$. Note that since $= E/\left(2\left(1+ \right)\right)$, changing for a constant E is equivalent to changing the shear modulus .

In an effort to demonstrate numerically the equivalence of the center of twist, x_T, and the shear center, x_F, the same geometry depicted in Figure 46 was treated as a cantilever beam with a transverse force acting on the free end of the beam. As anticipated by the Maxwell-Betti reciprocal principle, as long as the force resultant passes through the previously calculated center of twist, there should be no rotation and only translation will occur in the direction of the applied force for all points located on the axis of twist. This will not be true for other points in the beam cross-section, which are subjected to a combination of bending stresses and shear stresses, resulting in complex deformations that include transverse beam deflection and anticlastic curvature. Consistent nodal forces acting on the end of the beam, equivalent to a single transverse resultant force acting at the center of twist, can be applied using the remote force capability in Ansys [53]. Figure 49 shows contour plots of the axial stresses $_{zz}$, Figure 49(a), on the beam's exaggerated deformed configuration and the shear stresses, Figure 49(b)-(c), due to a resultant force passing

through the center of twist on the end face of the beam. The cantilever beam exhibits a linear variation in the bending stresses, $_{zz}$, with respect to the y-axis and a more complex distribution of shear stress due to the transverse loading and fixed boundary conditions at $z = 0$.

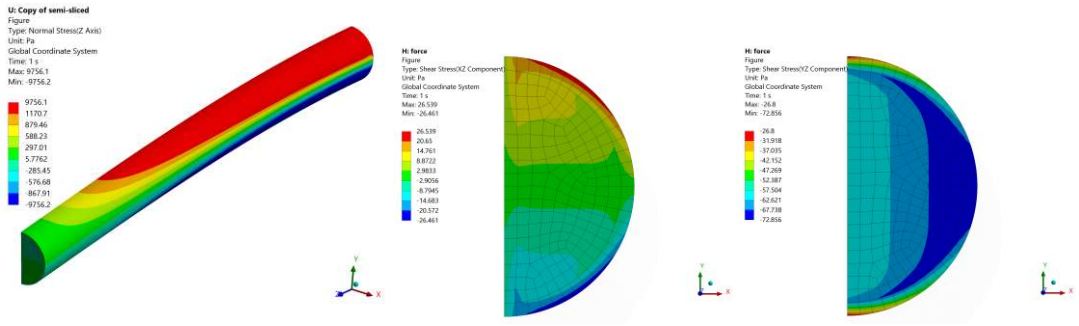

(a) (b) (c)

Figure 49. a) Contour plot of the σ_{zz} stress on the deformed configuration due to resultant force acting at end of beam at $x_T = x_F = 0.51015r$. b) Shear stress $\sigma_{xz}(x, y, L)$ on free end of cantilever beam. C) Shear stress $\sigma_{yz}(x, y, L)$ on free end of cantilever beam.

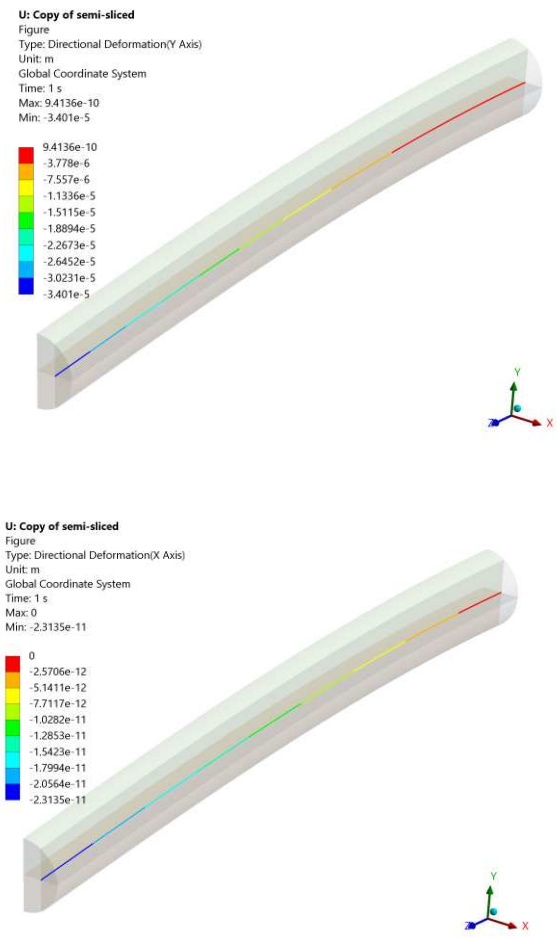

(a) (b)

Figure 50. Plots of displacements for points located on the axis of twist for the cantilever beam with a vertical resultant force at (0.51015r, 0, L). a) Displacements in vertical (y) direction: v (0.51015r, 0, z), b) Displacements in horizontal (x) direction: u (0.51015r, 0, z).

Figure 50 (a) contains a plot showing the vertical y-displacements along the previously determined axis of twist, while Figure 50(b) shows the displacements along this same axis in the x-direction. The calculated displacements, u, in the x-direction are at least 6 orders of magnitude smaller than the y-displacements, thus illustrating that the center of twist is identical to the shear center, i.e., displacements only occur in the y-direction for all points located on the axis of twist. This result does not change if the details of the resultant force loading on the end of the beam are changed. Figure 51 shows the stress components for the

same cantilever beam with a single concentrated force acting at the end of the beam passing through the center of twist. Although the detailed stress

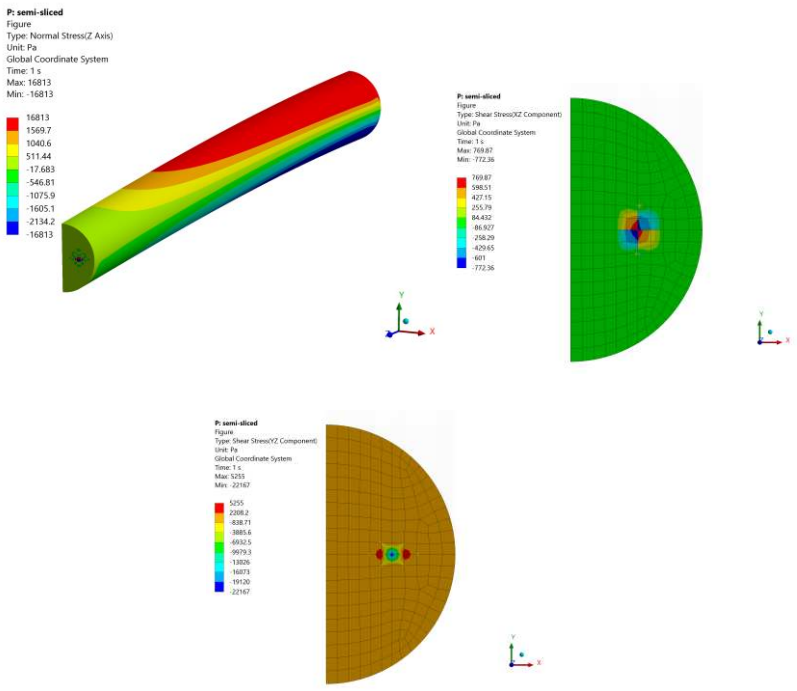

(a) (b) (c)

Figure 51. a) Contour Plot of the σ_{zz} stress component due a single concentrated force acting at the center of twist, $x_T = x_F = 0.51015r$. b) Shear stress $\sigma_{xz}(x, y, L)$ on free end of cantilever beam. C) Shear stress $\sigma_{yz}(x, y, L)$ on free end of cantilever beam.

distribution on the end of the beam is very different than the stresses shown in Figure 49, the deflection for all points on the shear center axis are identical (Figure 52), and there are no horizontal (u) displacements for points located on this axis.

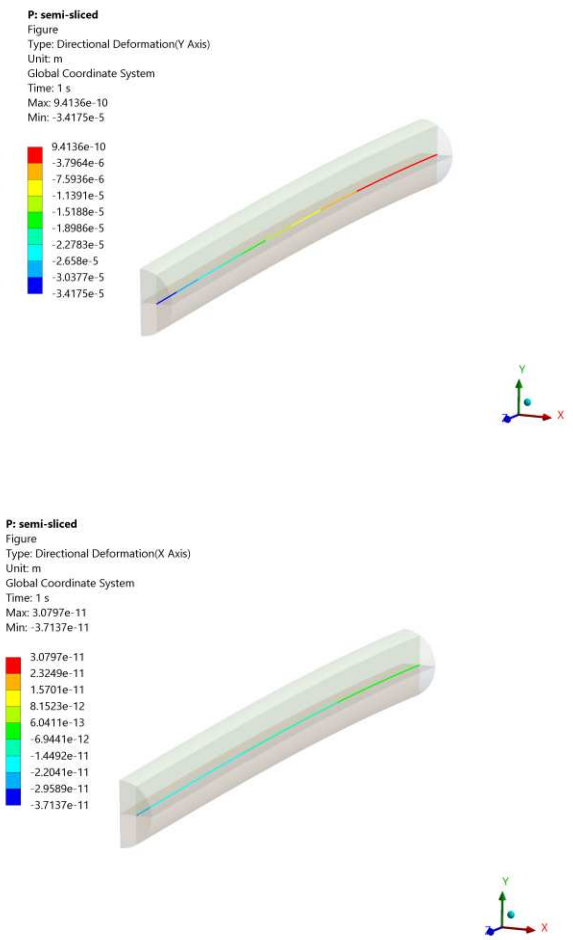

Figure 52. Plots of displacements for points located on the center of twist for the cantilever beam with a concentrated vertical end force located at (0.51015r, 0, L). a) Vertical displacement v (0.51015r, 0, z), b) Horizontal displacement u (0.51015r, 0, z).

C-Shaped Channel Cross-Section

For many important geometric configurations, the location of the center of twist (and thus the shear center) does not lie within the boundary of the solid geometry. Figure 53 shows the finite element mesh and the resulting twisting behavior for a fixed, C-shaped channel ($b/h = 19/18$, $t/h = 1/9$, $L/h = 100/9$), subjected to an applied torque with fixed boundary conditions at $z = 0$. The same material properties were used as the semicircular bar example, i.e., $E = 200$ GPa, $= 0.3$. The total deformation contour plot

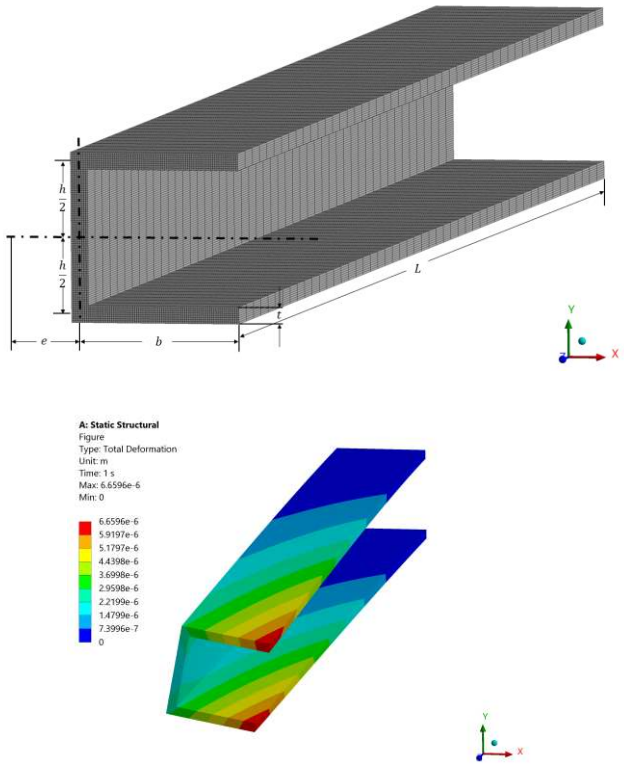

(a) (b)

Figure 53. a) Finite element mesh for a C-shaped channel, L/h=11.111. b) Deformation in C-shaped channel subjected to applied torque.

in Figure 53(b) depicts lines of constant deformation, given in terms of displacements as $= \sqrt{u^2 + v^2 + w^2}$. Figure 54(a-b) shows the distribution of the shear stress components $_{xz}\left(x, y, L\right)$ and $_{yz}\left(x, y, L\right)$ on the free surface of the channel section subjected to torsion, while Figure 54(c) shows the $_{zz}\left(x, y, 0\right)$ stress component on the $z = 0$ surface that

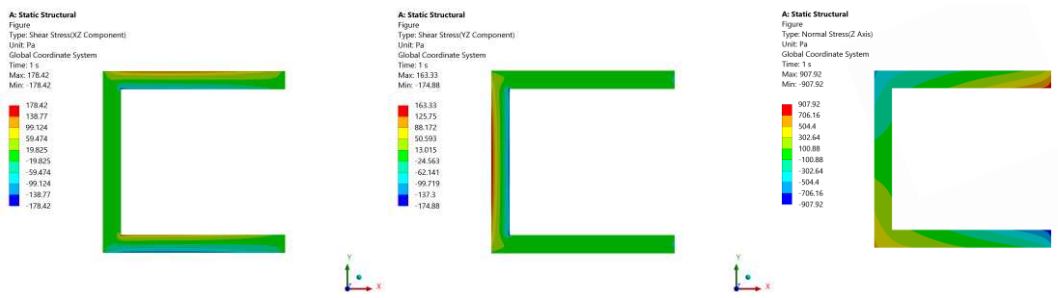

Figure 54. Contour plots of the stress components due to torsion loading: a) $\sigma_{xz}(x,y,L)$, b) $\sigma_{yz}(x,y,L)$, c) $\sigma_{zz}(x,y,0)$.

arises due to the fixed displacement constraint. As was observed for the semicircular bar, the fixed boundary condition resists the out-of-plane warpage due to the applied torque, resulting in relatively large $_{zz}$ stresses at certain x,y locations on the $z=0$ plane. The center of twist, computed from the in-plane displacements and the least squares procedure, is calculated to be outside the C-shaped cross-section at $x_T = 0.4257\,h$ to the left of the center of the vertical web as shown in Figure 53(a). A strength of materials estimated for the location of the shear center $x_F = e$, for this particular geometry, which assumes that the thickness $t \ll h$ and the shear stress is uniform through the thickness, is given by

$$\frac{e}{h} = \frac{h^4}{32.31I}\ ,\quad I = 0.068485h^4\ ,\therefore\ e = 0.4519h \tag{52}$$

The strength of materials estimated for e in this case is remarkably accurate and approximately 6% greater than the elasticity solution obtained from the finite element simulation. Of course, in this example, t is not "thin" and the cantilever beam is rigidly constrained at $z=0$. As shown in Figure 55, the axis of twist for this geometry is located well to the left of the channel's vertical web. It is interesting to note that the axis of twist over most of the channel section's length is given by $x_T = 0.4374\,h$ (Figure 55), which is 2.7% greater than the value for the center of twist x_T at $z=L$. This "interior" value for

the shear center is even closer to the strength of materials estimate given by (50). Close to the fixed boundary ($z/L<0.2$), the axis of twist increases to a value slightly greater than $h/2$ before decreasing to values closer to the structure's cross-section boundary. Varying Poisson's ratio from $=0.01$ to $=0.499$ only slightly changes the location of the center of twist at the end of the channel section, from $x_T=0.4220h$ to $x_T=0.4275h$.

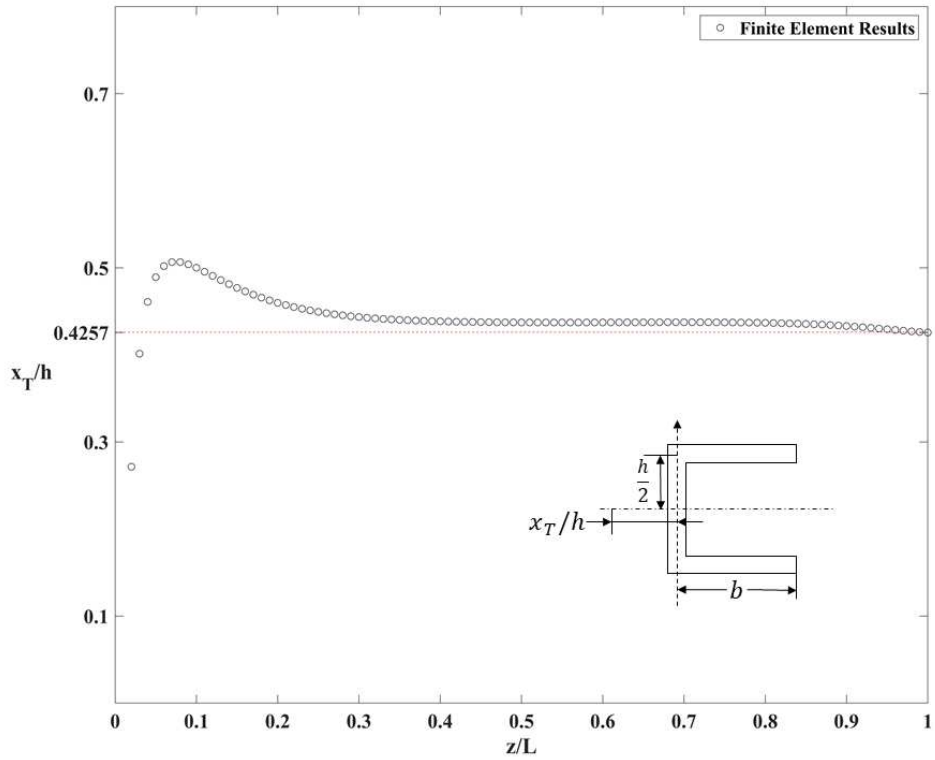

Figure 55. Plot Showing the axis of twist for the C-shaped bar as a function of z. $x_T = 0.4257h$. (b/h=19/18, t/h=1/9, L/h=100/9)

With the knowledge that the center of twist x_T is also the shear center x_F, a remote virtual force external to the C-shaped cross-section can be applied, Ansys [53], such that the resultant force passes through the center of twist at $x_T=e=0.4257h$, measured to the left of the vertical web's centerline. The resulting bending stresses, $_{zz}$, are shown in Figure 56(a) on the deformed configuration. The bending stresses and the vertical

displacements depicted in Figure 56(a) represent classical bending behavior in the absence of torsion. The shear stresses at $z = L$ are shown in Figure 56(b-c).

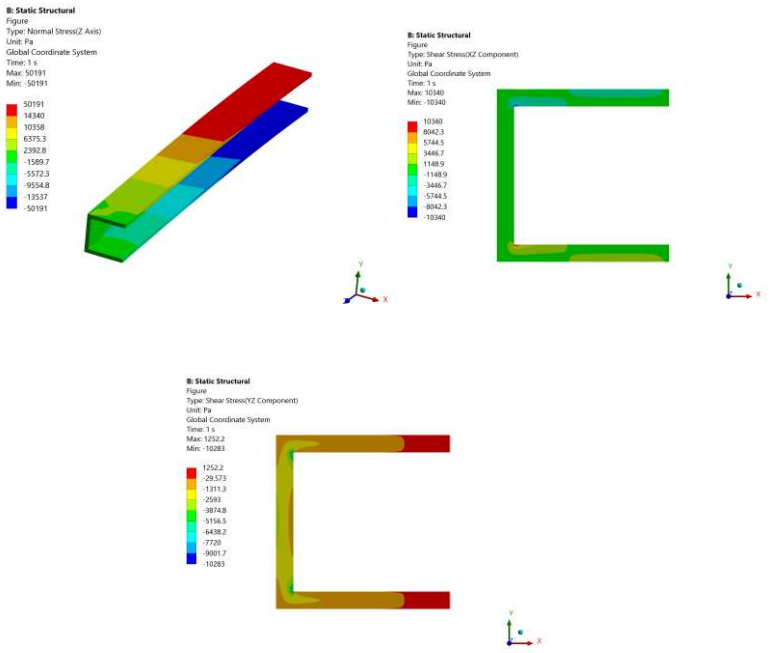

(a) (b) (c)

Figure 56. Contour plot of the σ_{zz} stress component for the C-shaped channel cantilever beam in the deformed configuration due to resultant transverse force acting at the center of twist, $x_T = e = 0.4257h$ b) Shear stress $\sigma_{xz}(x, y, L)$ on free end of cantilever beam. c) Shear stress $\sigma_{yz}(x, y, L)$ on free end of cantilever beam.

As was demonstrated for the semicircular beam, it can be confirmed numerically that the computed axis of twist is also the axis for the shear center. Figure 57 shows the vertical, v, displacements across the width of the channel's symmetry plane in the deformed configuration. The v-displacements for points on this plane are very uniform indicating that when the resultant force acts at the center of twist, this horizontal plane in the channel section experiences uniform displacement in the y-direction.

Figure 57. Contour plot of the vertical, , displacements on the deformed geometry for points located on the channel's symmetry plane. Vertical loading applied at the channel's center of twist located at $x_F = 0.4257h$ to the left of the vertical web centerline.

Airfoil Cross-Section

In wing design and the study of aeroelasticity, locating the position of the shear center is of critical importance. For example, in thin airfoil theory the pitching moment and lift force are usually applied at the ¼-chord point ($c/4$) behind the airfoil's leading edge. In order to determine the amount of twisting in a wing subjected to the lift force, it's necessary to know the position of the ¼-chord point with respect to the shear center. The semicircular and C-shaped channel beams in the previous examples have one plane of symmetry and thus the axes of twist and shear centers are also located on this symmetry plane. A representative example of a nonsymmetric airfoil/beam cross-section is the Göttingen 398 airfoil [68] with the cross-section shown in Figure 58(a). A finite element model of the extruded airfoil cross-section with $L/c = 10$, consisting of 58,880 elements and 263,791 nodes, is shown in Figure 58(b). The exaggerated deformation after the application of a

positive torque is shown in Figure 59(a) and the shear stress component $_{yz}\left(x,y,L\right)$ on the free end of the wing in Figure 59(b). The airfoil cross-section is rigidly restrained at $z=0$, which also results in $_{zz}$ axial stresses.

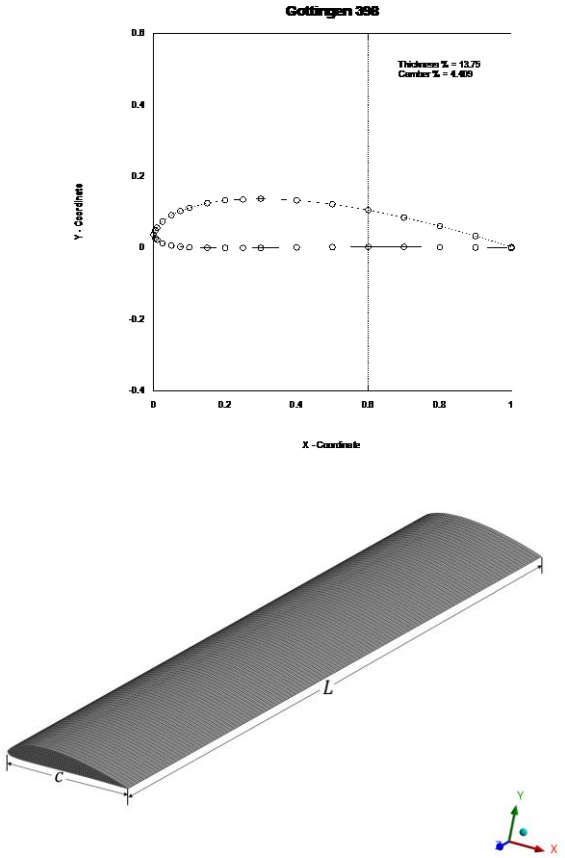

(a) (b)

Figure 58. a) Göttingen 398 airfoil cross-section. b) 3D Finite element mesh for the airfoil, L/c=10 .

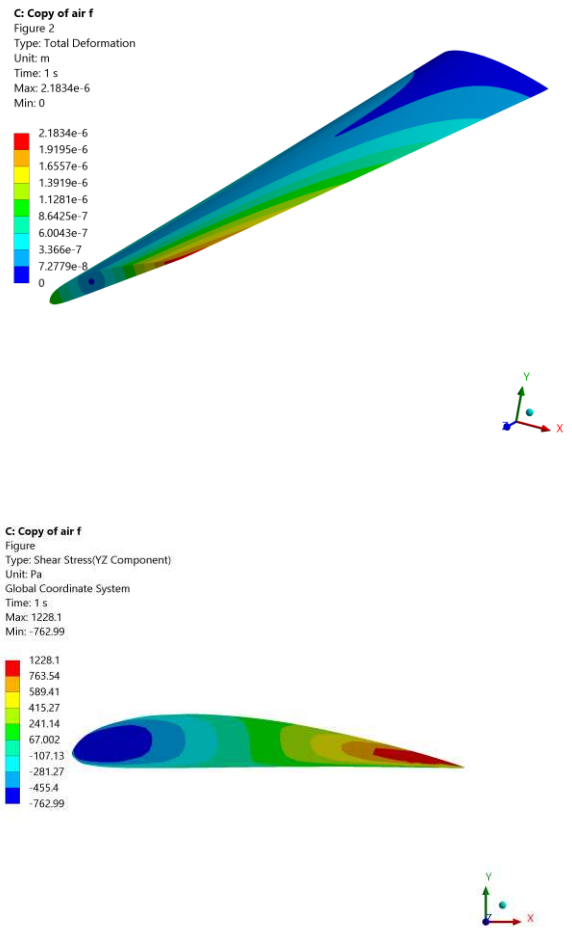

(a) (b)

Figure 59. a) Contour plot of displacement magnitudes on the deformed airfoil due to torsion. b) Distribution of torsional shear stress component $\sigma_{yz}(x, y, L)$ at L/c=10.

Using the same elastic constants as in the previous examples, the computed axis of twist is shown in Figure 60, generated along the axial length of the wing. Referring to the coordinate system shown in the Figure 60 inset, the center of twist for the airfoil is calculated to be at ($x_T = 0.3597\,c$, $y_T = 0.07526\,c$).

Application of a downwards-vertical load that passes through the center of twist, results in a very uniform cantilever bending deformation with the $_{zz}$ stress contours shown in Figure 61(a), and the transverse shear stress components in Figure 61(b-c).

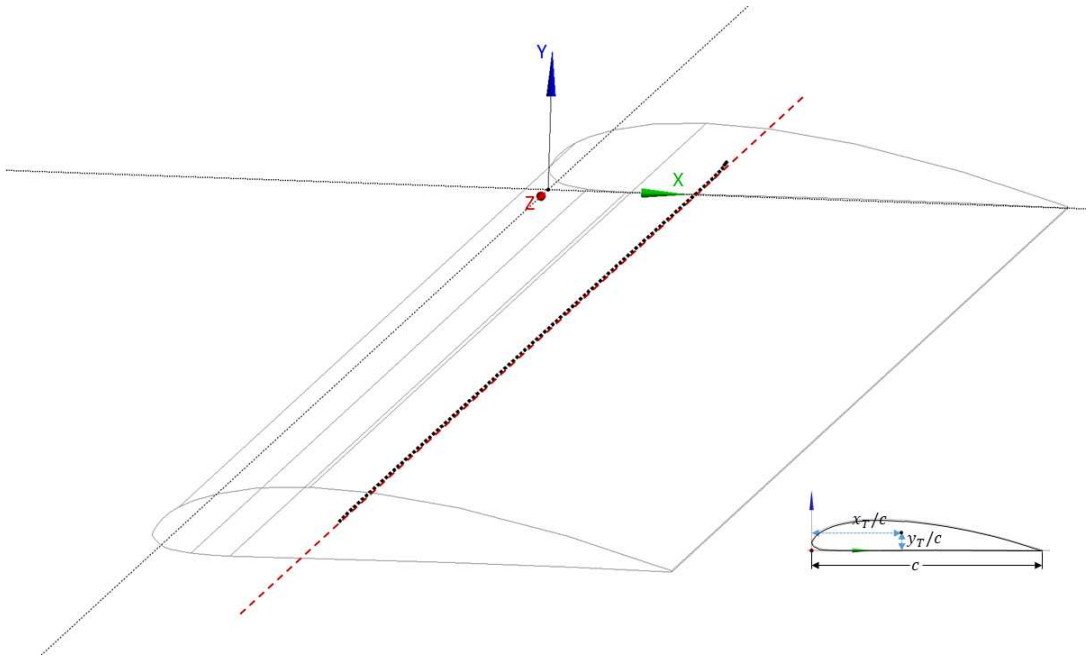

Figure 60. Plot showing the computed axis of twist ($x_T = 0.3597c$, $y_T = 0.07526c$) for the Göttingen 398 airfoil (0 < z/L < 1).

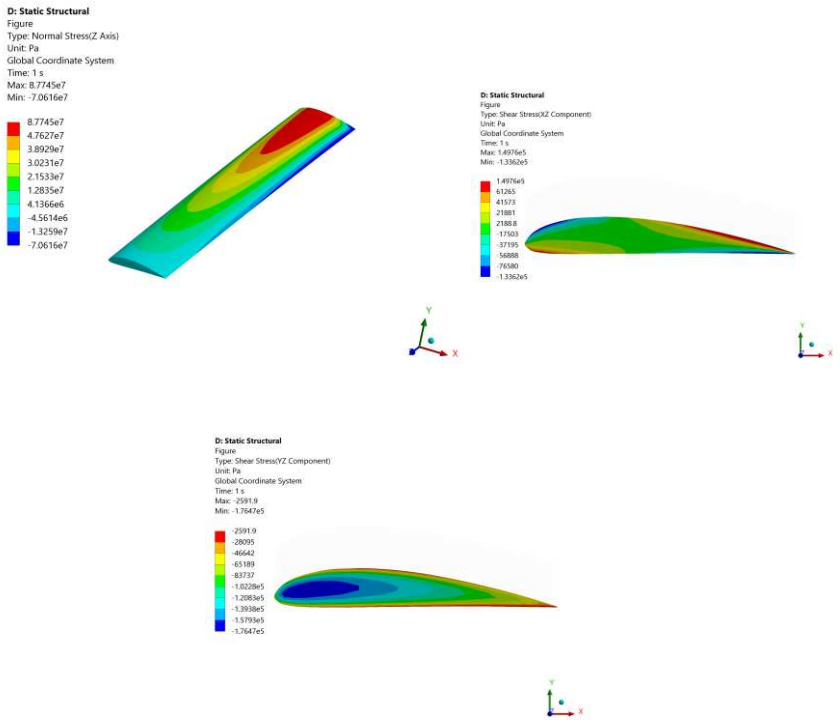

(a) (b) (c)

Figure 61. a) Contour Plot of the σ_{zz} stresses for the airfoil cantilever beam in the deformed configuration. b) Shear stress $\sigma_{xz}(x, y, L)$ on free end of cantilever beam. c) Shear stress $\sigma_{yz}(x, y, L)$ on free end of cantilever beam.

As a final example, the straight wing cross-section shown in Figure 58 is tapered from its cantilevered base to the wing tip in such a manner that the airfoil cross-section dimensions decrease by a factor of 2 (Figure 62). Keeping the wing's leading edge perpendicular to the $z=0$ plane (see inset Figure 62) results in a trailing edge with a 5.7106° taper from the wing's cantilevered base to the wing tip. Repeating the finite element torsion calculation for the tapered wing, results in an axis of twist defined by the space curve depicted by the dotted line shown in Figure 62, with the center of twist at $z/L=1$ given by

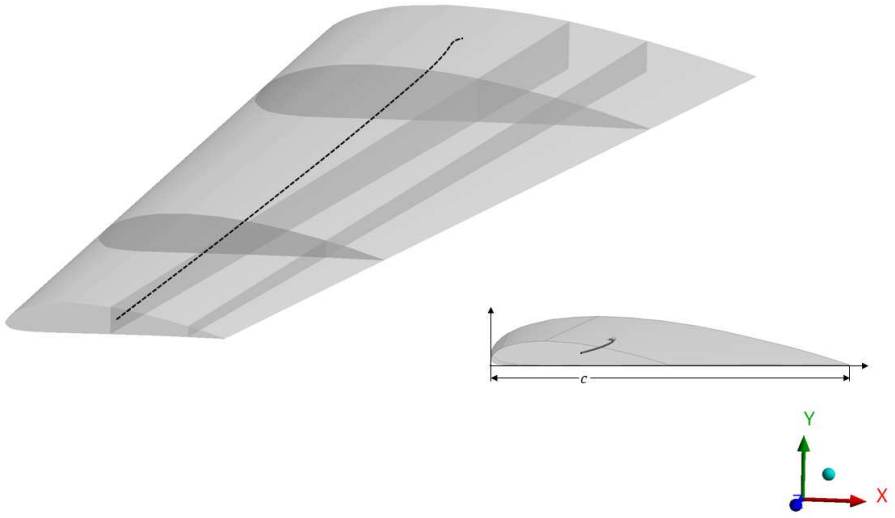

Figure 62. Plot showing the axis of twist for the Göttingen 398 airfoil cross-section as a space curve given as a function of x, y, z. ($x_T = 0.2518c, y_T = 0.0351c$) at z/L =1, and ($x_T = 0.3423c, y_T = 0.0712c$) at z/L =1.

($x_T = 0.2518\,c$, $y_T = 0.0351c$). As shown in Figure 62, the axis of twist varies considerably along the z-axis. For example, at $z/L=0.2$ the center of twist is located at

$\left(x_T = 0.3401c, y_T = 0.0670c\right)$. The deformed (twisted) configuration of the tapered wing is shown in Figure 63(a).

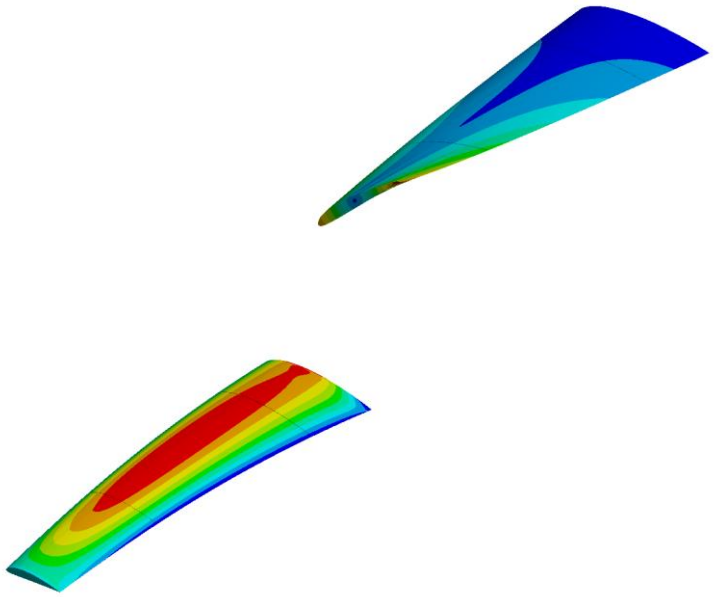

(a) (b)

Figure 63. a) Cantilevered tapered airfoil subjected to twisting (contours represent deformation), b) σ_{zz} stress contours for the cantilevered tapered airfoil subjected to vertical force acting at the shear center on the end of the wing.

Application of a vertical force at the center of twist at the end of the tapered wing results in the bending deformation and bending stresses shown in Figure 63(b). The shear stresses at the end of the tapered cantilever beam, subjected to the vertical end load, are shown in Figure 64. It's interesting to compare the differences in the bending stresses (Figure 61(a) vs. Figure 63(b)) and the distribution of the shear stresses Figure 61(b-c) vs. Figure 64) between the straight and tapered wing. As was observed in the previous examples, application of loads that pass through the center of twist results in a bending

deformation with displacements for the points on the axis of twist only in the direction of the applied force.

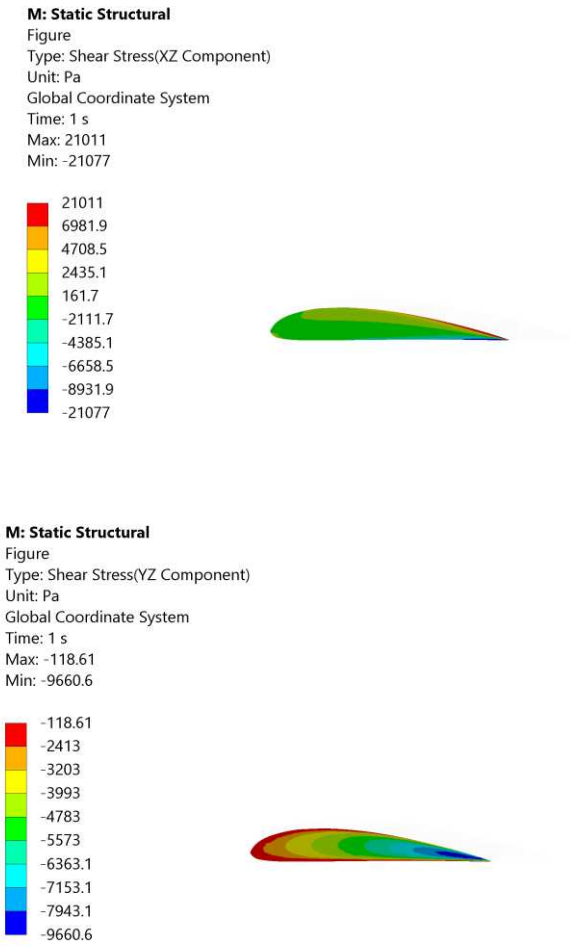

Figure 64. a) Shear stress $\sigma_{xz}(x, y, L)$ on free end of tapered cantilever beam. b) Shear stress $\sigma_{yz}(x, y, L)$ on free end of tapered cantilever beam.

3.3. Shear Center Effect in Crack Propagation

The previous section presented the distribution of shear centers in cantilever beams with various cross-sections. This section focuses on the influence of the shear center on the propagation of surface cracks in cantilever beams. As shown in the Figure 65, a cantilever beam model with a semi-elliptical cross-section is used in this study. A quarter-circular

surface crack is introduced near the free end of the cantilever beam to serve as the initial crack.

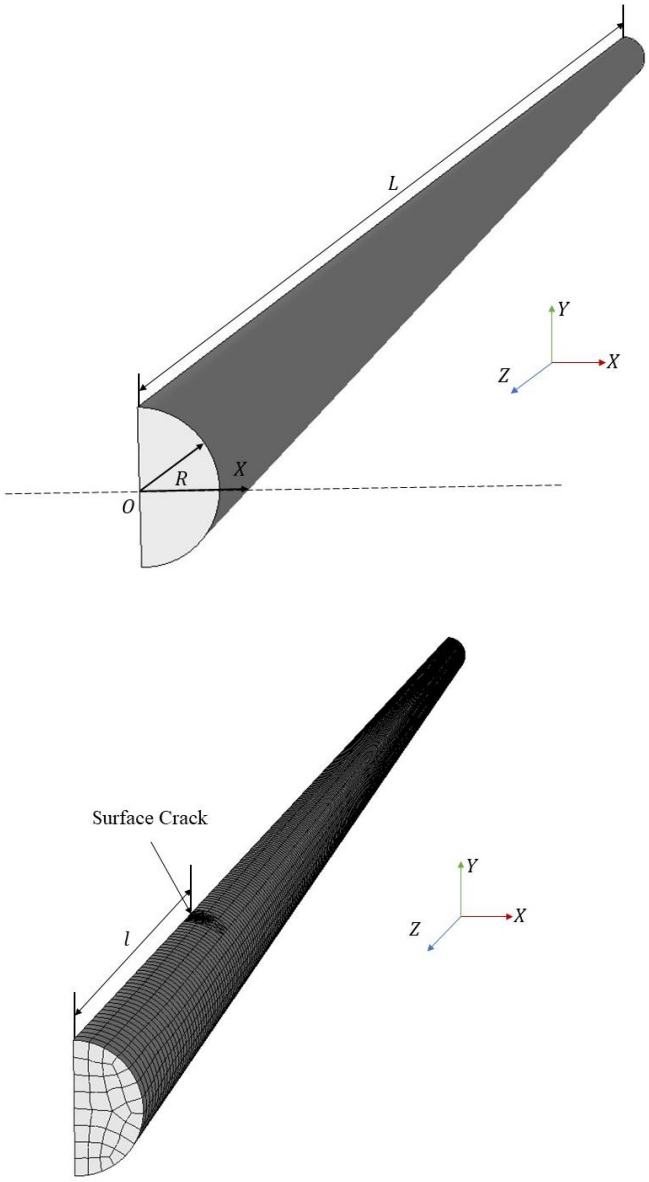

Figure 65. a) Semi-circular cantilever beam model. b) Mesh of the model

In this model, the ratio of the radius to beam length is set as $R/L = 1/100$, and the ratio of the position of the crack to beam length is set as $l/L = 1/10$. This is because, as shown in the figure, the closer the section is to the free end of the cantilever beam, the closer the shear center position, calculated using the least squares method, approaches its converged

value. The Figure 66 illustrates the location and size of the quarter-circular surface crack within the cantilever beam. In this model, the ratio of the crack length to the cross-section radius is set as $a/R = 2/10$.

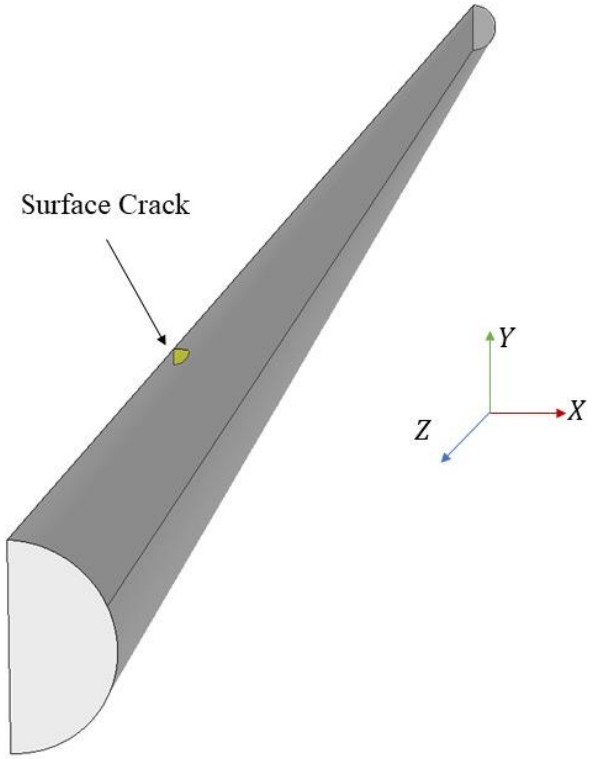

Figure 66. Surface crack in the Semi-circular beam.

To investigate the influence of the shear center on crack propagation, four sets of loads with identical magnitudes are applied to the free end of the cantilever beam as shown in Figure 67. These loads are introduced as remote forces at different locations along the beam's cross-section. The specific loading positions are listed in the Table 5. In load num.1, the position of the applied load corresponds to the shear center of the semicircular beam, as identified in the section 3.2.

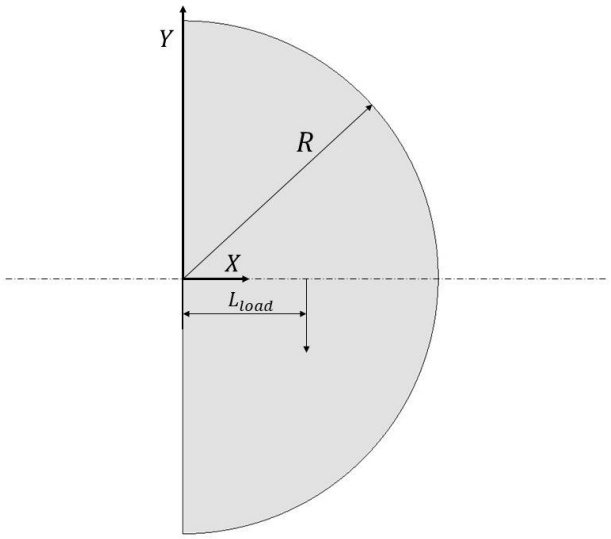

Figure 67. Load location vs the radius of the beam

Table 5. Load cases of semi-circular beam with surface crack

Load Num.	1	2	3	4
Location (L_{load}/R)	0.51015	5	10	50

The boundary conditions of the beam remain consistent with those defined in the previous section: one end of the beam is fully fixed, while the other end is left free. All stress intensity factors were normalized by using the following formula similar to (35):

$$Normalized\ K_{I,II,III} = K_{I,II,III}/K_0 \tag{53}$$

where

$$K_0 = \frac{8Fl}{\pi R^3}\sqrt{\pi a} \tag{54}$$

Where F is the applied load; l is the distance from the load application to the free surface; R is the radius of the beam; a is the radius of the surface crack. In this study, the applied load F=1000N; the radius of beam R=1m; the length of the beam L=100m.

As shown in the Figure 68, the distributions of stress intensity factors at the crack front under load num.1 and load num.4 conditions are presented for comparison. Although the applied load positions differ, both conditions yield comparable K_I. This is attributed to the fact that K_I is primarily governed by the tensile stress component perpendicular to the crack surface. In both cases, the vertical downward force generates same tensile stresses, resulting in identical K_I values.

Under the load num.1, where the force is applied at the shear center of the beam cross-section, the resulting deformation is characterized by a pure vertical displacement along the global y-axis. Consequently, the beam does not experience significant torsional or out-of-plane deformation, and the corresponding K_{II} and K_{III} remain negligibly small.

In contrast, load num.4 condition involves force application far from the shear center, introducing not only vertical displacement but also rotation about the z-axis. This mixed-mode deformation leads to a substantial increase in both K_{II} and K_{III} . Notably, at the ends of the crack front, K_{II} even exceeds K_I, indicating a pronounced K_{II} dominance in these regions.

As a result, the crack propagation behavior differs significantly between the two cases. For the load num.1condition, crack growth is K_I dominated, and the crack is expected to propagate along its original direction. In contrast, for the load num.4 condition, the elevated K_{II} and K_{III} induce larger propagation angles, causing the crack to deviate from its initial path in subsequent growth stages due to strong mixed-mode effects.

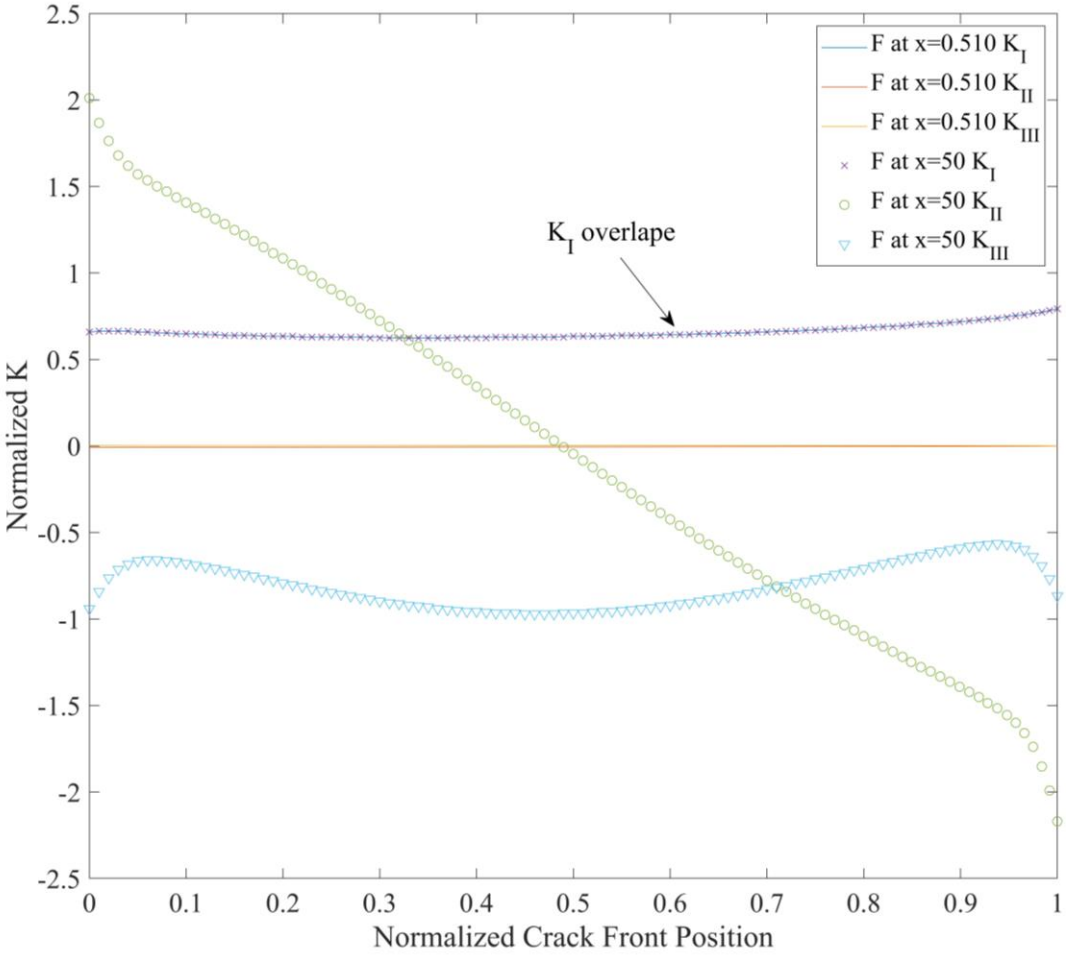

Figure 68. Stress intensity factors at load num. 1 and load num. 4.

As shown in Figure 69(a) and Figure 69(b), as the applied load position moves progressively farther from the shear center, both the K_{II} and K_{III} stress intensity factors at the crack front exhibit a noticeable increase. This trend indicates that the degree of rotational deformation in the cantilever beam also intensifies accordingly.

Although the magnitude of the applied load remains constant, the increasing values of K_{II} and K_{III} with the load's offset from the shear center leads to a significant rise in the K_{eq}. This increase not only causes the crack to deviate from its original propagation path, but also results in a reduction in the fatigue life of the cantilever beam due to enhanced mixed-mode loading effects.

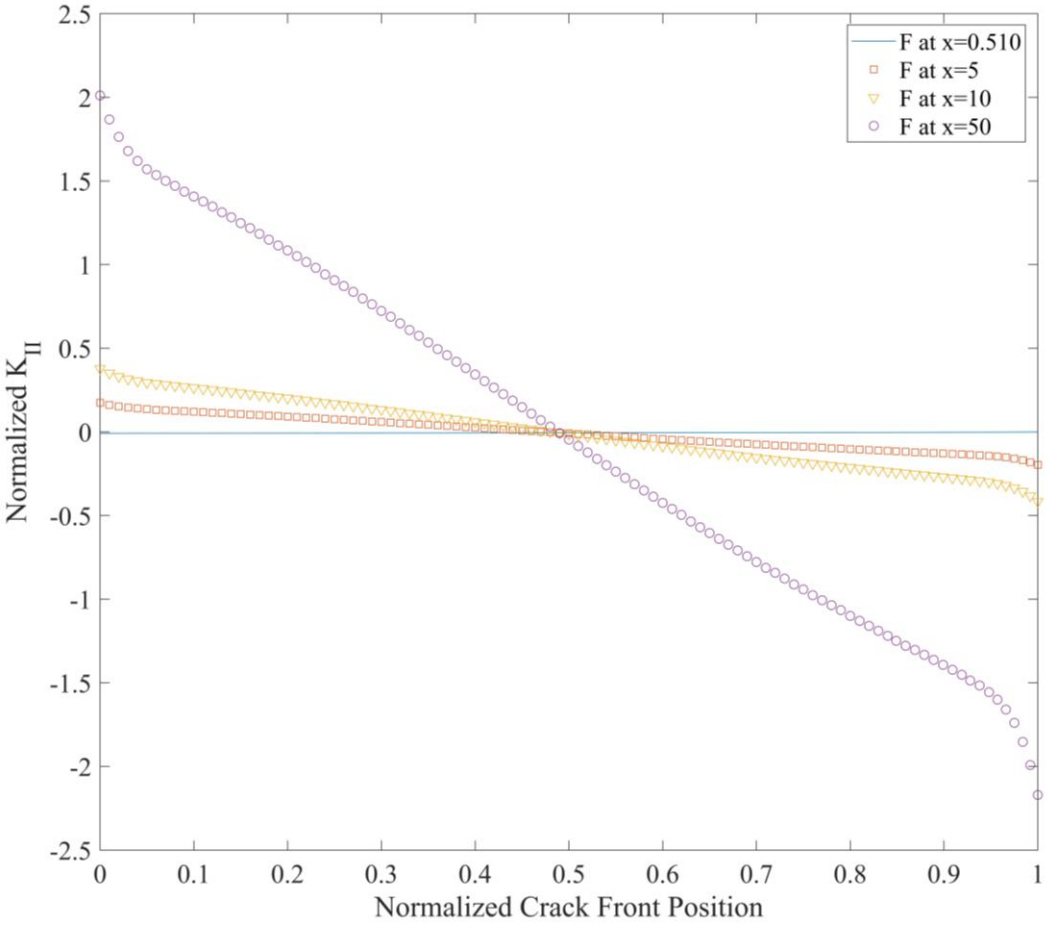
F at x=0.510
F at x=5
F at x=10
F at x=50
Normalized K_{II}
Normalized Crack Front Position
2.5
2
1.5
1
0.5
0
-0.5
-1
-1.5
-2
-2.5
0
0.1
0.2
0.3
0.4
0.5
0.6
0.7
0.8
0.9
1

(a)

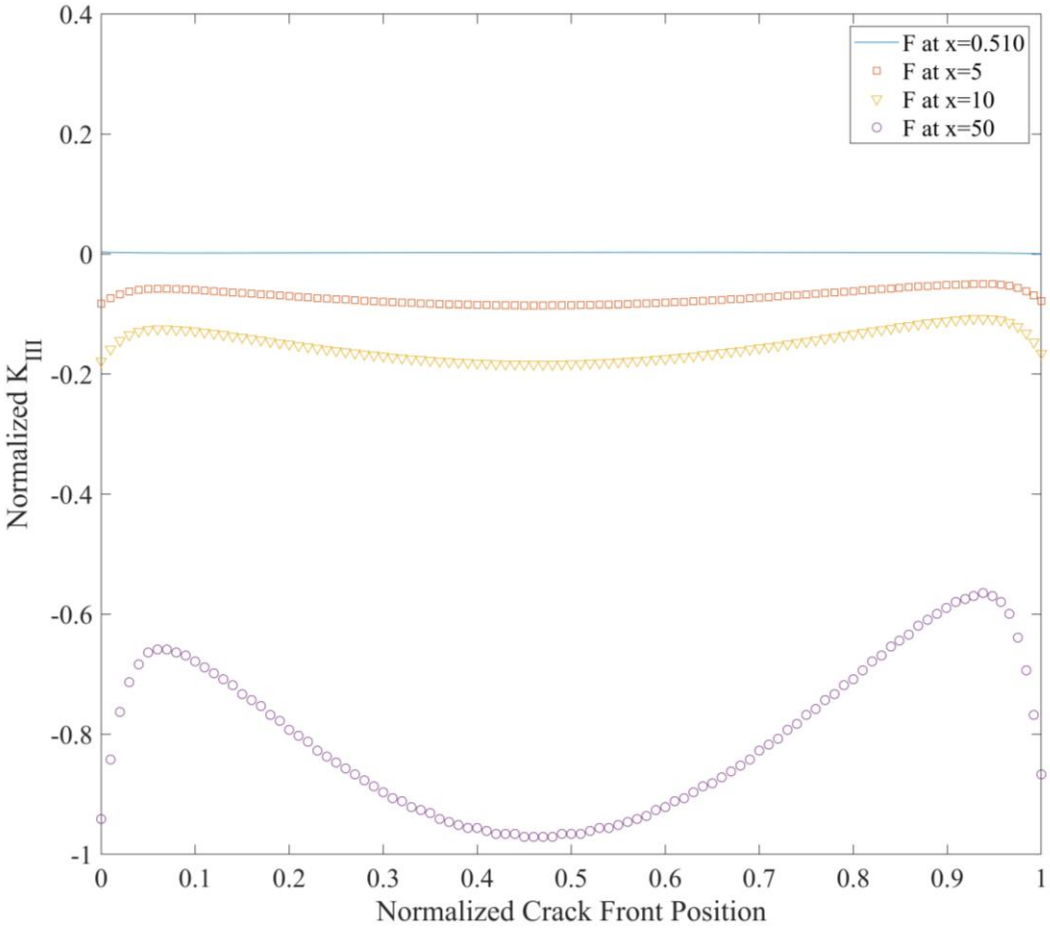

(b)

Figure 69. . $K_{II}$and K_{III} variation in 4 different load cases: a) K_{II}variation; b) K_{III} variation.

The crack growth path obtained from fatigue fracture simulations under two different loading conditions are shown in the Figure 70: load num.1 and load num.4. In the case of load num.1, the crack extension is mainly controlled by the K_I. As a result, the crack expands steadily in the initial direction without significant deviation and maintains a relatively straight growth path. On the contrary, under load num.4 condition, the applied load is far from the shear center and generates a large torque loading in the structure. This resulted in strongly mixed-mode loading conditions, especially involving K_{II} and K_{III}. As a result, the crack deviates from its original orientation as early as the first increment and

this deviation intensifies in the subsequent steps. Eventually, the crack surface develops a twisted and deformed geometry, as shown in Figure 70 (c).

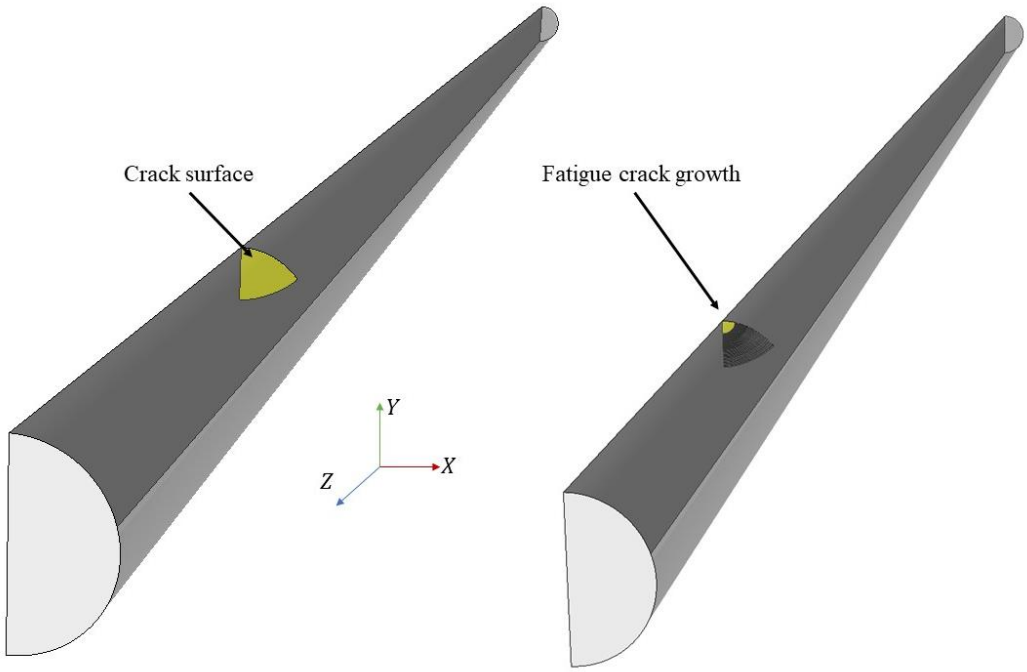

(a)

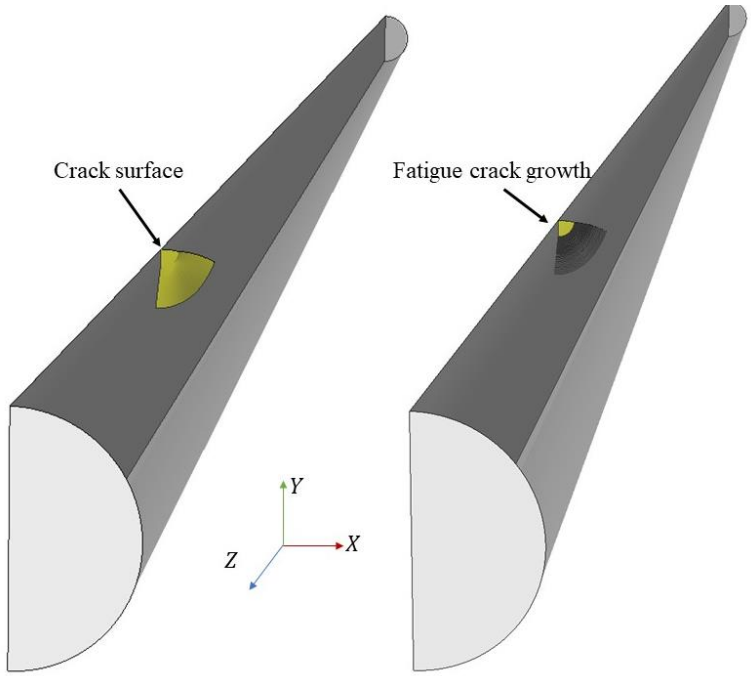

(b)

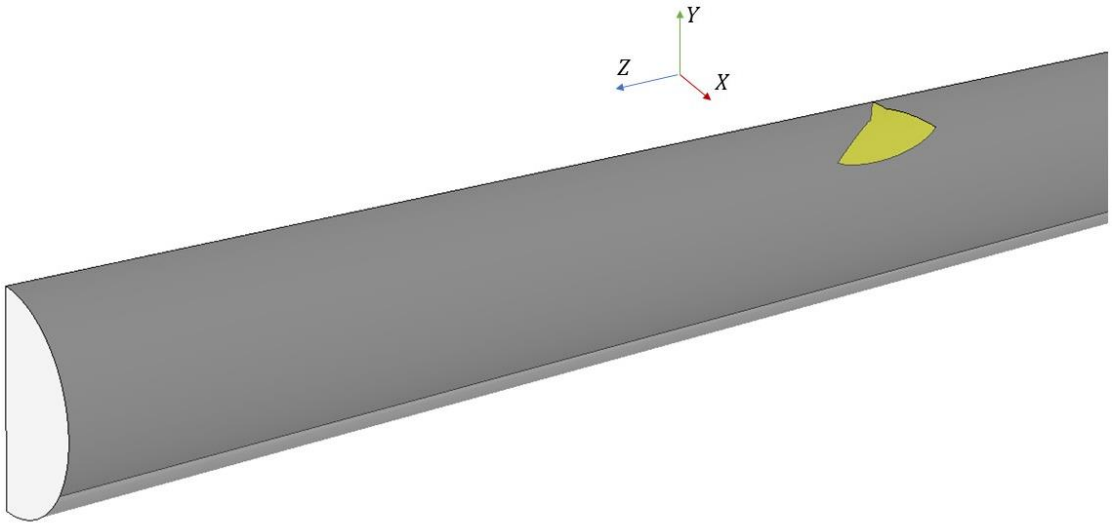

(c)

Figure 70. Fatigue crack growth simulation on load num.1 and load num.4: (a) crack growth of load num.1; (b) crack growth of load num.4; (c) Side view of load num.4.

3.4. Brittleness Temperature Range (BTR) Update

This section primarily presents the finite element simulation results of the Trans-Varestraint Test and the Houldcroft Test. Based on the simulation outcomes and existing experimental data from the literature, the Brittleness Temperature Range (BTR) is updated. Furthermore, by comparing the updated BTR with the results of the Houldcroft Test, the effectiveness of BTR in predicting hot cracking susceptibility is demonstrated.

Trans Varestraint Test

The Figure 71 illustrates the temperature field distribution during the welding process under a double-ellipsoid heat source. It can be observed that the maximum temperature reaches 2206 °C, which exceeds the melting point of austenitic stainless steel 316 (SS316), approximately 1400 °C.

Given that the externally applied loads in the test model are relatively small, the heat generated by plastic deformation is negligible compared to the energy input from the

welding heat source. Therefore, the thermal analysis model considers only the heat contribution from the welding source.

The results of the transient thermal welding analysis are subsequently applied as thermal loads in the transient thermo-mechanical analysis, serving as the input for evaluating the stress and strain responses in the coupled simulation model.

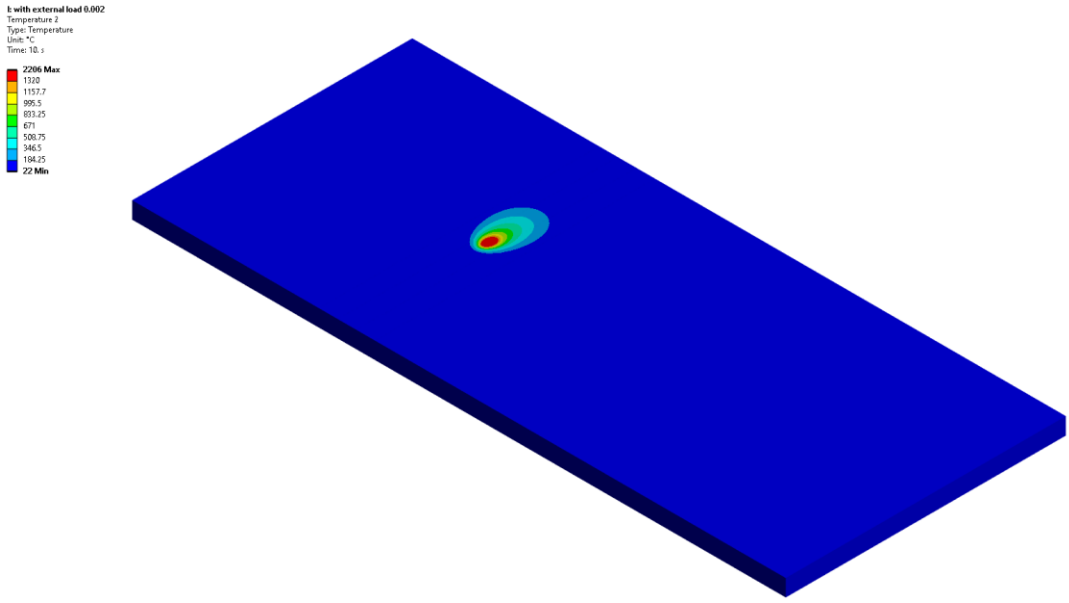

(a)

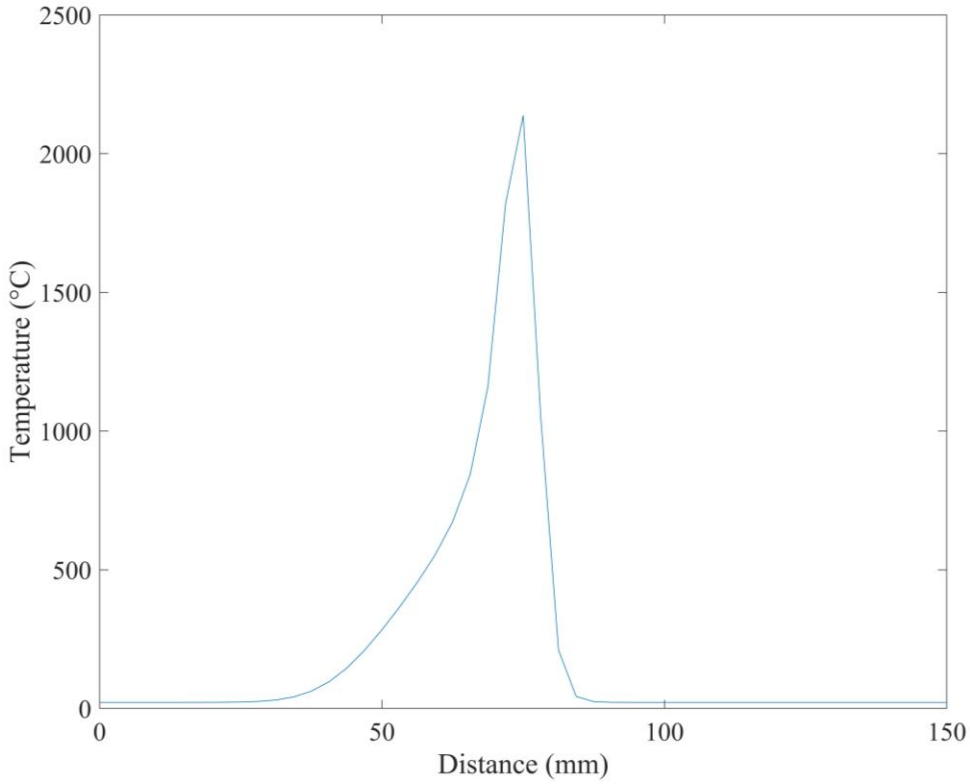

(b)

Figure 71. Temperature distribution on the specimen during the Test: (a) Temperature field on model; (b) Temperature curve on weld line.

The Figure 72 demonstrates the application of the element birth and death technique in the welding simulation. It is important to note that ‘killing’ an element does not imply its physical removal from the model. Instead, it involves multiplying the element's stiffness matrix by a very small reduction factor, effectively removing it from the mechanical response of the system. Elements that are ‘killed’ are excluded from load transfer during the calculation, and their mass, damping, and specific heat values are also set to zero. Additionally, once an element is deactivated, its strain history is cleared. In both welding simulations and hot cracking susceptibility simulations, this technique is particularly valuable for accurately reproducing metal phase transformation processes. By employing element birth and death, the melting and solidification of the weld region can be

effectively modeled. Furthermore, because the strain history of a ‘killed’ element is reset, the method facilitates the monitoring of strain evolution from the onset of solidification, which is critical in evaluating hot cracking behavior. In this model, the temperature field results obtained from thermal analysis are used as input loads. Prior to the mechanical analysis, elements with temperatures exceeding the melting point are identified and deactivated. During subsequent steps, if the temperature of a previously ‘killed’ element drops below the melting point, the element is reactivated, allowing for a realistic simulation of the solidification process.

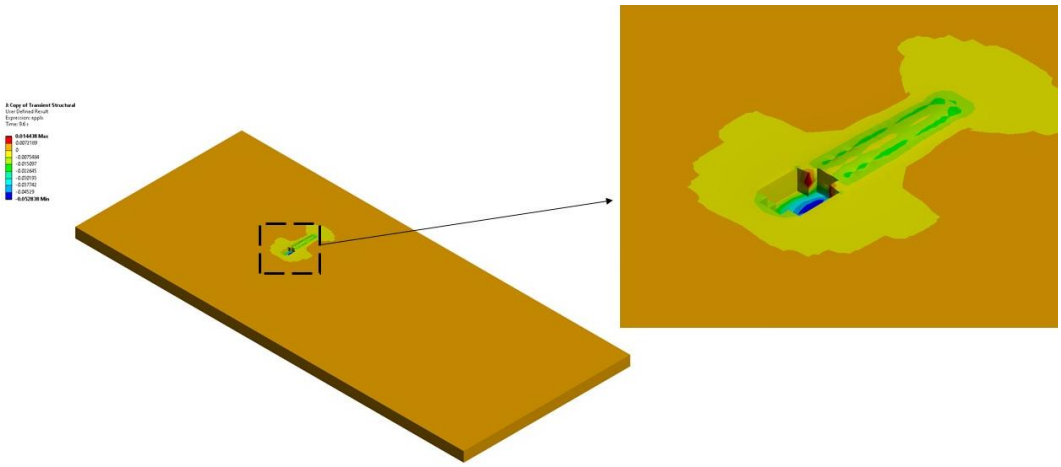

Figure 72. Element birth and death application.

The Figure 73 illustrates the distribution of longitudinal and radial normal stresses during the Trans Varestraint Test. It can be observed that significant compressive stresses are present in front of and on both sides of the heat source for both stress components. This phenomenon arises due to the rapid thermal expansion of the metal in the vicinity of the heat source, which exerts pressure on the surrounding cooler regions that have not yet been heated. The interaction between the expanding hot metal and the unheated zones leads to the development of compressive stresses. To maintain mechanical equilibrium, tensile

stresses appear ahead of these compressive zones, balancing the internal stress distribution generated during the welding process.

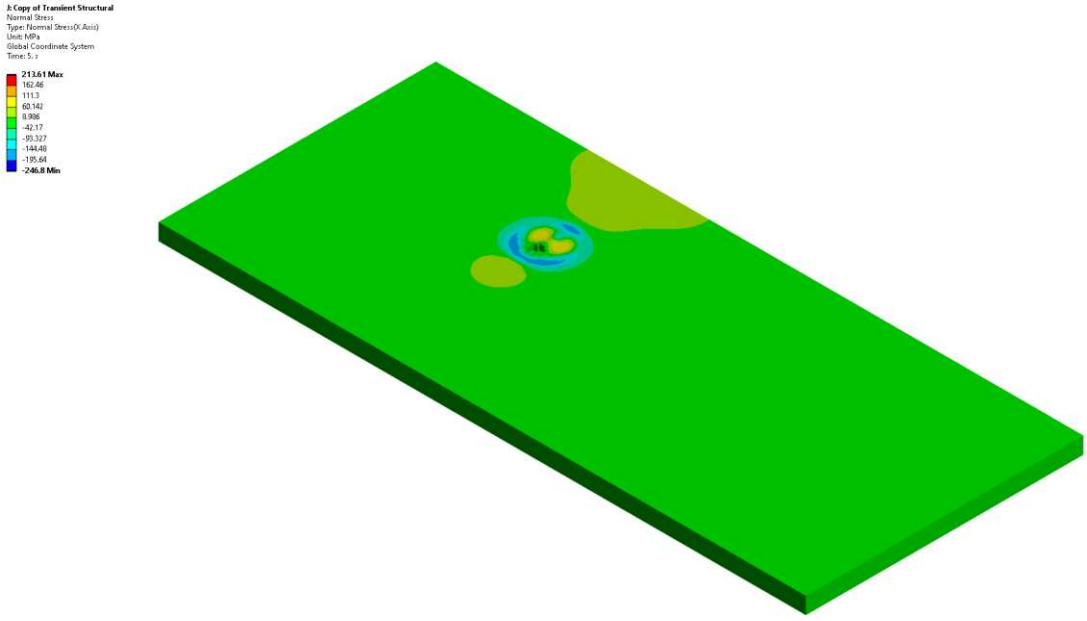

(a)

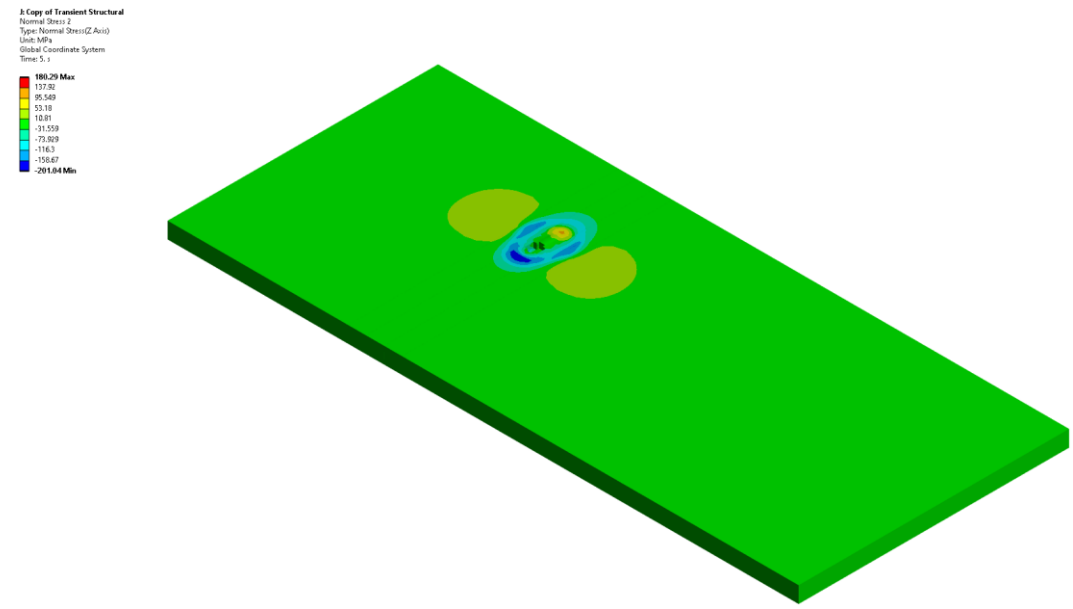

(b)

Figure 73. Normal stresses distribution during welding process: (a) Transverse normal stress; (b) Longitudinal normal stress.

As shown in the Figure 74, under pure mechanical loading (without welding), the tensile strain distribution on the top surface of the specimen along the welding centerline is approximately 0.2%.

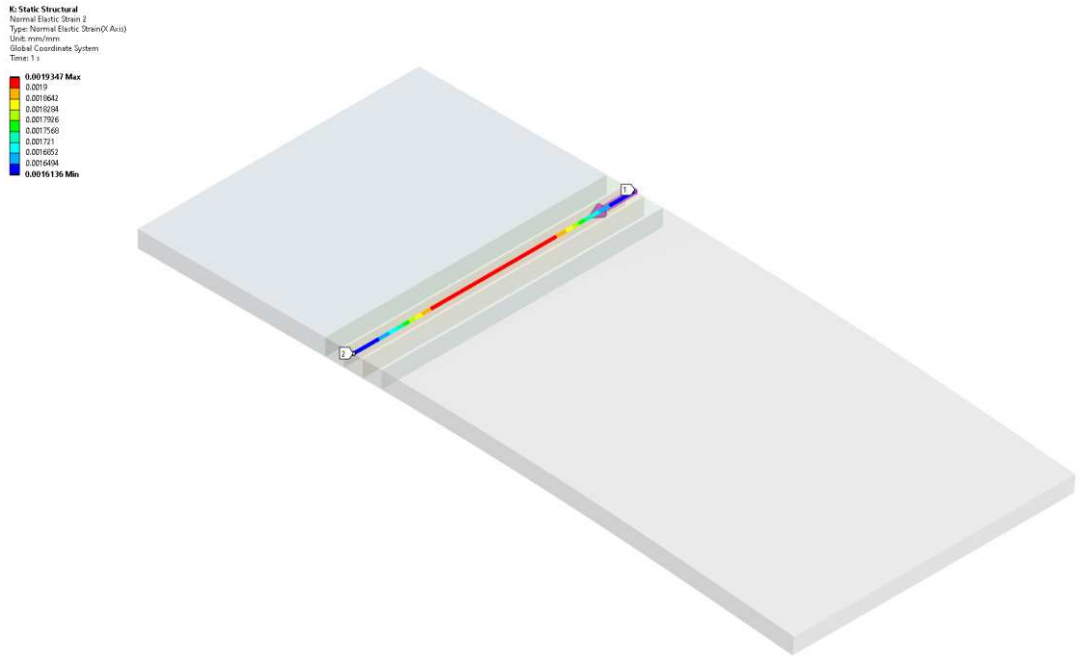

(a)

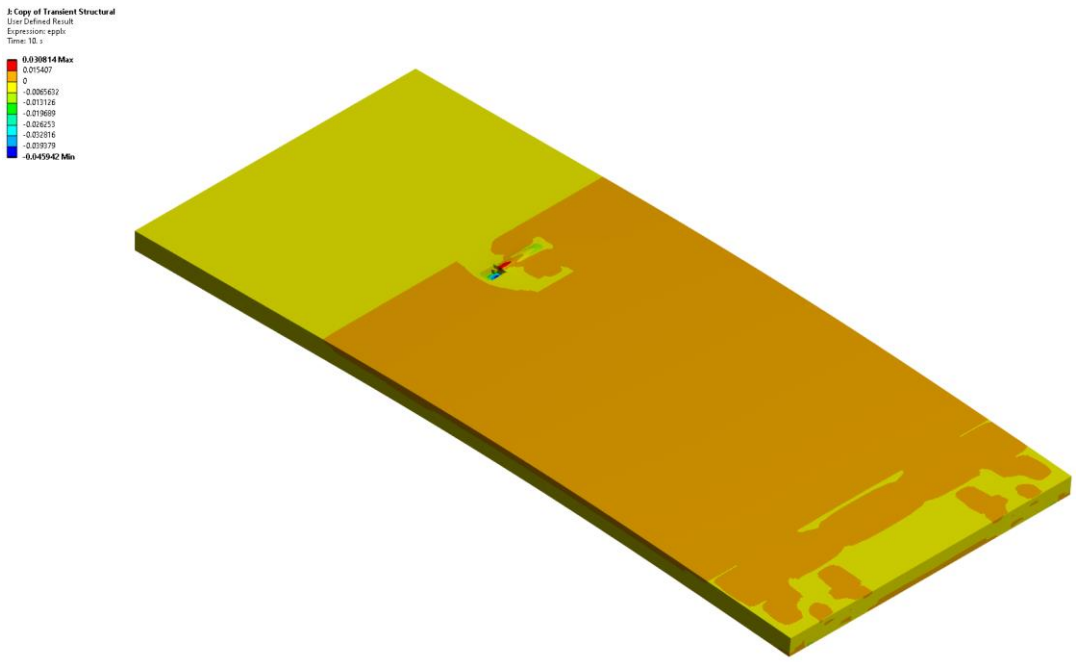

(b)

Figure 74. Strain distribution on weld: (a) 0.2% Mechanical strain from cold bending; (b) Total strain with welding and mechanical strain.

The Figure 75 presents the strain distributions along the welding centerline under two conditions: one with both a 0.2% externally applied mechanical strain and thermal stress, and the other with thermal stress only, i.e., without any external mechanical loading. In both cases, the maximum tensile strain appears in the region where the metal has just begun to solidify. This is attributed to the significant volumetric contraction that occurs during solidification, which leads to the development of tensile strain in the newly solidified zone. However, in the model with external mechanical loading, the maximum tensile strain reaches approximately 2.9%, which far exceeds the sum of the applied mechanical strain (0.2%) and the thermal strain (approximately 0.28%). This result clearly demonstrates that, in the Trans Varestraint Test, it is insufficient to consider only the externally applied mechanical strain; additional factors such as thermal strain and volumetric shrinkage due to phase transformation must also be taken into account. Therefore, in this study, a series

of simulations with varying levels of externally applied tensile strain are conducted to update the original BTR (Brittleness Temperature Range) curve proposed by Senda et al. [49] The updated critical strain values under different loading conditions are used to refine the prediction of hot cracking susceptibility. The finite element results under different external loading conditions are provided in the appendix. Additionally, Table 6 summarizes the original critical strain values and the updated critical temperature values for SS316 under various temperatures and externally applied strain levels.

Table 6. Critical strains under different temperature of BTR curve.

Temperature(°C)	Senda's BTR	Update BTR
1400	0.001	0.02107
1330	0.002	0.02917
1300	0.004	0.03829
1290	0.006	0.04737
1280	0.009	0.05517

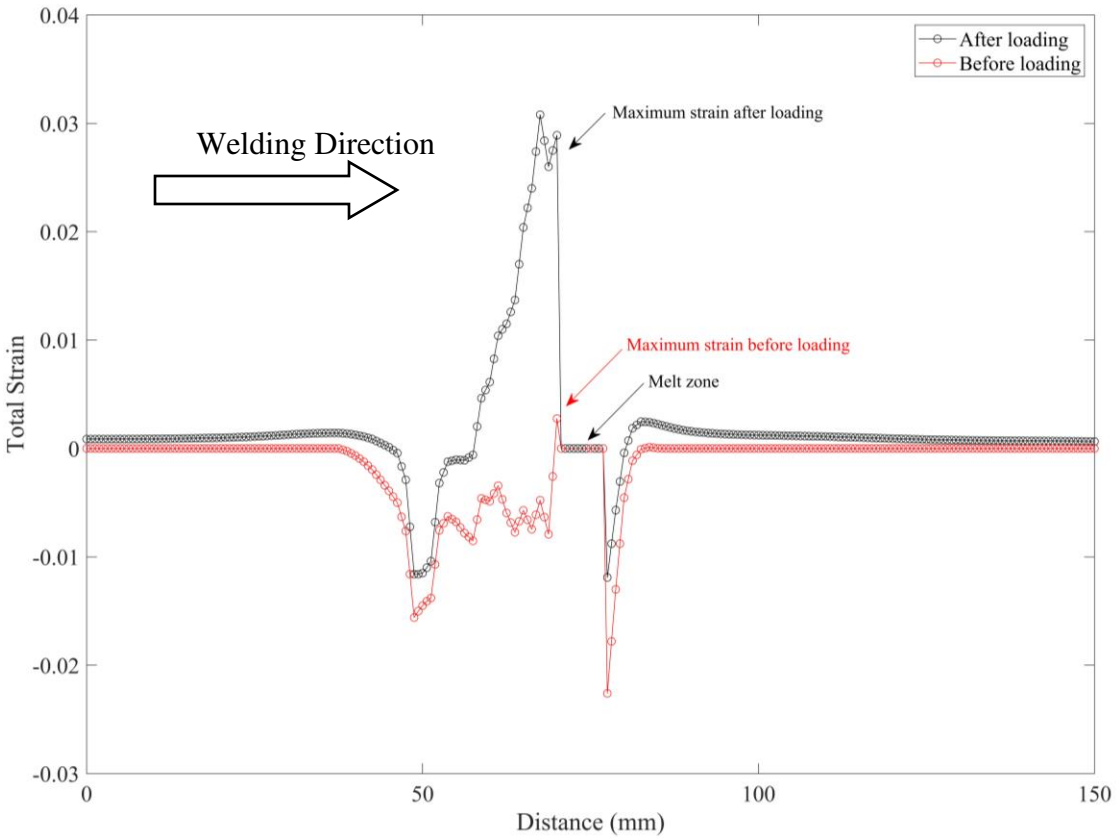

Figure 75. Transverse strain comparison between 0.2 % mechanical load and without load.

The Figure 76 shows a comparison between the original BTR curve proposed by [49] and the updated BTR curve developed in this study. Due to the inclusion of additional factors such as thermal loading and volumetric shrinkage during solidification, the updated BTR curve exhibits a significant upward shift. This updated curve provides a more accurate representation of the critical conditions for hot cracking. Consequently, the subsequent hot cracking predictions in this study are based on the revised BTR curve.

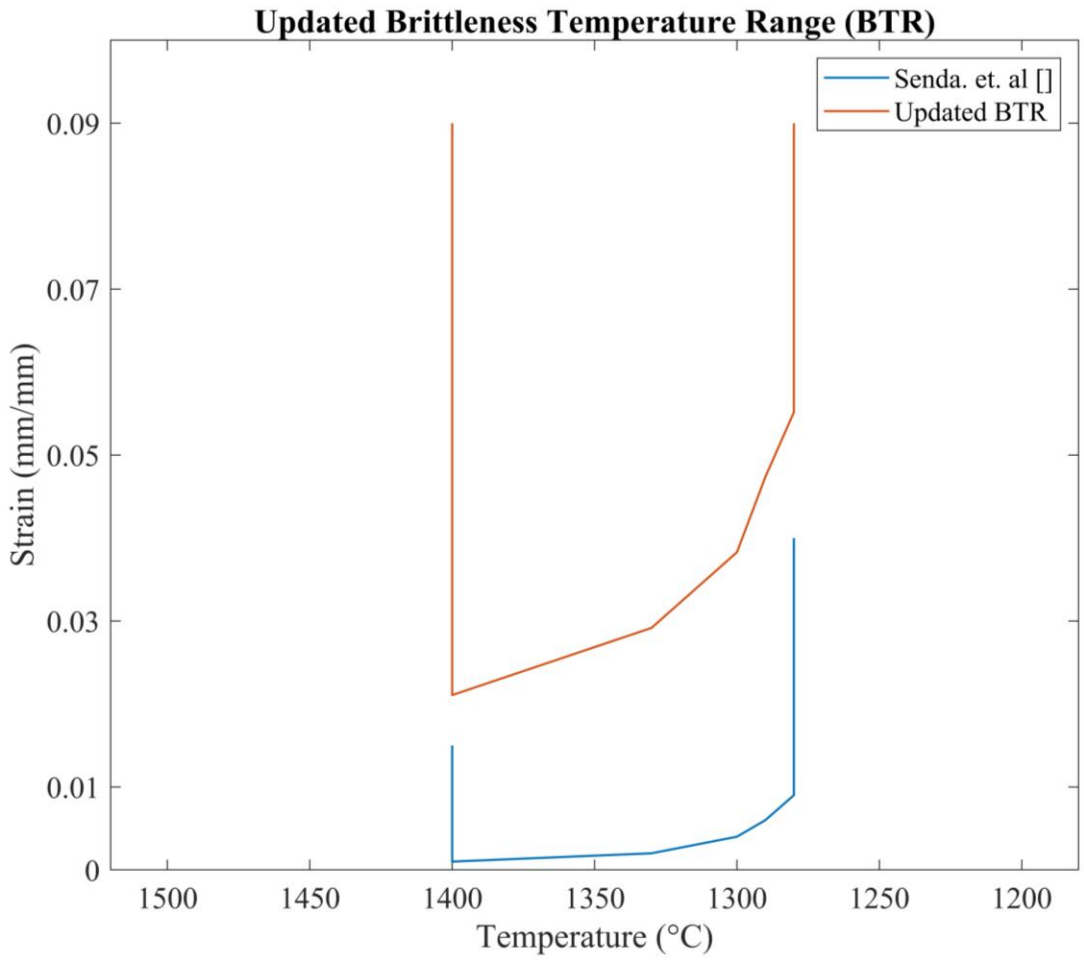

Figure 76. Updated BTR and mechanical only BTR.

Houldcroft Test

In this study, the Houldcroft Test is conducted using autogenous welding under unconstrained boundary conditions. The hot cracking susceptibility simulations are divided into two groups: 1. Constant total heat input (J) with varying welding speeds; 2. Constant heat input per unit length (J/mm) with varying welding speeds. In this context, the heat input refers to the power of the heat source, defined as the product of voltage (U) and current (I). The heat input per unit length represents the amount of thermal energy delivered per unit distance, calculated as the ratio of power (W) to welding speed (mm/s). Under constant heat input, the heat input per unit length decreases as the welding speed increases,

since the interaction time between the heat source and the material becomes shorter. This reduced exposure leads to insufficient energy delivery to the weld zone, resulting in a decline in weld quality. In extreme cases, the available heat may become inadequate to fully melt the base metal, increasing the likelihood of incomplete fusion or poor weld formation. In contrast, under constant heat input per unit length, the power of the heat source must be increased proportionally with the welding speed. While this ensures that sufficient thermal energy is delivered per unit length. To evaluate the influence of welding speed on hot crack length, the strain evolution curves at the solidification point of nodes are compared against the updated BTR curve. This approach allows for the prediction of hot cracking behavior based on the thermal-mechanical history during welding. The welding input parameters for the two test groups are summarized in the Table 7.

Table 7. Welding parameters of Houldcroft Test modeling

Constant	Heat input (W) =550		Heat input per unit (J/mm)	
Parameter	Heat input per unit (J/mm)	Welding speed (mm/s)	Heat input (W)	Welding speed (mm/s)
Case1	1850	0.893	491.15	0.893
Case2	1232	1.340	737	1.340
Case3	924	1.787	982.85	1.787

The Figure 77(a)-(d) illustrates the stress distributions in the early and intermediate stages of welding during the Houldcroft Test. At the initial stage (t=5s) of welding, the stress distribution on the specimen resembles that observed in the Trans-Varestraint Test. Due to the rapid thermal expansion of the metal near the heat source and the constraint imposed by the surrounding cooler, unheated regions, compressive stresses develop in both the longitudinal and transverse directions around the heat source. To maintain equilibrium,

tensile stresses arise adjacent to the compressive zones to counterbalance the internal forces. However, during the intermediate stage (t=24s) of welding, the heat source reaches a region with deeper slots. These slots provide greater compliance and freedom for thermal expansion, significantly reducing the constraint imposed on the heated metal. As a result, the stress levels near the heat source drop rapidly, reflecting the stress-relief effect introduced by the groove geometry in this phase of the welding process.

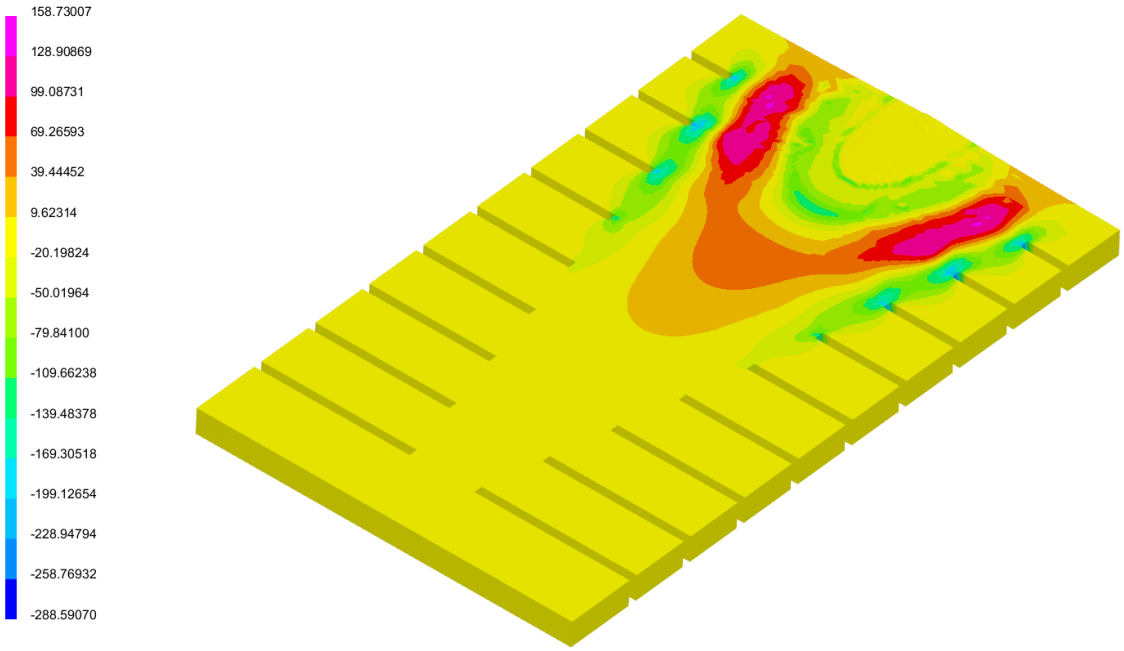

(a)

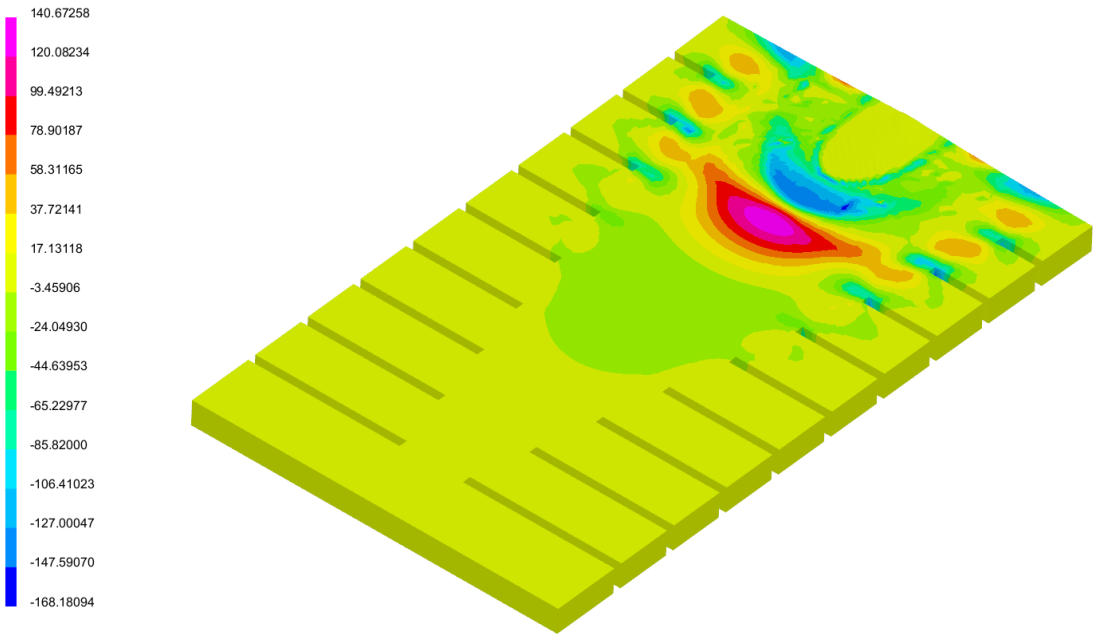
140.67258
120.08234
99.49213
78.90187
58.31165
37.72141
17.13118
-3.45906
-24.04930
-44.63953
-65.22977
-85.82000
-106.41023
-127.00047
-147.59070
-168.18094

(b)

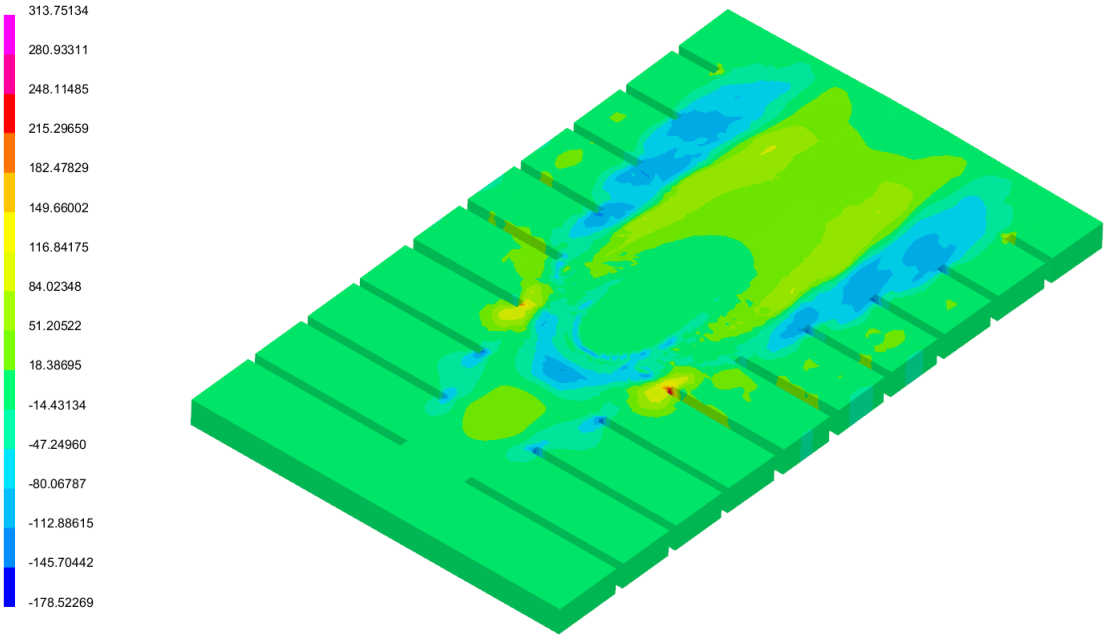
313.75134
280.93311
248.11485
215.29659
182.47829
149.66002
116.84175
84.02348
51.20522
18.38695
-14.43134
-47.24960
-80.06787
-112.88615
-145.70442
-178.52269

(c)

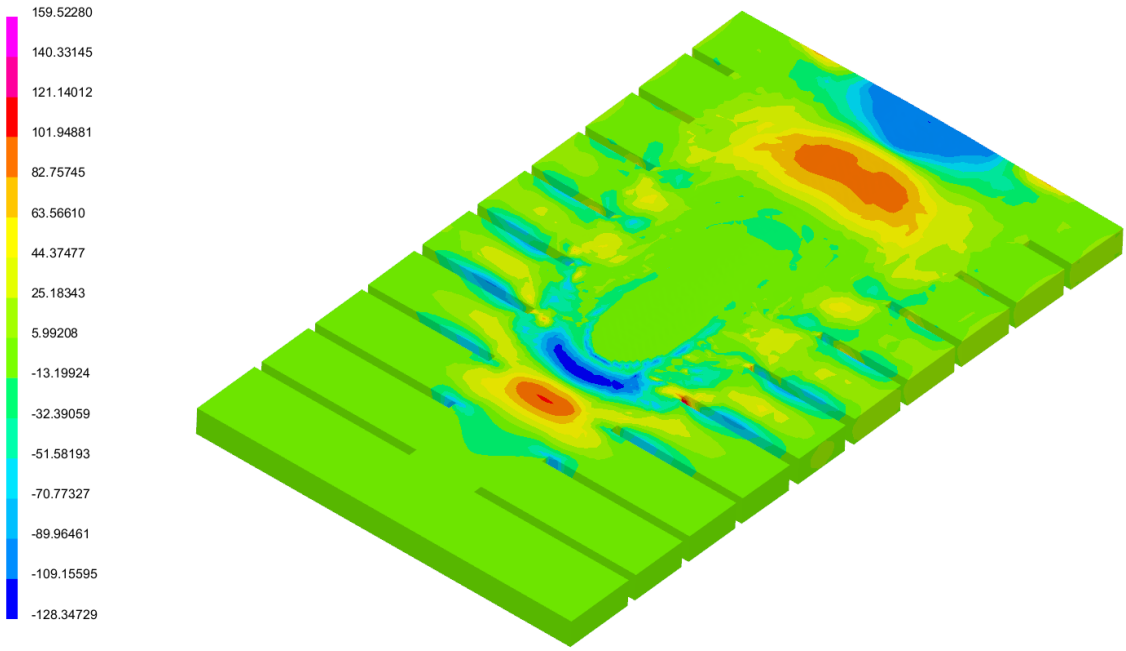

(d)

Figure 77. Normal stresses distribution during welding test of case 1: (a) Longitudinal normal stress at t=5s; (b) Transverse normal stress at t=5s; (c) Longitudinal normal stress at t=24s; (d) Transverse normal stress at t=24s.

Prior to conducting hot cracking predictions, it is essential to examine the maximum temperature distribution recorded in the specimen model. This step ensures that the temperature in the crack observation region reaches or exceeds the melting point of the material, thereby validating the occurrence of melting and subsequent solidification, which are prerequisites for hot crack formation. The Figure 78 presents the maximum temperature distribution for Case 1. The gray-shaded regions indicate the locations of elements that reached the melting point of the material during the welding process. These regions represent the zones where melting and solidification occurred.

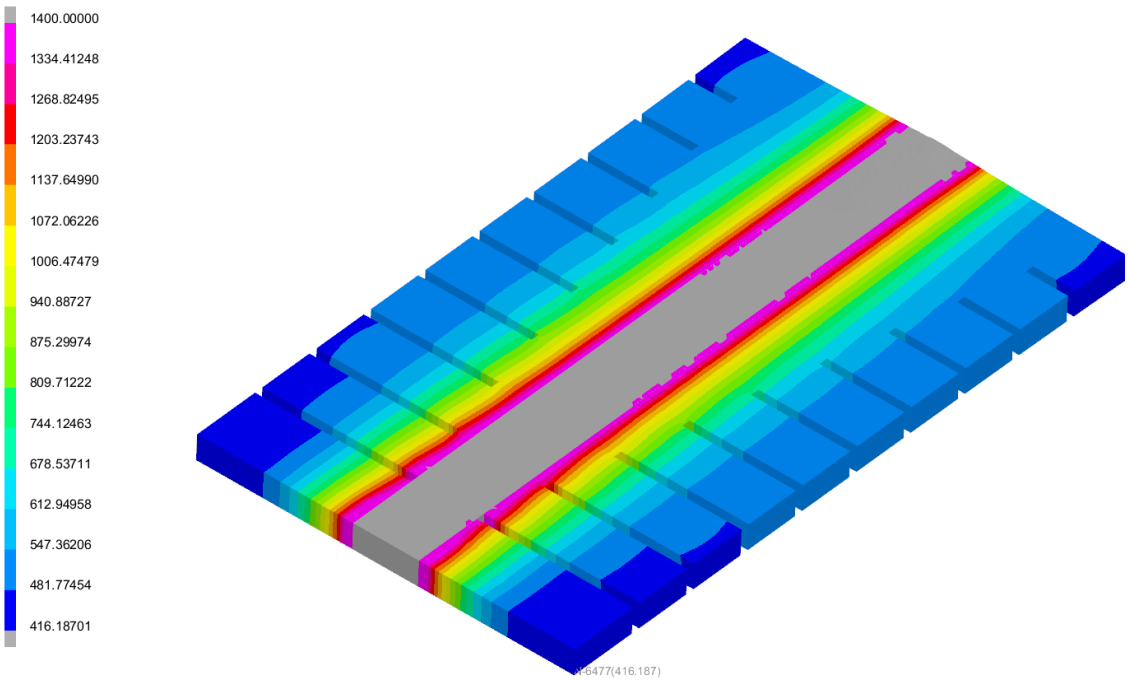

Figure 78. Maximum temperature on the specimen model.

To facilitate a more accurate comparison of the influence of different welding speeds on hot cracking susceptibility, point A is selected as a reference location. As shown in the Figure 79, point A is positioned along the welding centerline, at a distance of 3.13 mm from the welding starting edge.

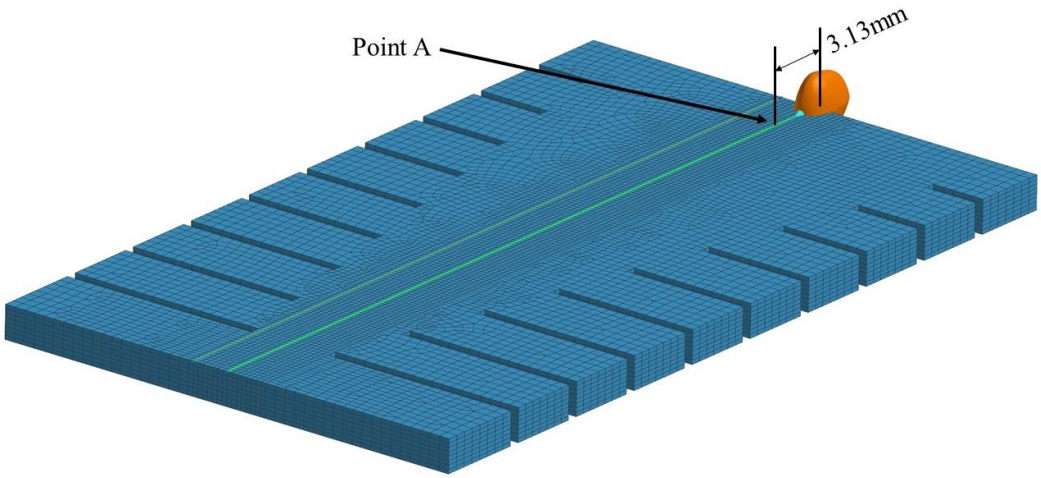

Figure 79. Point A location on the Houldcroft Test specimen model.

The Figure 80 shows the strain evolution at point A under different welding speeds with constant heat input. For all three welding cases, the strain during cooling at point A exceeds the critical strain for hot cracking, indicating the occurrence of hot cracking at this location in each scenario. By comparing the strain values as the temperature decreases, it is evident that case 2 exhibits the highest strain, while case 3 shows the lowest strain, barely exceeding the critical value for hot cracking. This trend aligns with the previously discussed behavior of heat input distribution. Under conditions of constant total heat input, when the energy input is sufficient to induce hot cracking, the length of hot cracks tends to increase with welding speed due to the reduced interaction time and concentrated thermal gradients. However, as the welding speed continues to increase beyond a certain threshold, the available thermal energy per unit length becomes insufficient, and the tendency for hot cracking begins to diminish. The final hot crack lengths resulting from the three welding speeds are summarized in the table. These values quantitatively reflect the effect of welding speed on hot cracking behavior under constant heat input conditions.

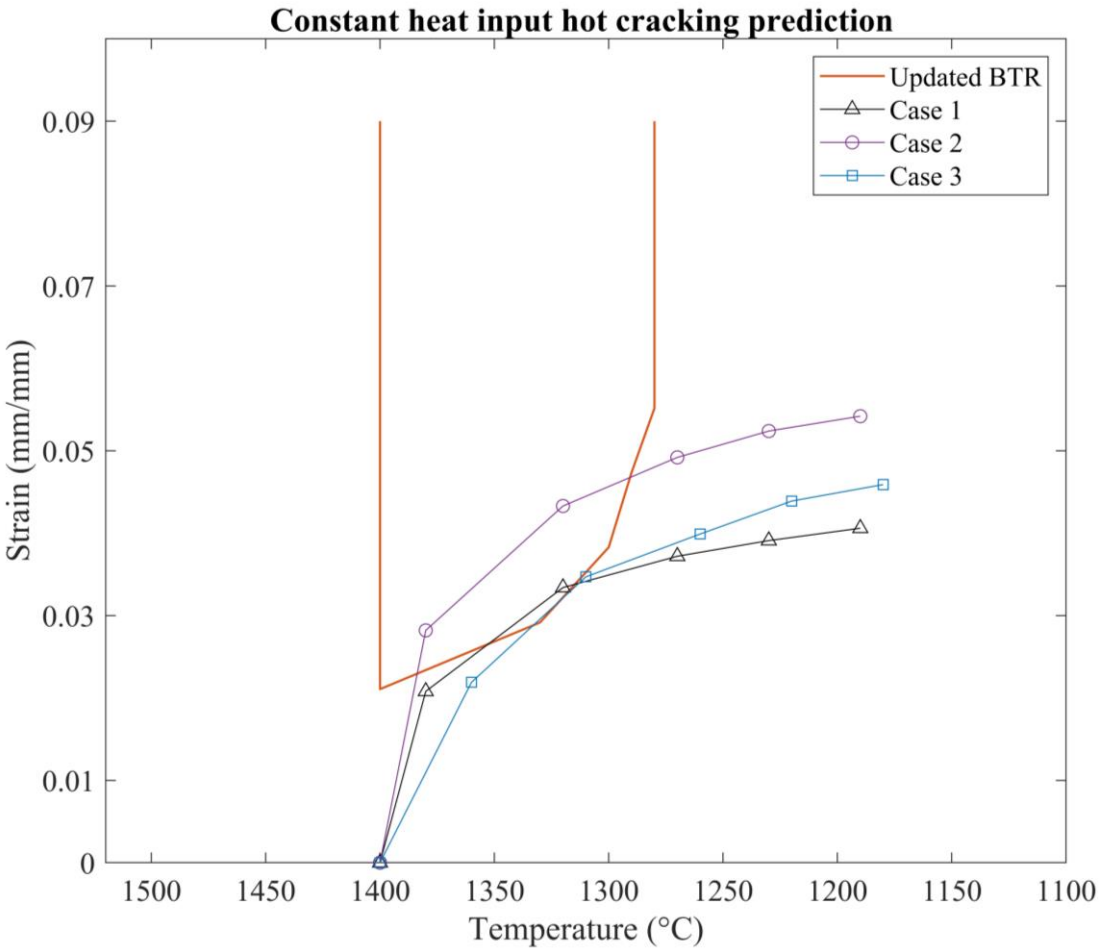

Figure 80. Strain variations of 3 cases at point A in constant heat input condition.

The Figure 81 presents the maximum temperature distribution for case 1 under the condition of constant heat input per unit length. It can be observed that in case 1, the melting point of the material is only reached in the regions near the start and end of the weld path, indicating that the welding parameters used in this case are insufficient to achieve effective melting across the entire weld length. Maintaining a constant heat input per unit length implies that the same amount of total energy is applied to each unit length of the weld. However, to keep the heat input per unit length unchanged while varying the welding speed, it is necessary to adjust the welding power accordingly. Specifically, when the welding speed decreases, the welding power must also be reduced to maintain a

constant energy input per unit length. As a result, the instantaneous power delivered to the weld pool per unit time is significantly reduced, leading to a lower peak temperature generated by the arc. In addition, the combination of reduced power and slower welding speed prolongs the heating duration, allowing more heat to dissipate into the surrounding material. This diffusion effect further prevents the local temperature from reaching the required melting threshold. Therefore, even though the heat input per unit length remains the same, the actual thermal behavior within the material is altered. The lower peak heating temperatures and diminished power density may result in a smaller effective molten region. This explains why, in case 1, only the regions at the beginning and end of the weld reach sufficient temperatures to achieve effective melting, despite a constant heat input per unit length.

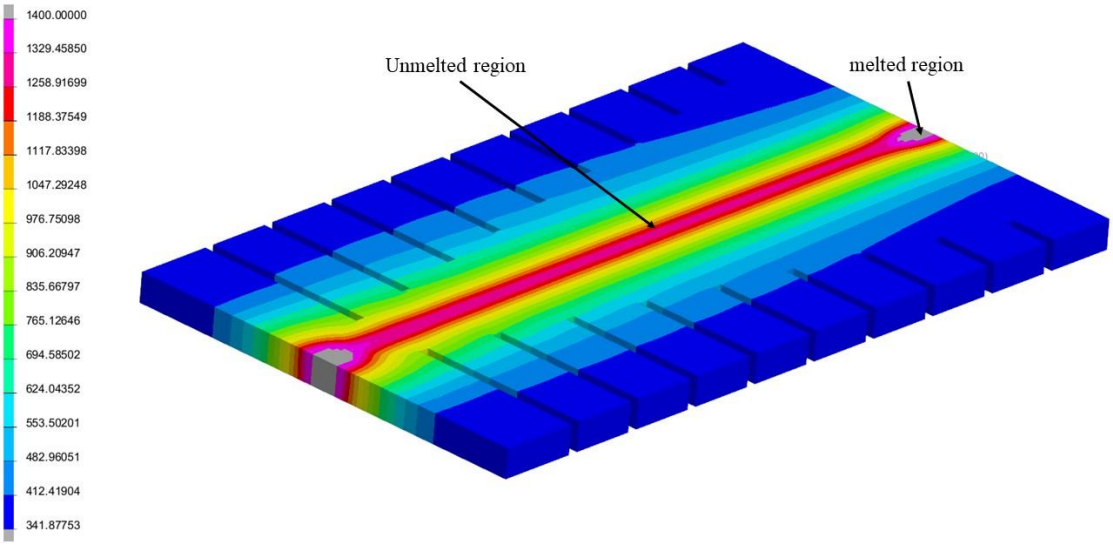

Figure 81. Maximum temperature of constant heat input per unit case 1.

The Figure 82 illustrates the strain evolution at point A under the condition of constant heat input per unit length. Under this condition, as the welding speed decreases, the size of the molten pool becomes smaller, due to the corresponding reduction in welding power. In

case 1, this effect is particularly evident, as point A does not reach the melting point and therefore fails to undergo effective melting. Although the strain at point A in case 1 exceeds the critical strain defined by the BTR curve, it is considered invalid for hot cracking evaluation because melting does not occur at this location. In contrast, in cases 2 and 3, Point A does melt effectively; however, the strain evolution remains below the critical BTR threshold, indicating that no hot cracking occurs at this location. The final hot crack lengths for the three cases under constant unit-length heat input are summarized in the accompanying table. These results reveal that heat input magnitude significantly influences the temperature distribution and solidification rate of the molten pool, which in turn affects hot crack formation. When the heat input is low, the resulting molten pool is smaller, and the tensile stress generated during solidification due to volumetric shrinkage is correspondingly reduced. As reflected in the Table 8, case 3 exhibits the longest hot crack length, while case 1 produces no hot cracks, consistent with the observation that insufficient melting prevents crack initiation in the absence of adequate thermal energy.

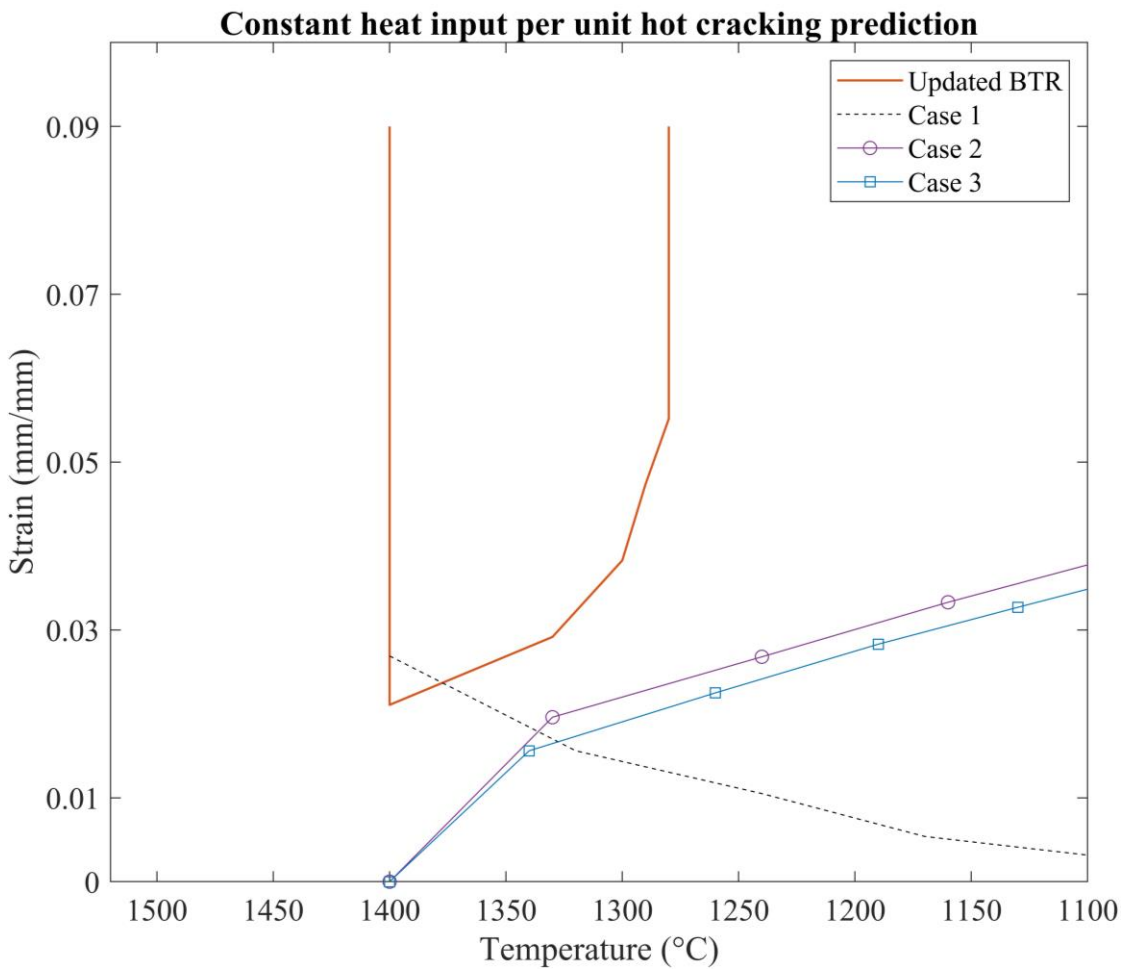

Figure 82. Strain variations of 3 cases at point A in constant heat input per unit condition.

Table 8. Hot crack length of Houldcroft Test

Constant	Heat input (W) =550	Heat input per unit (J/mm)
Parameter	Crack length (mm)	Crack length (mm)
Case1	3.13	No hot crack
Case2	4.47	0.89
Case3	3.57	1.34

3.5. Welding Process Simulation

The welding simulations conducted in this study include both a T-joint welding model and a multi-pass welding model. The finite element results from these simulations encompass thermal analysis, hot cracking prediction, and welding residual stress evaluation. Among these, the residual stress fields obtained from the simulations are used as initial loads in the subsequent three-dimensional crack growth models, enabling the simulation of crack propagation under welding residual stress environments.

T-joint Welding

The Figure 83 illustrates the process of weld deposition simulation in the T-joint welding model using the element birth and death technique. This method allows for the stepwise activation of elements in the weld region, effectively capturing the sequential material addition and thermal evolution during the welding process.

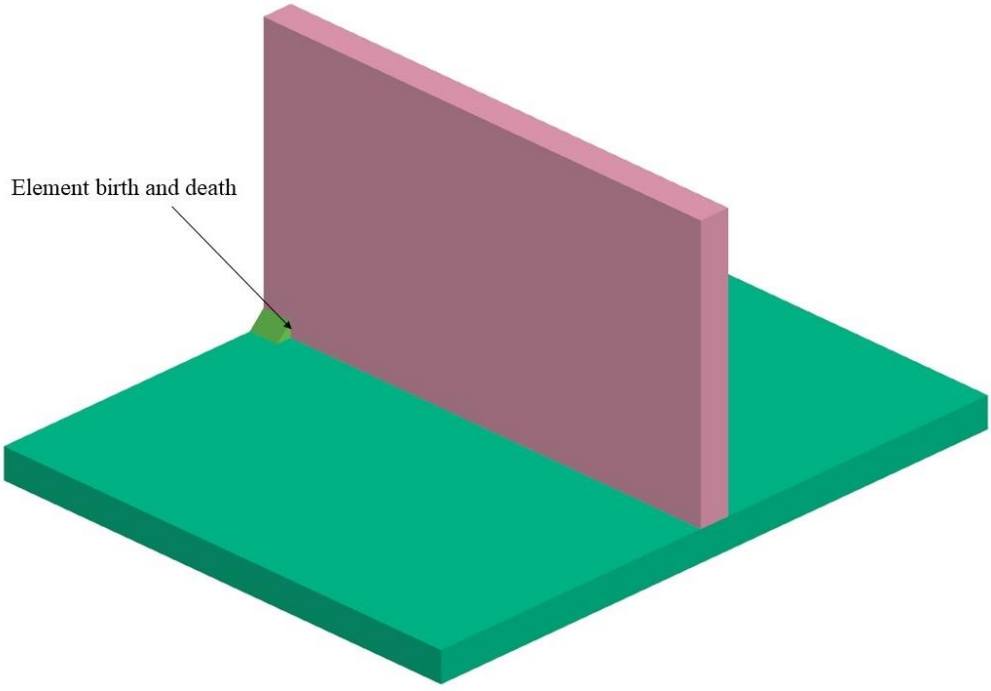

Figure 83. Weld applied by element birth and death.

Figure 84 (a)–(d) depict the temperature distributions at the start and end of the two weld passes in the T-joint welding model. The temperature fields clearly reveal the extent of the effective fusion zones, allowing for verification that the weld metal properly melts and integrates with the adjacent base material. These results confirm that the thermal input is sufficient to achieve sound metallurgical bonding at the weld interfaces. To better approximate realistic welding conditions, a scaling factor is applied to the heat input at the start and end of each weld pass. At the beginning of the weld, the model is at room temperature, and additional energy is required to initiate effective melting. Therefore, the heat input is increased by applying a larger scaling factor to ensure sufficient fusion. Conversely, at the end of the weld, the surrounding material has already been preheated by the preceding heat input. To avoid overheating and excessive weld penetration at the termination point, the heat input is reduced by applying a smaller scaling factor.

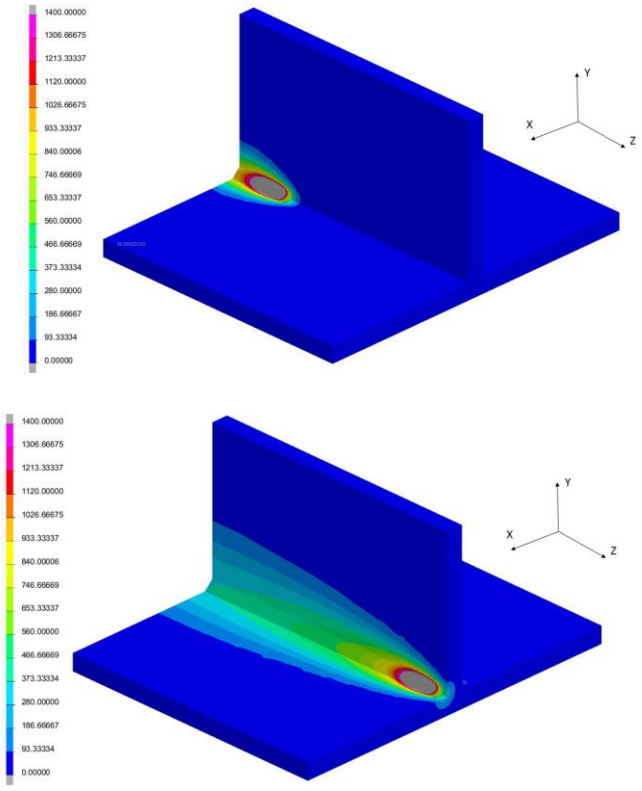

(a) (b)

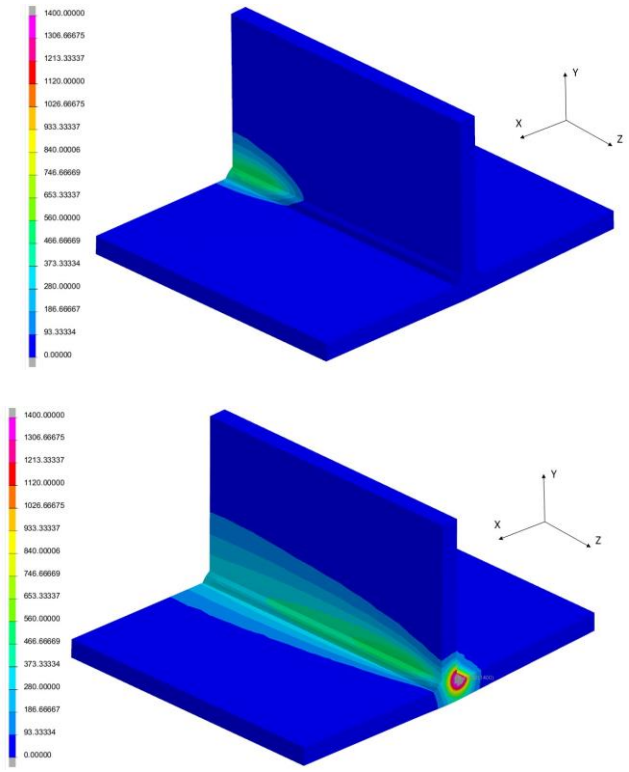

(c) (d)

Figure 84. Temperature distribution at the start and end of the weld passes: (a)1st weld pass start; (b)1st weld pass end; (c)2nd weld pass start; (d)2nd weld pass end.

Figure 85 (a)-(e) illustrate the residual stress distributions in different directions after cooling in the T-joint welding model. Figure 85(a) and (b) show the transverse normal stress distribution from different viewing angles. The maximum and minimum stresses occur in the base plate, with compressive stresses appearing at the start and end of both welds. The maximum tensile stress is located at the midsection of the base plate, near the sides of the web plate. Since the transverse stress direction aligns with the thickness direction of the web plate, which has relatively small dimensions, the web plate is less prone to developing significant residual stresses in this direction. In contrast, Figure 85(c) and (d) display the longitudinal residual stress distribution, which is notably different. Because the web and base plates have similar dimensions in the longitudinal direction, the

residual stress distributions in both components are also similar. The maximum tensile stress appears in regions adjacent to the welds, while compressive stresses form in areas farther from the welds to maintain equilibrium with the tensile stress zones.

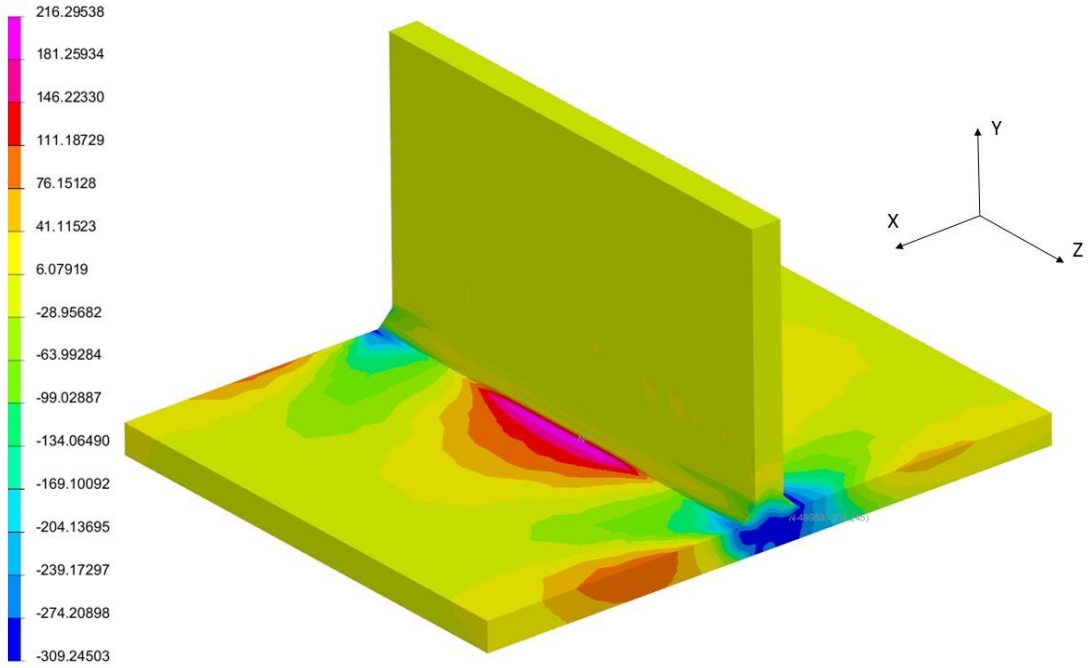

(a)

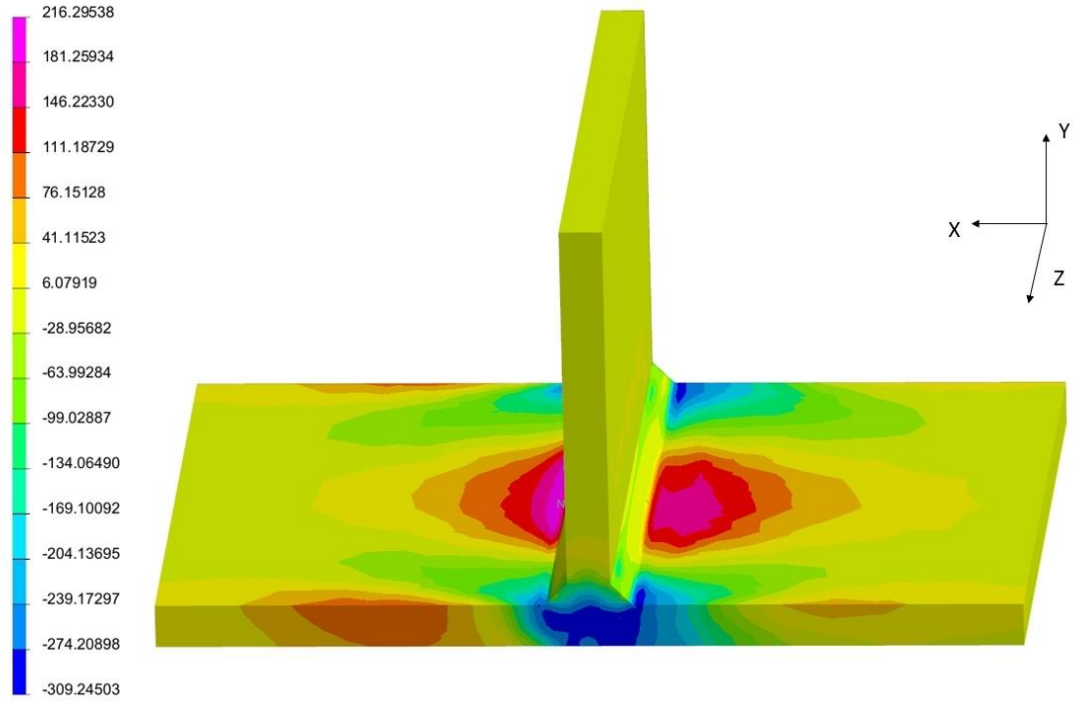

(b)

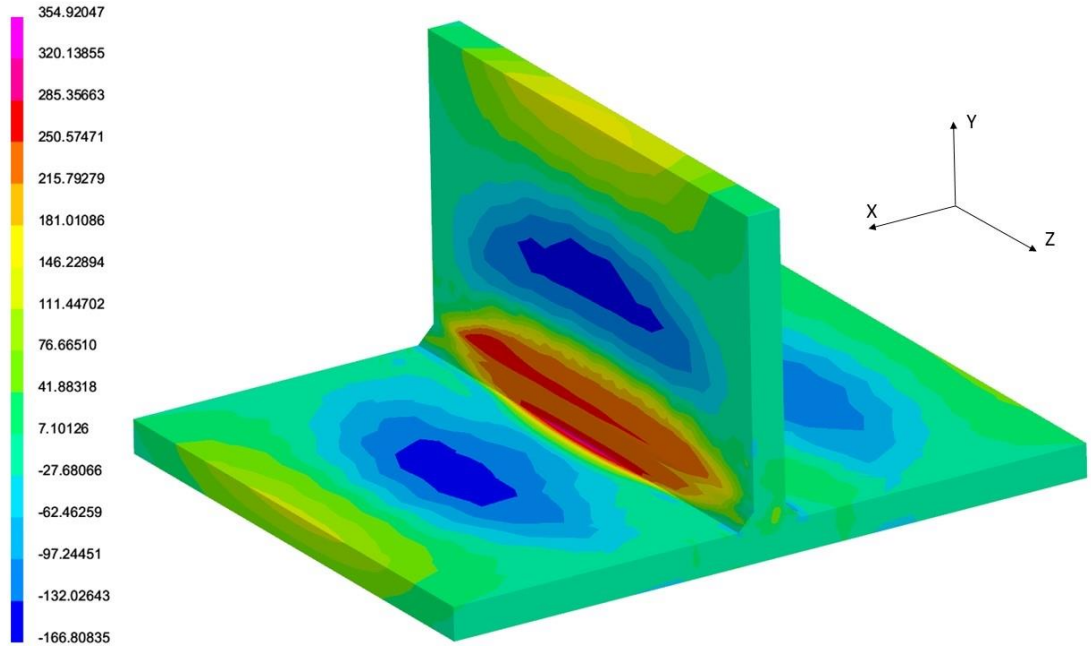
354.92047
320.13855
285.35663
250.57471
215.79279
181.01086
146.22894
111.44702
76.66510
41.88318
7.10126
-27.68066
-62.46259
-97.24451
-132.02643
-166.80835
Y
X
Z

(c)

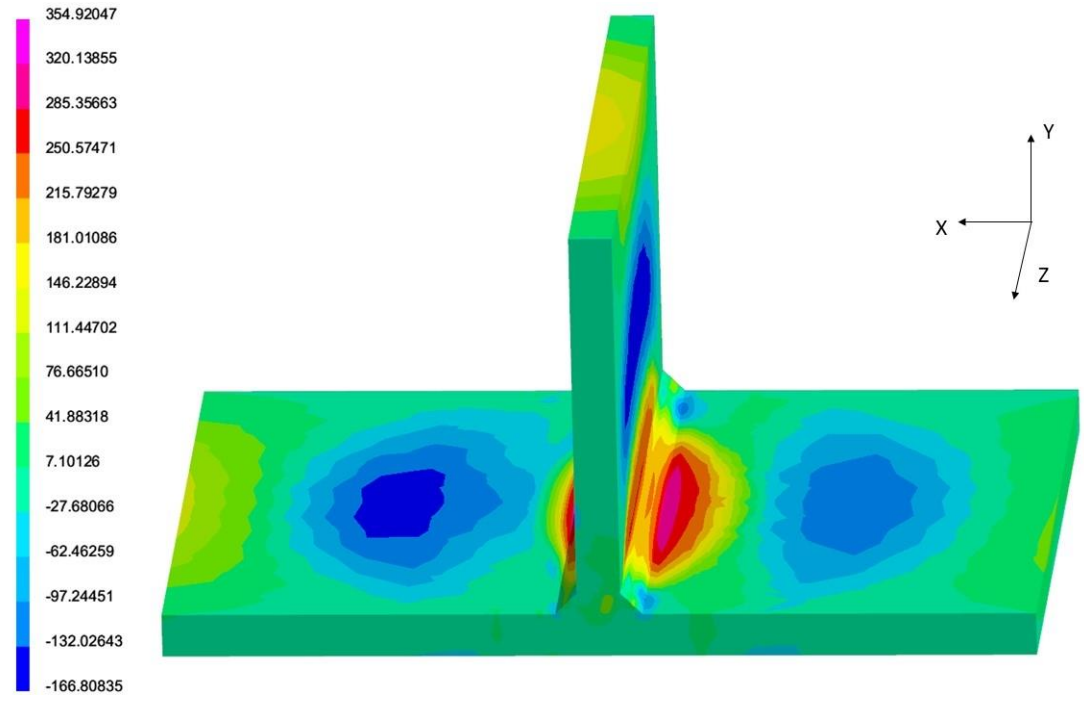
354.92047
320.13855
285.35663
250.57471
215.79279
181.01086
146.22894
111.44702
76.66510
41.88318
7.10126
-27.68066
-62.46259
-97.24451
-132.02643
-166.80835
Y
X
Z

(d)

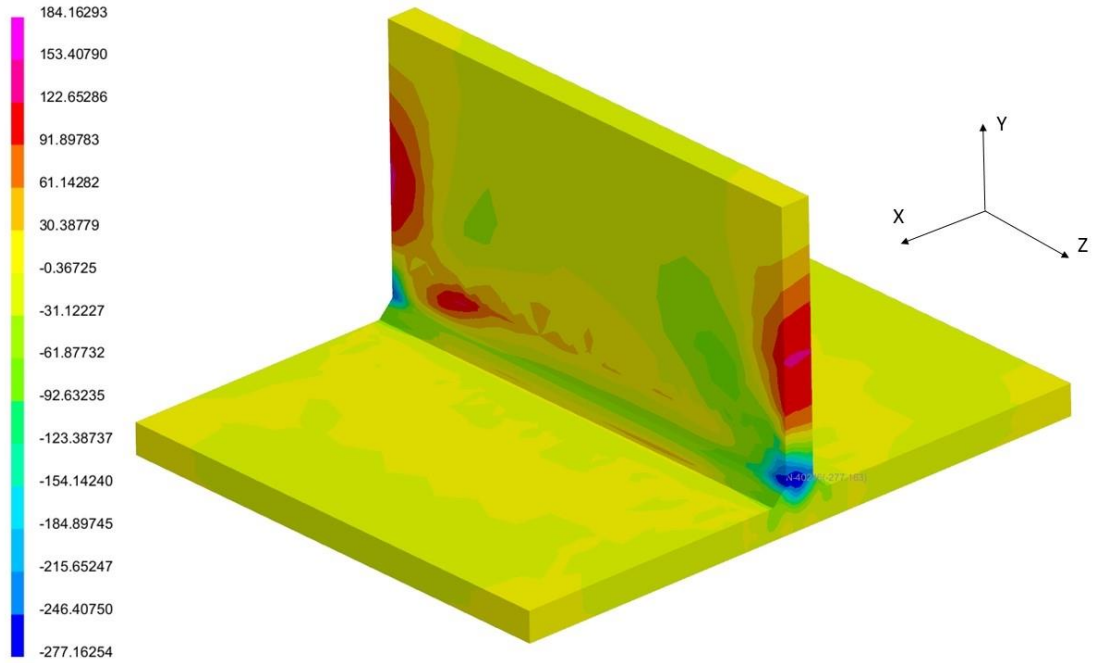

(e)

Figure 85. Welding residual stresses in T-joint welding: (a) Transverse stress (Normal stress in X) view 1; (b) Transverse stress (Normal stress in X) view 2; (c) Longitudinal stress (Normal stress in Z) view 1; (d) Longitudinal stress (Normal stress in Z) view 2; (e) Vertical stress (Normal stress in Y).

Multi-pass Welding

Figure 86(a)–(d) depict the temperature distributions in the multi-pass welding model. Figure 86 (a) shows the initial model setup, in which all weld elements are deactivated using the element birth and death technique prior to the start of the simulation. Figure 86 (b) and (c) display the temperature fields at two key moments: the beginning of the first weld pass and just before the completion of the final weld pass, respectively. Figure 86(d) presents the maximum temperature distribution recorded throughout the entire welding process. It clearly shows that the weld metal and the adjacent regions reach the melting temperature, confirming that sufficient fusion has been achieved at the weld, indicating effective welding.

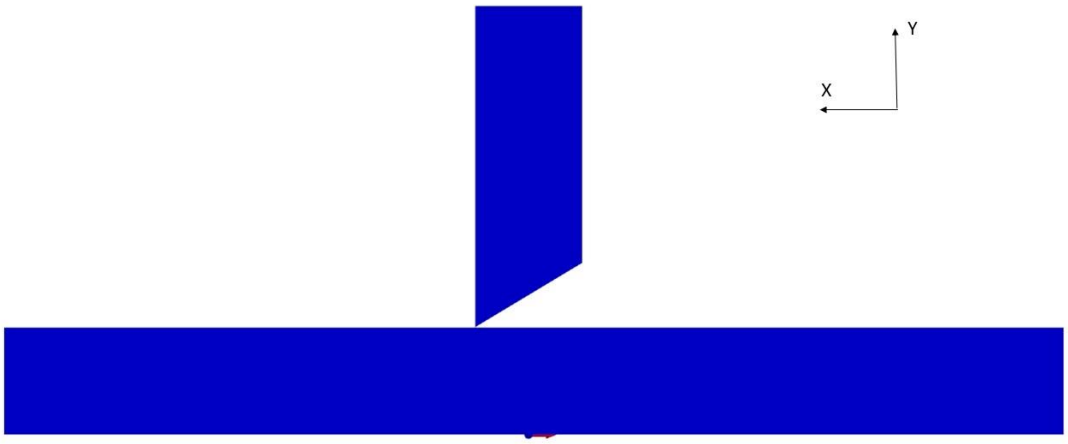
Y
X

(a)

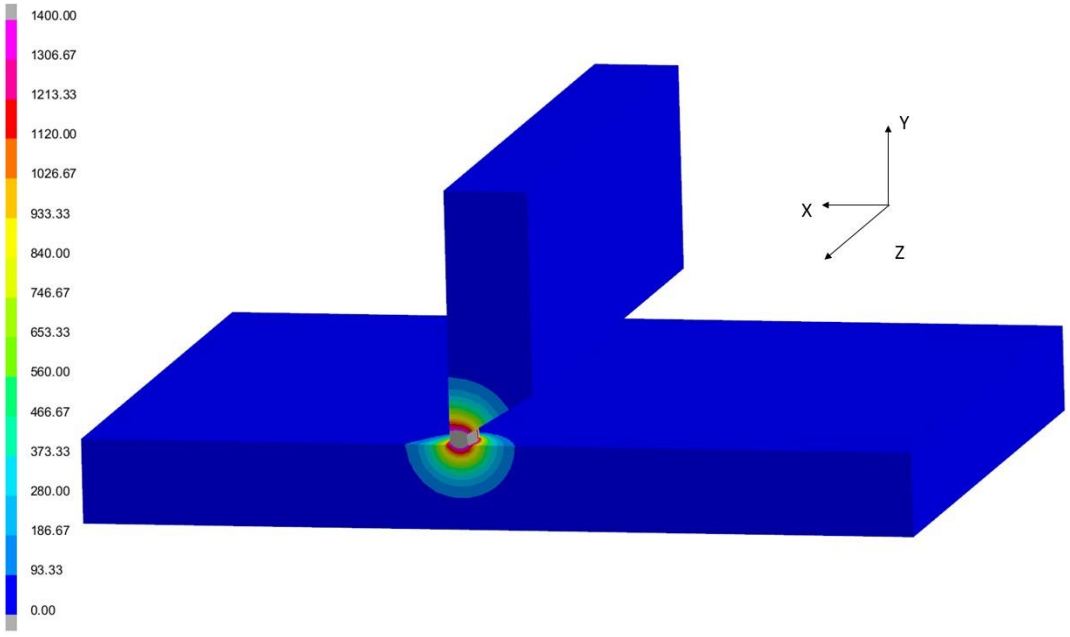
1400.00
1306.67
1213.33
1120.00
1026.67
933.33
840.00
746.67
653.33
560.00
466.67
373.33
280.00
186.67
93.33
0.00
Y
X
Z

(b)

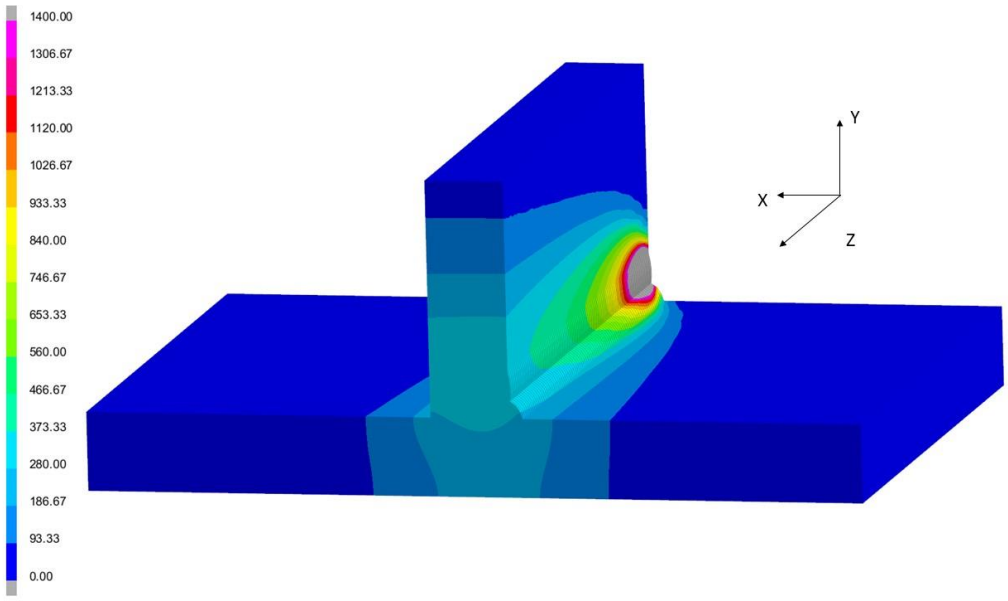

(c)

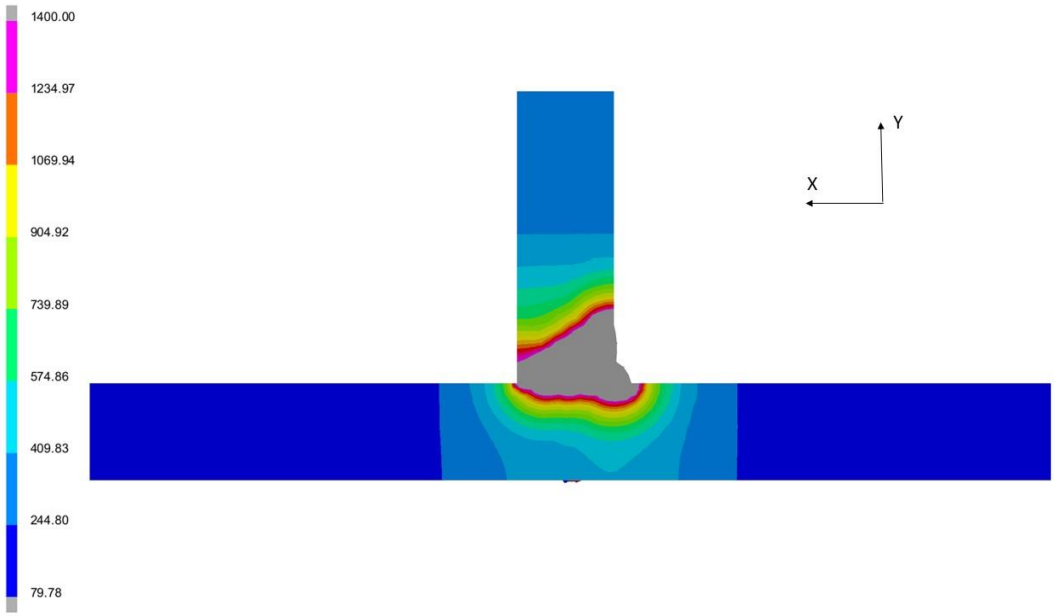

(d)

Figure 86. Temperature distribution in multi-passes welding: (a) Welding model at the starting stage; (b) First weld pass at the beginning; (c) Final weld pass at the ending; (d) The maximum overall weld passes.

Due to slight variations in the geometry and size of each weld pass in the model, the corresponding heat sources (double-ellipsoid heat) also differ in both shape and heat input

for each layer. To facilitate a more detailed examination of the stress distribution in the intermediate weld layers, a cross-section B–B, located at the mid of the web plate, is defined, as shown in the Figure 87.

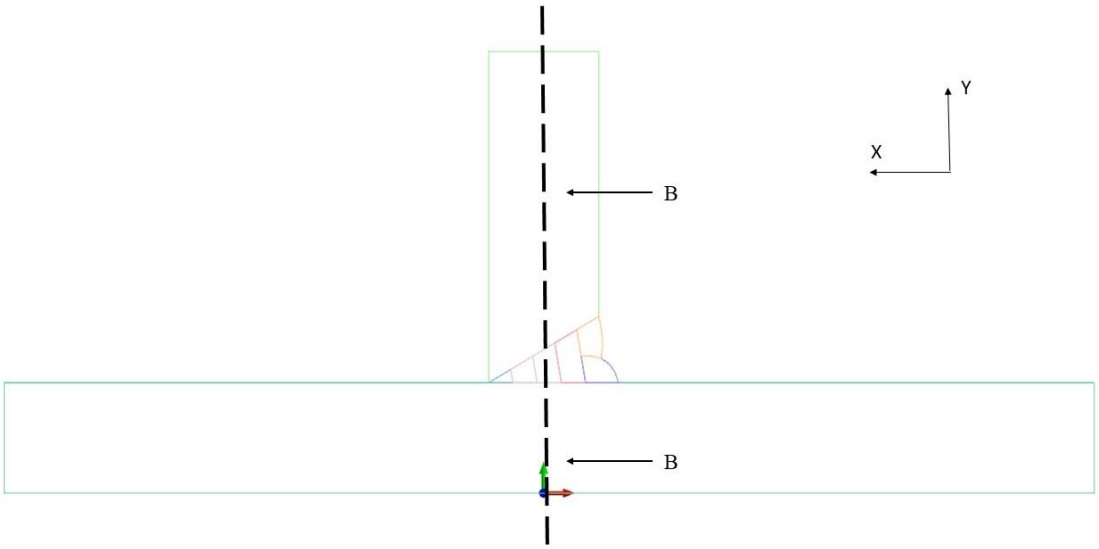

Figure 87. Cross-section B-B schematic.

Figure 88 and Figure 89 show the normal welding residual stresses in different directions, corresponding to cross-section B-B and the whole model, respectively. Given that the model is a multi-passes weld in a T-joint structure, the residual stress distribution is similar to that in the T-joint weld model. However, due to the increased web thickness in the multi-passed welded structure and the different heat inputs for the different passes, the tensile residual stresses induced by the previous passes will not be fully released during the subsequent welding process. As a result, the B-B sections show significant residual stresses in all three major directions, indicating the accumulation and retention of stresses throughout the multilayer overlay welding process.


374.79
279.18
183.57
87.95
-7.66
-103.27
-198.88
-294.49
-390.11
Y
Z

(a)

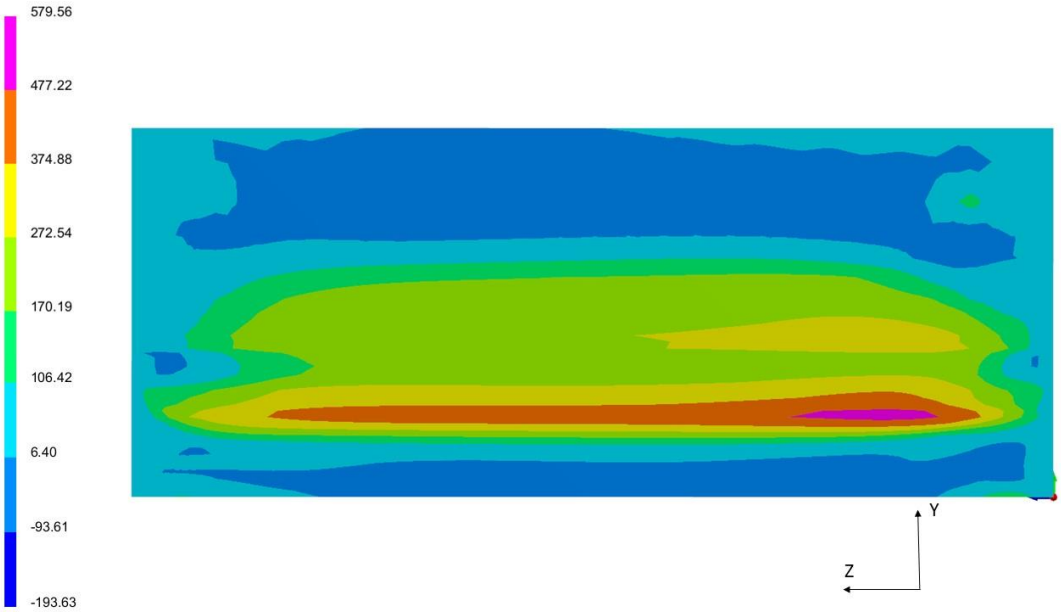
579.56
477.22
374.88
272.54
170.19
106.42
6.40
-93.61
-193.63
Y
Z

(b)

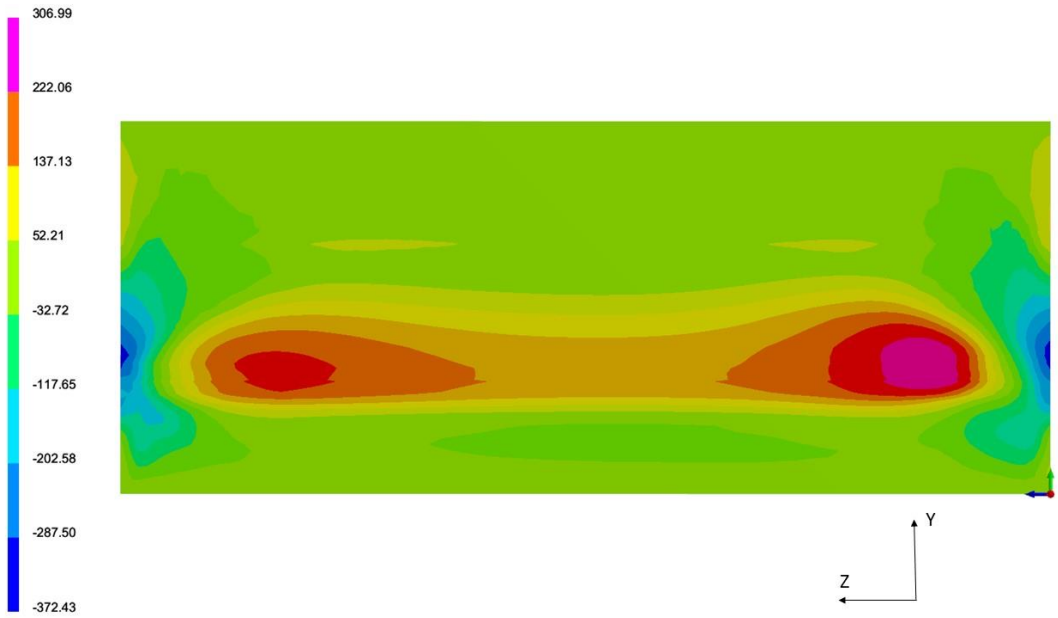

(c)

Figure 88. Normal welding residual stresses distribution on cross-section B-B: (a) Transverse stress; (b) Longitudinal stress; (c) Vertical stress.

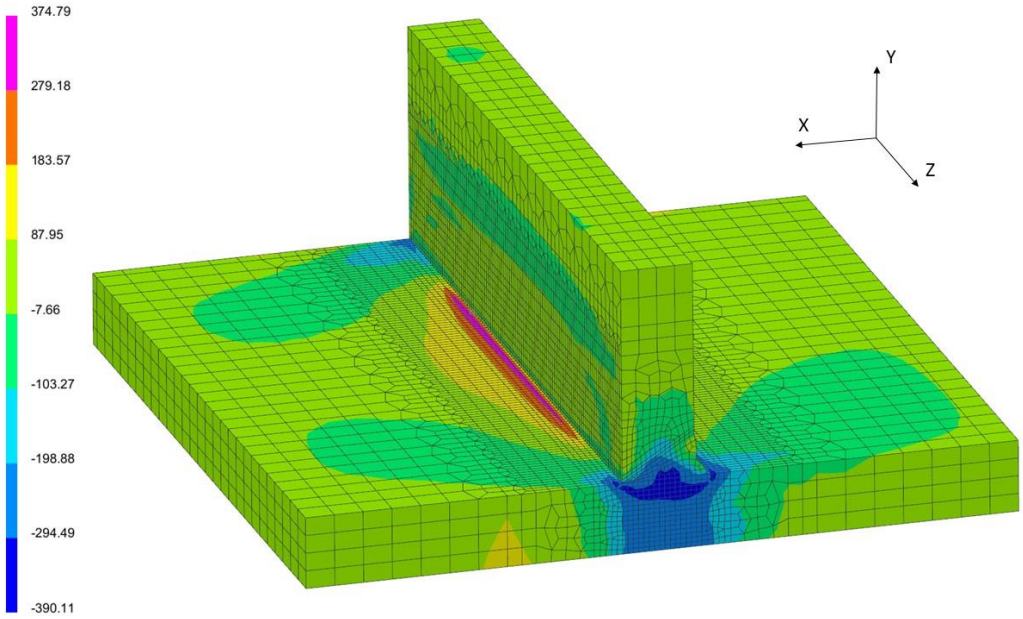

(a)

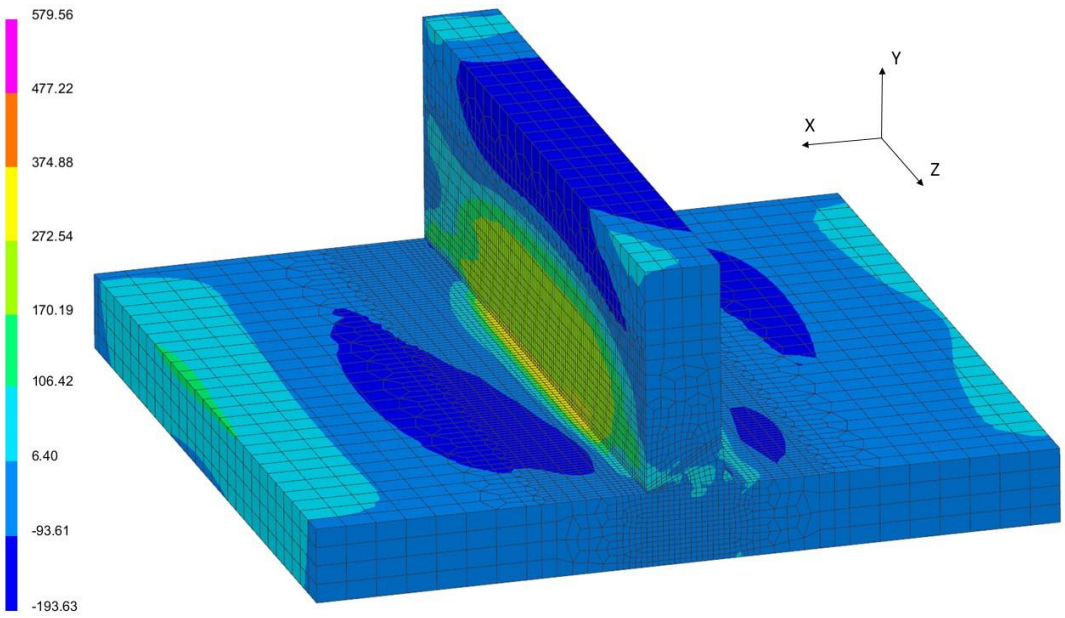

(b)

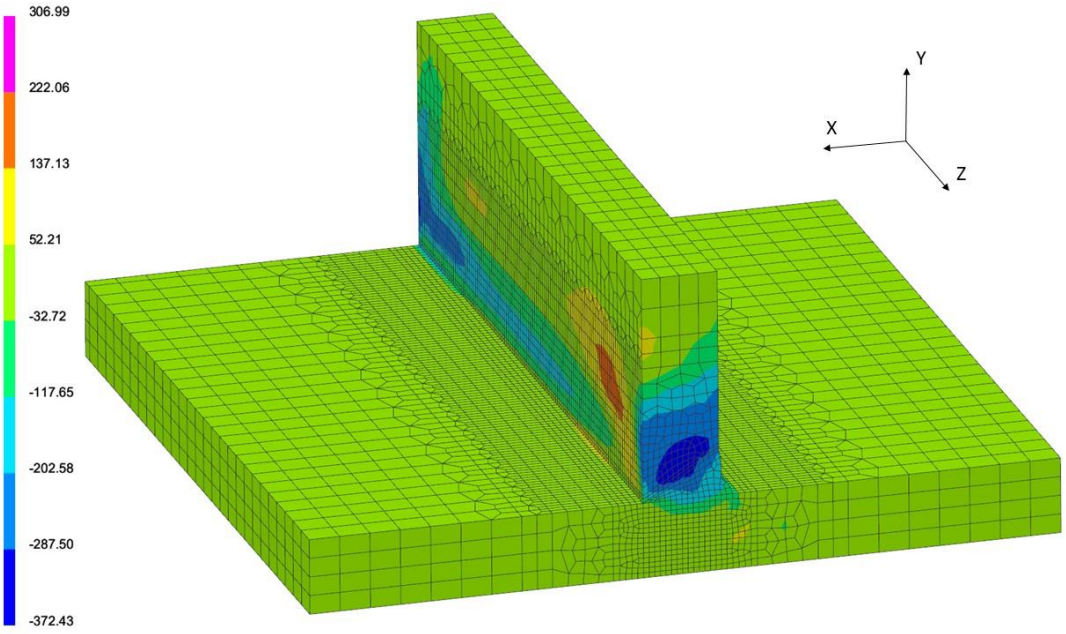

(c)

Figure 89. Normal welding residual stresses on the model: (a) Transverse stress; (b) Longitudinal stress; (c) Vertical stress.

3.6. Crack Propagation under Welding Residual Stresses Environment

This section presents the integration of fracture mechanics simulation with welding finite element analysis, enabling the investigation of crack propagation under the combined effects of welding residual stress and external mechanical loading. Since the welding simulation and the crack growth simulation are conducted in SYSWELD and SimModeler, respectively, the two finite element models differ significantly in terms of mesh, particularly in the cracked region. Therefore, to accurately apply the residual stress field obtained from SYSWELD to the crack growth model, it is necessary to map the stress data onto the nodes of the crack model prior to the start of the fracture simulation. The mapping procedure is based on spatial matching of node positions between the two models. When nodes in the source and target meshes do not coincide exactly but are sufficiently close, the stress values are transferred using shape functions and interpolation methods. After the mapping is completed, a stress rebalancing step is performed to ensure equilibrium in the target model. To maximize the fidelity of the mapped residual stresses, it is critical to maintain consistent boundary conditions between the source and target models. This stress mapping method is applied in both the T-joint welding model and the multi-pass welding model.

Mapping welding residual stresses

Figure 90(a)–(d) compare the model geometry and mesh structures used in SYSWELD and SimModeler, both of which share the same overall dimensions. In the SimModeler model, a finer mesh density is applied specifically in the weld region and its adjacent zones to more accurately capture the mapped welding residual stress field. When mapping results between two different software platforms, the transition areas of the model are susceptible to stress concentrations, especially where there are differences in mesh topology or element

interpolation. To mitigate this effect, the SimModeler model in this study incorporates rounded corners at the junction of the weld and the base plate. This geometric modification helps to smooth the stress transition, effectively reducing artificial stress concentrations and ensuring a more accurate and stable stress field in fatigue crack growth simulations.

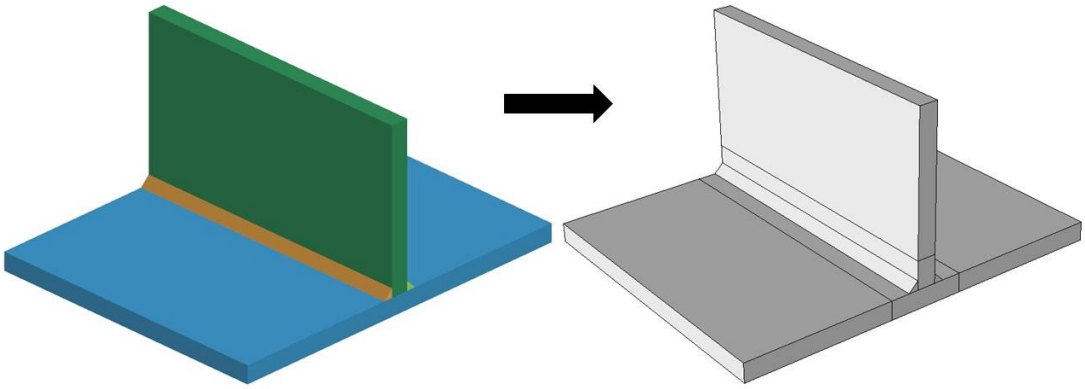

(a)

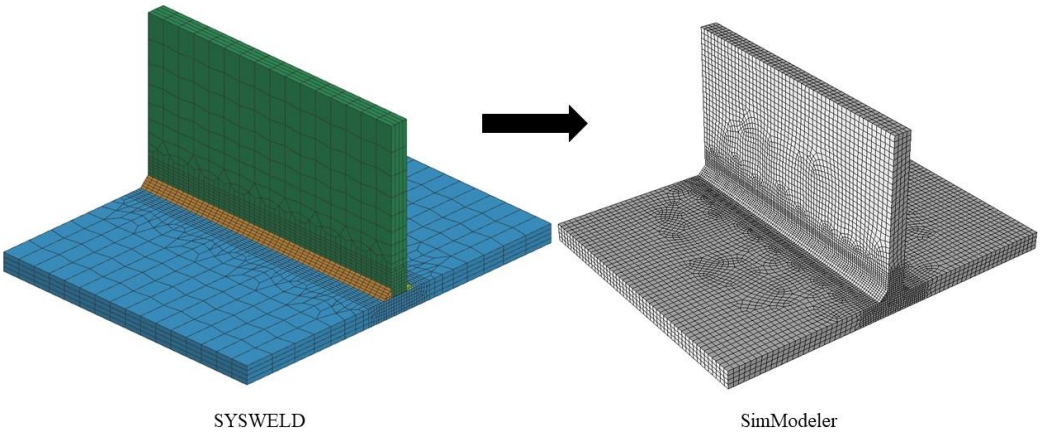

(b)

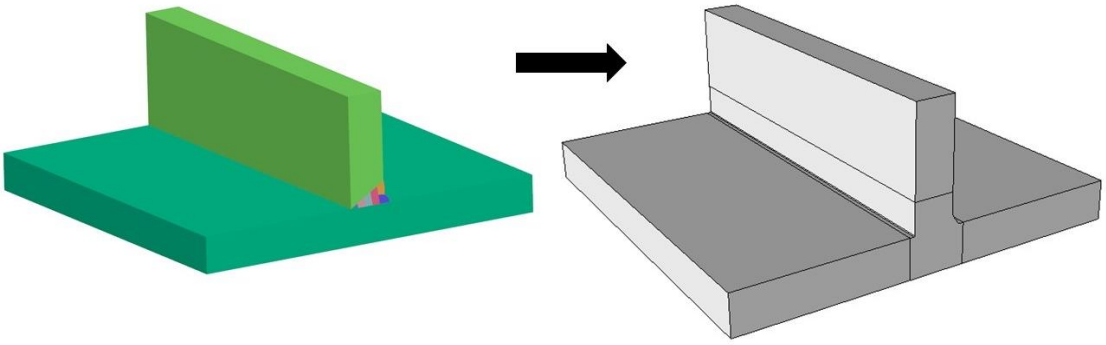

(c)

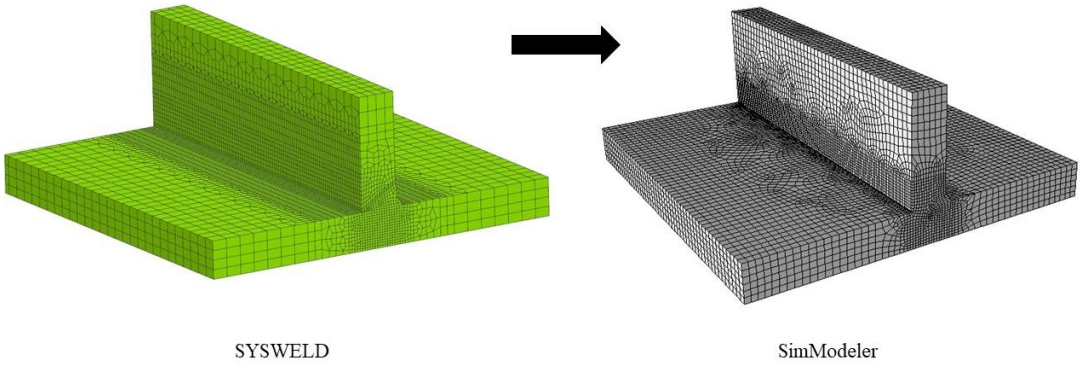

(d)

Figure 90. Model and mesh used in SYSWELD and SimModeler: (a) T-joint welding model; (b)T-joint welding mesh; (c) Multi-pass welding model; (d) Multi-pass welding mesh.

The Figure 91 presents the mapped normal stresses results in the three directions for both the T-joint welding model and the multi-pass welding model. Although there are some minor discrepancies in the stress distributions due to the mesh inconsistency between SYSWELD and SimModeler, the overall agreement of the mapped stress fields is highly satisfactory. Since the focus of this study is on the influence of welding residual stress on crack propagation, local stress accuracy in the vicinity of the crack front is of primary importance. As such, discrepancies in regions far from the crack are not critical to the objectives of this research and may be safely disregarded.

Table 9 lists the maximum tensile stresses in different directions for two welding models, joint welding and multi-pass welding, obtained from two different software platforms: SYSWELD and Ansys. The Table 9 also reports the mapping error after transferring the residual stress field between the two platforms. The results show that for both welding models, the mapping errors are within 2% for most directions, indicating a high degree of agreement between the mapped data and the raw stress data. The only exception is the vertical direction in the multi-pass welding model, where the maximum tensile stress error reaches 2.2%. This small deviation is mainly attributed to geometric adjustments in the SimModeler model, such as rounded transitions introduced to reduce stress concentrations. In addition, the simplification of the weld geometry in the multi-channel model may also contribute to the observed deviation. However, as mentioned earlier, this study focuses on the stress distribution near the crack front. Given that the stress fields mapped in these critical regions are in good agreement with the original results, the mapping accuracy is considered to be sufficient to meet the objectives of this study.

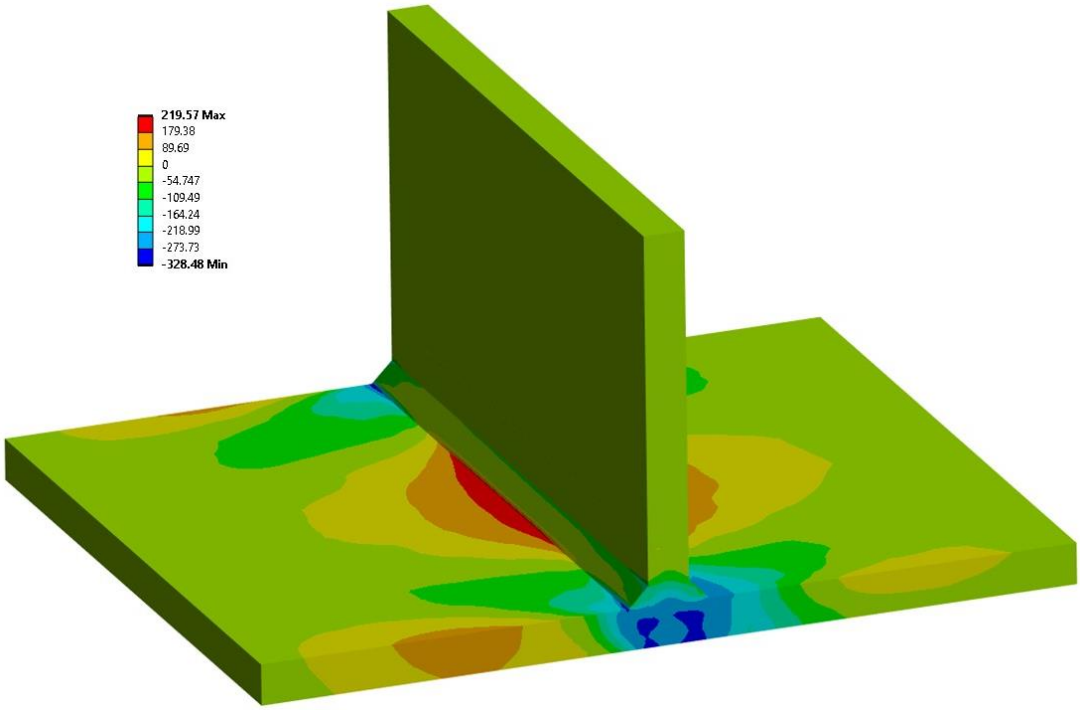
219.57 Max
179.38
89.69
0
-54.747
-109.49
-164.24
-218.99
-273.73
-328.48 Min

(a)

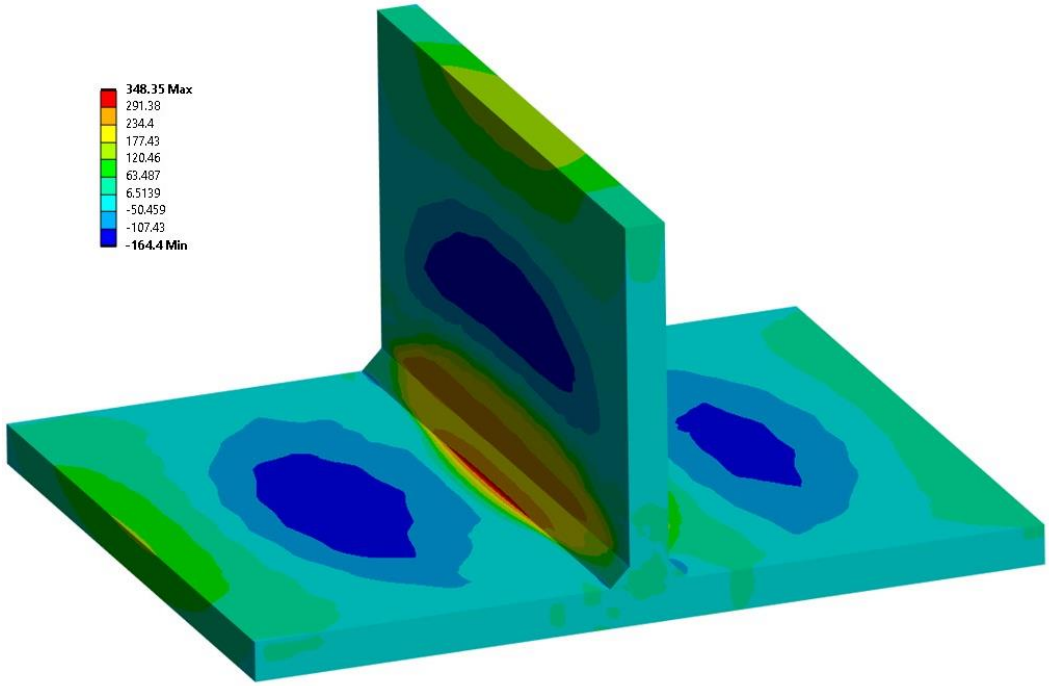
348.35 Max
291.38
234.4
177.43
120.46
63.487
6.5139
-50.459
-107.43
-164.4 Min

(b)

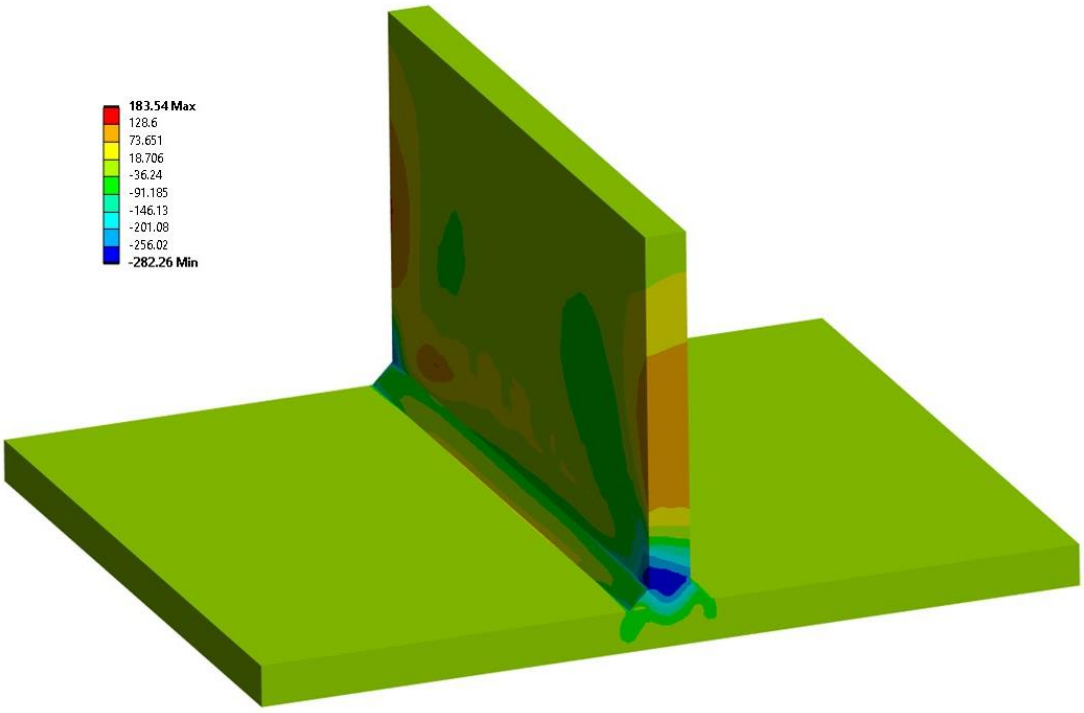
183.54 Max
128.6
73.651
18.706
-36.24
-91.185
-146.13
-201.08
-256.02
-282.26 Min

(c)

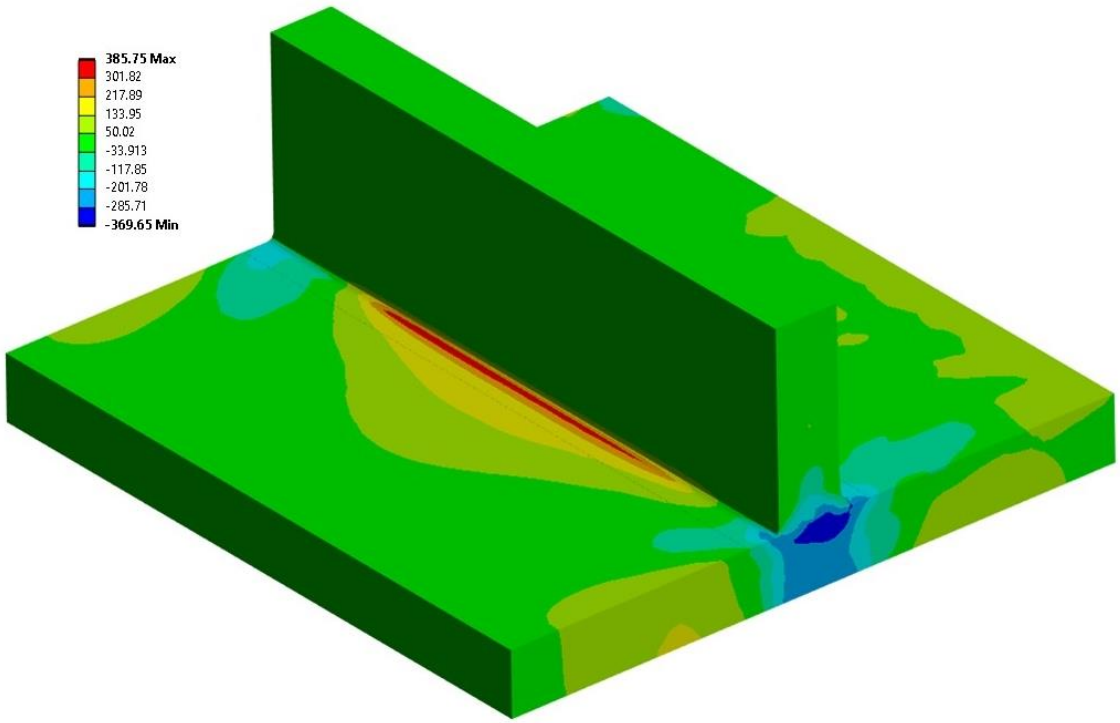
385.75 Max
301.82
217.89
133.95
50.02
-33.913
-117.85
-201.78
-285.71
-369.65 Min

(d)

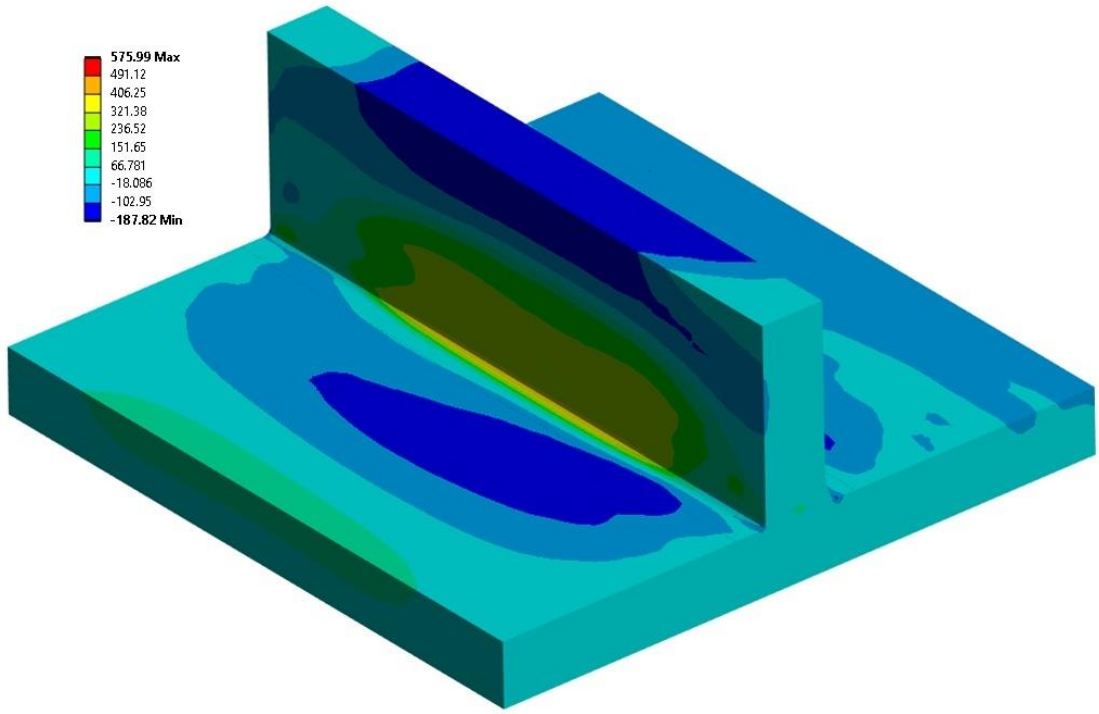
575.99 Max
491.12
406.25
321.38
236.52
151.65
66.781
-18.086
-102.95
-187.82 Min

(e)

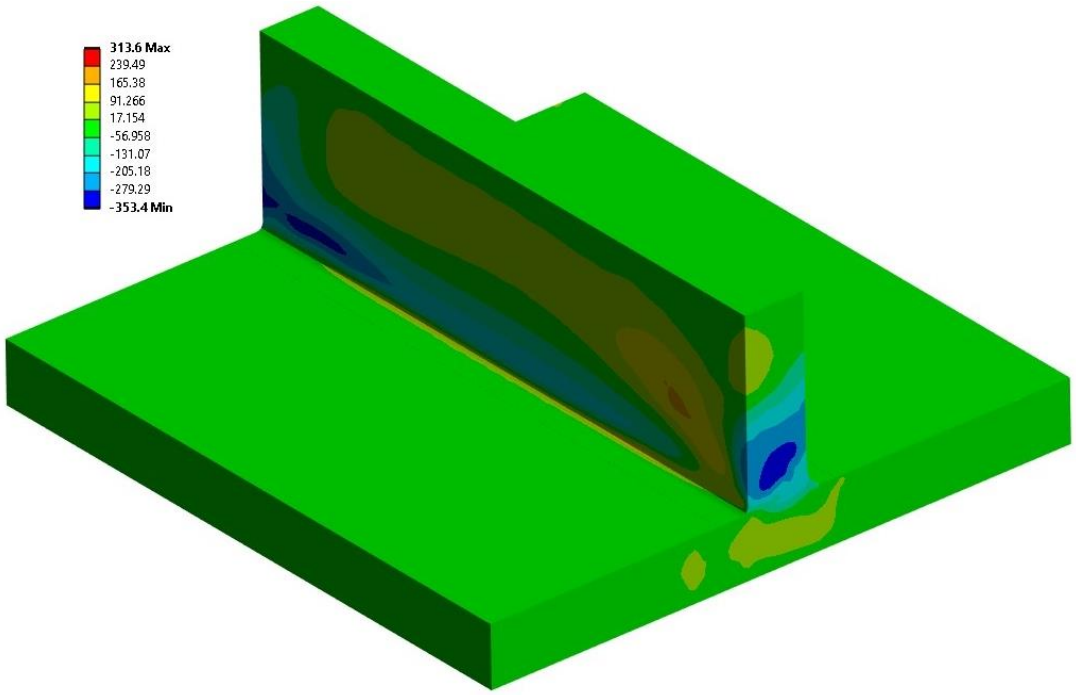

(f)

Figure 91. Mapped stresses results: (a) Transverse stress of T-joint welding; (b) Longitudinal stress of T-joint welding; (c) Vertical stress of T-joint welding; (d) Transverse stress of multi-pass welding; (e) Longitudinal stress of multi-pass welding; (f) Vertical stress of multi-pass welding.

Table 9. Errors of mapped maximum residual normal tensile stresses in different directions

	T-joint welding			Multi-pass welding		
Parameters	SYSWELD	Ansys	Error	SYSWELD	Ansys	Error
Transverse (MPa)	216.3	219.5	1.36 %	374.8	370.7	1.07 %
Longitudinal (MPa)	354.9	348.4	1.72 %	579.6	575.9	0.69 %
Vertical (MPa)	184.1	183.5	0.32 %	306.9	313.6	2.2%

Cracked model with residual stresses

Based on the boundary conditions and cyclic loading defined in Figure 20, the crack was localized such that the crack plane was parallel to the longitudinal direction and perpendicular to the transverse direction of weld models. The crack is located in the region showing the maximum transverse tensile residual stress to ensure that it is subjected to the most critical stress conditions in the fatigue crack extension analysis. Figure 92 shows the locations of the crack insertion determined from the residual stress distribution. In addition to the crack setup in the region of maximum transverse tensile stress, an additional crack is introduced in the stress transition region in each model, where the residual stress changes from tensile to compressive stress. With this setup, it is possible to investigate how the change of stress ratio (34) affects the growth behavior of fatigue cracks, especially in the region where the local stress state may change the crack growth rate or the direction of extension.

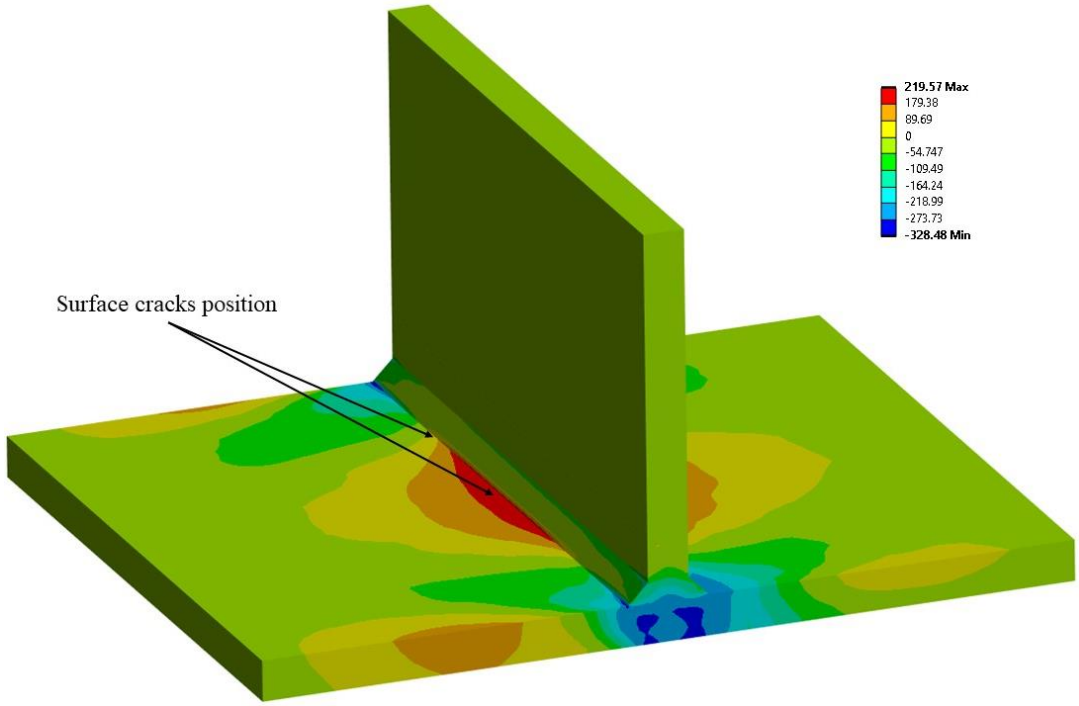

(a)

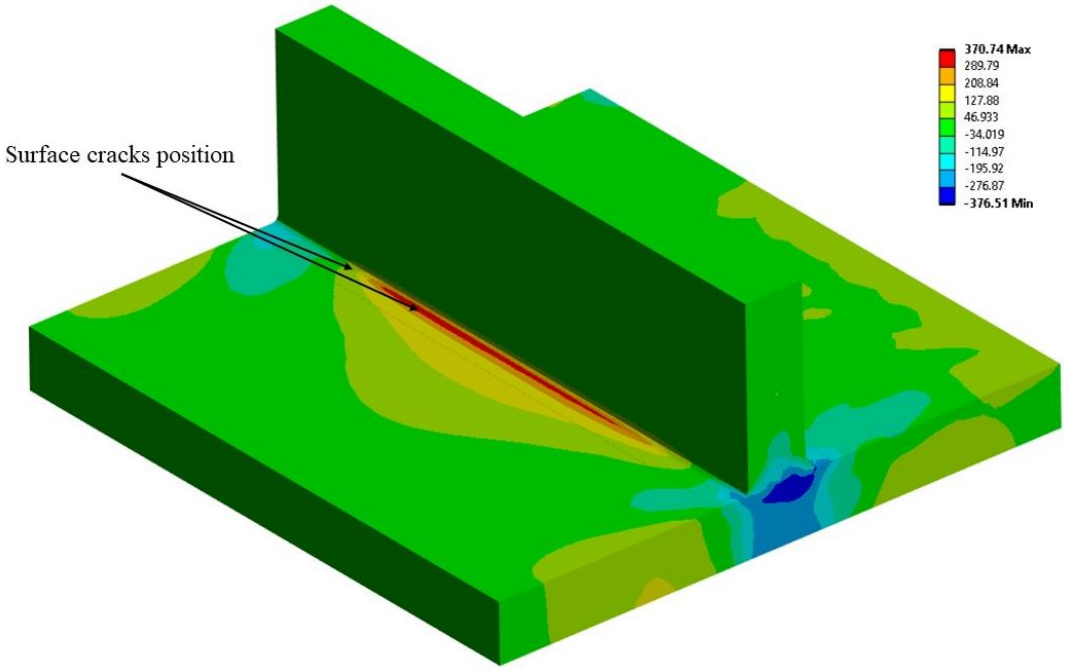

(b)

Figure 92. Cracks position in weld model: (a) Positions of crack in T-joint welding; (b) Positions of crack in Multi-pass welding.

Fatigue crack simulation in WRS environment

Figure 93 illustrates the location of the semicircular initial crack insertion in the T-joint welding and multi-pass welding models. The cracks are sequentially located at the following locations: the region of maximum residual stress in the T-joint welding model, the region of maximum residual stress in the multi-pass welding model, the region of minimum residual stress in the T-joint welding model, and the region of minimum residual stress in the multi-pass welding model. The purpose of inserting cracks at these specific

locations is to investigate the effect of residual stress and the corresponding stress ratio R on the fatigue crack growth behavior.

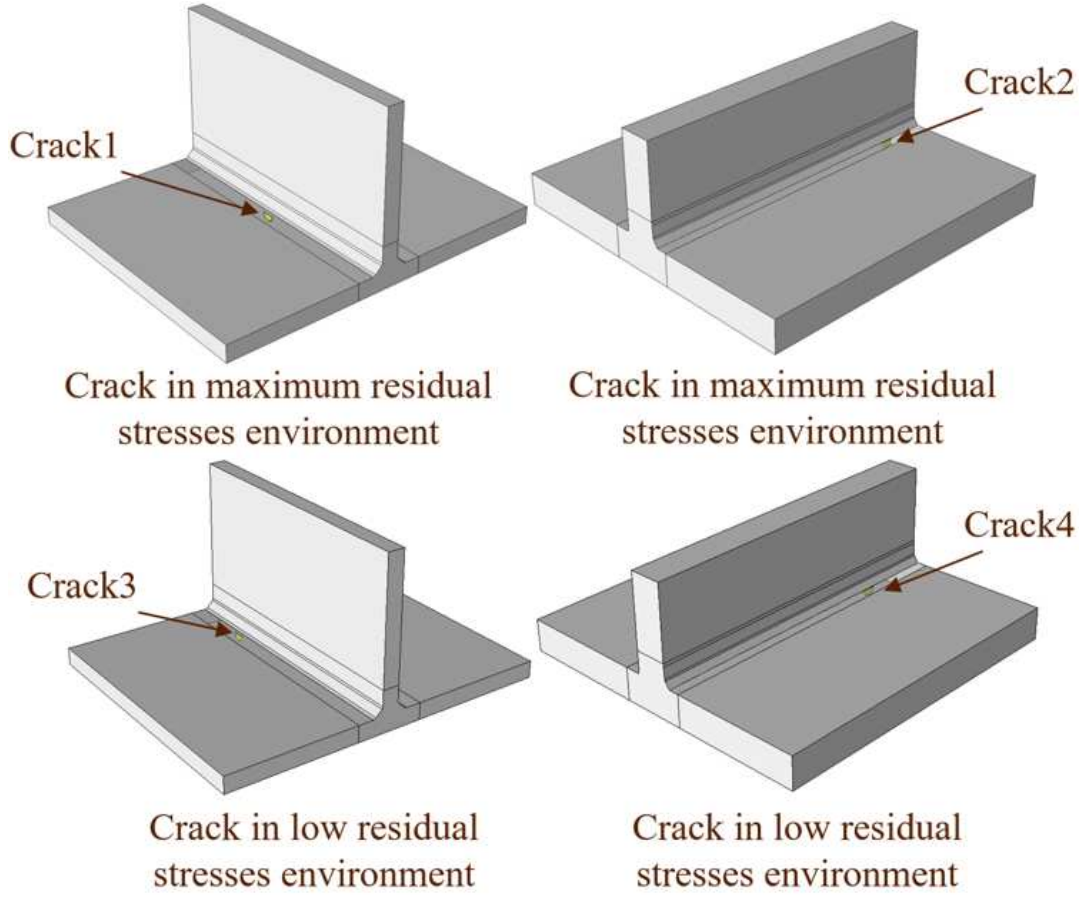

Figure 93. Cracks order in welding models.

Figure 94, Figure 97, Figure 100, and Figure 101 present the fatigue crack growth simulation results for Cracks 1 to 4 under different fatigue growth criteria, with each figure including both the front view and the side view of the crack surfaces. The target crack extension length is set to 4.75 mm. Figure 95 and Figure 99 show the initial Stress Intensity Factor (SIF) distributions for Crack 1 and Crack 3, respectively. From Figure 94 and Figure 95, it can be observed that, because the Walker equation also utilizes ΔK as a basis for crack growth calculation, the SIF distributions in Figure 95(a) and (c) are identical. However, the Walker equation additionally accounts for the influence of the stress ratio R,

as shown in Figure 96. In this figure, the maximum R ratio occurs at the two ends of the crack front, resulting in faster crack growth at the crack ends in Figure 94(c) compared to (a), thus producing a noticeable difference in crack shape evolution. On the other hand, in Figure 95(b), which is based on the maximum stress intensity factor K_{max} criterion, the maximum K_I reaches up to 400 at the ends of the crack front.

Since Crack 2 is inserted into a region of maximum tensile residual stress, similar to Crack 1, the crack growth behavior shown in Figure 97 exhibits a pattern that is quite similar to that observed for Crack 1. Both cracks experience accelerated growth at the regions corresponding to higher stress intensity factors, influenced by the combined effects of welding residual stresses and cyclic external loading. As a result, the overall crack front evolution and growth characteristics under different fatigue crack growth criteria are notably consistent between the two cases.

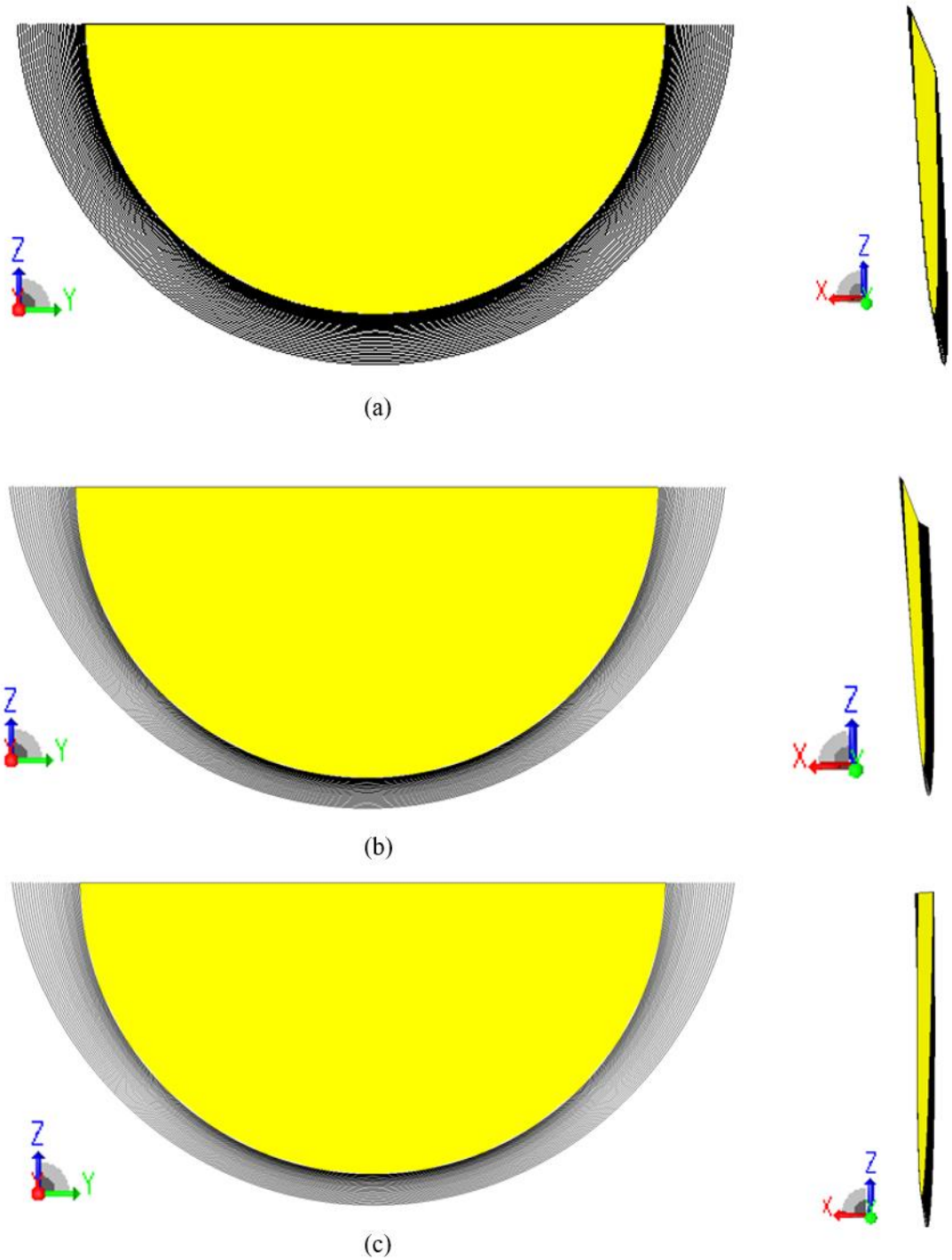

Figure 94. Fatigue crack simulation results of crack1 in different criteria: (a) Paris Law based on ΔK; (b) Paris Law based on K_{max}; (c) Walker equation.

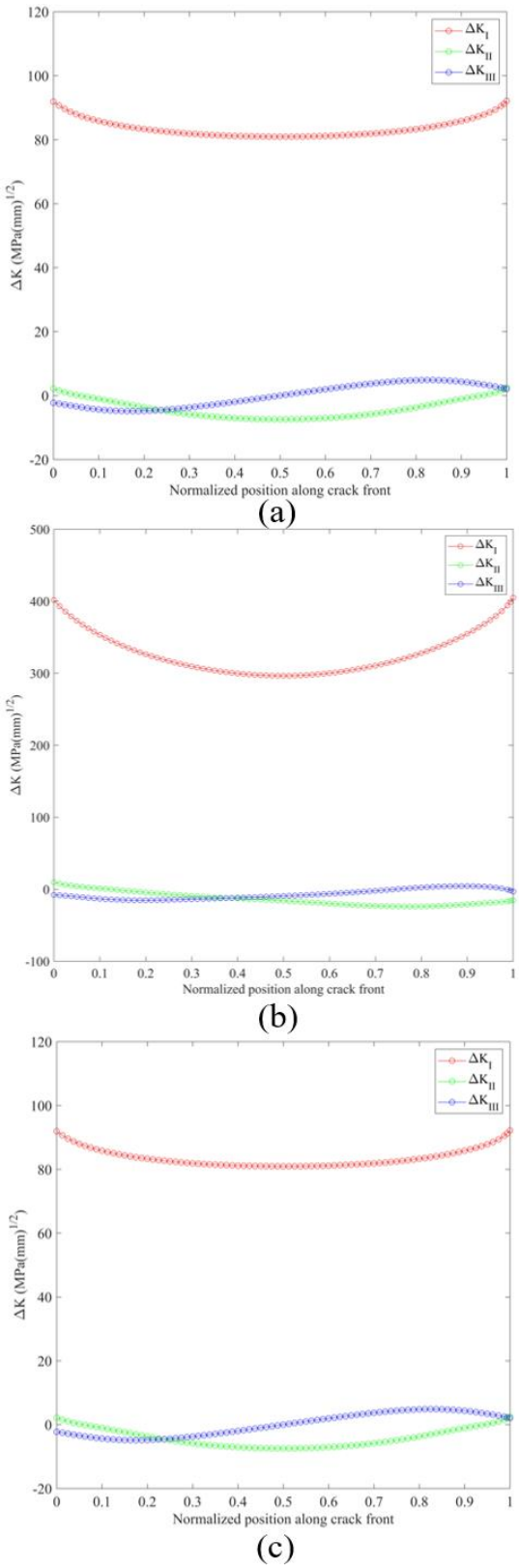

Figure 95. SIFs along the initial crack front of crack1 results: (a) Paris Law based on ΔK; (b) Paris Law based on K_{max}; (c) Walker equation.

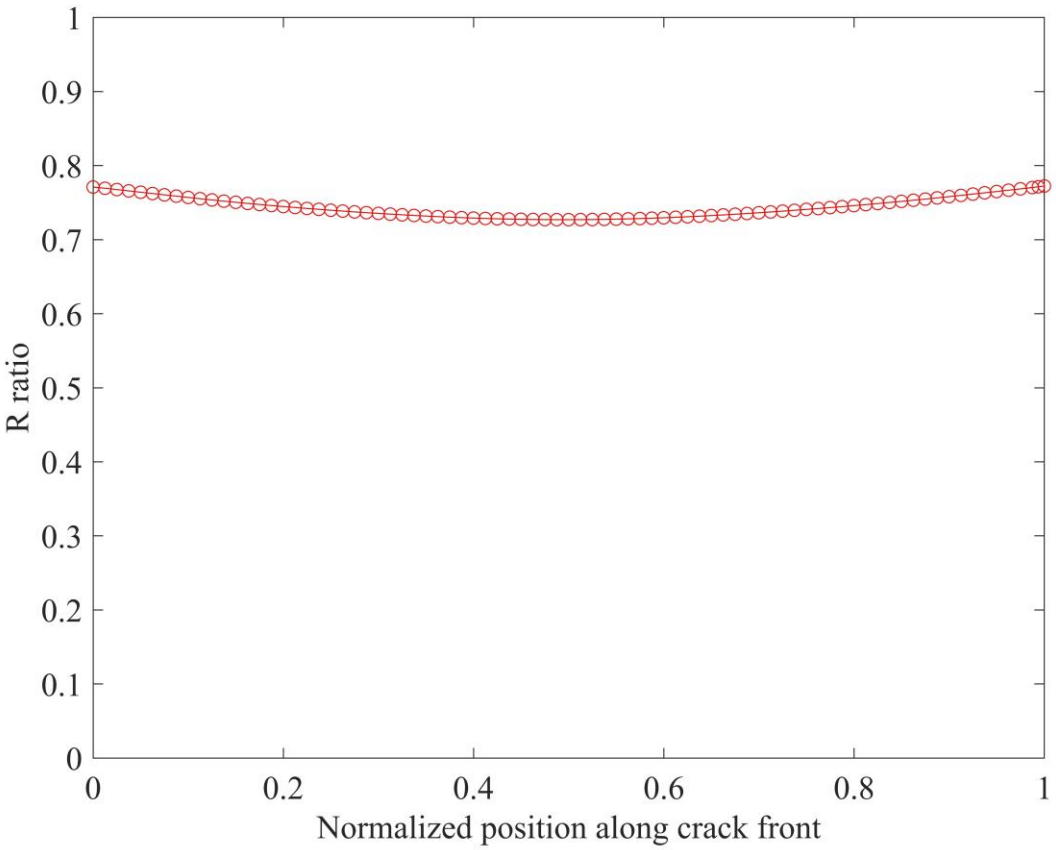

Figure 96. *R* ratio along initial crack front of crack1.

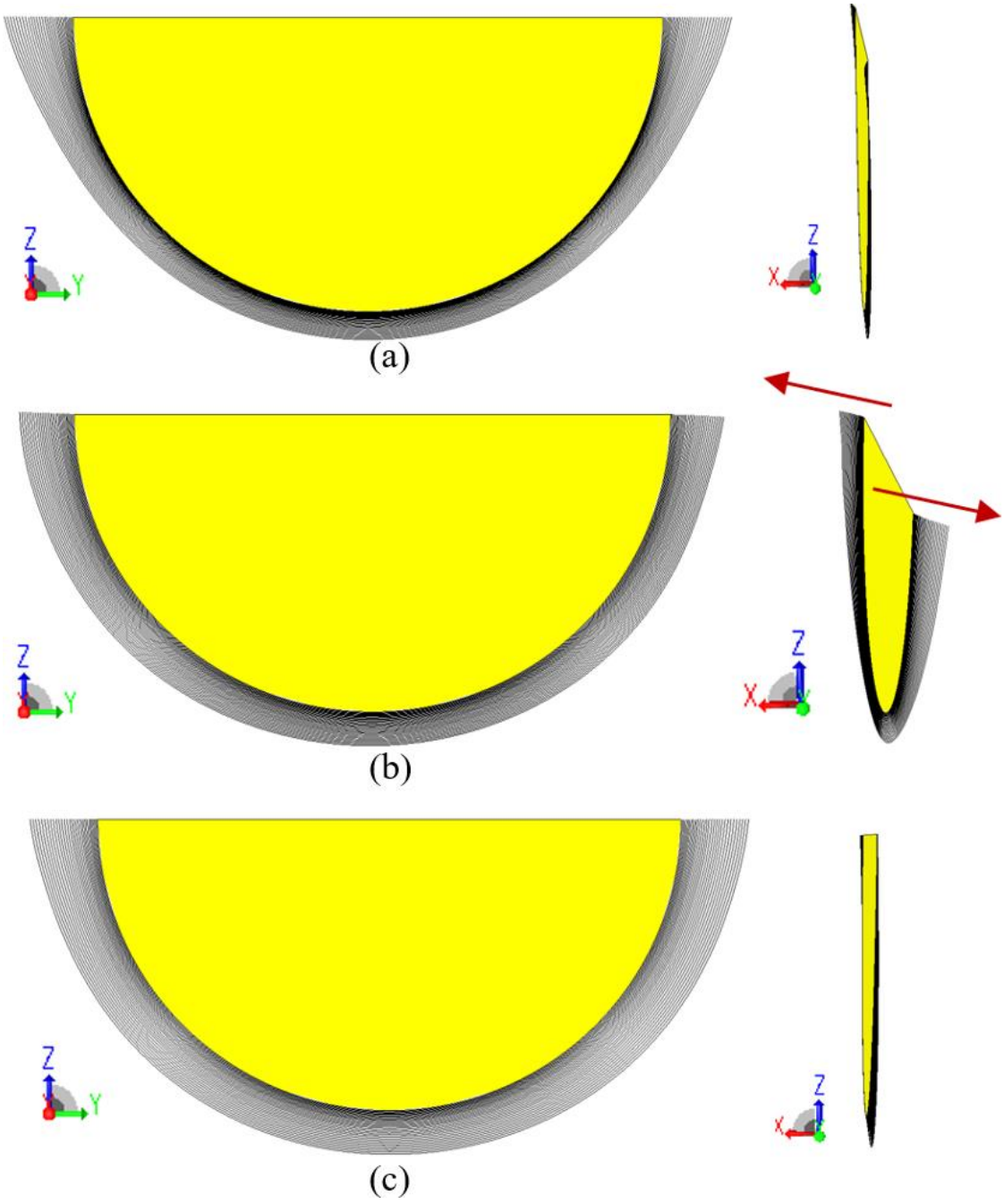

Figure 97. Fatigue crack simulation results of crack2 in different criteria: (a) Paris Law based on ΔK; (b) Paris Law based on K_{max} ; (c) Walker equation.

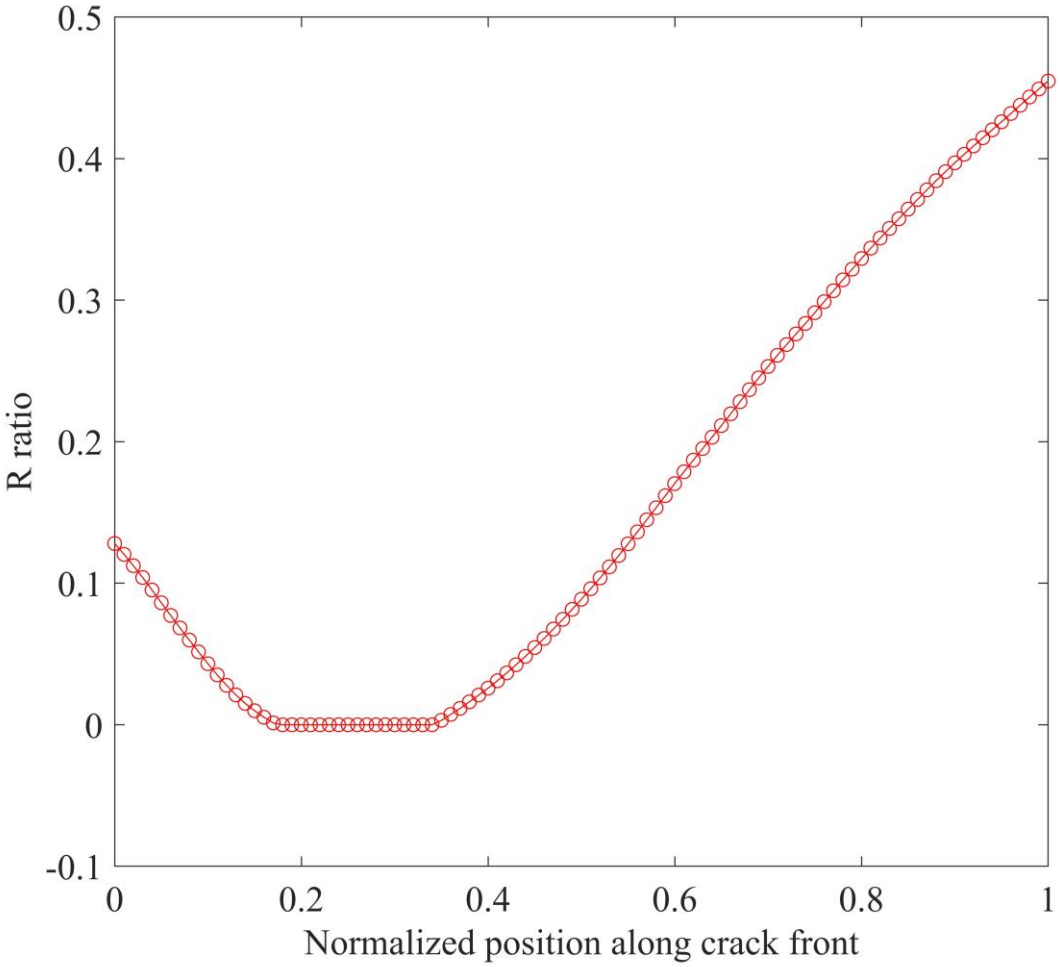

Figure 98. *R* ratio along initial crack front of crack3.

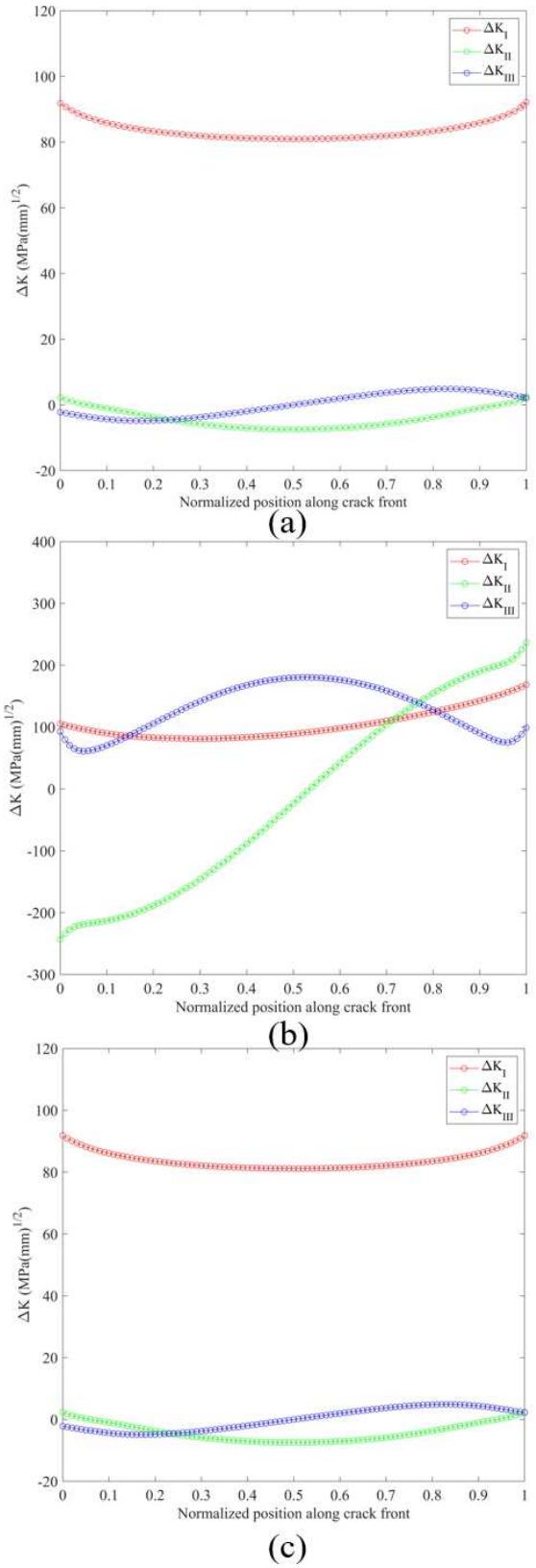

Figure 99. SIFs along the initial crack front of crack3 results: (a) Paris Law based on ΔK; (b) Paris Law based on K_{max}; (c) Walker equation.

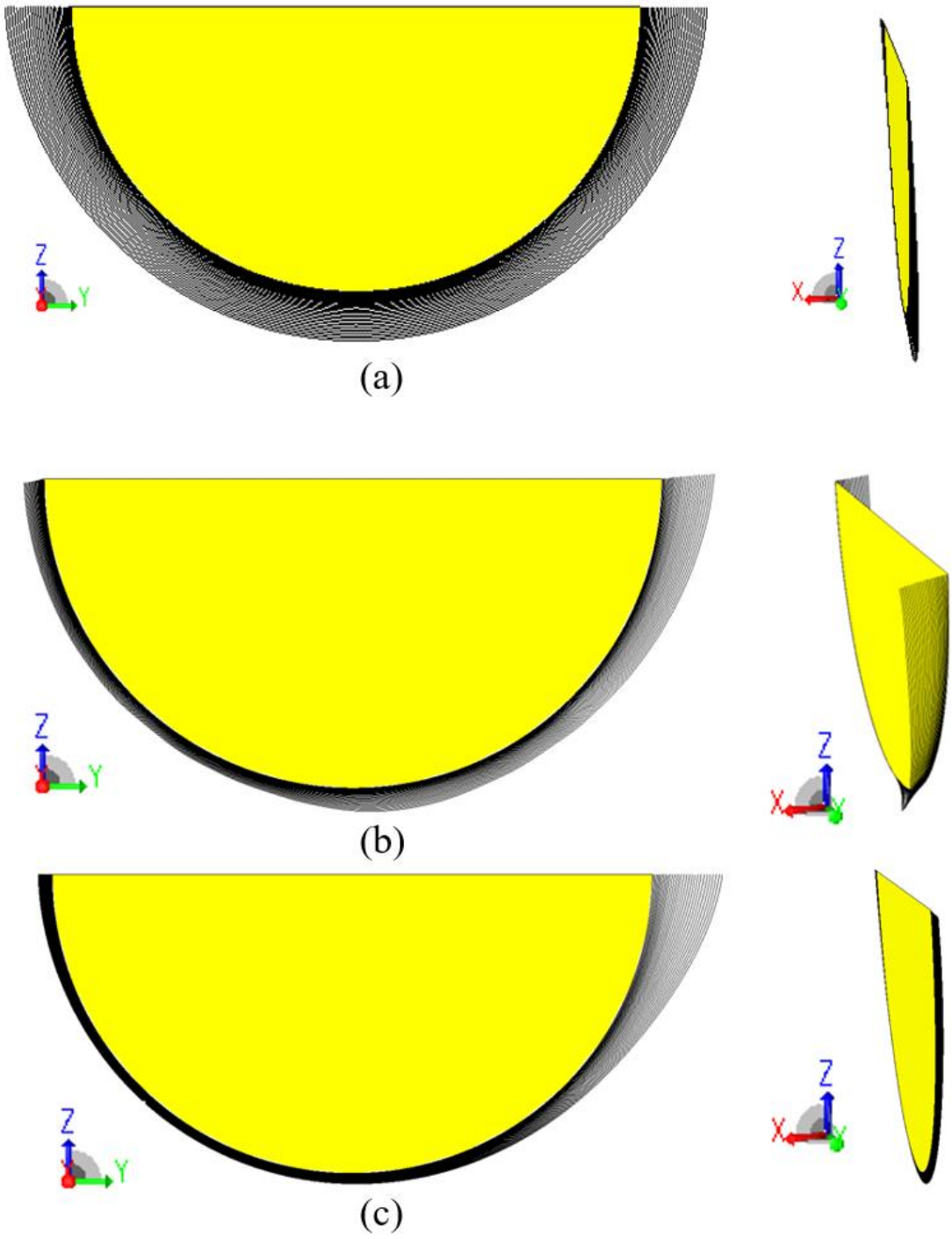

Figure 100. Fatigue crack simulation results of crack3 in different criteria: (a) Paris Law based on ΔK; (b) Paris Law based on K_{max}; (c) Walker equation.

Unlike Crack 1 and Crack 2, which were inserted into regions of high residual tensile stress, Crack 3 and Crack 4 were placed in regions of relatively low residual stress. As a result, their crack growth behavior is dominated by the cyclic external loading, as shown in Figure 100 and Figure 101. From Figure 100(a), it can be observed that under the traditional Paris Law, which considers only ΔK, the crack growth behavior remains largely unaffected by the residual stress field. As long as the cyclic external load remains unchanged, the final crack growth results show minimal variation, regardless of the crack's initial location. In contrast, Figure 100(b) reveals that, since cyclic loading dominates crack propagation in this case, the crack grows at a much steeper angle. This behavior is consistent with Figure 99(b), where K_{II} at the crack tips exceeds K_I , driving the crack propagation in a mixed-mode loading. By further analyzing Figure 98, Figure 99(c), and Figure 100(c), it can be concluded that in regions with low and rapidly varying residual stresses, the stress ratio R has a more pronounced effect on crack growth. Although K_I at both crack tips in Figure 99(c) has similar magnitudes, the right crack tip experiences a higher R ratio. Consequently, as shown in Figure 100(c), crack growth is primarily concentrated at the right tip, highlighting the strong influence of the stress ratio in low residual stress environments.

In addition, it is commonly assumed that cracks can only propagate under tensile stress. However, in practice, crack growth can also occur under compressive cyclic loading, provided that tensile residual stresses exist around the crack tip.

During cyclic compressive loading, the crack surfaces initially close due to the applied external force. Nevertheless, as the load cycle progresses, the tensile residual stress

surrounding the crack tip can reopen the crack, thereby completing a full opening–closing cycle and leading to fatigue crack propagation.

Figure 102 and Figure 103 illustrate the simulation results of crack growth under compressive cyclic loading, and the distributions of the initial Stress Intensity Factors (SIFs) and stress ratio R at the crack tip, respectively. The Walker equation is employed as the fatigue crack growth criterion for these simulations.

The results demonstrate that the crack can successfully propagate under such conditions. For this type of model, the maximum stress intensity factor is generated solely due to the residual stress field, while the minimum stress intensity factor occurs during the phase when external compressive loads are applied. This behavior highlights the important role of residual tensile stress in driving crack growth, even in environments dominated by compressive external loading.

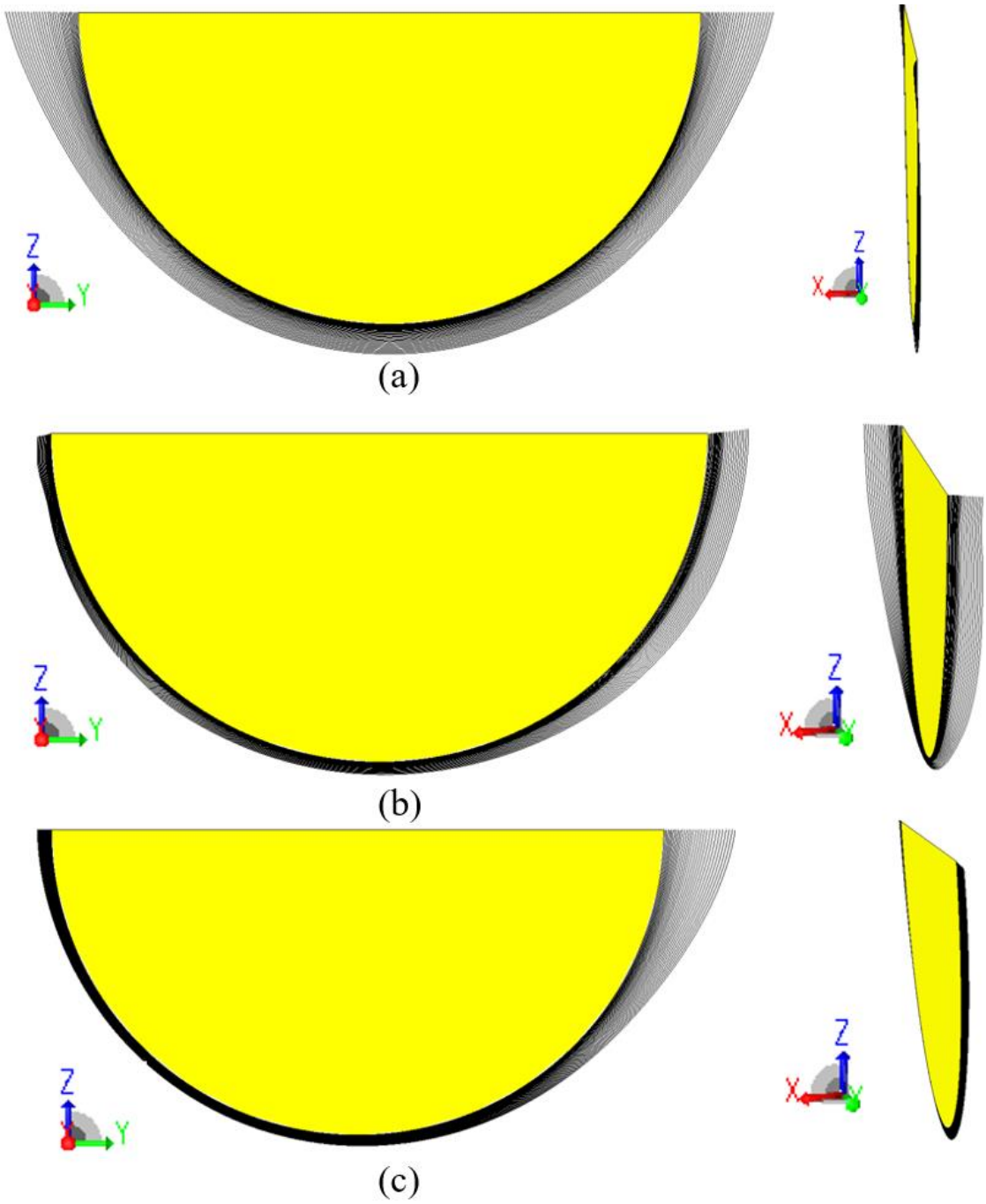

Figure 101. Fatigue crack simulation results of crack4 in different criteria: (a) Paris Law based on ΔK; (b) Paris Law based on K_{max}; (c) Walker equation.

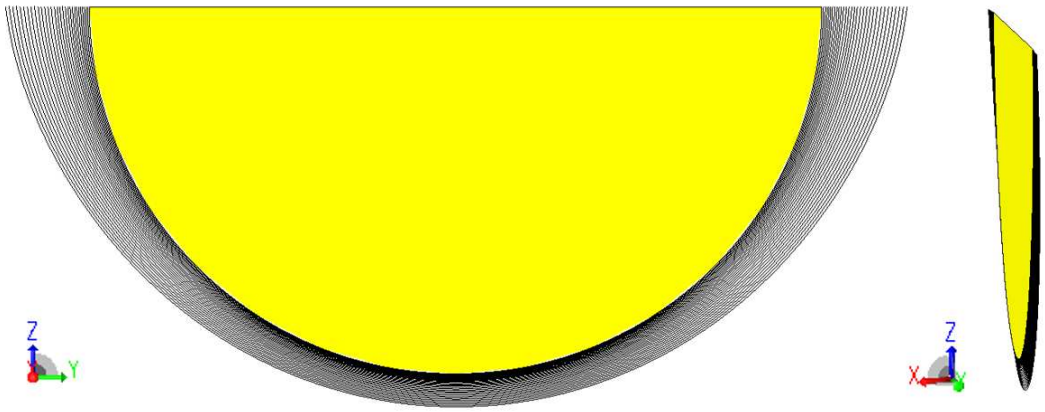

Figure 102. Fatigue crack growth under compression for crack1.

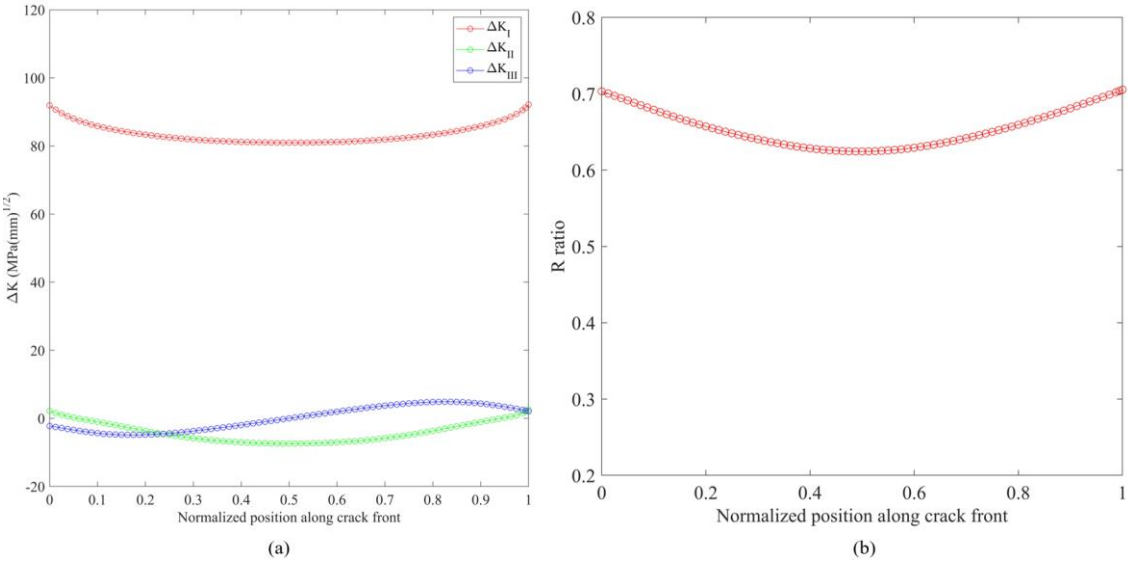

Figure 103. Fatigue crack growth data along the initial crack front: (a) SIFs value; (b) R ratio.

4. Conclusion and Future work

Cylinders with small preexisting flaws on the outer radial surface often exhibit crack growth in either a subcritical manner, or sudden catastrophic fracture due to a single applied critical torque. It is shown that small surface cracks will grow in a very predictable manner perpendicular to the maximum principal stress on the cylindrical surface when subjected to a pure torque. As the crack grows from a small surface flaw, the fracture surface assumes a more complex, spiral shaped, 3-D geometry. The evolving shape of the crack surface can be determined incrementally based on the asymptotic stress state characterized by the stress intensity factors K_I, K_{II}, K_{III}. In this study, the 3-D fracture surfaces for a solid cylinder and two hollow cylinders, subjected to pure torsion, were generated. The predicted results based on the crack growth simulations were shown to very closely match the fracture surfaces obtained from torsion tests performed on PMMA acrylic cylinders. The computed stress intensity factors obtained in this study are also given as polynomial curve fits as a function of crack length. Using the results generated in this study in their empirical form, fatigue crack growth predictions for cylinders subjected to alternating torsional loads can be performed for a variety of suitable crack rate growth laws, without repeating the detailed finite element simulations described in this paper. Of particular interest in this study is the secondary cracking that occurs in hollow cylinders after a spiral crack has propagated circumferentially ~340°. Because of the shift in the center twist as the spiral crack grows in length, very high circumferential tensile stresses develop on the inner wall of a hollow cylinder containing a spiral crack. The circumferential stresses result in the formation of a secondary crack that connects the separate spiral crack fronts. The final result is a fracture

surface that exhibits a very sharp point close to the end of the spiral crack. This does not occur in solid cylinders subjected to torsion.

In addition, a straightforward least squares procedure was described for the extraction of displacements and the determination of the center of twist for 3D structures subjected to an applied torque. The least squares procedure, when used as a post-processing step with finite element models, provides a computationally efficient methodology for visualizing the space curve about which all points rotate along a predefined axis. The examples in this study were also used to demonstrate the equivalence of the shear center axis and the axis of twist, as predicted by the Maxwell-Betti reciprocal principle, as long as the same support conditions are applied in both the torsion and cantilever beam bending problems. Thus, for 3D cantilevered structures subjected to transverse loading, it is possible to minimize twisting along the structure's axial dimension by first performing a torsion analysis to determine the axis of twist. Once the axis of twist is known, transverse forces whose resultants pass through the center of twist (shear center), will only cause displacements, with no rotation, for points located on this axis. Visualization of the axis of twist and an understanding of the relationship between the axis of twist and the structure's shear center is a very useful tool for the efficient design of structures subjected to complex transverse loading.

The study modeled fatigue crack growth under welding residual stress conditions and numerically simulated Trans Varestraint and Houldcroft tests. After mapping the residual stress field into a model containing predefined fatigue cracks, simulations were carried out using various fatigue crack growth criteria and the results were compared to assess their predictive accuracy. Of the methods evaluated, the Walker equation proved to be the most

effective in capturing crack extension behavior in a residual stress environment. In contrast, the Paris law significantly underestimated the number of loading cycles required, while the maximum stress intensity factor criterion failed to accurately predict the direction of crack growth. Welding residual stresses have a strong influence on the stress ratio R at the crack tip, thus directly affecting the crack growth behavior. In particular, the effect of the stress ratio on fatigue crack extension is more pronounced in regions with low residual stresses. Hot cracking simulation helps to refine the brittle temperature range (BTR) curve. The solidification and melting behavior during the welding process can be accurately reproduced by using the elemental birth and death technique and a mobile dual ellipsoid heat source model. It is worth noting that elemental solidification exacerbates the development of tensile strains, which are critical for temperature variations during the welding process.

5. Reference

[1] Miller, B.A., and Swartzentruber, P., "Failures of Shafts," ASM Handbook, Volume 11A, Analysis and Prevention of Component and Equipment Failures B.A. Miller, R.J. Shipley, R.J. Parrington, D.P. Dennies, editors, (2021).

[2] Haghshenas, M., and Savich, W., "A Case Study on Fatigue Failure of a Transmission Gearbox Input Shaft," J. Fail. Anal. And Preven., 17, 1119-1125, (2017).

[3] Lorentzen, T., Kjaer, N. E., and Henriksen, T. K., "The Application of Fracture Mechanics to Surface Cracks in Shafts," Engng Fracture Mech., 23(6), 1005-1014, (1986).

[4] Thompson, K. D., and Sheppard, S. D., "Stress Intensity Factors in Shafts Subjected to Torsion and Axial Loading," Engng Fracture Mech., 42(6), 1019-1034, (1992).

[5] Thompson, K. D., and Sheppard, S. D., "Fatigue Crack Growth in Notched and Plain Shafts Subjected to Torsion and Axial Loading," Engng Fracture Mech., 43(1), 55-71, (1992).

[6] Carpinteri, A. and Majorana, C., "Fatigue Growth of Edge Flaws in Cylindrical Bars," Strength of Materials, 27(1), 14-22, (1995).

[7] Lassen, T., and Spagnoli, A., "Fatigue Crack Paths in Shafts Subjected to Bending and Torsion," Proceedings: Int. Conference on Crack Paths (CP 2006), Parma, Italy, (2006).

[8] Wang, J.-A., and Tan, T., "A Method for Evaluating the. Fatigue Crack Growth in Spiral Notch Torsion Fracture Toughness Test," Arch. Appl. Mech., 89, 813-822, (2019).

[9] Fahem, A., Kidane, A., and Sutton, M.A., "Geometry Factors for Mode I Stress Intensity Factor of a Cylindrical Specimen with Spiral Crack Subjected to Torsion," Engng Fracture Mech., 214, 79-94, (2019).

[10] Zdro, R., McConnell, A.J., Peskun, C., Syed, K.A., and Schemitsch, E.H., "Biomedical Measurements of Torsion-Tension Coupling in Human Cadaveric Femurs," J. Biomech Eng., 133(1), Jan. (2011).

[11] Cheong, S. V., Karunaratne, A., Amis, A., Bull, A. M.J., "Strain Rate Dependency of Fractures of Immature Bone," J. Mech Behav Biomed Mater, 66, 68-76, (2017).

[12] Ren, T., and Dailey, H.L., "Mechanoregulation modeling of bone healing in realistic fracture geometries," Biomech Model Mechanobiol, 19, 2307-2322, (2020).

[13] Khor, F., Cronin, D. S., Watson, B., Gierczycka, D., and Malcolm, S., "Importance of Asymmetry and Anisotropy in Predicting Cortical Bone T Response and Fracture Using Human Body Model Femur in Three-Point Bending and Axial Rotation," J. Mech Behav Biomed Mater, 87, 213-229, (2018).

[14] Atluri, S.N., and Nishioka, T., Computational Methods for Three-dimensional Problems of Fracture, Computational Methods in The Mechanics of Fracture, Vol. 2 in Computational Methods in Mechanics, Atluri, S. (ed.), Elsevier Science Publishers: Amsterdam, 229-287, (1986).
[15] Cruse, T.A., "Application of the Boundary-Integral Equation Method to Three Dimensional Stress Analysis," Computers and Structures, 3, 509-527, (1973).
[16] Blackburn, W.S., and Hellen, T.K., "Calculation of Stress Intensity Factors in Three Dimensions by Finite Element Methods," Int. J. Numer. Methods Eng.,11, 211-229, (1972).
[17] deLorenzi, H.G., "Energy Release Rate Calculations by the Finite Element Method," Engng Fracture Mech., 21(1), 129-143, (1985).
[18] Barsoum, R.S., "On the Use of Isoparametric Finite Elements in Linear Fracture Mechanics," Int. J. Numer. Methods Eng., 10, 25-37, (1976).
[19] Carter, B.J., Wawrzynek, P.A., Ingraffea, A.R., "Automated 3-D Crack Growth Simulation," Int. J. Numer. Methods Eng., 47(1-3), 229-253, (2000).
[20] Sukumar N., Moës, N., Belytschko, T., Moran, B., "Extended Finite Element Method for Three-Dimensional Crack Modeling," Int. J. Numer. Methods Eng.,, 48(11), 1549-1570, (2000).
[21] Benzley, S. E., "Representation of Singularities with Isoparametric Finite Elements," Int. J. Numer. Methods Eng., 8, 537-545, (1974).
[22] Hilton, P.D., Kiefer, B.V., and Sih, G.C., "Specialized Finite Element Procedures for Three-Dimensional Crack Problems," Proceedings of the International Conference on Numerical Methods in Fracture Mechanics, Luxmore, A.R., Owen, D.R.J. (eds), Swansea: UK, 411-421, (1978).
[23] Ayhan, A.O. and Nied, H.F. "Stress Intensity Factors for Three-Dimensional Surface Cracks using Enriched Finite Elements," Int. J. Numer. Methods Eng., 54, 899-921, (2002).
[24] Ozkan, U., Kaya, A. C., Loghin, A., Ayhan, A. O., and Nied, H. F., "Fracture Analysis of Cracks in Anisotropic Materials Using 3DFAS and ANSYS," Proceedings of ASME IMECE2006, Chicago, Illinois, Nov. 5-10, (2006).
[25] da Fonte, M., and de Freitas, M., "Stress Intensity Factors for Semi-Elliptical Surface Cracks in Bars under Bending and Torsion," Int. J. Fatigue, 21(5), 457-463, (1999).
[26] Ismail, A.E., Ariffin, A.K., Abdullah, S., Ghazali, M.J., and Daud, R., "Mode III Stress Intensity Factors of Surface Crack in Round Bars," Adv. Mat. Res., 214, 192-196, (2011).
[27] Ismail, A.E., Ariffin, A.K., Abdullah, S., and Ghazali, M.J., "Stress Intensity Factors for Surface Cracks in Round Bar under Single and Combined Loadings," Meccanica, 47, 1141-1156, (2012).

[28] Predan, J., Močilnik, V., and Gubeljak, N., "Stress Intensity Factors for Circumferential Semi-Elliptical Surface Cracks in a Hollow Cylinder Subjected to Pure Torsion," Engg. Fracture Mech., 105, 152-168, (2013).
[29] Teh, S., Andriyana, A., Ramesh, S., Putra, I. S., Kadarno, P., Purbolaksono, J., "Tetrahedral Meshing for a Slanted Semi-Elliptical Surface Crack at a Solid Cylinder, Eng. Fracture Mech., 241, 1-9, (2021).
[30] Citarella, R., Lepore, M., Shlyannikov, V., and Yarullin, R., "Fatigue Surface Crack Growth in Cylindrical Specimen under Combined Loading," Eng Fracture Mech., 131, 439-453, (2014).
[31] Imran, M., Lim, S. F. E., Putra, I. S., Ariffin, A. K., Tan, C. J., Purbolaksono, J., "Assessment of a Planar Inclusion in a Solid Cylinder," Eng. Fail. Anal., 48, 236-245, (2015).
[32] Ramezani, M. K., Purbolaksono, J., Andriyana, A., Ramesh, S. and Putra, I. S., "Empirical Solutions for Stress Intensity Factors of a Surface Crack in a Solid Cylinder Under Pure Torsion," Engng Fracture Mech., 193, 122-136, (2018).
[33] Tanaka, K., Takahash, H., and Akiniwa, Y., "Fatigue Crack Propagation from a Hole in Tubular Specimens under Axial and Torsional Loading," Int. J. Fatigue, 28, 324-334, (2006).
[34] Chandra, D., Putra, I. S., Ariffin, A. K., Mardi, N. A., Nukman, Y., and Purbolaksono J., "Fatigue Growth Analysis of a Surface Crack in a Solid Cylinder under Combined Cyclic Axial-Torsion Loading, Exp. Tech., 40, 1397-1407, (2016).
[35] Chandra, D., Purbolaksono, J., and Nukman, Y., "Surface Crack Growth in a Solid Cylinder Under Combined Cyclic Bending-Torsion Loading," ARPN Journal of Engineering and Applied Sciences, 13(3), (2018).
[36] Okada, H., Kawai, H., Tokuda, T., and Fukui, Y., "Fully Automated Mixed Mode Crack Propagation Analyses Based on Tetrahedral Finite Element and VCCM (virtual crack closure-integral method), Int. J. Fatigue, 50, 33-039, (2013).
[37] Kurt, E., Demir, O., and Ayhan, A. O., "Three-Dimensional Non-Planar Crack Growth Analysis Using Enriched Finite Elements," Int. J. Solids Struct., 241, 11497, (2022).
[38] Timoshenko, S.P., and Goodier, J.N., Theory of Elasticity, 3rd ed., McGraw-Hill, (1970).
[39] Sokolnikoff, I.S., Mathematical Theory of Elasticity, 2nd ed., McGraw-Hill, (1956).
[40] Weinstein, A., "The Center of Shear and the Center of Twist," Q. of Appl. Math., 5, 97-99, (1947). DOI: https://doi.org/10.1090/qam/20437
[41] Stephen, N.G., and Maltbaek, J. C., "The Relationship between the Centres of Flexure and Twist," Int. J. Mech. Sci., 21, 373-377, (1979).

[42] Zerbst U, Ainsworth R, Beier HT, Pisarski H, Zhang Z, Nikbin K, Nitschke-Pagel T, Münstermann S, Kucharczyk P, Klingbeil D. Review on fracture and crack propagation in weldments–A fracture mechanics perspective. Eng Fract Mech 2014;132:200–76. http://dx.doi.org/10.1016/j.engfracmech.2014.05.012.

[43] Malschaert, D., Veljkovic, M., Maljaars., Numerical simulations of residual stress formation and its effect on fatigue crack propagation in a fillet welded T-joint, Eng Fracture Mech., 306, (2024). https://doi.org/10.1016/j.engfracmech.2024.110236.\

[44] Chen S, Guo M, Li Y, Dong X, He J. Effects of residual stresses on fatigue crack propagation of T-joint using extended finite element method (XFEM). Metals 2022;12(8):1368. http://dx.doi.org/10.3390/met12081368.

[45] Wang D, Zhang H, Gong B, Deng C. Residual stress effects on fatigue behaviour of welded T-joint: a finite fracture mechanics approach. Mater Des 2016;91:211–7. http://dx.doi.org/10.1016/j.matdes.2015.11.106.

[46] Zhang W, Jiang W, Zhao X, Tu S-T. Fatigue life of a dissimilar welded joint considering the weld residual stress: Experimental and finite element simulation. Int J Fatigue 2018;109:182–90. http://dx.doi.org/10.1016/j.ijfatigue.2018.01.002.

[47] Gadallah R, Shibahara M, Thickness and weld orientation effects on fatigue crack growth after a single tensile overload, Int. J. Pressure Vessels Piping, 2023, 206. https://doi.org/10.1016/j.ijpvp.2023.105020.

[48] Gadallah R, Shibahara M, Investigation of fracture parameters for a surface-cracked multi-pass T-joint considering welding residual stress, Eng Fract Mech, 2023, 127. https://doi.org/10.1016/j.tafmec.2023.104080.

[49] Senda,Tomio, Matsuda,Fukuhisa, Takano,Genta, Watanabe,Kiyoshi , Kobayashi,Tadaaki, Matsuzaka,Takeshi, Fundamental Investigations on Solidification Crack Susceptibility for Weld Metals with Trans-Varestraint Test, Transactions of the Japan Welding Society, Japan Welding Society, 2, 2, 141-162.

[50] Messler, R. (1999). Weldability and Weld Testing. In Principles of Welding (pp. 577–624). essay, WILEY-VCH.

[51] Citirik, E., Ozkan, U., and Nied, H.F., “Three-Dimensional Fracture Analysis of I-Beams with Fillet Welds,” Int. J. of Terraspace Science and Engineering, 1, 89-97, (2009).

[52] Ayhan, A.O., “Simulation of Three-Dimensional Fatigue Crack Propagation Using Enriched Finite Elements,” Comput. Struct., 89, 801-812, (2011).

[53] ANSYS. Version 12.0 Ansys Inc. Canonsburg, PA, USA, 2009.

[54] Simmetrix Inc, SimModeler Crack 11.0, Installation, User Guide Release Notes,, 10 Executive Park Drive, Clifton Park, NY 12065 USA: http://www.simmetrix.com/index.php/simmodeler/overview.

[55] Erdogan, F., and Sih, G. C., “On the Crack Extension in Plates Under Plane Loading and Transverse Shear,” J. Basic Eng., 85(4), 519-525, (1963).

[56] Paris, P., and Erdogan, F., "A Critical Analysis of Crack Propagation Laws," J. Basic Eng., 85(4), 528-533, (1963).
[57] Southwell, R.V., An Introduction to the Theory of Elasticity, 2nded., Dover Publications, (1969).
[58] Trefftz, E., "Über den Schubmittelpunkt in einem durch eine Einzellast gebogenen Balken," ZAMM, 4, 220-225, (1935).
[59] Leko, T., "The Center of Flexure of an Equilateral Triangle and a Semi-Circular Cross-Section," Int. J. Mech. Sci., 7, 771-775, (1965).
[60] Ecsdei, I., and Baksa A., "Notes on the Centre of Shear," Int. J. of Mech. Eng. Educ., 40(3), 171-260, (2012). https://doi.org/10.7227/IJMEE.40.3.6
[61] Andreas, U.G., and Ruta, G.C., "A Review of the Problem of the Shear Centre(s)," Continum Mech. Thermodyn., 10, 369-380, (1998).
[62] Walker K. The effect of stress ratio during crack propagation and fatigue for 2024-T3 and 7075-T6 aluminum. 1970, http://dx.doi.org/10.1520/STP32032S.
[63] Sanford, R. J. (2003). Principles of Fracture Mechanics. Prentice Hall.
[64] Tada, H., Paris, P. C., and Irwin, G. R., Analysis of Cracks Handbook, ASME Press, New York, (2000).
[65] Lawn, B., Fracture of Brittle Solids, 2nd ed., Cambridge University Press, (1993).
[66] Katori, Hiroaki, "Determination of Shear Center of Arbitrary Cross-Section," World J. of Mech., 6, 249-256, (2016).
[67] Jacobs, J.A., "The Centre of Shear of Aerofoil Sections," J. R. Aero. Soc., Technical Notes, 57, 235-237, (1953).
[68] Anderson, R.F., "The Aerodynamic Characteristics of Six Commonly Used Airfoils Over a Large Range of Positive and Negative Angles of Attack," N.A.C.A, Technical Note No. 397, (1931).

Appendix

Double Ellipsoid heat source:

```
*SET,a,3E-3
*SET,b,4E-3
*SET,c,5E-3
*SET,Q,1200
*SET,t0,20
*SET,v,2.5E-3
*SET,X0,0
*SET,Y0,9E-3
*DEL,_FNCNAME
*DEL,_FNCMTID
*DEL,_FNC_C1
*DEL,_FNC_C2
*DEL,_FNC_C3
*DEL,_FNC_C4
*DEL,_FNC_C5
*DEL,_FNC_C6
*DEL,_FNC_C7
*DEL,_FNC_C8
*DEL,_FNCCSYS
*SET,_FNCNAME,'DE'
*DIM,_FNC_C1,,1
*DIM,_FNC_C2,,1
*DIM,_FNC_C3,,1
*DIM,_FNC_C4,,1
*DIM,_FNC_C5,,1
*DIM,_FNC_C6,,1
*DIM,_FNC_C7,,1
```

```
*DIM,_FNC_C8,,1
*SET,_FNC_C1(1),Q
*SET,_FNC_C2(1),A
*SET,_FNC_C3(1),B
*SET,_FNC_C4(1),C
*SET,_FNC_C5(1),X0
*SET,_FNC_C6(1),Y0
*SET,_FNC_C7(1),V
*SET,_FNC_C8(1),T0
*SET,_FNCCSYS,0
! /INPUT,..\welding\heatsource\DE_HEAT_C.func,,,1
*DIM,%_FNCNAME%,TABLE,10,56,1,,,,%_FNCCSYS%
!
! Begin of equation: 6*sqrt(3)*Q/A/B/C/{PI}/sqrt({PI})*exp(-3*({X}-X0)^2/A^2)*
! exp(-3*({Y}-Y0)^2/B^2)*exp(-3*({Z}-(V*(T0+{TIME})))^2/C^2)
*SET,%_FNCNAME%(0,0,1), 0.0, -999
*SET,%_FNCNAME%(2,0,1), 0.0
*SET,%_FNCNAME%(3,0,1), %_FNC_C1(1)%
*SET,%_FNCNAME%(4,0,1), %_FNC_C2(1)%
*SET,%_FNCNAME%(5,0,1), %_FNC_C3(1)%
*SET,%_FNCNAME%(6,0,1), %_FNC_C4(1)%
*SET,%_FNCNAME%(7,0,1), %_FNC_C5(1)%
*SET,%_FNCNAME%(8,0,1), %_FNC_C6(1)%
*SET,%_FNCNAME%(9,0,1), %_FNC_C7(1)%
*SET,%_FNCNAME%(10,0,1), %_FNC_C8(1)%
*SET,%_FNCNAME%(0,1,1), 1.0, -1, 16, 3, 0, 0, 0
*SET,%_FNCNAME%(0,2,1), 0.0, -2, 0, 6, 0, 0, -1
*SET,%_FNCNAME%(0,3,1),   0, -3, 0, 1, -2, 3, -1
*SET,%_FNCNAME%(0,4,1), 0.0, -1, 0, 1, -3, 3, 17
*SET,%_FNCNAME%(0,5,1), 0.0, -2, 0, 1, -1, 4, 18
```

*SET,%_FNCNAME%(0,6,1), 0.0, -1, 0, 1, -2, 4, 19

*SET,%_FNCNAME%(0,7,1), 0.0, -2, 0, 1, -1, 4, 20

*SET,%_FNCNAME%(0,8,1), 0.0, -1, 0, 3.14159265358979312, 0, 0, -2

*SET,%_FNCNAME%(0,9,1), 0.0, -3, 0, 1, -2, 4, -1

*SET,%_FNCNAME%(0,10,1), 0.0, -1, 16, 3.14159265358979312, 0, 0, 0

*SET,%_FNCNAME%(0,11,1), 0.0, -2, 0, 1, -3, 4, -1

*SET,%_FNCNAME%(0,12,1), 0.0, -1, 0, 0, 0, 0, 0

*SET,%_FNCNAME%(0,13,1), 0.0, -3, 0, 1, 0, 0, -1

*SET,%_FNCNAME%(0,14,1), 0.0, -4, 0, 1, -1, 2, -3

*SET,%_FNCNAME%(0,15,1), 0.0, -1, 0, 3, 0, 0, -4

*SET,%_FNCNAME%(0,16,1), 0.0, -3, 0, 1, -4, 3, -1

*SET,%_FNCNAME%(0,17,1), 0.0, -1, 0, 1, 2, 2, 21

*SET,%_FNCNAME%(0,18,1), 0.0, -4, 0, 2, 0, 0, -1

*SET,%_FNCNAME%(0,19,1), 0.0, -5, 0, 1, -1, 17, -4

*SET,%_FNCNAME%(0,20,1), 0.0, -1, 0, 1, -3, 3, -5

*SET,%_FNCNAME%(0,21,1), 0.0, -3, 0, 2, 0, 0, 18

*SET,%_FNCNAME%(0,22,1), 0.0, -4, 0, 1, 18, 17, -3

*SET,%_FNCNAME%(0,23,1), 0.0, -3, 0, 1, -1, 4, -4

*SET,%_FNCNAME%(0,24,1), 0.0, -1, 7, 1, -3, 0, 0

*SET,%_FNCNAME%(0,25,1), 0.0, -3, 0, 1, -2, 3, -1

*SET,%_FNCNAME%(0,26,1), 0.0, -1, 0, 0, 0, 0, 0

*SET,%_FNCNAME%(0,27,1), 0.0, -2, 0, 1, 0, 0, -1

*SET,%_FNCNAME%(0,28,1), 0.0, -4, 0, 1, -1, 2, -2

*SET,%_FNCNAME%(0,29,1), 0.0, -1, 0, 3, 0, 0, -4

*SET,%_FNCNAME%(0,30,1), 0.0, -2, 0, 1, -4, 3, -1

*SET,%_FNCNAME%(0,31,1), 0.0, -1, 0, 1, 3, 2, 22

*SET,%_FNCNAME%(0,32,1), 0.0, -4, 0, 2, 0, 0, -1

*SET,%_FNCNAME%(0,33,1), 0.0, -5, 0, 1, -1, 17, -4

*SET,%_FNCNAME%(0,34,1), 0.0, -1, 0, 1, -2, 3, -5

*SET,%_FNCNAME%(0,35,1), 0.0, -2, 0, 2, 0, 0, 19

```
*SET,%_FNCNAME%(0,36,1), 0.0, -4, 0, 1, 19, 17, -2
*SET,%_FNCNAME%(0,37,1), 0.0, -2, 0, 1, -1, 4, -4
*SET,%_FNCNAME%(0,38,1), 0.0, -1, 7, 1, -2, 0, 0
*SET,%_FNCNAME%(0,39,1), 0.0, -2, 0, 1, -3, 3, -1
*SET,%_FNCNAME%(0,40,1), 0.0, -1, 0, 0, 0, 0, 0
*SET,%_FNCNAME%(0,41,1), 0.0, -3, 0, 1, 0, 0, -1
*SET,%_FNCNAME%(0,42,1), 0.0, -4, 0, 1, -1, 2, -3
*SET,%_FNCNAME%(0,43,1), 0.0, -1, 0, 3, 0, 0, -4
*SET,%_FNCNAME%(0,44,1), 0.0, -3, 0, 1, -4, 3, -1
*SET,%_FNCNAME%(0,45,1), 0.0, -1, 0, 1, 24, 1, 1
*SET,%_FNCNAME%(0,46,1), 0.0, -4, 0, 1, 23, 3, -1
*SET,%_FNCNAME%(0,47,1), 0.0, -1, 0, 1, 4, 2, -4
*SET,%_FNCNAME%(0,48,1), 0.0, -4, 0, 2, 0, 0, -1
*SET,%_FNCNAME%(0,49,1), 0.0, -5, 0, 1, -1, 17, -4
*SET,%_FNCNAME%(0,50,1), 0.0, -1, 0, 1, -3, 3, -5
*SET,%_FNCNAME%(0,51,1), 0.0, -3, 0, 2, 0, 0, 20
*SET,%_FNCNAME%(0,52,1), 0.0, -4, 0, 1, 20, 17, -3
*SET,%_FNCNAME%(0,53,1), 0.0, -3, 0, 1, -1, 4, -4
*SET,%_FNCNAME%(0,54,1), 0.0, -1, 7, 1, -3, 0, 0
*SET,%_FNCNAME%(0,55,1), 0.0, -3, 0, 1, -2, 3, -1
*SET,%_FNCNAME%(0,56,1), 0.0, 99, 0, 1, -3, 0, 0
! End of equation: 6*sqrt(3)*Q/A/B/C/{PI}/sqrt({PI})*exp(-3*({X}-X0)^2/A^2)*exp
! (-3*({Y}-Y0)^2/B^2)*exp(-3*({Z}-(V*(T0+{TIME})))^2/C^2)
!-->
/SOLU
NROPT,FULL, ,ON
ANTYPE,4
TRNOPT,FULL
TREF,22
PRED,ON
```

```
KBC,0
OUTRES,ALL,ALL
TIMINT,ON
AUTOTS,ON
ALLSEL
CMSEL,S,COOLING
SF,ALL,CONV,50,22
ALLSEL
TIMINT,ON
*DO,I,0.2,20,0.2
TIME,I
DELTIM,0.2,0.2,0.2
CMSEL,S,WELD_PART
BF,ALL,HGEN, %DE%
ALLSEL
SOLVE
BFDELE,ALL,HGEN
*ENDDO
```

Welding:

/PREP7

*DIM,MELTDATA,ARRAY,100,400

*VREAD,MELTDATA,'E:\welding\command summary\MELTDATA\MELTDATA',TXT,,JIK,400,100,1

(400E16.6)

*dim,n_loc,array,17979,2

*vread,n_loc,'E:\welding\command summary\meltdata\disp_y',txt,,JIK,2,17979,1

(2E16.7)

KE=1 !KILLED ELEMENT

/SOLU

NROPT,FULL,,ON

ANTYPE,4

TRNOPT,FULL

NLGEOM,ON

TREF,22

PRED,ON

KBC,0

OUTRES,ALL

TIMINT,ON

AUTOTS,ON

EQSLV,SPARSE,,2

LNSRCH,ON

PSTRES,1

LUMPM,0

WSPRINGS

ALLSEL

CMSEL,S,FIXEDS

D,ALL,ALL

```
KKK=1
ALLSEL
*DO,I,0.2,12,0.2
ALLSEL
LDREAD,TEMP,KKK,,,,'E:\welding\DISSERTATION_files\dp0\SYS-
8\MECH\FILE',RTH!
TIME,I
DELTIM,0.2,0.2,0.2,ON
ALLSEL
NROPT,FULL,,ON
*DO,J,1,400,1
KE=MELTDATA(KKK,J)
*IF,KE,GT,0,THEN
NSEL,S,,,KE
ESLN,S,,,
EKILL,ALL
ALLSEL
*ENDIF
*ENDDO
ALLSEL
*IF,I,GE,10,THEN
ALLSEL
*DO,LL,1,17979
D,n_loc(LL,1),uy,n_loc(LL,2)
*ENDDO
*ENDIF
ALLSEL
NEQIT,100
SOLVE
KKK=KKK+1
```

```
ALLSEL
EALIVE,ALL
ALLSEL
*ENDDO
ALLSEL
```

Center of twist:

```
/PREP7                                  !Enter pre-preparation section
NUM_LAYER=101                           !Number of layers along the length
*DIM,TCENTER,ARRAY,NUM_LAYER,3,1, , , !NUM_LAYER X 3 matrix
K=1                                     !Set up surface increment
/POST1                                  !Enter post-solution section
*DO,I,1,101,1                           !Enter loop
SUCR,CUTSURF,CPLANE,,                   !Generate surface
SUSEL,S,CUTSURF!SELECT SURF
SUMAP,,U,X!MAP RESULTS IN X             !Mapping results on the surface
SUGET,CUTSURF,UX,X1,1
SUMAP,,U,Y!MAP RESULTS IN Y
SUGET,CUTSURF,UY,Y1,1
*GET,LENGTH,PARM,X1,DIM,1
AA=0                                    !Apply least square method
BB=0
CC=0
CC1=0
CC2=0
DD=0
EE=0
FF=0
FF1=0
FF2=0
*DO,J,1,LENGTH,1
AA=AA+2*X1(J,8)*X1(J,8)
BB=BB+2*X1(J,8)*Y1(J,8)
CC1=CC1+2*X1(J,8)*X1(J,8)*X1(J,1)+X1(J,8)*X1(J,8)*X1(J,8)
CC2=CC2+2*Y1(J,8)*X1(J,8)*X1(J,2)+Y1(J,8)*Y1(J,8)*X1(J,8)
DD=DD+2*X1(J,8)*Y1(J,8)
```

```
    EE=EE+2*Y1(J,8)*Y1(J,8)
    FF1=FF1+2*Y1(J,8)*Y1(J,8)*Y1(J,2)+Y1(J,8)*Y1(J,8)*Y1(J,8)
    FF2=FF2+2*Y1(J,8)*X1(J,8)*X1(J,1)+X1(J,8)*X1(J,8)*Y1(J,8)
    *ENDDO
    CC=CC1+CC2
    FF=FF1+FF2
    X0=(-EE*CC+BB*FF)/(AA*EE-DD*BB)
    Y0=(-AA*FF+DD*CC)/(AA*EE-DD*BB)
    TCENTER(I,1)=-X0                    !Enter calculated shear center (center of twist)
into matrix
    TCENTER(I,2)=-Y0
    TCENTER(I,3)=(I-1)*K
    *IF,I,LT,101,THEN
    WPOFFS,,,K                          !Offset the surface
    *DEL,,17
    *DEL,,18
    SUDEL,CUTSURF
    *ENDIF
    *ENDDO
    FINISH
```

VITA

Haomin Fu was born on July 28, 1997 in Zhengzhou, China. Before attending Lehigh University, he earned his Bachelor of Engineering in Nanjing University of Science & Technology in May 2019 in Nanjing, China. He pursued Mater of Science in Mechanical Engineering in Lehigh University from 2019 to 2021 and continue his Ph.D. career with Professor Herman F. Nied in Mechanical Engineering.